Electrocatalytic Activity and Selectivity - a Density Functional Theory Study

Karamad, Mohammadreza

Publication date:
2013

Document Version
Publisher's PDF, also known as Version of record

Electrocatalytic Activity and Selectivity-a Density Functional Theory Study

Mohammadreza Karamad

Ph.D. Thesis
November 2013

Center for Atomic-scale Materials Design
Department of Physics
Technical University of Denmark
DK-2800 Kgs. Lyngby, Denmark

Contents

Preface

This thesis is submitted for the Ph.D. degree in physics from Technical University of Denmark (DTU). The work has been carried out at the Center for Atomic-scale Material Design (CAMd), Department of Physics between November 2010 and November 2013, under the supervision of Associate Professor Jan Rossmeisl.

First and foremost, I would like to express the deepest appreciation to my supervisor Professor Jan Rossmeisl, who has shown the attitude and the substance of a genius. I would like to thank him for the excellent supervision and constant flow of ideas throughout the three years of my Ph.D. course. I feel privileged for having worked with him.

I would also like to thank Professor Jens Nørskov who allowed me to visit his group in Stanford University and enjoy the pleasure of working on an exciting project and adoring his brilliant supervision. A special thanks to Heine A. Hansen for all his insightful comments, wonderful collaboration, and all the valuable discussions during my stay.

Furthermore, this would have not been such an adventure if I had not had collaboration with experimentalists at CINF. I specifically wish to thank Professor Ib Chorkendorff and Ifan Stephens, Ana Sofia Varela Gasque, and Arnau Verdaguer Casedeval for the valuable and insightful ideas and discussions.

I have been very privileged to get to know other great people in the department of physics who I call them friend now including Anne Hansen and Inge Toldsted. Thank you for your hospitality and all of your helps.

I also want to thank Mårten Bjorketon and Vladimir Tripkovic for their entire treasured discussion we had during my PhD, which broadened my horizon. I also like to thank Mårten for all the shared moments.

Special thanks to my officemates, Simon Hedegaard Brodersen, Ulrik Grønbjerg Vej-Hansen, Rizwan Ahmed and Tuhin Suvra Khan for creating such an enjoyable environment. Thanks to Simon and Ulrik for translating the abstract. Here, I want to thank to thank all my CAMd friends.

I want to thank Mårten Bjorketon,Vladimir Tripkovic and Mohnish Pandey for proofreading the thesis.

My everyday work would have not been productive without valuable help from computer staff Marcin Dulak and Ole Holm Nielsen. Special thanks to Marcin who have always been supportive and kind to help me regarding the errors in calculations.

I also would like to thank the head of administration Marianne Ærøse who has been supportive for the administration issues and made these three years smooth.

Dozens of people have made life enjoyable and were supportive in all the hard moments. Here I wish to thank all my Persian friends and their families including Gonabad, Maknun, Abbas, and Ali Akbar. Thanks to all of you for sharing the moments and I am happy that I have friends like you.

I would like also to appreciate three of my best friends Hazhir Afzali, Hamid Bohlul and Sanjeev Kumar for all their encouragements.

Finally, I wish to thank my parents for their endless support in my life. I owe them everything and wish I could show them just how much I love and appreciate them. I would like to thank my brothers and sisters for their support and encouragements. Last but not least, I wish to extend my deepest gratitude to my beloved wife, Samira, whose love and encouragement allowed me to finish this journey. She already has my heart so I will just give her a heartfelt “thanks”.

Mohammadreza Karamad

November 2013

Abstract

The focus of the current PhD thesis is to design new electro-catalysts, by changing the morphology and composition of the catalysts, to tune the electro-catalytic performance. We use Density Functional Theory (DFT) calculations, to examine activity, selectivity and stability of the designed electro-catalysts towards two appealing electrochemical reactions: 1)electroreduction of CO_2 to hydrocarbons and alcohols, and 2) electrochemical production of hydrogen peroxide, i.e. H_2O_2, from its elements i.e. H_2 and O_2.

The thesis is divided into three parts:

In the first part, electro-catalytic activity of different Pt/Cu(111) systems forming by incorporating some quantities of Cu into first and second layers of Pt(111) including Surface Alloys (SA), Cu Overlayer (OL) and Near Surface Alloy (NSA) is considered. This study shows how the reactivity of Pt(111), i.e. interaction with adsorbates, changes by the location of Cu atoms into different layers of Pt(111). While the presence of Cu into the surface layer strengthens the interaction between surface and adsorbates, the presence of Cu atoms into the subsurface layer has the opposite effect. These findings can be used to design new electro-catalysts for electrochemical reactions. We consider electrochemical oxidation of CO as a test reaction to evaluate the catalytic activity of different Pt/Cu(111) systems, and find unique agreement between experiments and DFT calculations.

In the second part, we tackle two associated remarkable problems to the electrochemical reduction of CO_2 at the cathode side: 1) high overpotential that hinders this reaction from being an energy efficient process, and 2) low selectivity towards desired reaction products. We have taken two approaches to improve the selectivity and activity in the reduction of CO_2. Firstly, we create the isolated sites that are active for CO_2 reduction and surrounded by inactive elements towards both hydrogen evolution reaction (HER) and CO_2 reduction to direct the selectivity towards favorable products. In the next step, using this concept we screen for suitable catalysts. Our screening includes

both metallic and functionalized graphene catalysts. Secondly, we considered CO_2 reduction on RuO_2, which has a distinctive catalytic activity and selectivity compared to Cu to get insight into mechanistic pathway of the CO_2 reduction.

Finally, in the last part, we have taken advantage of the isolated active site concept to tune the activity and selectivity for oxygen reduction towards H_2O_2 production. We screen for new catalysts that exhibit both high catalytic activity and selectivity by constructing activity volcano plots for ORR towards water and H_2O_2. Moreover, the stability of these catalysts is examined. Our model predicts Pt–Hg as a promising catalyst with unprecedented combination of activity, selectivity and stability.

Resumé

Fokus i denne Ph.d. afhandling er på at designe nye elektrokatalysatorer ved at ændre morfologien og kompositionen af katalysatorer med henblik på at forbedre den elektrokatalytiske effekt. Vi benytter Tætheds Funktional Teori (DFT) til at undersøge aktivitet, selektivitet og stabilitet af de designede elektrokatalysatorer med henblik på to tiltalende elektrokemiske reaktioner: 1) reduktion af CO_2 til kulbrinter og alkoholer, og 2) produktion af hydrogen peroxid, H_2O_2, fra dets elementer ilt og brint.

Afhandlingen er delt i tre dele:

I første del studeres den elektrokatalytiske aktivitet af forskellige Pt/Cu(111) systemer, hvor varierende mængder af Cu er integreret i det første og andet lag af Pt(111), herunder overflade legeringer, Cu overlag og nær overflade legeringer. Dette studie viser hvordan reaktiviteten af Pt(111), givet ved interaktionen med adsorbater, ændres af placeringen af Cu atomerne. Mens tilstedeværelse af Cu i overfladen forøger interaktionen mellem overflade og adsorbat, så reduceres interaktionen ved tilstedeværelsen af Cu under overfladen. Disse resultater kan blive brugt til at designe nye elektrokatalysatorer til elektrokemiske reaktioner. Elektrokemisk reduktion af CO benyttes som testreaktion til at vurdere de forskellige Pt/Cu(111) systemers katalytiske aktivitet, og vi finder en unik sammenhæng mellem eksperimenter og DFT beregninger.

I anden del håndtere vi to knyttede og bemærkelsesværdige problemer med elektrokemisk reduktion af CO_2 ved katoden: 1) det høje overpotentiale, som forhindrer denne reaktion i at være energieffektiv, og 2) den lave selektivitet i forhold til ønskede produkter. Vi har forfulgt to forskellige metoder til at forbedre selektiviteten og aktiviteten af reduktionen af CO_2. For det først har vi etableret isolerede steder, der er aktive i forhold til reduktion af CO_2 og omringet af inaktive elementer, i forhold til både hydrogen evolution og reduktion af CO_2, med henblik på at tilrette selektiviteten, så de ønskede produkter dannes. Dette koncept er blevet benyttet til at screene for anvendelige katalysatorer, hvor både katalysatorer af metaller og funktionaliseret grafen er taget i betragtning. For det andet har vi undersøgt reduktionen af CO_2 på RuO_2 katalysatorer, som har en markant anderledes katalytisk aktivitet og selektivitet sammenlignet med Cu, for at opnå indsigt i

den mekanistiske reaktionsvej for reduktion af CO_2.

I sidste del udnytter vi konceptet med et isoleret aktivt sted til at justere aktiviteten og selektiviteten af reduktionen af oxygen med henblik på produktion af H_2O_2. Vi screener for nye katalysatorer, der udviser både høj katalytisk aktivitet og selektivitet, ved at konstruere vulkanplots af aktiviteten for reduktion af oxygen til vand of H_2O_2. Herudover er stabiliteten af katalysatorerne også undersøgt. Vores model forudsiger, at Pt-Hg vil være en lovende katalysator med en hidtil uset kombination af aktivitet, selektivitet og stabilitet.

List of Included Papers

Paper I

Design of an Active Site towards Optimal Electrocatalysis: Overlayers, Surface Alloys and Near-Surface Alloys of Cu/Pt(111)

A. S. Bandarenka, A. S. Varela, M. Karamad, F. Calle-Vallejo, L. Bech, F. J. Perez-Alonso, J. Rossmeisl, I. E. L. Stephens, and I. Chorkendorff

Angew. Chemie **124,** 12015–12018 (2012).

Paper II

Electrochemical CO_2 and CO Reduction on Metal-Functionalized Porphyrin-like Graphene

V. Tripkovic, M. Vanin, M. Karamad, M. E. Björketun, K. W. Jacobsen, K. S. Thygesen, and J. Rossmeisl

J. Phys. Chem. C, **117,** 9187–9195 (2013).

Paper III

Enabling direct H_2O_2 production through rational electrocatalyst design

S. Siahrostami, A. Verdaguer-Casadevall, M. Karamad, D. Deiana, P. Malacrida, B. Wickman, M. Escudero-Escribano, E. A. Paoli, R. Frydendal, T. W. Hansen, I. Chorkendorff, I. Stephens, and J. Rossmeisl

Nat. Mater., **12,** 1137–1143 (2013).

Paper IV

Intermetallic alloys as CO_2/CO reduction electrocatalysts – the role of electronic and geometric Effects

M. Karamad , V. Tripkovic, and J. Rossmeisl

To be submitted.

Paper V

Mechanistic pathway in the electrochemical reduction of CO_2 to methanol on RuO_2

M. Karamad, H. A. Hansen, J. Rossmeisl, and J. K. Nørskov

To be submitted.

Patent

Filed Patent application EP 13165265.3, Title: Alloy catalyst material, 2013.

Introduction

Fossil fuels including coal, oil and natural gas are currently the primary sources of energy and chemical products [[1]]. However, the fossil fuels are not infinite and they are going to drop. On top of that, the growth in the world's population as well as industrialization of developing countries has increased global demand for fuel and the concern is whether world fuel supplies will be able to fulfill increasing demand. On the other hand, burning of fossil fuels causes environmental effects by emission of greenhouse gas such as CO_2. This calls for replacement of fossil fuels with other clean renewable energy resources such as hydro, wind and solar [[2]]. However, the intermittency of these renewable energy resources raises some issues, and calls for practical energy storage. This can be accomplished by storing the excess energy into chemical bonds for later and on-demand uses. More specifically, it has a great impact in reducing the amount of CO_2, if the excess energy is used to convert CO_2, captured from atmosphere, into chemical fuels such as methane and methanol [[3]]. Clearly, catalysts play a central role in achieving this goal.

In principle, these processes involve converting electrical energy to chemical energy and electrochemistry plays an important role in this area. To make an electrochemical reaction an efficient process, a desired catalyst with high activity and selectivity towards favorable reaction products is needed. The selectivity and activity of a given catalyst are governed by the chemical properties of the active sites on the surface [[4]]. Recent developments in Density Functional Theory (DFT) calculations and surface science techniques have provided atomic-scale insight into the nature of active sites and fundamental understanding of electrochemical reactions [[5]]. For example, electrochemical reduction of CO_2 to hydrocarbons and alcohols, and electrochemical production of hydrogen peroxide, H_2O_2, from its elements, i.e. H_2 and O_2, are two appealing electrochemical reactions in a future energy perspective, where DFT calculations have been used to elucidate their reaction mechanisms by identifying reaction intermediates and the factors that control their electrocatalytic activity and selectivity [[6,7]]. Additionally, these examples also reveal that in practice, there are many challenges associated with designing catalysts and tuning both selectivity and activity.

In the electrochemical reduction of CO_2, hydrogen evolution reaction (HER)

presents a parasitic reaction that should be avoided to achieve high selectivity towards desired products, such as hydrocarbons and alcohols[8]. Moreover, electrochemical reduction of CO_2 is accompanied with high overpotential even on the best-known metallic catalysts, i.e. Cu, hindering this reaction from being an energy efficient process. On the other hand, global spread and implementation of electrolytic cells for electrochemical synthesis of H_2O_2 is contingent upon development of catalysts that exhibit a combination of activity, selectivity and stability [9].

In this thesis, our goal is to address the aforementioned challenges by designing catalysts with specific sites to tune the activity and selectivity for the two above appealing electrochemical reactions.

Outline

In Chapter 1, a brief introduction to the electronic structure theory and the methods relevant to the thesis will be given. Chapter 2 describes the change in the reactivity of Pt(111) when Cu atoms are incorporated in two first layers of Pt(111), forming Cu/Pt(111) surface alloy (SA), near surface alloy and overlayer systems. We find that the position of Cu in Pt(111) controls its interaction. We examine electro-catalytic activity of different Cu/Pt(111) systems for CO electro-oxidation as a test reaction. Experiments performed by Ib Chorkendorff and co-workers on the same systems show an unprecedented agreement between DFT calculations and experiment.

In chapter 3, we describe a new strategy to suppress HER in the electrochemical reduction of CO_2 by creating isolated sites on the surface that only facilitate reduction of CO_2. We consider electrochemical reduction of CO_2 on Cu/Pt(111) surface alloy (SA) and Pt/Hg alloys, two model systems with isolated sites on the catalyst surface. This consideration defined the criteria that should be fulfilled to suppress HER. In Chapter 4, we employ the concept of isolated active sites and these criteria to screen a pool of binary bulk alloy catalysts for selective electrochemical reduction of CO_2. Among the pool of binary alloys considered in this work, five alloys were found to be highly selective for CO reduction. In chapter 5, we consider electrochemical reduction of CO_2 on functionalized graphene, namely metal-functionalized graphene structures with metal atoms as isolated active site. We construct volcano plots using scaling relations between

CO_2 reduction intermediates to identify the best catalyst candidate. Moreover, we examine the catalytic activity of the metal–porphyrins for HER/HOR.

In chapter 6, we take advantage of the isolated site concept and screen for new catalysts with high selectivity and activity for electrochemical reduction of oxygen to H_2O_2. We identify $PtHg_4$ as a catalyst that exhibits exceptional combination of activity, selectivity and stability for H_2O_2 production. Subsequent experiments performed by Ifan Stephen and co-workers confirm the theoretical predictions.

In chapter 7, we consider CO_2 reduction on RuO_2, which has a distinctive catalytic activity and selectivity compared to Cu, to get insight into mechanistic pathway. We construct the free energy diagram for the minimum energy pathway for CO_2 reduction on the stable surface structures under electrochemical conditions. This mechanistic pathway is being compared with the one for CO_2 reduction on Cu.

Chapter 1

Theoretical Background

1.1 Electronic Structure Calculations

In this section I will provide a short summary of the basics of the density functional theory (DFT) that has been used in this thesis. In particular, I will briefly review the formalism of the DFT.

1.1.1 The Many-Body Problem

In Physics and chemistry, many material properties can be determined by solving the time independent Schrödinger equation:

$$H_{tot}\,\Psi_{tot}(R,r) = E_{tot}\,\Psi_{tot}(R,r) \qquad (1\text{-}1)$$

where H_{tot} , $\Psi_{tot}(R,r)$ and E_{tot} are the total Hamiltonian of the system, total wavefunction and total energy of the system, respectively. The Hamiltonian itself contains the following terms:

$$H_{tot} = \frac{\hbar^2}{2m}\sum_{i=1}^{N}\nabla_i^2 - \sum_{i,I}^{N}\frac{Z_I e^2}{|r_i - R_I|} + \frac{1}{2}\sum_{i,j}^{N}\frac{e^2}{|r_i - r_j|} - \frac{\hbar^2}{2M}\sum_{I}^{N}\nabla_I^2 + \frac{1}{2}\sum_{i,j}^{N}\frac{Z_I Z_J e^2}{|R_I - R_J|} \qquad (1\text{-}2)$$

where the first term is the kinetic energy of the electrons, the second term is Columbic

interaction between electrons and nuclei, the third term describes the Columbic interaction between electrons, the forth term describes the kinetic energy of the nuclei, and the last term describes the Columbic interaction between nuclei. We note that the first three terms describe the electronic part, while the last two terms describe the nuclei part of the Hamiltonian. Solving of the Schrödinger equation will determine E_{tot} and Ψ_{tot} for the electronic system. However, solving this equation except for the simple cases where there are few atoms is not possible. Therefore, to study the properties of the materials that consist of huge number of electrons and nuclei, other approaches for solving Schrödinger equation should be used.

1.1.2 Born-Oppenheimer Approximation

In Born-Oppenheimer Approximation, the electrons and nuclear degrees of freedom are separated [10]. This is due to the fact that nuclei are much larger and massive than electrons. Therefore, the nuclei are fixed and the kinetic terms of the nuclei (the last two terms in (1-2)) is neglected and added to the electronic part of the Hamiltonian. This simplifies the electronic problem and allows for separation of the wave function in two parts, electronic and nuclei parts as following:

$$\Psi_{tot}(R, r)= \Psi_e(R,r)\Psi_n(R) \qquad (1\text{-}3)$$

where $\Psi_e(R,r)$ and $\Psi_n(R)$ are the electronic and nuclei wave functions, respectively. With this simplification the Hamiltonian can be separated to two independent Schrödinger equations. Here we focus on the electronic part:

$$H_e\, \Psi_e(R,r)= E_e\, \Psi_e(R,r) \qquad (1\text{-}4)$$

where H_e is the Hamiltonian for the electronic part, and

$$H_e=\hat{T}_e+\hat{V}_{ee}+\hat{V}_{ext}= \frac{\hbar^2}{2m}\sum_{i=1}^{N}\nabla_i^2 + \frac{1}{2}\sum_{i,j}^{N}\frac{e^2}{|r_i-r_j|} - \sum_{i,I}^{N}\frac{Z_I\, e^2}{|r_i-R_I|} \qquad (1\text{-}5)$$

$\hat{T}_e$, $\hat{V}_{ext}$ and $\hat{V}_{ee}$ are the kinetic energy of electrons, the potential energies from the nucleus-electron and electron-electron, respectively. $\hat{V}_{ext}$ represents the external potential

that the electrons move in.

Even with the Born—Oppenheimer simplification, this equation cannot be solved for many-electron systems and another approximation is needed. In fact, for an electronic system consists of N electrons, there are 3N degrees of freedom that make it difficult to solve equation (1-4). Basically, there are two different approaches for solving the electronic part: wave function based, such as Hartree-Fock approximation, and electronic density-base. In the first category, the wave function, i.e. a function of electrons coordination, is used as a variable to solve equation (1-4). On the other hand, in the density-based approximation, the electron density, $\rho(r)$, which is independent of the number of electrons, is the central quantity to solve the equation (1-4). This means the number of variables will decrease from 3N in the wavefunction-based approach to 3 in the density-based for a N-electron system. Since we use electronic density-based approach, in the following we restrict our discussion to the density-based approach. Two theorems, which were introduced by Hohenberg and Kohn in 1964 and then developed, by Kohn and Sham are the basis of the density functional theory [[11]]. In the following we briefly explain these two theorems.

1.1.3 Hohenberg-Kohn Theorems

1.1.3.1 First Theorem

The first theorem states that the external potential and hence the Hamiltonian is uniquely determined by the ground state electron density. Therefore, the total energy of the system can be written as a functional of the electron density:

$$E[\rho] = \left\langle \Psi_0[\rho] \middle| \hat{H} \middle| \Psi_0[\rho] \right\rangle = T[\rho] + V_{ee}[\rho] + V_{ext}[\rho] = F_{HK}[\rho] + V_{ext}[\rho] \quad (1\text{-}6)$$

where the Hohenberg-Kohn functional, $F_{HK}[\rho]$ can be evaluated as below and is not dependent on external potential:

$$F_{HK}[\rho] = \left\langle \psi[\rho] \middle| \hat{T} + \hat{V}_{ee} \middle| \psi[\rho] \right\rangle \quad (1\text{-}7)$$

1.1.3.2 Second Theorem

The second theorem suggests a way to find the wave function corresponding to the external potential. It states that the ground-state density, $\rho_0(r)$, is the density that minimizes $E[\rho]$. This means, for a given density, ρ, the energy provides an upper bound to the exact ground state energy E_0:

$$E_0=E[\rho_0(r)]\leq E[\rho(r)] \tag{1-8}$$

This means, the ground state energy is obtained through a minimization problem. However, this theoretical foundation does not give any means to determine the ground state wave function. Therefore, these theorems alone cannot be used to treat large systems using quantum mechanics.

1.1.4 Kohn-Sham equations

A possible route to solve the problem of finding the ground-state energy was suggested by Kohn and Sham in 1965 [12]. The idea to calculate the electron density of a real interacting electronic system is to assume a non-interacting electronic system, Kohn-Sham system that has the same electronic density as the real interacting electronic system and experiences an effective potential. In fact, all other contributions for the interacting system including non-direct electron-electron interactions, i.e. exchange and correlation contributions are incorporated into one term $E_{xc}[\rho]$ that is added to non-interacting system. In this formalism, the Kohn-Sham Hamiltonian is expressed as below:

$$H_{KS}(r)=-\frac{1}{2}\nabla^2+V_{eff}(r) \tag{1-9}$$

where,

$$V_{eff}(r)=V_{ext}(r)+V_{Hartree}(r)+V_{xc}(r) \tag{1-10}$$

$V_{ext}(r)$ is the external potential and $V_{Hartree}(r)$ is the classically self-interaction energy of the density:

$$V_{Hartree}(r) = \frac{1}{2}\int d^3r\, d^3r' \frac{\rho(r)\rho(r')}{|r-r'|} \qquad (1\text{-}11)$$

and $V_{xc}(r)$, is the functional derivative of the exchange-correlation energy functional, $E_{xc}[\rho]$:

$$V_{xc}(r) = \frac{\delta\, E_{xc}([\rho],r)}{\delta\rho(r)}\bigg|_{\rho=\rho_0} \qquad (1\text{-}12)$$

We note that V_{eff} is a functional of the electronic density, $\rho(r)$. To calculate the ground state energy, the Schrödinger equation with the effective potential should be solved:

$$\left(\frac{\hbar^2}{2m}\sum_{i=1}^{N}\nabla_i^2 + V_{eff}(\rho)\right)\phi_i(r) = E_i\,\phi_i(r) \qquad (1\text{-}13)$$

The wavefunctions $\phi_i(r)$ are not known and should be calculated by solving (1-13) self consistently. In this scenario, the ground state density is calculated as below:

$$\rho(r) = \sum_{i=1}^{N}|\phi_i(r)|^2 \qquad (1\text{-}14)$$

Now, the problem reduces to adequately determine the exchange-correlation potential. There are different approaches for calculating exchange-correlation potential. The simplest one is local density approximation (LDA) that suggested by Kohn and Sham [12]. In this approach, the inhomogeneous electronic system is approximated as uniform electron gas:

$$E_{xc}^{LDA}[\rho] = \int \rho(\vec{r})\ \varepsilon_{xc}^{uni}(\rho(\vec{r}))\ d\ \vec{r} \qquad (1\text{-}15)$$

Though LDA perform reasonably well in predicting the lattice parameters, it gives overestimated binding energies.

Improvement over LDA has been suggested by taking into account the density gradients which is called generalized gradient approximation (GGA). In this formalism, the exchange-correlation potential is not only the function of electron density, but also is a function of the density gradient:

$$E_{xc}^{GGA}[\rho] = \int \rho(\vec{r})\ \varepsilon_{xc}^{GGA}(\rho(\vec{r}), \nabla\rho(\vec{r}))\ d\ \vec{r} \qquad (1\text{-}16)$$

Several functionals according to the GGA are developed such as Perdew-Wang-91(PW-91) [13], Perdew-Burke-Ennzerhof (PBE) [14], revPBE[15] and RPBE[16]. Though PBE have been widely used to calculate the binding energies, RPBE has improvements over PBE in calculating the binding energies. Throughout this thesis, RPBE has been used as functional.

1.1.5 Psedopotentials

The electrons in atoms can be divided into two parts: tightly bound core electrons due to strong Coulomb attraction from nucleus and valance electrons. The core electrons do not participate in the chemistry and therefore, the chemical properties of the atoms depend on the valance electrons. On the other hand, the wavefunctions oscillate at the region near the core making it computationally expensive to describe the behavior of all the electrons. It fact, the description of the wavefuction at the core region presents one of the problems in implementation of DFT codes. The approach to deal with this problem is to describe the core electrons by psedopotentials that are smoother and easier to describe numerically. We note that the psedopotentials should describe the potential that is felt by valance electrons. The behavior of the core electrons is described differently when implementing different codes. In Dacapo code, this is accomplished by using ultra-soft

psedopotentials. In the Projected Augmented Wave (PAW) method, on the other hand, is an all-electron method where the all-electron wave function is described in terms of the smooth psedo-wavefunction in the valance region and the local basis sets in the core region.

1.1.6 Implementation

Throughout this thesis, two DFT codes have been used: GPAW (Grid based Projected Augmented Wave) and DACAPO. In the following, I will briefly overview some important aspects of these two codes.

1.1.6.1 Dacapo

Since we are considering systems that are periodic in either two- or three-dimensional space, such as bulk and surface of metals respectively, a periodic approach in solving the Kohn-sham equations is more suitable as it allows for taking advantage of periodic boundary conditions. Therefore, in Dacapo code, we take advantage of Bloch's theorem where the wave function can be written as the product of a plane wave and a function with the periodicity of system's lattice:

$$\Psi_{nk}(r)= e^{ik.r}u_{nk}(r) \qquad (1\text{-}17)$$

where r is the position vector and k is the wave vector. We note that $u_{nk}(r)$ is the periodic function with the periodicity of the system's lattice. Therefore, $u_{nk}(r)$ can be expanded in terms of plane waves:

$$\Psi_i(r)= \sum_j C_{ij}\ \Phi_j(r)= \sum_G C_{i,k+G}\, e^{i(k+G)r} \qquad (1\text{-}18)$$

where, G is the reciprocal lattice vectors. Owing to the periodic boundary conditions, it is possible to simulate periodic systems in three dimensions by just assuming a super cell. For example, to simulate the extended surface of metals, one just needs to introduce a

vacuum region perpendicular to the surface and impose the periodic boundary conditions in all three dimensions.

In principle, infinity number of k-point is needed in (1-18) to expand the wave function. However, in practice, only limited number of plane wave for each k-point in the first Brillion zone is needed to properly approximate the wavefunction and total energy. Therefore, a plane wave cut-off is introduced as following:

$$\left(\frac{\hbar^2}{2m}\right)|k+G_{cut}|\leq E_{cut} \tag{1-19}$$

1.1.6.2 Projected Augmented Wave (PAW) method

As mentioned above, the pseudopotential is introduced to cope with the rapid oscillations in the core region. However, the drawback of this approach is that all electron information is lost. In PAW method, a transformation operator, $\hat{\mathcal{T}}$, is defined that linearly transforms the smooth wave function, i.e. the pseudo-wave function $|\tilde{\psi}_n\rangle$ in the valance region to the all-electron KS wave function $|\psi_n\rangle$, retaining all-electron information.

$$|\psi_n\rangle = \hat{\mathcal{T}}|\tilde{\psi}_n\rangle \tag{1-20}$$

where the transformation operator is expressed as below:

$$\hat{\mathcal{T}} = \sum_a \sum_i (|\phi_i^a\rangle - |\tilde{\phi}_i^a\rangle)\langle\tilde{p}_i^a| \tag{1-21}$$

and $|\phi_i^a\rangle$ and $|\tilde{\phi}_i^a\rangle$ are all-electron and smooth atomic orbitals, respectively and $\langle\tilde{p}_i^a|$ are the projection function that are non-zero inside a region that is called augmentation sphere.

1.1.6.3 Grid-based Projected Augmented Wave (GPAW) method

In GPAW code, there three types of basis is used: 1) grid mode where the wavefunctions are presented on a three dimensional real-space grids, 2) plane wave that the wave functions are expanded in terms of plane waves, and 3) localized bases sets that are produced by linear combination of atomic orbitals (LCAO).

1.2 Computational hydrogen electrode (CHE) model

Throughout this thesis to calculate the reaction adsorption energies of the intermediates of the electrochemical reactions, we have used CHE model, introduced by Nørskov and co-workers [17]. Before describing CHE model, I briefly discuss about standard hydrogen electrode (SHE) that is the analogue of the CHE model and it is used as the reference electrode. The SHE is based on the following electrode reaction and its absolute electrode potential is estimated to be 4.44±0.02 V. However, since SHE is the reference for all the electrode reactions, it is set to be zero.

$$(H^+ + e^-) \rightarrow 1/2H_2 \qquad (1\text{-}22)$$

In the CHE model, it is assumed that at zero potential and standard conditions (pH = 0, $P(H_2)$ = 1 atm, T = 298 K), the electrons and protons are in thermodynamic equilibrium with that of $1/2H_2(g)$. This allows for replacing the chemical potential of protons and electrons, which are difficult to calculate using DFT, with the one for hydrogen in the gas phase, which can be calculated from DFT. For the electrochemical reactions, including oxygen reduction reaction (ORR), CO_2 reduction, and hydrogen evolution reaction (HER) that involve electron-proton transfer steps, the chemical potential of electrons and protons are replaced with the one for hydrogen in the gas phase. Within this approach the adsorption energies of different adsorbates that involve electron-proton transfer can be calculated. For example, at the cathode side of the proton exchange membrane (PEM) fuel cell, where reduction of oxygen to water occurs, the last intermediate is the protonation of adsorbed hydroxyl to form water as following [17]:

$$OH^* + (H^+ + e^-) \rightarrow H_2O(l) + * \qquad (1\text{-}23)$$

where * denotes the free adsorption site. According to the CHE model, the reaction free energy is calculated as below:

$$\Delta G^\circ = \mu(H_2O) - \mu(OH^*) - [\mu(H^+) - \mu(e^-)] = \mu(H_2O) - \mu(OH^*) - \frac{1}{2}[\mu(H_2(g)] = \Delta E + \Delta ZPE - T\Delta S \qquad (1\text{-}24)$$

where μ is chemical potential, ΔE is the difference in the electronic energies calculated from DFT, ΔZPE is the difference in the zero point energies of reactants and products that are calculated from vibrational analyses, ΔS is the change in entropy and T is temperature.

At potentials different from zero, i.e. U ≠0 V, the chemical potential of electrons changes by eU, which causes the shift in the free energy of a state that involves electron-proton transfer by eU. Similarly, at the pH values different from 0, the change in the chemical potential of protons due to the change in the concentration is $-kT\ln[H^+] = kT\ln10\times pH$. Taking into account the potential and pH effects, the change in the Gibbs free energy of reaction (1-24) is calculated as below:

$$\Delta G(U)=\Delta G^{\circ}+\Delta ZPE-T\Delta S+eU+kT\ln10\times pH \qquad (1\text{-}25)$$

1.3 **Reactivity and d-band model**

The reactivity of the surface in the electrochemical reactions is defined by the interaction between the adsorbate and the catalyst surface. This, in turn, is related to the electronic structure of the surface atoms that defines the binding energies of the intermediates involved in the reaction. Therefore, development of models that correlate the adsorption energies with the electronic structure of the catalyst surface are critical in developing new electrocatalysts for different electrochemical reactions. More specifically, understanding the variations in the adsorption energies from one transition metal to the next can be used to predict the reactivity of the surface.

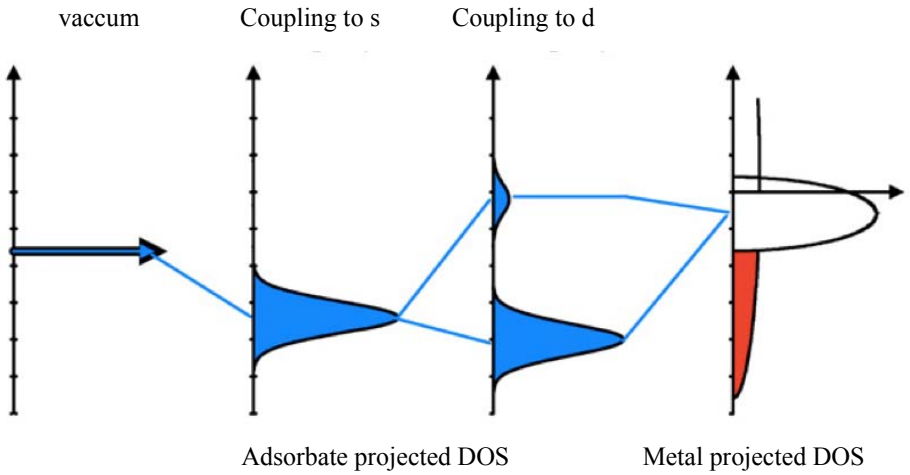

Figure 1-1: Schematic illustration of the change in the density of states (DOS) projected onto metal atom and adsorbate showing the formation of a chemical bond between an adsorbate valence level and the s- and d-states of a transition metal surface (From Ref.[18]).

The interaction between adsorbate and transition metal surface is related to the electronic properties of the surface by the d-band model [18–21]. The advantage of the d-band model is that it provides the possibility to predict the reactivity of the surface without calculating the binding energy. In the d-band model, the interaction between surface and adsorbate is divided into two parts: interaction of adsorbate orbitals with 1) the s-electrons, and 2) with the d electrons of the surface metal atoms. Interaction of the adsorbate orbitals with s-electrons of the metal atoms, results in the broadening and shifting of the adsorbate orbitals. On the other hand, interaction of the adsorbate orbitals with metal d-electrons (d-band) results in the splitting of the adsorbate orbitals to bonding and anti-bonding states as is shown in Figure 1-1. It is also assumed that the interaction between the adsorbate orbitals and s-electrons of the transition metals is metal independent as all of the transition metals have half- filled s-band. Therefore, the binding of the adsorbate to the surface is governed by the interaction of the adsorbate orbitals with the d-band. Of course, this assumption could fail for the cases that d-electrons will not interact with adsorbate orbitals.

The bond strength of the adsorbate to the metal is defined by the occupation of the anti-bonding states, i.e. if they locate below or above the Fermi level. We note that the occupation of the anti-bonding states depends on their position relative to Fermi level and

not filling of the d-band. However, if the width of the d-band is changed, given that the number of electrons in the d-band remains constant, the only way to accommodate the electrons is to shift the d-band center, which in turn changes the occupation of anti-bonding states. A downward shift in the d-band center would result in occupation of more anti-bonding states and hence weaker binding between adsorbate and metal atoms, whereas an upward shift will have the opposite effect and results in less occupied anti-bonding states and hence stronger binding between adsorbate and metal atoms. In this way, the reactivity of the surface is correlated to the d-band width that is proportional to the d-band center. Similarly, modifying the d-band can be used as a tool to tune the reactivity of the surface and to discover and search for new catalysts. At this point it is important to understand the factors that define the d-band width and hence the d-band center. The d-band width of a metal atom on the surface is governed by the interaction of the d-orbitals of that atom with the neighboring atoms, in particular, the overlap between the orbitals. The bond distance between that metal atoms and neighboring metal atoms as well as intrinsic properties of that metal atom and neighboring atoms, in turn, defines this interaction [4]. Clearly, tuning the d-band center is possible by changing the distance between metal atoms on the surface that in turn changes the overlap between metal atoms on the surface and neighboring atoms (strain effect). On the other hand, alloying where the neighboring atoms are replaced with different metal elements gives rise to the modification of the electronic structure and hence the d-band center (ligand effect). Another way is to change the coordination of the metal atom on the surface that changes the extent of coupling between d-orbitals (structural effect).

Chapter 2

Electro-catalytic Activity of Pt/Cu(111) Systems

Electrocatalytic activity of a catalyst is governed by the chemical properties of the active sites [21]. Change in the chemical properties of the active sites, in turn, changes interaction of the active sites with adsorbed species. Clearly, altering the chemical properties of metal atoms on the surface to tune their electrocatalytic activity and selectivity is of upmost importance in development of new catalysts. Alloying has been widely used to tune electronic structure and chemical properties of the active sites in many electrochemical reactions, and it is well known that alloys have different catalytic properties than their constituents [22,23]. In general, there are three mechanisms that have been widely used to tune the chemical properties of the active sites: 1) strain effect in which the distance between metal atoms on the surface is different from the ones for parent metals [24,25,26], 2) ligand effect in which the electronic structure of the atoms on the surface are modified through the neighboring atoms [24,18,27], and 3) bi-functional effect in which binding of reaction intermediates to the alloying element is different from that of host element, resulting in improved catalytic activity [28,29]. In this scenario, the electronic properties of the active sites depend on the location of alloying element; depending on the position of the alloying element, one or two of the aforementioned effects will govern the change in the chemical properties of the active sites.

Our effort in this chapter is to tailor the chemical properties of Pt atoms on

Pt(111) surface by incorporating some quantities of Cu atoms into different layers of Pt(111), i.e. surface and subsurface layer. We perform electrochemical characterization and DFT calculations to define their electrocatalytic activity. The electro-catalytic activity of different Cu/Pt(111) systems for CO electro-oxidation as a test reaction is examined using both DFT calculations and electrochemical measurements. We find a consistent agreement between DFT calculations and electrochemical measurements. These findings can be used to tune electrocatalytic activity of other reactions.

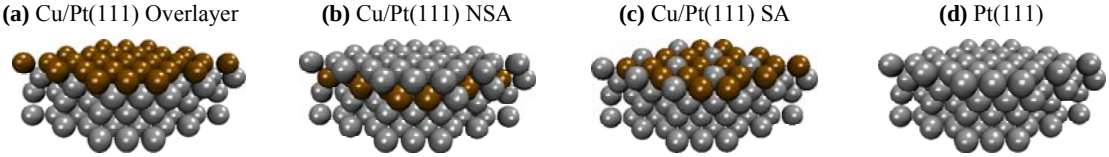

Figure 2-1: Cu/Pt systems considered in this study. They form by varying the position of Cu atoms into the surface and subsurface layers of Pt(111): (a) Cu/Pt(111), (b) Cu/Pt(111) NSA, ,(c) Cu/Pt(111) SA, and (d) Pt(111).

2.1 Cu/Pt(111) systems

The following Cu/Pt(111) systems were studied by locating copper atoms in surface and subsurface layer of Pt(111) as depicted in Figure 2-1.

2.1.1 Cu/Pt(111) Overlayer (OL)

In this system a monolayer of copper is deposited on top of Pt(111). The distance between copper atoms on the surface is similar to the one for Pt(111) atoms. Given that copper has smaller lattice parameter than platinum, there is a tensile strain for copper atoms on the surface. Moreover, the electronic properties of copper atoms are affected by the underneath platinum atoms. Hence, in this system strain and ligand effects coexist.

2.1.2 Cu/Pt(111) near surface alloy (NSA)

In this system, some quantities of copper atoms are incorporated in subsurface layer of Pt(111) and both surface layer and inner layers consist of platinum atoms. Since copper atoms are located into subsurface layer, the lattice constant of platinum atoms on the surface does not change and is similar to pure platinum. Hence, there is no strain effect

for the platinum atoms on the surface. On the other hand, copper atoms in the subsurface layer affect the electronic structure of platinum atoms and only ligand effect exists.

2.1.3 Cu/Pt(111) surface alloy (SA)

In this system, both platinum and copper atoms coexist on the surface maintaining the lattice constant of platinum. Therefore, there is no strain effect compared to Pt(111) surface [30]. On the other hand, ligand effect exists due to the presence of copper atoms on the surface. Moreover, unlike Cu/Pt(111) OL and Cu/Pt(111) NSA where there are just one type of atoms on the surface, Cu and Pt respectively, on Cu/Pt(111) SA, both Cu and Pt atoms present on the surface. As will be explained later, this is an interesting system for studying bifunctional mechanism.

2.2 Experimental Findings

In this part, I briefly review the previous experimental and theoretical findings for different Cu/Pt(111) systems that have been performed at CINF and CAMD. Both Cu/Pt(111) SA and NSA, have been well studied before. Kundsen and co-worker studied Cu/Pt(111) NSA as a catalyst for improving water gas shift (WGS) reaction [31]. They showed that the presence of copper in the subsurface layer weakens the CO binding energy. Moreover, the fact that on Cu/Pt(111) NSA, OH binds much more weakly than on Pt(111) and Cu(111), makes OH and CO poisoning less severe compared to Pt(111) and Cu(111).

Anderson and co-workers have studied Cu/Pt(111) NSA both in the presence and absence of CO [32]. Their studies showed that for Cu/Pt(111) NSA at temperatures between 473 and 723 K, segregation of Cu atoms from subsurface to surface occurs, making Cu/Pt(111) NSA to Cu/Pt(111) SA. This is due to the fact that CO binds strongerly to Pt atoms on the Cu/Pt(111) SA when compared to the Cu/Pt(111) NSA, creating a driving force to segregate less reactive Cu atoms from subsurface to the surface. They also concluded that the coverage of Cu atoms on the surface is 2/3 ML, whereas the coverage of Pt atoms is 1/3 ML.

Stephens and co-workers studied Cu/Pt(111) NSA under electrochemical conditions for oxygen reduction reaction [30]. As noted above, in this system only ligand

effect is present and the change in the activity is attributed to the ligand effect. They showed that OH binding energy varies with the concentration of Cu in the subsurface layer, and that the OH binding energy on Cu/Pt(111) NSA decreases when compared to Pt(111). This resulted in improving the catalytic activity of Cu/Pt(111) NSA for oxygen reduction reaction.

2.2.1 XPS characterization

The samples were prepared according to the procedure explained in Ref.[30]. Angle resolved X-ray photo-electron spectroscopy (AR-XPS) was used to verify if the desired structures are formed. According to Figure 2-2, for Cu/Pt(111) OL, the AR-XPS shows that Pt is not present on the surface and the surface only contains Cu. However, while Pt content increases from 0% to 100% at around 7Å depth, the Cu content decreases to 0 %. On the other hand, for Cu/Pt(111) SA, the depth AR-XPS profile, shows the presence of both Pt and Cu on the surface, and the concentration of Cu decreases to 0 %, whereas the Pt conctration increases to 100%.

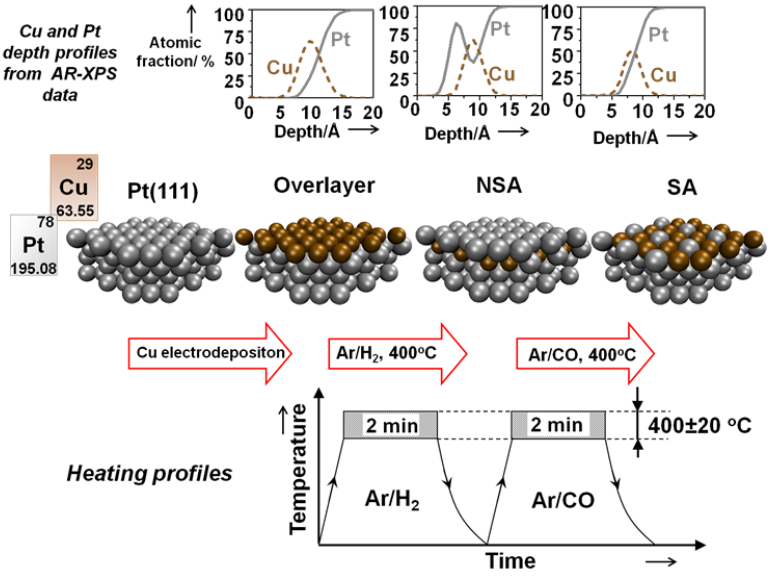

Figure 2-2: Depth profile for different Cu/Pt systems obtained using Angle resolved X-ray photo-electron spectroscopy (AR-XPS) along with heat profiles showing the scheme to prepare each Cu/Pt system.

As for XPS depth profile of Cu/Pt(111) NSA, the concentration of Cu at the surface is zero and in the lower depth, at around 9 Å, the peak corresponding to Pt decreases and a peak corresponding to Cu appears. This corresponds to the presence of 35% of Pt in the

depth of 9 Å. At lower depth, Pt has maximum concentration, while the concentration of Cu drops to zero, indicating the presence of Cu only at the depth of 9 Å. In summary, the XPS depth profiles show the formation of desired structures.

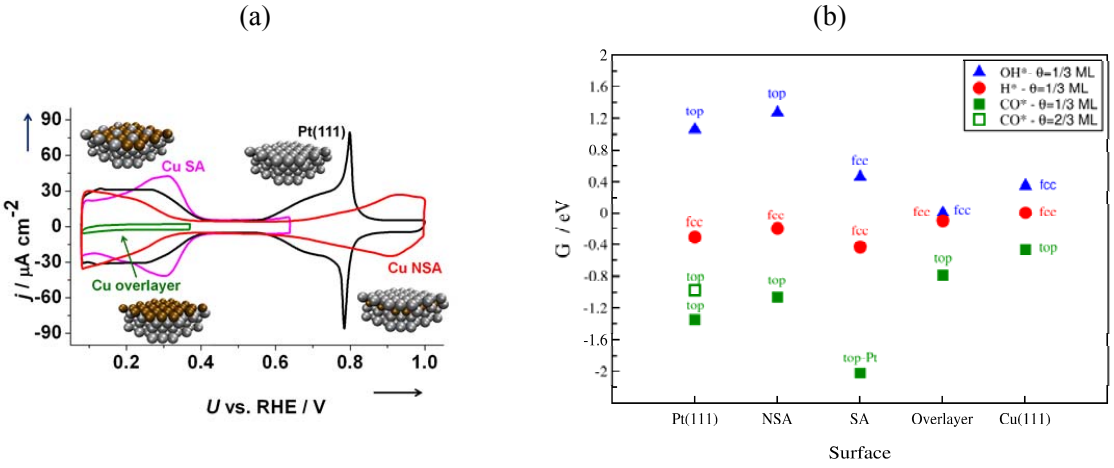

Figure 2-3: (a) Cyclic voltammograms in 0.1M $HClO_4$ for different Cu/Pt systems: Pt(111), Cu OL on Pt(111), Cu/Pt(111) NSA, and Cu/Pt(111) SA. dU/dt = 50 mV/s. (b) Binding energies of HO, H and CO on different Cu/Pt systems referenced to $H_2O(l)$, $H_2(l)$ and CO(g) respectively. The adsorption site for each adsorbate is provided. For Pt(111) the CO binding energies corresponding to two difference coverages is provided.

2.2.2 Cyclic Voltammetry

Figure 2-3a shows the cyclic voltammograms of Pt(111), Cu/Pt(111) OL, Cu/Pt(111) NSA and Cu/Pt(111) SA in 0.1M $HClO_4$. As can be seen, there is a distinctive difference between the voltamograms of Pt(111) and other surfaces, indicating the presence of Cu atoms in different location of Pt(111) modifies the adsorption of adsorbates, namely OH* and H*, differently. To verify the observed CV features, we have calculated the binding energies of OH* and H* on the same surface structures (see **Error! Reference source not found.**b). Below, we describe the observed voltammograms corresponding to each surface and compare it to the one for Pt(111). Moreover, we compare the observed trend in the CVs of different surfaces with the calculated binding energies using DFT.

2.2.2.1 Pt(111)

At the potentials between 0.05 and 0.4 V, there is a reversible peak that corresponds to adsorption/desorption of H* [33]. On the other hand, around 0.8 V, there is a reversible peak that is attributed to adsorption/desorption of OH*.

2.2.2.2 Cu/Pt(111) OL

This surface exhibits a featureless CV in the range of potentials between 0.05 and 0.38 V. The CV was done in the limited potential range to avoid Cu dissolution. Even though DFT calculations predict that H* destabilizes on Cu/Pt(111) OL compared to Pt(111), such difference with Pt(111) cannot be seen from CV. However, DFT calculations predict that OH* stabilizes on Cu/Pt(111) OL compared to Pt(111) with binding energies of 1.06 and 0 eV, respectively. This means at this potential range, the surface is covered completely with OH*, and that is why the CV of Cu/Pt(111) OL is featureless.

2.2.2.3 Cu/Pt(111) SA

The potential range for CV for Cu/Pt(111) was limited to the potential range from 0.05 to 0.7 V, to avoid Cu dissolution. A reversible peak at 0.3 V is observed. According to DFT calculations, OH* binds the SA 0.6 eV stronger than Pt(111). Comparing the CVs of Cu/Pt(111) SA and Pt(111), there is an approximate shift of 0.5 between the reversible peaks for Cu/Pt(111) SA when compared to the peak for OH* adsorption/desorption on Pt(111), suggesting the peak is attributed to OH* adsorption/desorption on Cu/Pt(111) SA.

2.2.2.4 Cu/Pt(111) NSA

The CV for Cu/Pt(111) NSA has similar feature as that of Pt(111) meaning that there are adsorption/desorption reversible peaks corresponding to H* and OH*; however, at potentials different from the corresponding ones for Pt(111). The peak assigned to H* adsorption/desorption shifts to more negative potentials as compared to Pt(111), meaning that H* destabilizes on Cu/Pt(111) NSA compared to Pt(111). On the other hand, OH* adsorption/desorption peak shifts to more positive potentials, meaning that OH* destabilizes on Cu/Pt(111) NSA compared to Pt(111). These observations are in agreement with DFT calculations that predicts H* and OH* bind by 0.21 and 0.11 eV weaker on NSA than on Pt(111), respectively. These findings are also in agreement with previous DFT calculations performed on Cu/Pt(111) NSA by Kundsen and co-workers [[31]] that predicted weaker binding energies for OH* on Cu/Pt(111) NSA when compared with Pt(111).

The above CVs and DFT calculations on different Cu/Pt(111) systems indicate that the

reactivity of the surface strongly depends on the position of Cu atoms: for the Cu/Pt(111) SA, where Cu atoms are present on the surface, both OH* and H* bind stronger than on Pt(111), while on the systems that Cu is present in the subsurface layer, i.e. NSA, both OH* and H* bind weaker than on Pt(111).

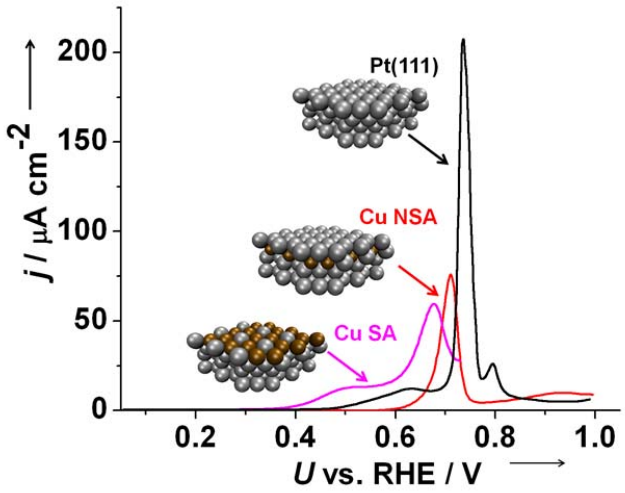

Figure 2-4: *CO stripping voltammograms for Pt(111), Cu/Pt(111) SA, and Cu/Pt(111) NSA, in $HClO_4$, dU/dt = 20 mV/s. The CO was adsorbed at 0.05 V, whereas the voltammogram was carried out in CO-free solution.

2.2.3 CO adlayer electro-oxidation

Following CV measurements on different Cu/Pt(111) systems and defining the trend in the binding energies of OH* and H*, in this section we examine catalytic activity of these systems for CO adlayer electro-oxidation. As will be discussed in the theoretical section, the electro-catalytic activity for CO electro-oxidation depends on both CO and OH binding energies. Hence, the information we obtained from CV measurements and DFT calculations on Cu/Pt(111) systems will be correlated to the catalytic activity for CO adlayer electro-oxidation.

The CO was pre-adsorbed on the surfaces by holding the potential at 0.05 V for 15 minutes in CO saturated 0.1M $HClO_4$. To make CO adlayer, Ar was purged to the electrolyte to remove the bulk CO in the solution. Figure 2-4 shows the CO stripping voltammograms for Pt(111), Cu/Pt(111) SA and Cu/Pt(111) NSA at scan rate of 20 mV/S and up to 1 V potential. The increase in the current can be attributed to the water

oxidation, i.e. OH* adsorption, or oxidation of CO adlayer to CO_2. Moreover, the area of the CO electro-oxidation peaks are related to the charge used to oxidize adsorbed CO* and hence the coverage of CO adlayer on the surface. Since on Cu/Pt(111) SA, CO electro-oxidation is accompanied by OH* adsorption and Cu dissolution, the area of the CO electro-oxidation peaks cannot be attributed to just CO electro-oxidation. This is not the case for Pt(111) and Cu/Pt(111) NSA. Moreover, we note that the charge corresponding to Pt(111) is higher than the ones for Cu/Pt(111) SA and Cu/Pt(111) NSA, meaning that the CO coverage on Pt(111) is higher than on Cu/Pt(111) SA and Cu/Pt(111) NSA. As will be discussed, the corresponding coverage of CO on each Cu/Pt(111) system is determined by calculating the differential free energy of adsorption of CO. We also note that the position of the peak is related to required overpotential to oxidize the CO adlayer. This means that Cu/Pt(111) SA has lowest overpotential among these systems followed by Cu/Pt(111) NSA and Pt(111).

2.3 DFT calculations

In this section, we calculate the equilibrium CO adlayer coverage on each system by calculating differential CO coverage on each system. Then I will discuss about modeling CO electro-oxidation on different Cu/Pt(111) systems and compare the DFT and experimental results. Then we apply Sabatier principle to construct the volcano plot for CO electro-oxidation.

2.3.1 Equilibrium CO coverage

The equilibrium coverage defines the most stable coverage as a function of potential. However, since CO adsorption from CO(g) is not potential dependent, the equilibrium coverage at any potential is similar to the one at zero potential. It is calculated using integral and differential free energies of adsorption. The integral free energy is defined as the total adsorption free energy of all CO molecules on the surface per surface atom, which in turn is defined as the product between average free energy and the coverage [34]. The differential free energy of adorption is defined as the free energy required increasing the coverage of CO on the surface by the differential amount of $d\theta$. The integral and differential free energies of adsorption are related through the following expression:

$$G_{diff} = \frac{d(G_{int})}{d\theta} = \frac{d(G_{avg}\theta)}{d\theta} \qquad (2\text{-}1)$$

Where θ, G_{diff},G_{int} and G_{avg} are the coverage, differential, integral and average free energies of adsorption of CO, respectively. We would like to emphasize that the same expression can be used to calculate the equilibrium coverage of other adsorbates such as OH* and O*. In the case of CO adsorption, the equilibrium coverage is defined as the coverage above which adsorption of more CO molecules on the surface is exergonic. Given that CO adsorption is not potential dependent, the equilibrium coverage is defined at the point where $G_{diff} = 0$ eV. We note that since adsorption of other adsorbates such OH* and O* is potential dependent, the stability of adsorbates changes with potential, and the equilibrium coverage is also potential dependent.

Figure 2-5a shows the integral and differential free energies of adsorption of CO on Pt(111). We have used the configurations obtained by classical Monte-Carlo (MC) simulations reported by Shan and co-workers [35]. Adsorption of CO is favorable continuously up to 0.5 ML. However, differential increasing in CO coverage to the coverages higher than 0.5 ML is accompanied by huge change in free energy. This is due to increasing the lateral interactions between adsorbed CO molecules. Increasing the coverage of CO up to 0.7 ML is still energetically favorable. This means the equilibrium coverage of CO on Pt(111) is 0.7 ML in agreement with experimentally determined CO coverage obtained from the area of CO oxidation peak.

On Cu/Pt(111) SA (

Figure 2-5b), starting from low CO coverage, CO only adsorbs on atop site of Pt atoms. The adsorption site as well as differential free energy of adsorption remains constant up to 0.33 ML coverage where CO occupies all Pt atoms. This is due to the fact that Pt atoms are away from each other and there is a negligible repulsion between adsorbed atop CO molecules. On the other hand, when CO coverage surpasses 0.33 ML, CO starts to occupy Cu atoms, making coverage increment energetically unfavorable. The coverage of 0.33 ML is in agreement with the experimental value, which is equal to the Pt coverage on Cu/Pt(111) SA.

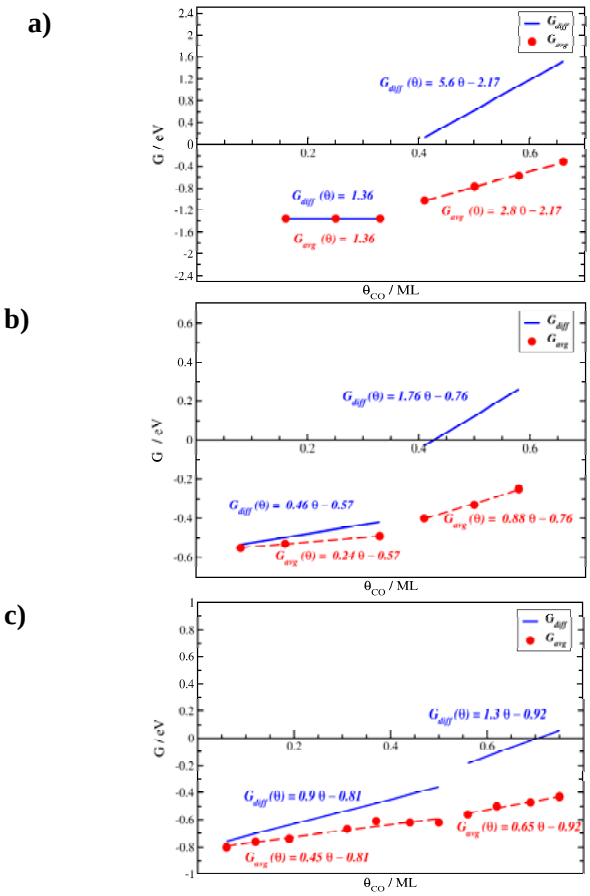

Figure 2-5: Differential and average free energies of adsorption of CO on (a) Cu/Pt(111) SA, (b) Cu/Pt(111) NSA, and (c) Pt(111). The red points are calculated average free energies of adsorption of CO at different coverages and the red dashed lines are their linear fit. The blue lines are the corresponding differential free energies of adsorption calculated using equation (2-1).

Figure 2-5c shows, the differential free energy of adsorption of CO on Cu/Pt(111) NSA. Adsorption of CO is energetically favorable up to 0.44 ML. This coverage of 0.44 ML is slightly higher than the experimental value, i.e 0.33 ML. This difference is attributed to the uncertainity in DFT calculations. Moreover, we expect to obtain a better agreement by examining all possible adsorption configurations at each coverage, for example using Monte-Carlo (MC) simulations [[35]]. We note that even though both Pt(111) and Cu/Pt(111) NSA contain Pt in the outer layer, the equilibrium CO coverages are different (**Error! Reference source not found.**a). This is attributed to the presence of Cu

atoms in the subsurface layer that modifies the electronic properties of the Pt atoms on the surface.

2.3.2 CO electro-oxidation

Electrochemical CO oxidation is widely used as a test reaction [36,37,38]. It is a fairly simple reaction that involves two charge transfer steps. The reaction involves two intermediates CO^* and HO^* on the surface:

$$CO(g) + * \rightarrow CO* \quad (2\text{-}2)$$

$$H_2O(l) + ** \rightarrow OH** + H^+(aq) + e^- \quad (2\text{-}3)$$

$$OH** + CO* \rightarrow CO_2 + H^+(aq) + e^- + * + ** \quad (2\text{-}4)$$

where * and ** refer to free sites on the surface where CO* and OH* respectively binds to. The first elementary reaction is adsorption of CO from gas phase to the surface on which the coverage of CO is differentially lower that the equilibrium one, which means the first reaction step is the differential adsorption of CO. This reaction step is irreversible for CO adlayer oxidation. The second elementary reaction is the dissociation of water to oxygen-containing species that is believed to be OH [39,40]. Similar to CO adsorption, this step defines the adsorption of OH on the surface with CO coverage that is differentially lower than equilibrium one. The last reaction step is the recombination of CO* and OH* that is a Langmuir-Hinshelwood type reaction [39]. In fact, CO* and OH* are recombined to form COOH* which is not an electrochemical step. Then COOH* is oxidized to CO_2 and an electron-proton pair. The binding free energies corresponding to above reaction steps are as following:

$$\Delta G_1 = \Delta G_{CO^*} = G(CO^*) - G(CO(g)) - G(*) \quad (2\text{-}5)$$

$$\Delta G_2 = \Delta G_{OH^*} = G(OH^*) + \frac{1}{2} G(H_2(g)) - G(H_2O(l)) - G(CO^*) - eU - kT\ln(a_{H^+}) \quad (2\text{-}6)$$

$$\Delta G_3 = G(CO_2(g)) + \frac{1}{2} G(H_2(g)) + 2G(*) - G(CO^*) - G(OH^*) - eU - kT\ln(a_{H^+}) \quad (2\text{-}7)$$

where U is the electrode potential versus standard hydrogen electrode (SHE) and –

$kTln(a_{H+})$ is the chemical potential of protons. Clearly, for an optimal catalyst for CO electro-oxidation, all the reaction free energies of the above reaction steps, i.e. ΔG_1, ΔG_2 and ΔG_3 should be thermoneutral.

We note that the present intermediates, i.e. CO* and OH* may bind differently to the surface or there could be different sites on the surface to which these adsorbates bind. CO normally binds through carbon atom, while OH binds through oxygen atom. Therefore, there is not a scaling relation between CO and OH binding energies. This provides the possibility of optimizing the reactivity towards CO electro-oxidation by designing bifunctional sites with different reactivity towards CO and OH. That means the binding energies of OH and CO and hence their reactivity can be optimized independently to make ΔG_1, ΔG_2 and ΔG_3 simultaneously as close as possible to zero. Among the Cu/Pt(111) systems, only Cu/Pt(111) SA has such bifunctional sites: Cu is more reactive than Pt towards water dissociation, while Pt is more reactive than Cu for CO adsorption. We note that the change in adsorption free energies of the above three reaction steps and hence the catalytic activity towards CO electro-oxidation can be described by two parameters that are the free binding energies of CO* and OH*, and these are the only parameters that are catalyst dependent. At this point, the overpotential, that in turn is proportional to catalytic activity is defined by the step that has the most positive change in free energy [17]:

$$U_{Overpotential} = \frac{Max\left[\Delta G^{\circ}_{CO*}, \Delta G^{\circ}_{OH*}, \Delta G^{\circ}_{3}\right]}{e} \qquad (2\text{-}8)$$

where ΔG°_{CO*}, ΔG°_{OH*} and ΔG°_{3} are the change in free energies of the respective reactions at U = 0 V. Additionally, it means an activity volcano as a function of binding energies of CO* and OH* can be constructed [17].

2.4 **Volcano Plot**

Figure 2-6 shows the activity volcano for CO electro-oxidation. The overpotential is a function of free binding energies of CO and OH. The catalyst with zero binding energies of CO and OH makes all reaction steps thermoneutral and therefore has zero

overpotential, i.e. it has the highest catalytic activity towards CO electro-oxidation. For a non-ideal catalyst the overpotential is higher than zero and according to the reaction mechanism one of the following reaction steps could be potential determining step: CO adsorption (reaction (2-2)), water oxidation (reaction (2-3)) or the formation of CO_2 from OH* and CO* (reaction (2-4)). Accordingly, the volcano plot can be divided into three regions corresponding to these three potential determining steps.

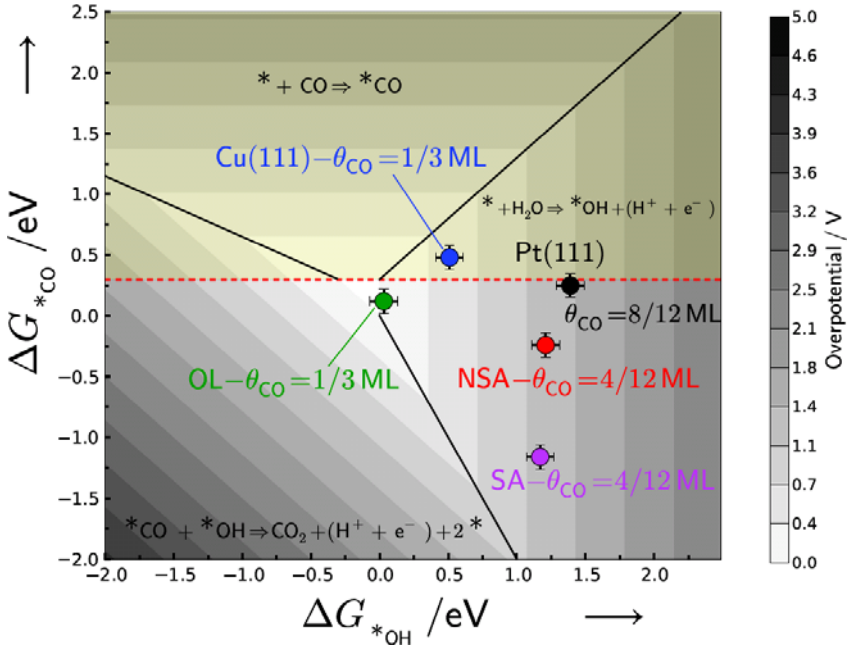

Figure 2-6: Volcano plot for CO electro-oxidation as a function of the differential free energies of adsorption of CO and OH on Pt(111), Cu(111), Cu/Pt(111) NSA, Cu/Pt(111) SA and Cu/Pt(111) OL. The coverage of CO is depicted for each surface. The potential determining step for each region is also defined. The dashed horizontal line denotes the chemical potential of CO in the gas phase above which CO does not bind to the surface.

As noted above, the first reaction step, i.e. adsorption of CO is not potential dependent and the change in potential will not affect CO binding. In other word, if the catalyst does not bind CO, the reaction could not take place. The red dashed line in the volcano defines the chemical potential of CO in the gas phase. Evidently, a catalyst with the CO binding above this line (yellow region) will not bind CO, and regardless of its OH binding energy cannot catalyze the electrochemical oxidation of CO. For example, even though Cu(111) lies in the low overpotential region of the volcano, it cannot catalyze the CO electro-oxidation reaction.

According to Figure 2-6, the potential determining step for all Cu/Pt(111) systems is the oxidation of water to OH*. Moreover, according to the calculations, Cu/Pt(111) OL exhibits highest catalytic activity followed by Cu/Pt(111) SA, Cu/Pt(111) NSA and Pt(111). However, as mentioned before, this system is not stable under reaction condition. The trend in electro-catalytic activity for other Cu/Pt(111) systems is in agreement with experimental findings that the overpotential (the position of the main peak in CO stripping measurements) required to oxidize CO increases in the following order: SA<NSA<Pt(111). Interestingly, Cu/Pt(111) SA shows higher activity over both Cu/Pt(111) NSA and Pt(111). This is due to the fact that, unlike Cu/Pt(111) SA and Pt(111), it has bifunctional sites, i.e. Cu and Pt to which OH and CO bind respectively. We would like to emphasize that the trends in the overpotential do not go hand–in-hand to experimental measured activity. This is because the kinetic details are not taken into account in our DFT calculations. However, this approach gives us an important insight in understanding the trend in the activity for electrochemical CO oxidation on different surfaces.

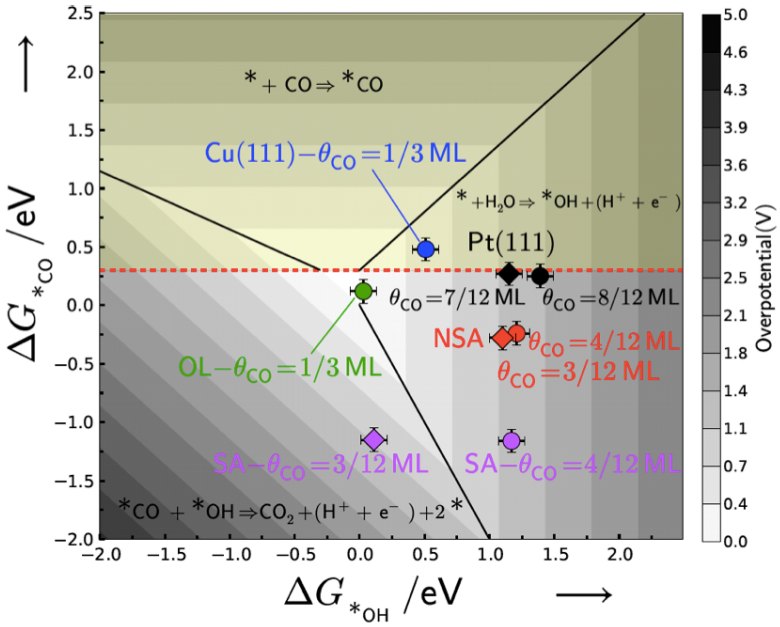

Figure 2-7: Similar to Figure 2-6 . The circles show the overpotential for CO electro-oxidation when the CO coverage is 2/3 and 1/3 ML on Pt(111) and all the other surfaces, respectively. Diamonds show the overpotential for CO electro-oxidation on NSA, SA and Pt(111) when the CO coverage is 1/12 ML lower than the corresponding saturation coverages.

We have also considered CO electro-oxidation on the surfaces with differentially lower CO coverage, 1/12 ML, than their corresponding equilibrium CO coverage. Lower CO coverages are assumed to model the change in the coverage during the reaction that could occur due to the presence of defects on the surfaces. As can be seen from Figure 2-7, the activity towards CO electro-oxidation improves when CO coverage decreased. However, the same trend in catalytic activity as for equilibrium CO coverage holds for lower CO coverages. Moreover, the potential determining step for CO electro-oxidation on Cu/Pt(111) SA changes from water activation to CO_2 formation. This is due to the fact that at lower CO coverage, there are more sites available to which OH would bind stronger when compared to the available sites at equilibrium CO coverage: at equilibrium coveage of CO, OH binds to atop site of Cu, whereas at the lower CO coverage, OH binds to the fcc hollow sites formed by Pt and Cu atoms. In fact, at equilibrium CO coverage all Pt atoms are occupied by CO, and adsorption of OH on the fcc sites due to the strong repulsion between adsorbed CO and OH is not favorable. On the other hand, when the CO coverage decreases, there are some Pt atoms that are not occupied by CO, and therefore OH bind to fcc sites more strongly due to absence of repulsion from neighboring adosrbed CO molecules.

Following the effect of defects on the CO electro-oxidation activity, we focus on well studied Pt(111) systems. It is known for Pt(111) that the CO electro-oxidation reaction is initiated at Pt step sites because water oxidation is facilitated on step Pt atoms when compared to terrace Pt sites [39]. Then neighboring terrace bound CO will react with step bound OH to oxidize CO. The observed pre-peak around 0.5 V in CO stripping measurement on Pt(111) is attributed to oxidation facilitated by the steps [39]. On the other hand, since higher potential is needed to activate water on terrace sites, the main peak is attributed to the reaction of terrace bound CO and OH. After the reaction is initiated at the defect sites, the coverage of CO is decreased, and water dissociation on terrace sites occurs at slightly lower overpotentials.

By comparing CO stripping voltammograms on Pt(111) and Cu/Pt(111) NSA, we note that for Cu/Pt(111) NSA the pre-peak is absent. This can be attributed to the fact that CO oxidation occurs only on terraces as the coverage of CO is lower and water dissociation could occur on the terrace sites.

These results are found to be completely consistent with a theoretically derived volcano plot, which in turn shows that CO electrooxidation is influenced by both CO* and OH* binding on the catalyst surfaces.

2.5 Summary and Outlook

Electrocatalytic activity of a catalyst is governed by the chemical properties of the active sites, which in turn are controlled by their atomic and electronic structure. In this chapter, both DFT calculations and electrochemical measurements were employed to study the electro-catalytic activity of different Pt/Cu(111) systems that form by incorporating some quantities of Cu into the first two atomic layers of Pt(111).

This study showed that the location of the alloying element can drastically change the chemical composition and hence the electrocatalytic activity of the atoms. This was evidenced by change in the binding energies of different adsorbates including CO*, OH* and H*. We used CO electro-oxidation as a test reaction to study the electro-catalytic activity of different Pt/Cu(111) systems. We find that their catalytic activities for CO electro-oxidation are different from the one for Pt(111). We note that, this is not unique to CO electro-oxidation, and this approach can be used to design optimal catalysts for other electrochemical reactions. Moreover, the fact that the theoretical results are found to be completely consistent with a experimental results, shows that DFT calculations can be used as a useful tool in understanding electrochemical reactions as well as predicting the electrocatalytic activity of the catalysts for different reactions.

Chapter 3

Tuning Selectivity in the Electrochemical Reduction of CO_2

Electrochemical reduction of carbon dioxide to hydrocarbons/alcohols using other renewable energy sources is considered as a possible way for clean fuel/chemical synthesis [2, 41].

In this scenario, development of a new catalyst that can efficiently and selectively reduces CO_2 is of importance. Hori who reported electrochemical reduction of CO_2 on pure metals made the first major contribution in the era of CO_2 reduction [8]. Diverse reaction products are produced during the reduction of CO_2 on pure metals. He reported that, CO_2 reduction products on pure metals can be classified based on catalysts' ability to bind CO and hydrogen. Table 3-1 summarizes the reaction products of CO_2 reduction on pure metals at a fixed current density of 5 mA/m^2. Formate is the primary product on metals with weak hydrogen and CO binding energies (Hg, Cd or Pb). On the other hand, metals with weak hydrogen and strong CO binding energies (Pt, Ni or Fe) reduce CO_2 to tightly adsorbed CO. The only group(s) of metals that can catalyze carbon-oxygen bond breaking in CO_2 reduction are those with moderate binding energies of CO and hydrogen such as Cu, Au and Ag. Since Au and Ag do not bind CO, further reduction of CO does not proceed on these metals. Cu is the only metal that does not desorb CO and can uniquely reduce CO_2 to significant quantities of hydrocarbons (mainly CH_4 and C_2H_4). As can be seen from Table 3-1, unfortunately, reduction of CO_2 on Cu is accompanied with a very high overpotential that hinders this reaction from being energy efficient. This

necessitates discovering new electrocatalysts that can selectively and efficiently catalyze this reaction to favorable products.

Table 3-1: Faradaic efficiency of products in CO_2 reduction at different metal surfaces at fixed current density of 5.0 mA/cm^2 (Adapted from [8]).

			Faradaic efficiency, %							
Metal	**U/V (SHE)**	**I (mA/cm^2)**	**CH_4**	**C_2H_4**	**EtH**	**PrOH**	**CO**	**HCOO**	**H_2**	**Total**
Pb	-1.63	5.0	0.0	0.0	0.0	0.0	0.0	97.4	5.0	102.4
Hg	-1.51	0.5	0.0	0.0	0.0	0.0	0.0	99.5	0.0	99.5
Tl	-1.60	5.0	0.0	0.0	0.0	0.0	0.0	95.1	6.2	101.3
In	-1.55	5.0	0.0	0.0	0.0	0.0	2.1	94.9	3.3	100.3
Sn	-1.48	5.0	0.0	0.0	0.0	0.0	7.1	88.4	4.6	100.1
Cd	-1.63	5.0	1.3	0.0	0.0	0.0	13.9	78.4	9.4	103.0
Bi	-1.56	1.2	-	-	-	-	-	77	-	-
Au	-1.14	5.0	0.0	0.0	0.0	0.0	87.1	0.7	10.2	98.0
Ag	-1.37	5.0	0.0	0.0	0.0	0.0	81.5	0.8	12.4	94.6
Zn	-1.54	5.0	0.0	0.0	0.0	0.0	79.4	6.1	9.9	95.4
Pd	-1.20	5.0	2.9	0.0	0.0	0.0	28.3	2.8	26.2	60.2
Ga	-1.24	5.0	0.0	0.0	0.0	0.0	23.2	0.0	79.0	102.0
Cu	-1.44	5.0	33.3	25.5	5.7	3.0	1.3	9.4	20.5	103.5
Ni	-1.48	5.0	1.8	0.1	0.0	0.0	0.0	1.4	88.9	92.4
Fe	-0.91	5.0	0.0	0.0	0.0	0.0	0.0	0.0	94.8	94.8
Pt	-1.07	5.0	0.0	0.0	0.0	0.0	0.0	0.1	95.7	95.8
Ti	-1.60	5.0	0.0	0.0	0.0	0.0	tr.	0.0	99.7	99.7

The primary reactions that occur at the copper surface, along with their equilibrium potential versus RHE, in the electrochemical reduction of CO_2 are listed below:

$$H^+ + e^- \rightarrow 1/2\ H_2(g) \qquad U = 0.0\ V \qquad (3\text{-}1)$$

$$CO_2(g) + 2(H^+ + e^-) \rightarrow HCOOH(aq) \qquad U = 0.20\ V \qquad (3\text{-}2)$$

$$CO_2(g) + 2(H^+ + e^-) \rightarrow CO(g) + H_2O(l) \qquad U = 0.12\ V \qquad (3\text{-}3)$$

$$CO_2(g) + 2(H^+ + e^-) \rightarrow CO + H_2O(l) \qquad U = 0.07\ V \qquad (3\text{-}4)$$

$$CO_2(g) + 6(H^+ + e^-) \rightarrow CH_3OH(aq) \qquad U = 0.03\ V \qquad (3\text{-}5)$$

$CO_2(g) + 8(H^+ + e^-) \rightarrow CH_4(g)$ U = 0.17 V (3-6)

As can be seen, thermodynamically electrochemical reduction of CO_2 to methane is exergonic with equilibrium potentials at 0.17 V. Unfortunately, this is not the case in practice and kinetically this does not happen. In fact, even on Cu, the best metal catalyst, the electrochemical reduction of CO_2 to CH_4 occurs at ~ -0.8 V versus RHE, with approximately -1V overpotential [42].

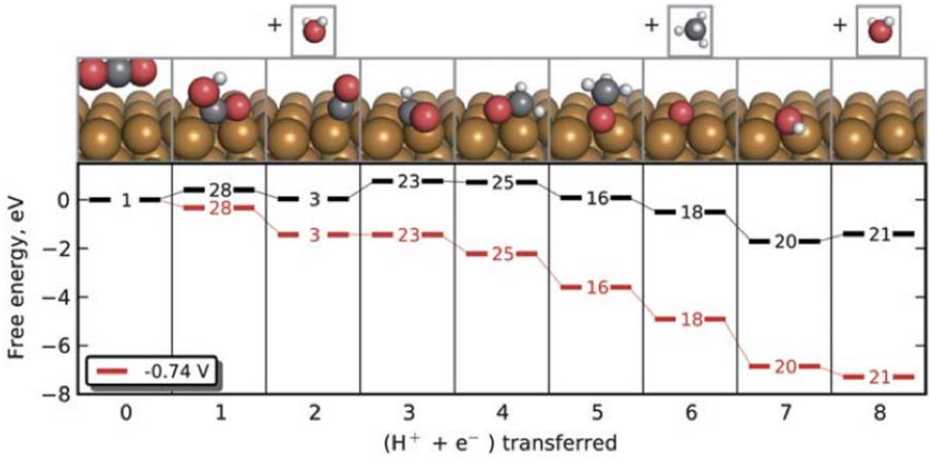

Figure 3-1: Calculated free energy diagram for the lowest energy pathways in the reduction of CO_2 to CH_4 at U = 0 V versus RHE (black) and at the theoretical overpotential of -0.74 V versus RHE (red). (Figure taken from [6])

3.1 **Reaction Mechanism**

Understanding the mechanism by which copper catalysis this reaction and the intermediates involved is necessary for the development of new catalysts with lower overpotential. Recently, a mechanism that explains copper's unique ability in reducing CO_2 to hydrocarbons and the origin of the high overpotential for the reduction of CO_2 was identified by DFT calculations in conjunction with computational hydrogen electrode (CHE) [6]. According to DFT calculations, on the Cu(211) surface the potential determining step at which each elementary step in the formation of hydrocarbons becomes downhill in energy, is the protonation of adsorbed CO to form CHO*, which occurs at -0.74 V versus RHE (cf. Figure 3-1). Since electrochemical CO_2 reduction to methane is an eight electron-proton transfer step that has seven intermediates, finding the

best catalyst in principle demands understanding of a seven-dimensional molecule-surface interaction space. Fortunately, the binding energies of carbon bounded species and oxygen bounded species scale with the binding energies of CO and OH, respectively [19,43,44]. These correlations reduce the dimensionality to two binding energies, namely CO and OH, and make it easier to screen different metals for the reaction. On the other hand, the correlation between the binding energies makes it difficult to change the binding energies independently, i.e. to change the binding of one intermediate, without affecting the binding energies of the other intermediates. Based on different reaction pathways and scaling relations Peterson and co-workers constructed volcano plots for different metals [44]. It was shown that regardless of the reaction pathway, changing the metal surface marginally changes the overpotential. Though several strategies were suggested to improve the catalytic activity for the reduction of CO_2, by decoupling the binding energies of CO* and CHO*/COH*, so far no electrocatalyst with activity superior to that of Cu has been reported to the best of our knowledge.

In general, there are three criteria that should be fulfilled in the pursuit for new catalyst materials: 1) The catalyst should have high selectivity towards desired products, 2) it should have high energy efficiency, i.e. a low reduction overpotential, 3) it should be stable at potentials of interest so that the activity does not degrade over time [45]. Stability is not such a rigorous requirement because negative potentials make much milder environment compared to that in e.g. PEMFCs. Therefore, in the following we will only focus on the first two the criteria in the search for new electrocatalysts.

3.1.1 Hydrogen evolution reaction

Thermodynamically hydrogen evolution, i.e. reaction (3-1), occurs at 0 V (RHE) through a single state H* [34]. The free energy of the intermediate, ΔG_{H^*}, calculated relative to hydrogen in the gas phase, defines the electrocatalytic activity of the catalyst for hydrogen evolution. Apparently, at negative potentials reduction of protons, i.e. $(H^+ + e^-) \rightarrow H^*$, is more favorable compared to zero potential and hence hydrogen adsorption will be in competition with CO_2 electroreduction. Given that there is a low thermodynamic barrier associated with electron-proton transfer to H*, the major reaction product will be hydrogen. Thus, one of the main challenges in the reduction of CO_2 is hindering

unfavorable HER while maintaining high activity and selectivity towards desired products. In this chapter, I discuss about a possible strategy to suppress HER and at the same time maintain good electrocatalytic activity and selectivity for CO_2 reduction by designing isolated sites on the catalyst surface. We use this strategy as a tool to search for new electrocatalysts.

3.1.2 Electronic and ensemble effects

The selectivity and activity towards HER and CO_2 reduction can be controlled via two effects: electronic effect and ensemble effect [5,46–49]. In the electronic effect, the chemical properties of the active sites on the surface are altered by the change in neighbor atoms. As discussed in chapter 2, these changes are manifested as ligand and strain effects. The ligand effect is related to the change in the electronic properties of active sites due to the change in neighboring atoms. On the other hand, the strain effect is related to the change in electronic properties resulting from changes in distance between active sites. Alloying readily facilitates such modifications. It is important to note that ligand and strain effects are usually inseparable effects. These effects have been used before to improve electro-catalytic activity of other electrochemical reactions such as CO electro-oxidation [50] and the oxygen reduction reaction (ORR) [22,30].

On the other hand, the ensemble effect is related to the arrangement of the atoms on the surface and how one element is surrounded by the other elements, i.e. to the number of contiguous atoms of the same type on the surface and their distribution.

Both ensemble and electronic effects affect the binding of hydrogen and also of the CO_2 reduction intermediates. This, in turn, means these effects could be used to tune the reactivity of the catalysts towards these reactions. The use of ensemble effect is not a new concept. It has been widely used in heterogeneous catalysis and electrocatalysis [46,48,51–55]. In this chapter, we try to elucidate how catalytic activity and selectivity towards HER and CO_2 reduction change with ensemble effect, and how it can be used to tune the electrocatalytic activity and selectivity of the CO_2 reduction by hindering HER without affecting high electrocatalytic activity and selectivity towards favorable CO_2 reduction products. The strategy that we follow to create specific active sites for CO_2 reduction on the surface that are surrounded by elements with poor catalytic activity towards both CO_2

reduction and HER. In practice, this can be achieved by alloying the elements that can catalyze the reduction of CO_2 with the ones that have poor catalytic activity or are inert towards HER. This is distinctly different from pure metals where the available active sites for CO_2 reduction and HER are the same and in competition between HER, the former dominates over the latter. More specifically, HER could be drastically suppressed if the active sites for CO_2 reduction are distributed in such a way that they form isolated active sites. Then, when CO_2 reduction intermediates adsorb on these isolated sites, hydrogen cannot adsorb on the same sites. Given that the surrounding atoms are inert towards HER and just one adsorbate can bind to these sites at a time, HER could be drastically inhibited and the selectivity would be directed towards desired products, i.e., hydrocarbons/alcohols. To elucidate how such ensembles affect electro-catalytic activity and selectivity, we consider electrochemical reduction of CO_2 on a Cu/Pt(111) surface alloy (SA) and Pt/Hg alloys, two model systems with isolated sites on the catalyst surface. After considering these two model systems, we expand our exploration and screen a pool of binary bulk alloy catalysts which have been formed by combining elements that can catalyze the reduction of CO_2 with elements that have poor catalytic activity or are inert towards HER.

3.2 CO_2 reduction on Pt(111) and Cu/Pt(111) Surface Alloy

As discussed in chapter two, on the Cu/Pt(111) SA, each Pt atom is surrounded by six Cu atoms, resulting in the formation of isolated Pt atoms on the surface [56]. In contrast, on the Pt(111) surface, Pt sites are located adjacent to each other. It is well known that hydrogen is the main reaction product on Pt in the reduction of CO_2 (cf. Table 3-1)[8]. This is due to the fact that on Pt CO_2 is reduced to tightly bound CO and high overpotentials are required to react off tightly bound CO. Under such circumstances, the primary reduction product is hydrogen, since HER on Pt occurs around 0 V versus RHE which is much higher than the potential needed for reduction of CO. Moreover, one can speculate that on Pt(111), CO and hydrogen adsorb on top and fcc-hollow sites, respectively which allows for intercalation of hydrogen when CO is adsorbed. This means hydrogen is evolved before CO is reduced, as much higher overpotential is needed to reduce CO. In fact, on Pt(111), the saturation coverage of CO at U = 0 V is 0.75 ML,

which leaves enough space for hydrogen to evolve [35]. At negative potentials the CO coverage will become even lower because H* will push weakly bound and more reactive CO off the surface. As a result the rate of HER will increase.

On Cu/Pt(111) SA, Pt atoms are isolated. CO_2 reduces to COOH* in the first electron-proton transfer. The second electron-proton transfer results in the formation of 0.33 ML-CO* that adsorb on the top site of Pt atoms. Further protonation of CO* could result in the formation of CHO* or COH*. However, the calculations show that CHO* is more stable than COH*. To examine the electrocatalytic activity of CO_2 reduction as well as reaction product, we inspect all possible reaction intermediates. Figure 3-2 shows the lowest free energy pathway in the reduction of CO_2 on Cu/Pt(111) SA.

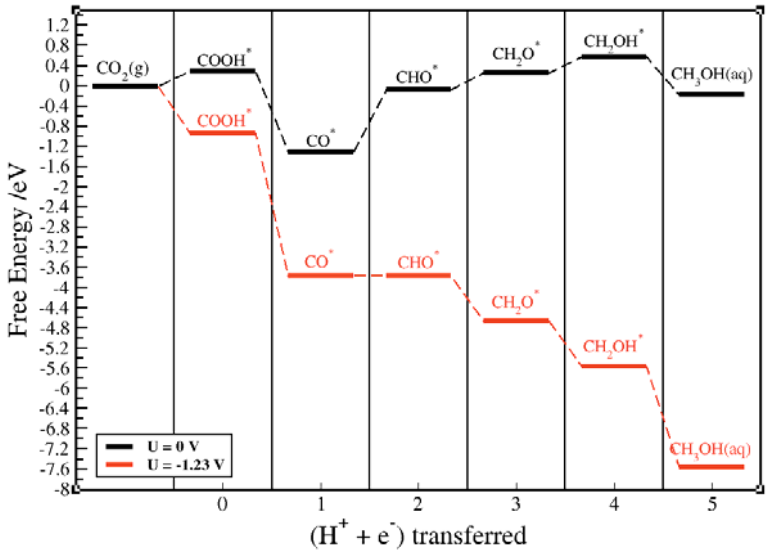

Figure 3-2: Free energy diagram for CO_2 reduction on Pt/Cu(111) surface alloy at: U = 0 V (black line) and U = -1.23 V (red line) where all the reaction steps become downhill in energy.

According to the CHE model, the potential determining step is protonation of CO* to form adsorbed CHO and the change in free energy corresponding to this step is 1.23 eV. This, in turn, means the reduction of CO_2 to CH_3OH occurs at a potential of -1.23 V versus RHE, corresponding to -1.26 V overpotential. Another reaction that occurs in parallel to CO_2 reduction is HER. Figure 3-3 shows the free energy diagram for HER on Cu/Pt(111) surface alloy. If hydrogen binds stronger than any of the intermediates of CO_2 reduction or if it co-adsorbs with CO_2 reduction intermediates, hydrogen poisons the

surface and at lower potentials HER prevails over CO_2 reduction. Since hydrogen adsorption is exergonic by -0.22 eV at 0 V versus RHE, it binds stronger than the first CO_2 reduction intermediate, COOH* at 0 V versus RHE. Moreover, since both COOH* and H* change similarly with the potential, decreasing the potential does not change their relative stability. Hence, it is expected that HER prevails over CO_2 reduction.

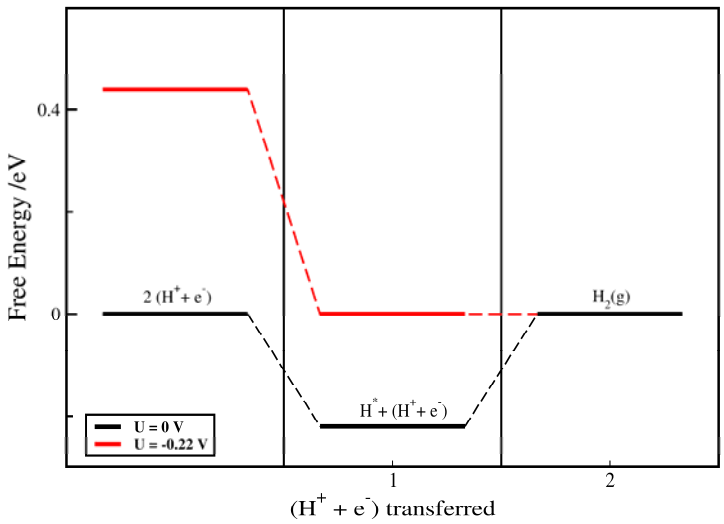

Figure 3-3: Free energy diagram for HER on Pt/Cu(111) surface alloy at: U = 0 V (black line) and U = -0.22 V (red line) where all the reaction steps become downhill in energy.

Therefore, to suppress H* poisoning the following two conditions should be fulfilled: 1) CO_2 reduction intermediates should bind stronger than H*, and 2) co-adsorption of hydrogen and CO_2 reduction intermediates at the potential where CO_2 reduction occurs should be avoided. CO is an inevitable intermediate in the reduction of CO_2, the reduction of which results in the same reduction product. Moreover, CO binding is not potential dependent, which makes it a possible alternative to COOH* to compete better with H*. Clearly, CO should bind to the surface to be able to compete with H*. In this scenario, one could also think of a tandem cathode where CO_2 is reduced to CO at the first cathode and then the product of the first cathode, CO, is further reduced at the second cathode. Using a tandem cathode has some advantages. Since the number of intermediates on each cathode is lower, it becomes easier to find a catalyst with optimal efficiency in catalyzing the related reaction [57]. For instance, on Au, CO is the major CO_2 reduction product, but Au is not a good catalyst for electrochemical reduction of CO

to hydrocarbons; it can be thus used as a catalyst in the first cathode, for the reduction of CO_2 to CO [8].

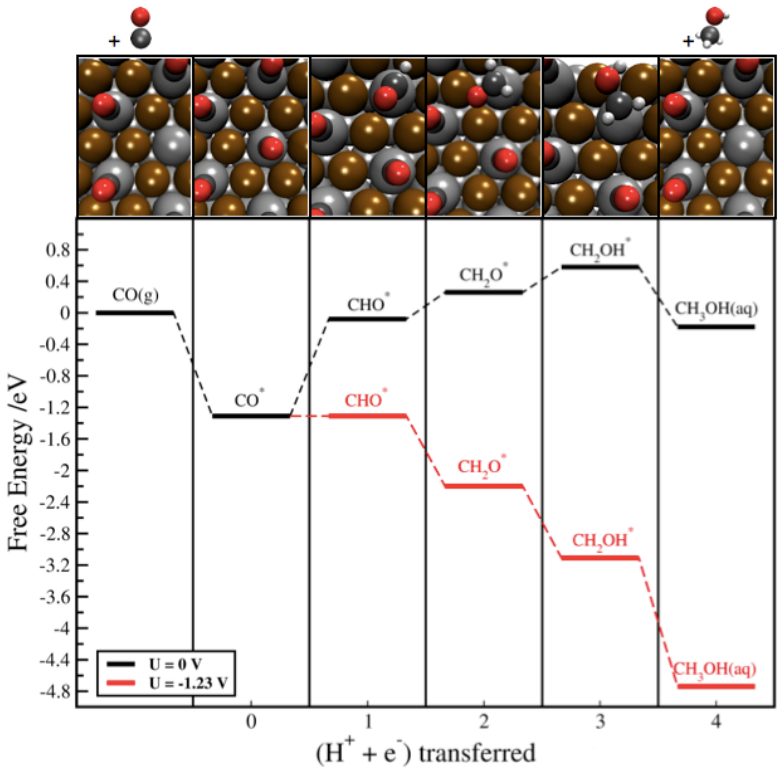

Figure 3-4: Free energy diagram for CO reduction on Pt/Cu(111) surface alloy at: U = 0 V (black line) and U = -1.23 V (red line) where all the reaction steps become downhill in energy.

As discussed in the previous chapter, the equilibrium coverage of CO* on the Cu/Pt(111) surface alloy is 0.33 ML, corresponding to adsorption of CO molecule on each Pt atom. Additionally, the binding free energy of CO is -2.02 eV which means it binds much stronger than H* on the top sites. Figure 3-4 shows the lowest free energy pathway for the reduction of CO on Cu/Pt(111) covered with 0.33 ML-CO*. Clearly, reduction of CO and CO_2 follow the same reaction pathways with the same PDS and overpotential: protonation of CO* to form adsorbed CHO* is PDS and the overpotential for reduction of CO to methanol is -1.23 V.

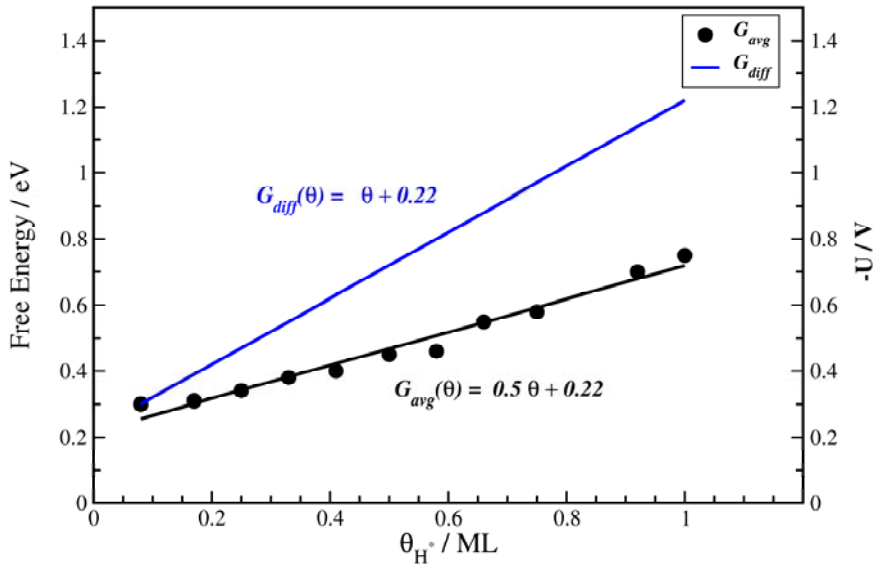

Figure 3-5: Differential and average free energies of adsorption of H on Cu/Pt(111) SA, co-adsorbed with 0.33ML CO. The black points are the calculated average free energies of adsorption of CO at different coverages and the black solid line is the fit to them. The blue line is the corresponding differential free energy of adsorption.

The second criterion that should be fulfilled to suppress HER is avoiding co-adsorption of CO and H*. To examine this, the differential free energy of H* adsorption on Cu/Pt(111) surface alloys pre-covered with 0.33ML-CO* was calculated. Differential free energy of H* adsorption defines the equilibrium coverage of H* co-adsorbed with 0.33ML-CO*. As can be seen from Figure 3-5, at -1.23 V, the potential at which CO reduction occurs, the hydrogen coverage on 0.33 ML-CO* is more than 1ML, indicating that HER dominates over CO reduction and the primary reaction product is hydrogen. This arises from the fact that H binds to the fcc site formed from Cu and Pt atoms on the surface and Pt atoms in the subsurface layer. Furthermore, DFT calculations show that the potential at which hydrogen evolves when co-adsorbed with CO i.e. U =-0.3 V versus RHE, is higher than the potential at which CO is reduced, i.e. -0.96 V. Therefore, HER dominates over CO reduction. We would like to emphasize that on pure Cu, even though intercalation of H* between adsorbed CO occurs, Cu binds CO moderately and H* binding is weaker. Therefore, H* poisoning is less severe compared to other metals that bind CO, which is consistent with the unique ability of Cu to reduce CO [[41]].

The above analysis demonstrates that embedding sites that can catalyze the reduction of CO_2 in a matrix of elements that have poor catalytic activity toward HER is

not sufficient to avoid HER; the subsurface atoms should also have poor catalytic activity towards HER. These findings encouraged us to investigate electrochemical reduction of CO_2 on Pt/Hg alloys, because Hg is inactive for HER and Pt binds CO and can catalyze the reduction of CO. According to early studies by Trasatti, mercury is one of the worst catalysts for HER and has the smallest exchange current compared to other metals [58]. It is expected that alloys of Hg with the transition metals that can catalyze the reduction of CO_2 will be able to suppress HER during reduction of CO_2.

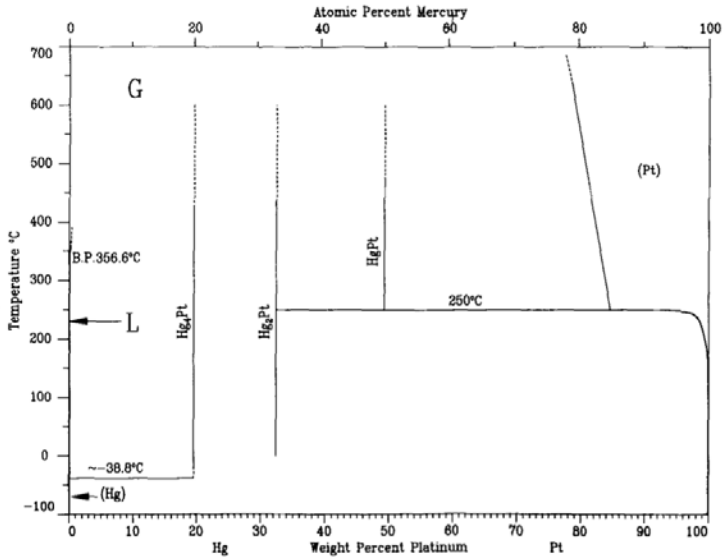

Figure 3-6: Phase diagram for the Pt-Hg system at standard pressure. (Ref. [59])

3.3 CO reduction on Pt/Hg alloy

In this section we draw our attention to Hg as a means of forming isolated Pt sites when alloyed with Pt. According to the phase diagram, Figure 3-6, several ordered intermetallic structures have been reported, including $PtHg_4$, $PtHg_2$ and PtHg. However from a thermodynamic point of view, previous experimental findings and our DFT calculations of the enthalpy of formation of different intermetallic structures suggest that formation of $PtHg_4$ is favored over $PtHg_2$.

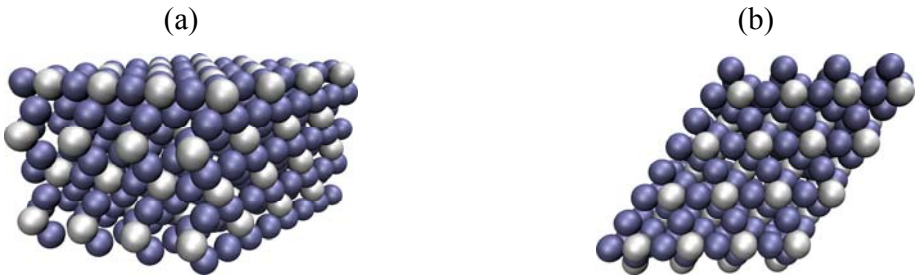

Figure 3-7: Side (a) and top (b) views of $PtHg_4(110)$ illustrating the isolated Pt sites surrounded by Hg atoms. White and blue atoms are Pt and Hg respectively.

The $PtHg_4$ crystal structure can be regarded as CsCl body-centered cubic (bcc) crystal structure where 3/4 of the Cs atoms have been removed. Hg can be easily electrodeposited onto Pt on Pt(111) and forms a self-organised surface structure of $PtHg_4$ and $PtHg_2$ at room temperature with (110) and (201) facets parallel to the Pt(111) subsurface, respectively [[60]]. Moreover, on $PtHg_4(110)$ each Pt atom is surrounded by Hg atoms, as can be seen from Figure 3-7, thus forming isolated Pt atoms on the surface, similar to Pt atoms on the Cu/Pt(111) surface alloy. However, unlike the Cu/Pt(111) surface alloy, the subsurface layer consists of only Hg. Hence, the co-adsorption of H* and CO* is prohibited as Hg atoms are completely inactive towards HER and Pt atoms are the only active sites on the surface for the reduction of CO. To elucidate this, we calculate the free energy of adsorption of hydrogen on Pt(111) and $PtHg_4$ (110) both in the presence and absence of CO*, as shown in Figure 3-8.

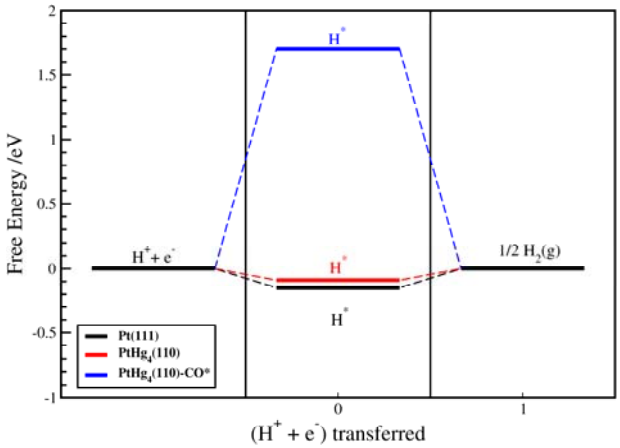

Figure 3-8: Free energy diagrams for HER on $PtHg_4(110)$ in the presence and absence of adsorbed CO and on Pt(111) at U = 0 V.

As can be seen, H* is significantly destabilized when co-adsorbed with CO* compared to the case when CO* is not present. Additionally, H* is destabilized on $PtHg_4(110)$, relative to Pt(111) which is attributed to the difference in their chemical properties resulting from alloying: on Pt(111) hydrogen binds to a three-fold hollow site while on $PtHg_4(110)$ it binds to a atop site of Pt atoms.

To investigate the electrochemical activity of $PtHg_4(111)$ for CO reduction, we construct a free energy diagram for the lowest energy pathway, obtained by examining the free energy of adsorption of all possible intermediates on $PtHg_4(110)$. As can be seen from Figure 3-9, the CO reduction product on $PtHg_4(110)$ is methanol and PDS is protonation of adsorbed CO to form CHO*, as on Cu(211).

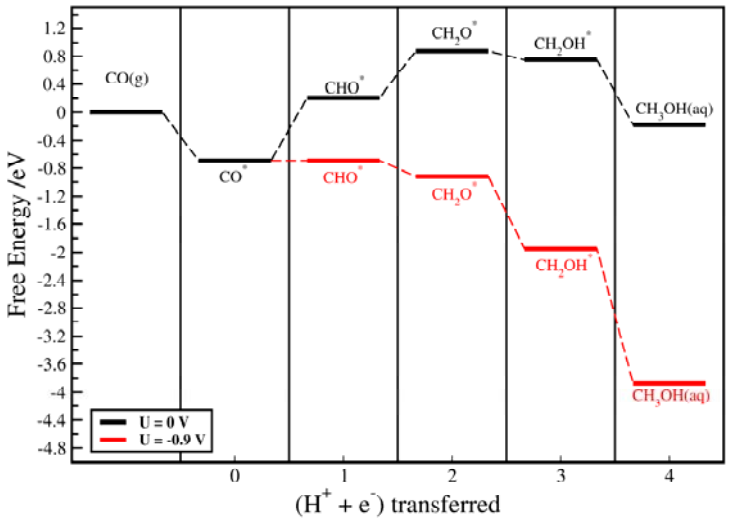

Figure 3-9: Free energy diagrams for CO reduction on $PtHg_4$(110). The black and red lines denote respectively the free energy levels at U = 0 V and U = -0.9 V, the potential at which all reaction steps become downhill.

At 0 V versus RHE, CO binds stronger than hydrogen. However, given that only isolated Pt atoms exist as reactive sites for both CO reduction and hydrogen adsorption, and due to the fact that H* stabilizes when the potential is reduced while CO does not, there will be a competition between CO and hydrogen for the Pt sites at negative potentials. If hydrogen binds stronger than CO* on Pt sites at the potential where CO* is reduced, CO* is replaced by H* and all Pt sites are blocked by H*. At -0.9 V where the reduction of CO* occurs, the H* binding free energy is -0.99 eV, which means H* binds 0.3 eV stronger than CO* and there is a driving force for replacement of CO* with H*. It is important to note that hydrogen poisoning is a more crucial issue on catalysts with isolated sites than on pure metals. This is because if isolated sites, that are the only available sites for the reduction of CO_2/CO, are blocked by any other adsorbate than CO_2 reduction intermediates, the CO_2/CO reduction will not proceed further.

3.4 Experimental Findings

In this section experimental results for electrochemical reduction of CO_2 on the Pt/Hg alloys are presented. These experiments have been performed by experimentalists at CINF at DTU including Arnau Verdaguer Casadevall, Professor Ifan Stephens and Professor Ib Chorkendorff.

3.4.1 Electrochemical measurements

To synthesize $PtHg_4$, a polycrystalline Pt disk is modified, following the procedure of Wu et al for Hg/Pt(111) [60]. ~10 monolayers (ML) of Hg were electrodeposited from $HgClO_4$. Ex-situ angle resolved X-ray photoelectron spectroscopy (AR-XPS) of the sample (Figure 3-10a) at this stage revealed the surface is composed of 20 % Pt and 80 % Hg, in agreement with a $PtHg_4$ structure. Figure 3-10bb shows a cyclic voltammogram in N_2-saturated solution for Pt and Hg-modified Pt. The voltammogram for Pt shows the typical hydrogen adsorption/desorption peaks at 0.05-0.5V, while Pt-Hg has a flat profile, suggesting a negligible amount of hydrogen adsorption. This is consistent with our DFT calculations, which show that H is destabilized on $PtHg_4$(110), relative to Pt(111) (Figure 3-8). On $PtHg_4$, hydrogen can only bind to atop of Pt atoms, the binding of which is weaker than the hydrogen atom that binds to a fcc hollow site on Pt(111). This means higher overpotential is needed to adsorb hydrogen on $PtHg_4$ compared to Pt(111). This can explain the flat profile of the voltammogram for $PtHg_4$ in the range of positive potentials. At lower potentials, as shown in Figure 3-11, hydrogen starts to evolve when the potential is decreased, confirming the weaker binding energy of hydrogen on $PtHg_4$.

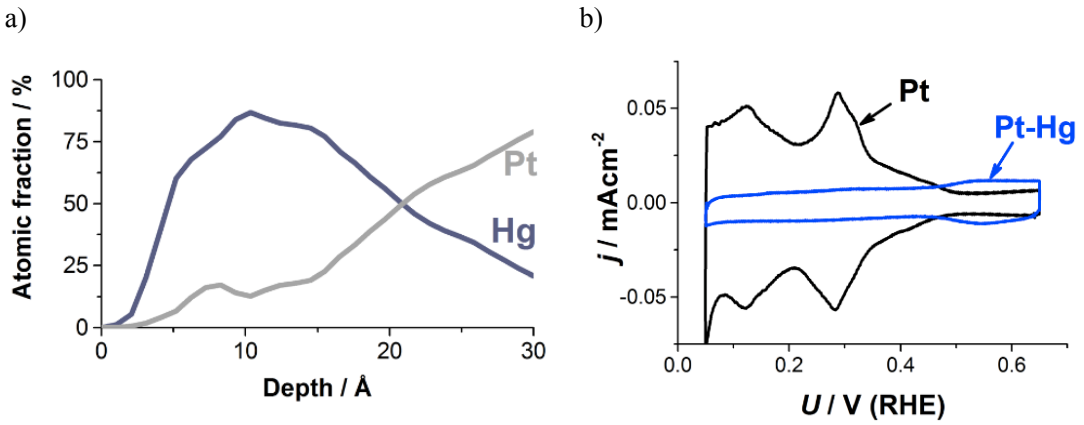

Figure 3-10: (a) AR-XPS depth profile of Pt-Hg and (b) Cyclic voltammograms in 0.1M $HClO_4$ for the Pt-Hg system. dU/dt = 50 mV/s

To further clarify the presence of isolated Pt sites on the surface of $PtHg_4$ alloy, the hydrogen oxidation reaction (HOR) was performed on both Pt and $PtHg_4$. It is generally accepted that HER (HOR) takes place through two different mechanisms, Volmer-

Heyrovsky (Heyrovsky-Volmer) and Volmer-Tafel (Tafel-Volmer) [34]. While the Volmer-Tafel mechanism requires the presence of two contiguous sites, one site is enough for the Volmer-Heyrovsky mechanism. It is observed that HOR occurs on Pt, while only a small current density corresponding to HOR on $PtHg_4$ is observed. The very low current density for HOR on $PtHg_4$ can be attributed to two factors: 1) due to lack of contiguous Pt sites on $PtHg_4$, HOR proceeds through Heyrovsky-Volmer mechanism which is accompanied with higher energy barrier when compared to Tafel-Volmer mechanism [34], 2) the coverage of Pt active sites on $PtHg_4$ is lower when compared to Pt(111) resulting in lower rate for HOR. This observation along with the flat voltammogram profile for $PtHg_4$, proves that Pt atoms on $PtHg_4$ are isolated and hence the Tafel-Volmer reaction is excluded for HOR.

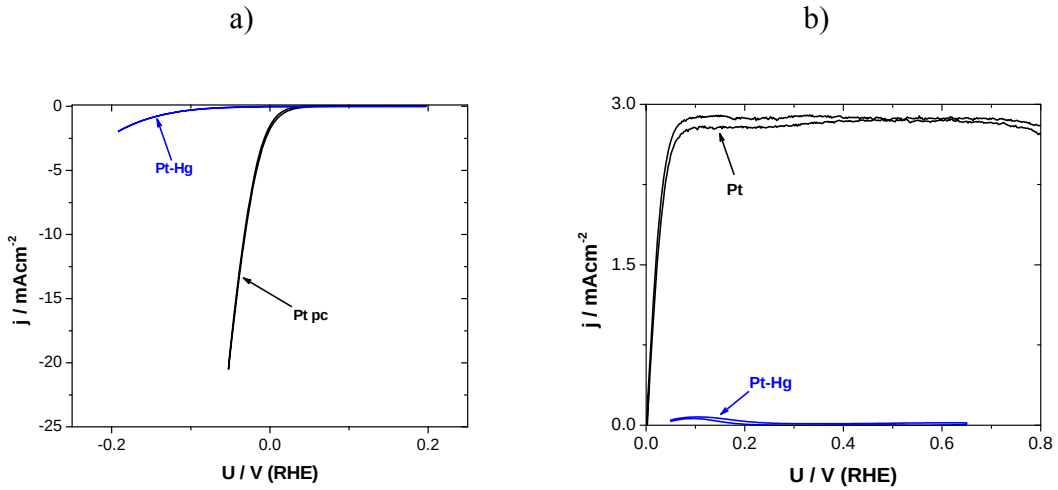

Figure 3-11: Polarization curve for HER (a) and HOR (b) on Pt and $PtHg_4$.

3.4.2 CO electro-reduction

In order to assess the electrocatalytic activity of $PtHg_4$ for reduction of CO, steady state measurement both in Ar and CO saturated solution was performed, as shown in Figure 3-12.

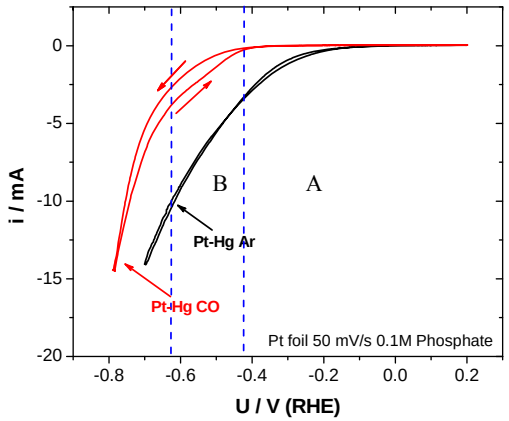

Figure 3-12: Cyclic voltammograms at 50 mV/s of PtHg4 in 0.1M HClO4 saturated with Ar (black line) and CO (red line). The blue dashed lines define different potential regions.

In the absence of CO, the cathodic current is observed at higher potentials compared to the one in the presence of CO (region A). The presence of CO shifts the onset potential to lower potentials. As discussed before, this is due to the fact that in the presence of CO, Pt sites are occupies by CO and hydrogen evolution is hindered. Increasing the current by decreasing the potential results in stabilization of hydrogen relative to CO, followed by displacement of CO by hydrogen (region B). Further decrease in the potential would result in evolution of hydrogen adsorbed on Pt sites. In summary, all the current is associated with HER and no current due to CO_2 reduction products is observed.

3.5 Summary and Outlook

Low Faradic efficiency towards desired products, in particular hydrocarbons/alcohols represents one of the major concerns in the electrochemical reduction of CO_2. On the catalysts that can catalyze the reduction of CO_2, HER prevails over CO_2 reduction, making CO_2 reduction an inefficient process. Therefore, to move ahead in increasing the efficiency, avoiding HER is crucial. In this chapter, we proposed a new strategy to suppress HER by designing catalysts with isolated active sites for CO_2 reduction, surrounded by elements that are inert towards both HER and CO_2 reduction. Pt/Cu(111) surface alloy (SA) and $PtHg_4$, two model systems with isolated Pt active sites surrounded by Cu and Hg respectively, were considered. DFT calculations on both Pt/Cu(111) SA and $PtHg_4$ and electrochemical measurements on $PtHg_4$ showed that although these catalysts retain the isolated sites, at negative potentials HER will prevail over CO_2/CO

reduction. On Pt/Cu(111) SA, co-adsorption of CO and hydrogen occurs at negative potential which causes HER to dominate over CO reduction. On $PtHg_4$, on the other hand, even though co-adsorption of CO and hydrogen does not occur due to inability of Hg atoms to bind CO and hydrogen, displacement of CO* by hydrogen at negative potential prevents further reduction of CO. These findings suggest that on catalysts with isolates sites, both co-adsorption of CO and hydrogen and CO displacement by hydrogen should be avoided. These criteria can be used to discover new and better performing catalysts with isolated sites.

Chapter 4

Selective Electrochemical Reduction of CO_2/CO on Intermetallic Alloys

In previous chapter, by investigating Cu/Pt surface alloy and Pt/Hg alloy, the criteria that the promising alloy should posses to direct the selectivity of CO_2 reduction to preferentially produce favorable products by suppressing hydrogen evolution reaction (HER) were discussed. I this chapter, using these criteria, we expand our search for discovering new electrocatalysts by creating specific ensembles on the surface of the catalysts. One way to create such ensembles is alloying. We consider CO_2/CO reduction by providing specific ensembles by combining transition metal (TM) elements (Ru, Co, Rh, Ir, Ni, Pd, Pt and Cu) that are capable of catalyzing CO_2 reduction with TMs (Ag, Au, Cd, Zn and Hg) or post-transition metal (PTM) elements (In, Sn, Pb, Sb and Bi) that are inert or have poor catalytic activity towards HER [8,61]. These ensembles span through the ensemble with isolated active sites and the ones with contiguous active sites. We examine different criteria that should be fulfilled for suppressing hydrogen evolution in the reduction of CO_2/CO on a pool of binary alloys. We compare electrocatalytic activity and selectivity of promising alloys with the ones for their constituent elements. Electrocatalytic activity and selectivity of promising alloys in the reduction of CO_2/CO is considered further by constructing free energy diagram and defining the CO reduction product.

4.1 **Binary Alloys**

According to our results on the reduction of CO_2 on Cu/Pt(111) surface alloy and Pt/Hg alloy, to suppress HER while allowing CO_2 reduction, two different sites on the surface are needed. Clearly such requirement is not accomplished on pure metals as the metals that can catalyze the reduction of CO_2 also have high activity towards HER. This means two different elements are needed to suppress HER: one element should be able to catalyze the reduction of CO_2 (breaking Oxygen-Carbon bond) and bind subsequent intermediates forming from reduction of CO_2, most notably CO, the reduction of which could result in the formation of hydrocarbons/alcohols; the other element should have low catalytic activity or be inert towards HER. Taking into account these requirements, we screened for new alloy catalysts of A_xB_y type, where A is the metal capable of catalyzing CO_2 reduction and B is the metal that has poor HER activity. For element A we took late TMs (Ru, Co, Rh, Ir, Ni, Pd, Pt and Cu) that can catalyze the reduction of CO_2 and bind CO. For element B, we took TMs (Ag, Au, Cd, Zn and Hg) and PTMs (In, Sn, Pb, Sb and Bi) that are very bad HER (and CO_2 reduction) catalysts [23,62]. The choice of the catalysts was guided by several rules: 1) the alloys should be thermodynamically stable according to their phase diagrams [63] and 2) they are not favored to form bulk oxides at potentials < 0 V versus RHE [45]. Table 4-1 lists the binary alloys along with their corresponding prototypes for their crystal structures and the corresponding facet(s).

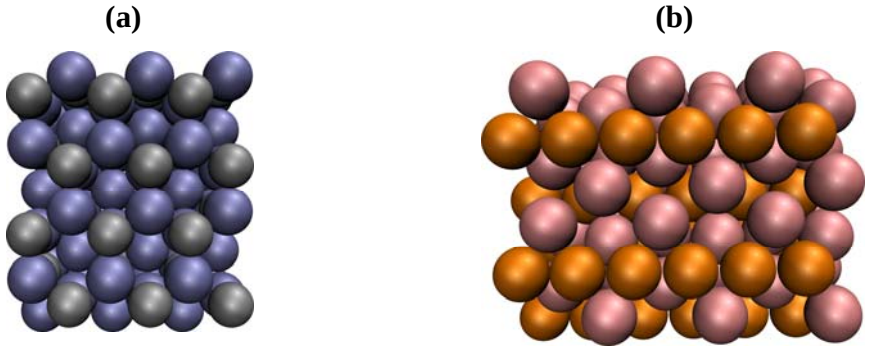

Figure 4-1: Top views of (a) $PtIn_2$(111) and (b) $PdPb_2$(100) alloys illustrating different arrangement of active sites. Gray and orange atoms are Pt and Pd active sites respectively, and blue and pink atoms are In Pb atoms as inert elements towards CO_2 reduction and HER respectively.

These sites provide the possibility to elucidate how selectivity and activity of the active pure metals for CO_2 reduction change when inert metal atoms towards HER surround them. These changes can be considered from the change in the electronic properties point of view that has been widely studied for other electrochemical reactions [18,24,64].

To reveal how different arrangements of the sites affect catalytic activity, alloys were classified into two groups based on the distribution of TM atoms on the surface: 1) alloys with an isolated TM site, where single metal A is completely surrounded by atoms B where atom A form isolated site, and 2) metal A forming rows of atoms embedded in the 'sea' of metal B.

Figure 4-1 shows $PtIn_2$ and CuAu as an example of the alloys with isolated and rows of A atoms. The alloys' surfaces with high A content were excluded because they resemble pure A solid phases and as such co-adsorption of CO_2 intermediates and hydrogen could occurs which indicate HER is dominated over CO_2 reduction. In contrary, the alloys' surface with low coverage of A atoms, make co-adsorption of CO_2 reduction intermediates less likely. This, in turn, will hinder HER. For instance, according to phase diagram, Pt and Sn form five stable alloys including: PtSn, $PtSn_2$, $PtSn_4$, Pt_3Sn and Pt_3Sn_2. While first three alloys are Sn rich phases, the last two are Pt rich phases that are excluded from screening.

4.2 Isolated sites as active sites for CO_2 reduction

We draw our attention to the alloys with isolate active sites. We would like to mention that the concept of isolated reaction centers is not new; it has previously been applied for other electrochemical reactions such as oxygen reduction reaction on both metallic and non-metallic catalysts [65,66]. Maroun and co-workers studied electrochemical adsorption of hydrogen and CO adsorption and electrooxidation on different ensembles of Pd on Pd/Au(111) surface alloys [67]. They showed that hydrogen adsorption requires more contingent Pd sites, while Pd monomers are the active sites for CO adsorption.

Table 4-1: List of binary alloys along with their representative prototypes for their crystal structures and their corresponding facet(s).

Alloy	**Crystal structure Prototype**	**Facet(s)**
RhIn	CsCl	(100)
$RhSn_2$	Al_2Cu	(100)
$RhPb_2$	Al_2Cu	(100)
$RhBi_2$	$CoSb_2$	(001)
IrSn	NiAs	(110),(100)
$IrSn_2$	CaF_2	(111)
IrPb	NiAs	(110),(100)
$IrSb_2$	$CoSb_2$	(001)
$NiHg_4$	$PtHg_4$	(110)
$PdAg_3$	$AuCu_3$	(111)
$PdAu_3$	$AuCu_3$	(111)
PdIn	CsCl	(110)
$PdSn_4$	$PtSn_4$	(010)
$PdPb_2$	Al_2Cu	(100)
$PdSb_2$	FeS_2	(100)
$PdBi_2$	$CuZr_2$	(010)
PtZn	AuCu	(100)
$PtHg_2$	$PtHg_2$	(201)
$PtHg_4$	$PtHg_4$	(110)
PtSn	NiAs	(110),(100)
$PtSn_2$	CaF_2	(111)
$PtSn_4$	$PtSn_4$	(001)
PtPb	NiAs	(110),(100)
$PtPb_4$	$PtPb_4$	(100)
PtSb	NiAs	(110),(100)
$PtSb_2$	FeS_2	(001)
PtBi	NiAs	(110),(100)
$PtBi_2$	FeS_2	(111)
CuAu	CuAu	(100)
$CuAu_3$	Cu	(111)
CuZn	CsCl	(110)
Cu_2Sb	Cu_2Sb	(001)

4.2.1 Selectivity

As discussed above, one of the important challenges in making CO_2 reduction efficient is related to selectivity of the catalysts towards HER. The selectivity is defined based on the competition between different adsorbates to bind to the active sites. In the pool of alloys we are considering, all active transition metals towards CO_2 reduction are also active for HER. Therefore, there is a competition between H* and the intermediates involved in the reduction of CO_2 for occupying active sites. Basically, all intermediates should bind stronger than CO_2 reduction intermediates. At this point, the competition between all involved intermediates and hydrogen should be considered by comparing their free energy of binding to the active sites. However, if H* binds stronger than any of the intermediates, the surface is poisoned and CO_2 reduction in hindered. In the reduction of CO_2, all possible reaction pathways proceed through COOH* (Carboxyl) or OCHO* (formate), and hence these are the first intermediate to be investigated for the competition with H*. To elucidate this, we calculate the free binding energy of adsorption of hydrogen and COOH* or OCHO*, depending on which one binds stronger to the surface. In Figure 4-2, the free binding energies of H* and COOH*/OCHO* are plotted against each other. To avoid H* poisoning, H* should bind weaker than COOH*/OCHO*, that is, the points should fall in the lower part of the graph where $G_{COOH*/OCHO*} < G_{H*}$. Unfortunately as can be seen from Figure 4-2 this in not the case and all on the points lie below the diagonal where H* binds stronger than COOH*/OCHO*. In addition, applying potential does not change the relative stability of H* and COOH*/OCHO* because they all change similarly with the potential: formation of H* and COOH*/OCHO* steps involve one electron-proton transfer and decreasing the potential will stabilize both COOH*/OCHO* and H* equally which means at negative potentials all active sites are blocked by H*. The only way to avoid H* poisoning is to avoid COOH* formation. This is accomplished by the reduction of CO instead of CO_2, the same approach that was followed in the reduction of CO_2 on Cu/Pt surface alloy.

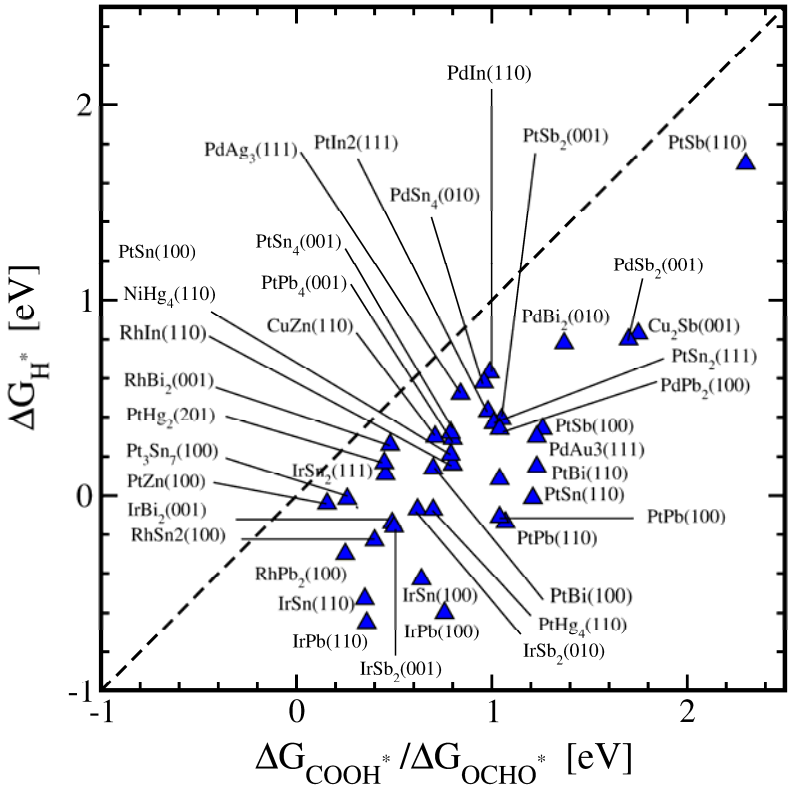

Figure 4-2: Free binding energies of COOH* and H* against each other that defines the selectivity towards CO_2 reduction or hydrogen poisoning. For the alloys that are located above the diagonal, as is the case for all alloys, hydrogen adsorption prevails over COOH* adsorption. Binding energies are calculated with reference to H_2(g), CO_2(g) and H_2O(l). The change in the potential will not change the relative free energies f binding of COOH* and H*, because both change, i.e. stabilize and destabilize, similarly with potential.

As mentioned also in reduction of CO_2 on Cu/Pt(111) surface alloys, this approach requires that CO binds to the surface, otherwise it will not be able to compete with H*, and the primary reaction product of CO reduction is expected to be hydrogen. As can be seen from Figure 4-3, on few alloys with positive free energy of binding, CO does not bind to the surface. However, we would like to emphasize that, on these alloys, a possible way to bind CO* is to increase partial pressure of CO.

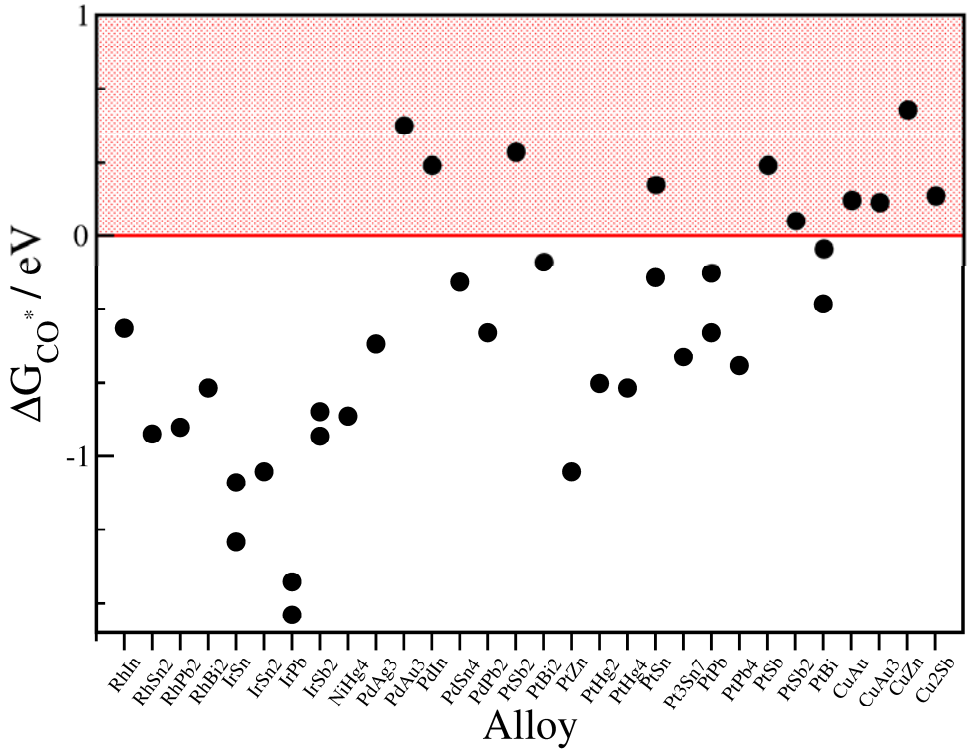

Figure 4-3: Free energies of binding of CO on different binary alloys. For some alloys two facets have been considered. The dashed horizontal red line designates the chemical potential of CO in the gas phase above which CO does not bind to the surface (shaded area).

On the other hand on the alloys with negative free energies of binding of CO, CO can potentially compete with H*. To avoid H* poisoning on these alloys, CO should bind stronger than H*. To elucidate H* poisoning on these alloys, the free binding energies of CO* and H* are plotted against each other in Figure 4-4. It can be seen that on all alloys, CO* binds stronger than H* at U = 0 V vs. RHE as all the points are located above the diagonal, i.e. $G_{CO*} < G_{H*}$. However, some care should be taken when decreasing the potential: unlike the binding energy of CO* that does not change, the binding energy of H*, i.e. the free energy of $H^+ + e^- \rightarrow$ H*, does change and H* stabilizes by decreasing the potential. Accordingly, the point would shift down in Figure 4-4, where H* binds stronger than CO*. For the points below the diagonal where $G_{H*} < G_{CO*}$, it is more favorable that CO* is displaced by H*. Consequently the selectivity would change towards HER. On the other hand for the alloys that remain above the diagonal, CO* would bind stronger than H*, i.e. $G_{CO*} < G_{H*}$, and CO* displacement would not occur. To examine if CO* displacement by H* happens on alloys, one needs to know the overpotential required for

reduction of CO*, i.e. U_{OP}. On the alloy catalysts that CO* binds stronger than H* at U_{OP}, i.e. $G_{CO*} < G_{H*}(U_{OP})$, CO* will not be displaced by H*. On the other hand, on the alloy catalysts that CO* binds weaker than H* at U_{OP}, i.e. $G_{H*}(U_{OP}) < G_{CO*}$, CO* will be displaced by H* and the active sites are blocked by H*.

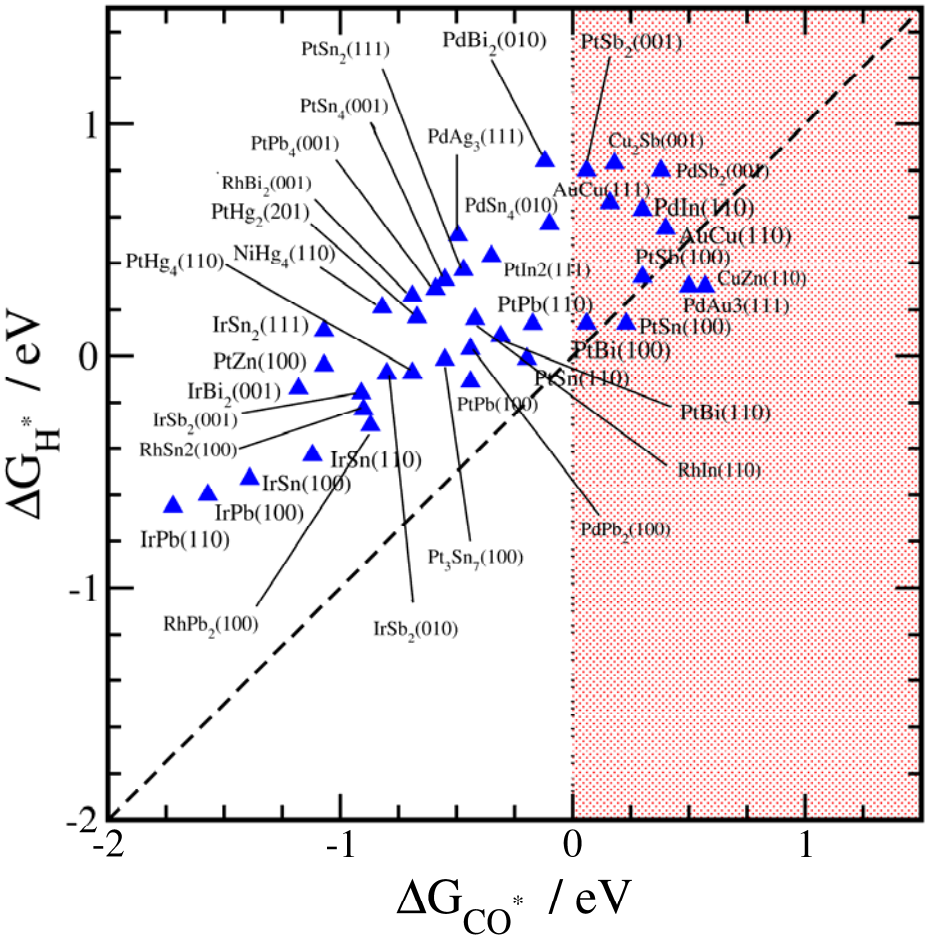

Figure 4-4: Correlation between free energies of binding of CO* and H* on alloys, referenced to CO(g) and H_2(g), defining the the selectivity towards CO reduction and hydrogen adsorption at U = 0V versus RHE. The alloys in the shaded area do not bind CO.

To calculate the overpotential for the reduction of CO*, we assume the same potential determining step for the reduction of CO* as on pure metals which is protonation of CO* to form CHO* or COH*, meaning that the overpotential is defined as below [6,68]:

$$U_{OP} = (\Delta G_{CHO^*/COH^*} - \Delta G_{CO^*})/e \qquad (4\text{-}1)$$

We note that the overpotential is proportional to the catalytic activity for the reduction of CO as the same time. In Figure 4-5, the binding free energies of CHO*/COH* are plotted against the corresponding ones for CO*. Ideal catalyst with zero overpotential should lie right on the diagonal. However, Figure 4-5 shows that all the alloys are located far from the diagonal indicating high overpotentials are needed to reduce CO*.

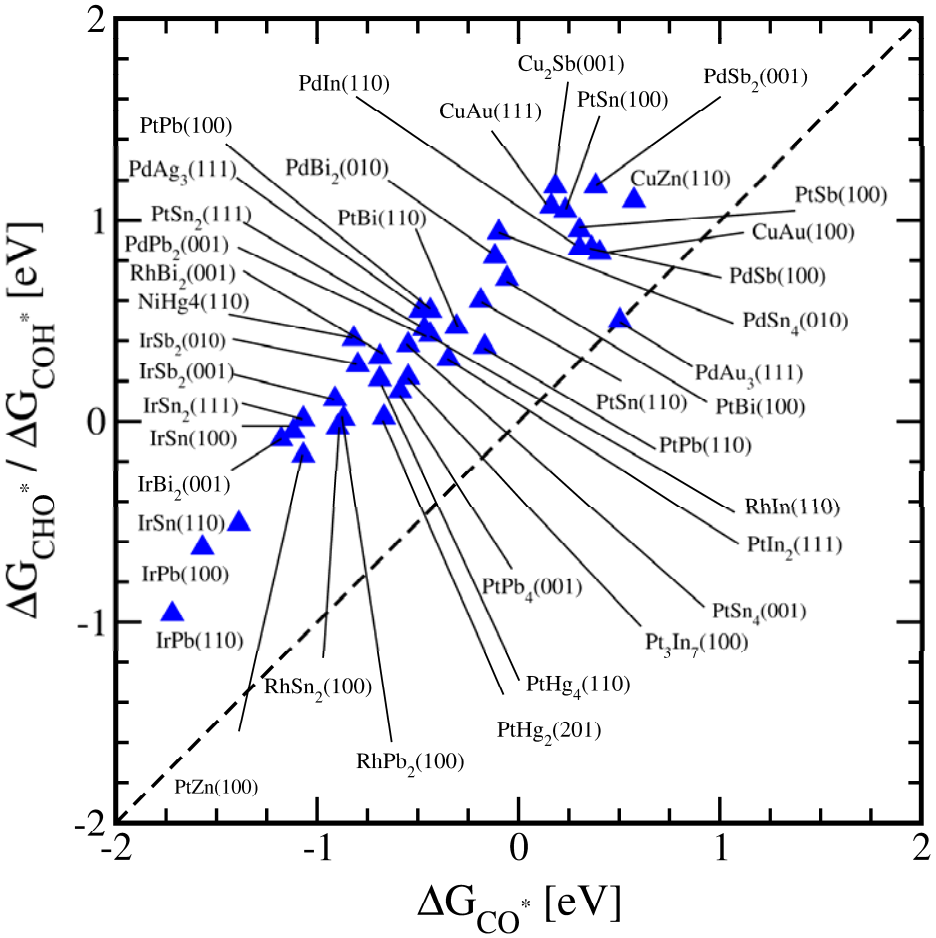

Figure 4-5: Correlation between free energies of binding of CO* and CHO*/COH* on alloys, referenced to CO(g) and H_2(g), defining the overpotential for the reduction of CO*. The overpotential is defined as the difference between the free energy of binding of CO* and CHO*/COH*. The alloys that are located on the diagonal, exhibit zero overpotential.

To examine if CO displacement occurs by H*, we note that at CO reduction potential, H* would bind by $-eU_{OP}$ stronger compare to the binding strength at U = 0 V (RHE). Therefore, to prevent CO* displacement by H*, CO* should bind stronger than H* at U_{OP}

potentials. We arrive to the following expression for the optimal binding energies of CO* and H* to avoid CO* displacement by H*:

$$G_{CO*} < G_{H*}(U_{OP}) \rightarrow$$
$$G_{CO*} < G_{H*}(U = 0) + e\,U_{OP} \rightarrow$$
$$G_{CO*} < G_{H*}(U = 0) - (G_{CHO*/COH*} - G_{CO*}) \rightarrow$$
$$(G_{CHO*/COH*} - G_{CO*}) < (G_{H*}(U = 0) - G_{CO*}) \qquad (4\text{-}2)$$

In Figure 4-6, the binding free energies of H* at required overpotentials to reduce CO* are plotted against the free binding energy of CO*. According to expression (4-2), to inhibit CO* displacement by H*, the points should lie above the diagonal. Unfortunately, only a few alloys including ($PtIn_2$(111), $PtHg_2$(201), $PtPb_4$(001), $PdBi_2$(111) and $IrSn_2$(111)) fulfill this condition, meaning that they could potentially reduce CO to valuable products without suffering from H* poisoning. For $PdBi_2$(111) and IrPb(100) that are located very close to the diagonal, there would be a strong competition between CO* reduction and H* adsorption and presumably these reactions are proceed in tandem on these alloys. We would like to emphasize that all of the promising alloys have isolated active sites surrounded by inert metals towards HER.

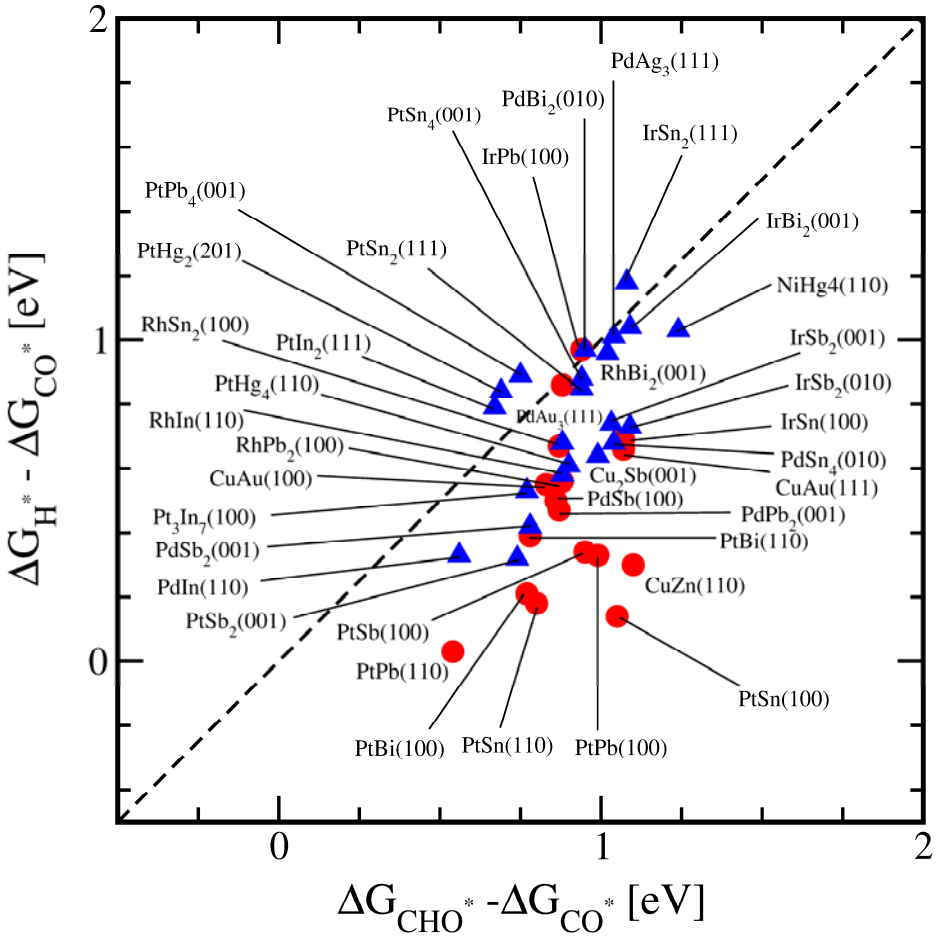

Figure 4-6: Selectivity criterion defining the preference towards CO reduction or H adsorption. The differences between the binding free energies of CO* and H* (potentials at which CO is displaced) are plotted against the differences between the binding free energies of CHO*/COH* and CO* (overpotentials required for CO* reduction). Blue triangles and red circles show the alloys with isolated TM sites and alloys with TM rows on the surface, respectively.

4.2.2 CO reduction product on promising alloys

To identify final reaction product on selective alloys ($PtIn_2$, $PtHg_2$, $PtPb_4$ and $IrSn_2$) the free energy diagrams were constructed by examining all possible reaction intermediates. Figure 4-7 shows the free energy diagrams for CO reduction on all promising alloys. As initially assumed, the PDS for CO reduction on all of the selective alloys is reduction of CO* to CHO*.

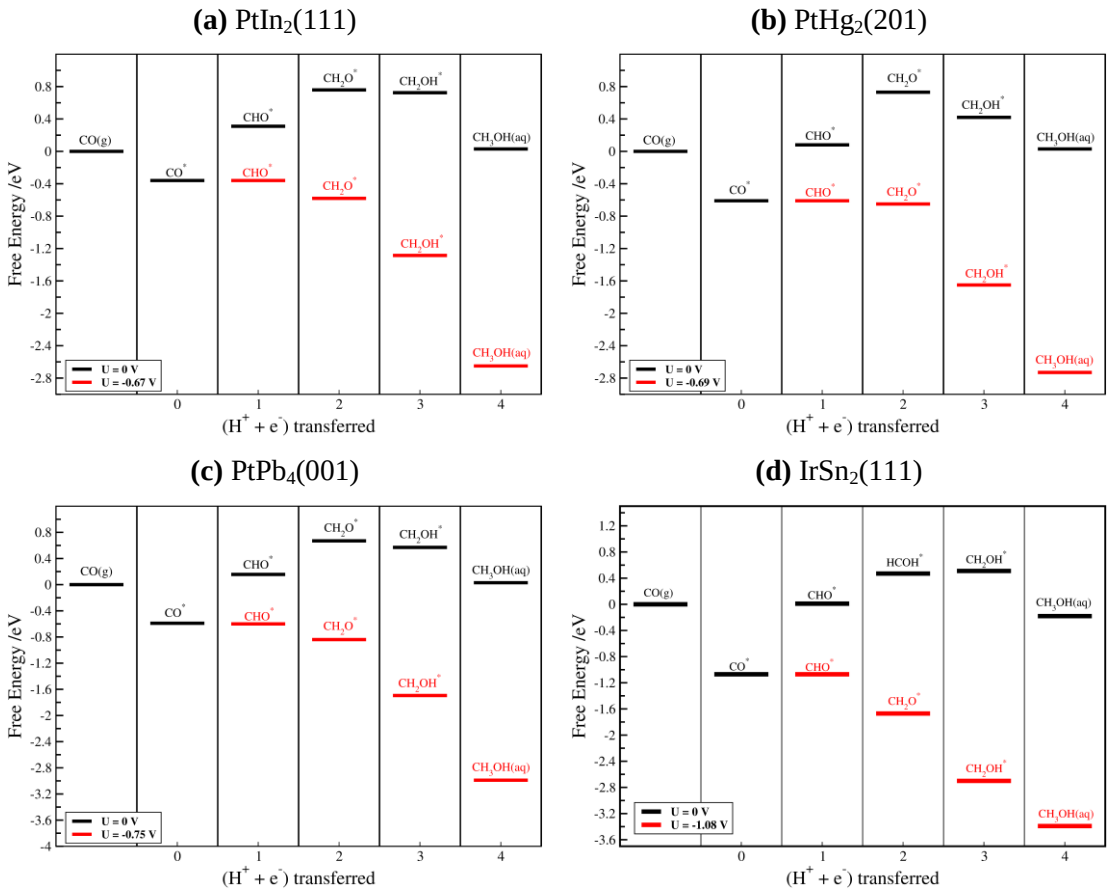

Figure 4-7: Free energy diagrams for CO reduction on selective alloys: (a) $PtIn_2$, (b) $PtHg_2$, (c) $PtPb_4$ and (d) $IrSn_2$. Black and red lines denote the free energy levels at 0 V and at the potential where all reaction steps become downhill in free energy.

Table 4-2 lists the final reduction product, the free binding energies of CO* and CHO*, potential at which CO reduction occurs, and the potential determining step for each selective alloy. As can be seen the reduction product on all selective alloys is methanol. Among the selective alloys, the most active catalyst for the reduction of CO is $PtIn_2$ which exhibits 0.67 V overpotential followed by $PtHg_2$(201), $PtPb_4$(001) and $IrSn_2$(111) with 0.69, 0.75 and 1.08 V overpotential respectively. Clearly $PtIn_2$ and $PtHg_2$ exhibit a considerable activity improvement over Cu (0.91 V), the most selective metal catalyst for CO reduction. Moreover, the final reaction product of CO reduction on all alloys is methanol that is different from that of Cu where methane and ethane are the main CO reaction products, and no methanol is observed as the CO reduction product on Cu. As a comparison, on Cu, the Faradaic efficiency for methane and ethane at a current density of 5 mA/Cm^2 (-1.04 V vs RHE) are 33.3 and 25.5%, respectively [8]. At this point,

achieving higher Faradic efficiency towards methanol with lower overpotential than on Cu, would be a breakthrough.

Table 4-2: Calculated potentials for CO reduction, reaction product and potential determining steps on four selective alloys, i.e. $PtIn_2$, $PtHg_2$, $PtPb_4$ and $IrSn_2$. The same data for Pt(111) and Pd(111) is given for comparison.

Alloy	G_{CO*} (eV)	G_{CHO*}/G_{COH*} (eV)	Potential determining step (pds)	Potential (V)	Reaction Product
Pt(111)	-0.87	-0.33	$CO^* \rightarrow COH^*$	-0.54	H_2
Pd(111)	-1.07	-0.1	$CO^* \rightarrow COH^*$	-0.96	H_2, CH_4
$PtIn_2$(111)	-0.60	0.18	$CO^* \rightarrow CHO^*$	-0.67	CH_3OH
$PtHg_2$(201)	-0.61	0.08	$CO^* \rightarrow CHO^*$	-0.69	CH_3OH
$PtPb_4$(001)	-0.52	0.24	$CO^* \rightarrow CHO^*$	-0.75	CH_3OH
$IrSn_2$(111)	-1.07	0.01	$CO^* \rightarrow CHO^*$	-1.08	CH_3OH

4.2.3 Role of electronic and ensemble effects in tuning the selectivity

In this section, I will discuss the role of ensemble and electronic effect in tuning the selectivity and hindering HER. As for the electronic effect, the role of electronic effect is more evident when the selectivity and activity of they alloys are compared with that of for alloys constituents, i.e. Pt and Pd. Hydrogen is the main reaction products on Pt and Pd. On Pt(111) and Pd(111), CO and hydrogen adsorb on top and fcc hollow-sites respectively. Moreover, as discussed before, co-adsorption of CO* and hydrogen also occurs on the same sites. This means hydrogen can be evolved before CO* is being reduced as lower overpotential is needed to reduced hydrogen. On the other hand, on alloys with isolates sites, due to change in the surface geometry, such hollow sites do not exist and instead there are sites forming from inert metals towards HER that are inactive in adsorbing CO* at the same time. This means, such co-adsorption is hindered, and only one adsorbate can bind to the surface at time. This is the way that ensemble effect comes to paly in hindering HER in the course of CO reduction.

On the other hand, changing the geometry of the atoms on the surface also modifies the electronic structure of the active sites and hence the binding strength of the

adsorbates bound to them. As can be seen from Table 4-2, the binding energies of CO*, CHO* and H* on Pt and Pd are different from the corresponding ones on selective alloys. More sepecifically, the overpotential for CO* reduction, i.e. the difference between CHO* and CO* free energies of binding on the selective alloys are different from the ones on Pt and Pd. This difference is manifested in the activity as well as preventing CO* displacement by H*. In summary, the combination of these two effects give rise to distinct selectivity and activity for CO reduction that is different from Pt and Pd.

4.3 **Summary and Outlook**

The main challenge to increase the selectivity for CO_2 reduction is to avoid parasitic HER. Following the strategy to create active sites for CO_2 reduction that are surrounded by inactive elements towards HER, we examined stable binary bulk alloys forming from transition metals (TMs) that can catalyze reduction of CO_2 and TM or PTMs that are inactive for HER. It turned out that all the alloys are poisoned by hydrogen as it binds stronger than the first intermediates in the CO_2 reduction path. To overcome this obstacle, CO is reduced instead, as it competes better with hydrogen for the active sites at zero potential. However, since hydrogen binding is potential dependent, while CO binding is not, at sufficiently negative potential H will displace CO from the surface. Among the pool of binary alloys considered in this work (40 in total), only five alloys $PtIn_2$, $PtHg_2$, $PtPb_4$, $PdBi_2$ and $IrSn_2$ are highly selective for CO reduction. Out of these $PtIn_2$, $PtHg_2$ and $PtPb_4$ possess higher activity than Cu, the best-known metal catalyst for the reaction.

In this work we have not just identified good potential catalysts for CO reduction but also revealed a class of materials that is not bound by the limitations set by volcano plots. This finding can open up an alternative path for screening new electrocatalysts for a range of other reactions.

Chapter 5

Electrochemical Reduction of CO_2/CO on Metal Functionalized Graphene

Metallic catalysts, such as binary alloys, are not the only systems that can preserve single sites. In the line search for finding the catalysts with isolates sites, in this chapter we consider electrochemical reduction of CO_2 on functionalized graphene, namely metal-functionalized graphene structures.

5.1 Electronic structure: Me-porphyrin structures versus extended surfaces

Catalytic activity of functionalized graphene, in particular nitrogen functionalized graphene, has been reported before for other electrochemical reactions, namely ORR [[69,70],]. The catalytic activity of these structures can be tuned when they are functionalized with transition metals, which can be attributed to the change in the electronic properties when they are anchored with transition metals. These metal functionalized porphyrin structures have been considered for ORR [[69,71]]. Siahrostami and co-workers considered the electroctalytic activity of Me-porphyrin catalysts for the reduction of oxygen to hydrogen peroxide.

Two different types of structures could form depending on the coordination of the nitrogen atoms with neighboring carbon atoms [[69]]. We have only considered the

configuration where each nitrogen atom belongs to two rings centered on the metal atoms, and the rings are composed of two and three carbon atoms. Figure 5-1a shows Pt Metallo-porphyrins (Me-Porphyrins) structure as an example of such structures. As noted in the previous section, the electronic properties of an isolated atom are different from those for pure metals. To shows this, we have compared the d-band projected density of states (DOS) of the Pt atom at the Pt porphyrin-like structure and the Pt atom on the extended Pt(111) surface structure (Figure 5-1b). Clearly there is a stark difference between the projected DOS of these systems: while Pt atom in extended Pt(111) surface structure has a broad band feature, the Pt atom in Pt-porphyrin system has sharp peaks, representing more an atomic-like features. This can also be seen by looking at the density of states at the Fermi level of Pt-porphyrin system where there is a big gap between the lowest occupied available states just below the Fermil level and the highest unoccupied available states above the Fermi level. On the other hand, for Pt atom in the extended Pt(111) surface structure, there is a continuity in the available states just below and above Fermi level. Such difference, in turn, could result in different catalytic activity from metal-based catalysts.

(a) (b)

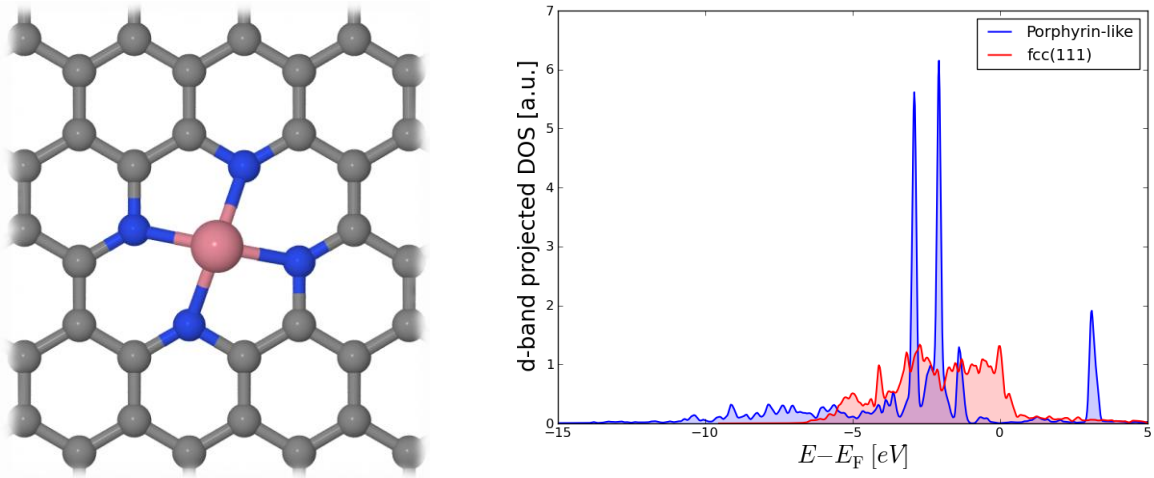

Figure 5-1: (a) Atomic structure of Pt-porphyrin structure. The Pt atom is coordinated to four nitrogen atoms. (b) Comparison between projected density of states into the d orbitals of Pt atom locates at the center of Pt-porphyrin and at the surface of Pt(111) extended surface.

The discontinuity in the available states below and above the Fermi level raises the

question that the potential and hence the binding energy does not change linearly. In fact, since there are discrete energy levels above the Fermi level, transferring electron from the occupied states below the Fermi level to the discrete empty states above the Fermi level is possible only at the certain potentials where the chemical potential of the electron is high enough to fill the empty states above the Fermi level. In other word, before reaching to that potential, no charge transfer occurs and hence the binding energy will not change. This is in contrast to CHE model that assumes the binding energies of the intermediates change linearly with potential. This, in turn, should be manifested in the cyclic voltammetry of these systems: if the binding energies of the adsorbates do not change linearly with voltage, there should be discrete peaks in cyclic voltammetry for Me-porphyrins. However, as evidenced from the CV diagram, this is not the case and CV diagram for these systems is continues and does not show abrupt peaks [[72,73]]. This can be explained by considering the formation of dipole at the interface of the electrode and solution: when a potential is applied, a dipole form due to the presence of protons in the solution and negative charges on the surface. Apparently, if the protons approach towards the surface, they will face a barrier due to the presence of dipole at the interface. We note that this is not a problem for non charged species such as H_2(g), because there is no interaction between H_2(g) and the dipole. Now, if the potential is changed, the dipole changes accordingly, making it easier or more difficult (depending on the charge and the voltage) for the charged species to overcome the barrier forming from dipole. We would like to emphasize that adding charge to the surface (applying potential) does not change the DOS and d-band center of the catalyst. Dipole at the interface is the only thing that changes and the energy levels will not move up or down in energy. Therefore, in this picture, empty states above the Fermi level will remain empty and filling of the states below the Fermi level will remain intact when the voltage is changed.

5.2 **Selectivity**

Similar to metallic binary alloys, we examine the stability of Me-porphyrin systems against hydrogen poisoning when they are used as catalysts for CO_2 reduction. These systems include: Cu, Ag, Au, Ni, Pd, Pt, Co, Rh, Ir, Fe, Ru, Os, B, Al, Ga, and Mg. We note that since there is just one site to which the adsorbates can bind, COOH* will be

more stable than OCHO*. This is due to the fact that normally two sites are needed for OCHO* binding. In Figure 5-2 the binding energies of COOH* and H* are plotted against each other. To avoid hydrogen poisoning, all the points should locate below the diagonal. However, as be seen all the points are below the diagonal where hydrogen binds stronger than COOH* and all the active sites are blocked by hydrogen.

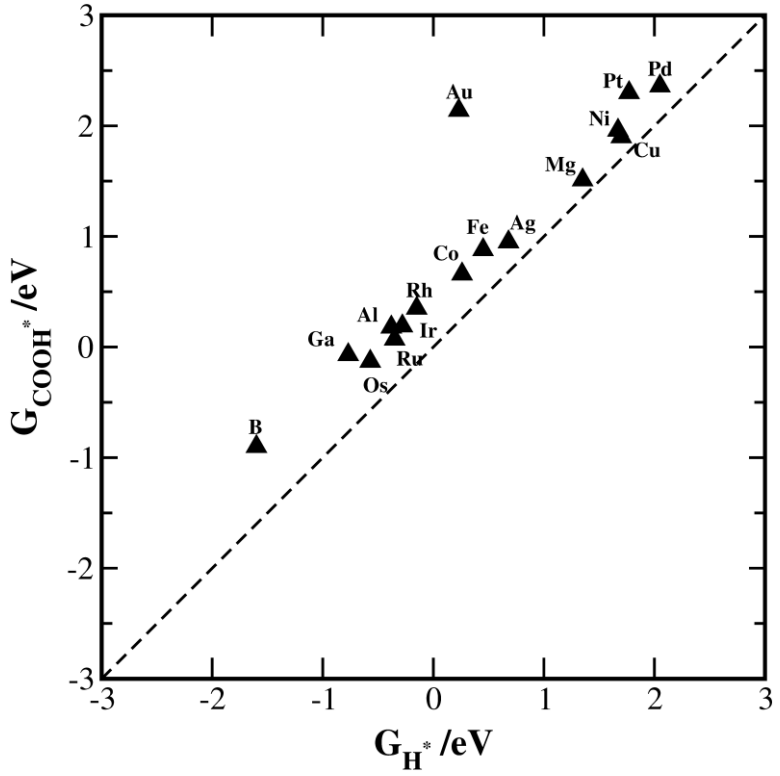

Figure 5-2: Free binding energies of COOH* and H* against each other that defines the selectivity towards CO2 reduction or hydrogen poisoning. For the Me-porphyrins that are located above the diagonal, as is the case for all Me-porphyrins, hydrogen adsorption prevails over COOH* adsorption. Binding energies are calculated with reference to H_2(g), CO_2(g) and H_2O(l). The change in the potential will not change the relative free energies of binding of COOH* and H*, because both change, i.e. stabilze or destabilize, similarly with potential.

To get around the hydrogen poisoning problem, we use CO as a viable alternative to CO_2 that competes better than COOH* with hydrogen for occupying isolated sites. This requires CO binds to the surface at the first step to be able to compete with hydrogen poisoning. To investigate if CO can impede hydrogen poisoning, we have plotted binding energies of CO* and H* against each other in Figure 5-3. For the alloys that lie below the diagonal, CO* would bind stronger than H*. We would like to emphasize that this is not

the case for the Me-porphyrins that locate below the diagonal, i.e. with positive free binding energies of CO*. On these Me-porphyrins, CO does not bind, and H* would stabilize by decreasing the potential, while CO* binding does not change. This means at negative potential on the alloys with positive free energy of adsorption of CO*, hydrogen poisoning prevails over CO reduction, as occurs for Ga, Al, Au, Mg, Cu, Ni, Pt and Pd-porphyrins.

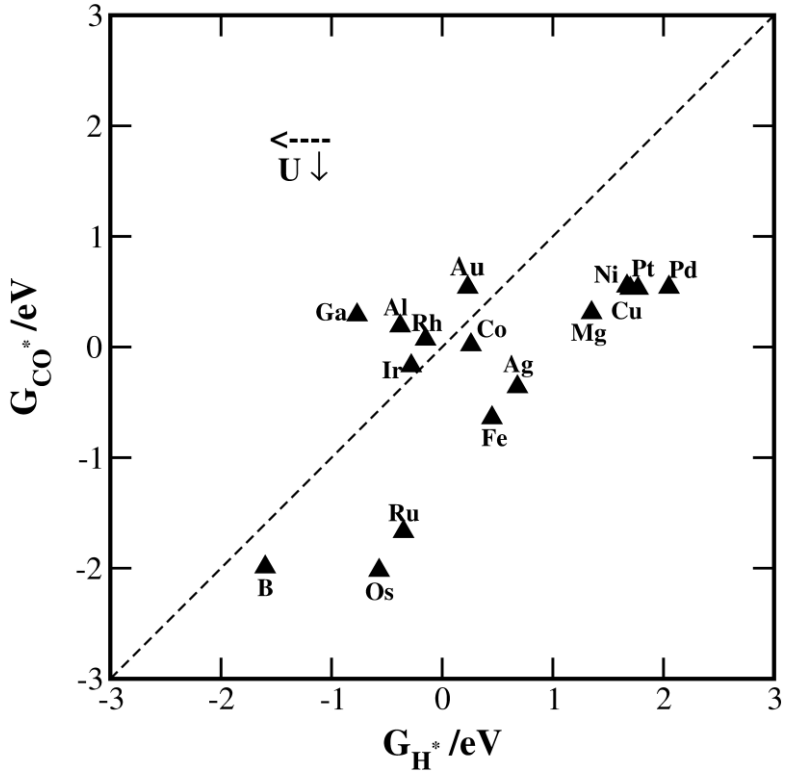

Figure 5-3: Free binding energies of CO* and H* against each other, defining the selectivity towards CO binding and hydrogen poisoning. For the Me-porphyrins that are located above the diagonal, hydrogen adsorption prevails over CO* adsorption. CO and hydrogen binding energies are calculated with reference to H_2(g), CO(g). The horizontal arrow shows how the hydrogen binding energies change with potential (vertical arrow).

For the Me-porphyrins that bind CO weaker than H*, one way to bind CO is to cycle the potential to positive values where CO* bind stronger than H*. For example, Rh locates very close to the diagonal and the selectivity will be towards hydrogen reduction. However, at a very small positive potential, CO would bind stronger than H* and the active sites are cleared from H* and are occupied by CO*. Now, if the potential is decreased to negative values, CO* can be reduced. Hence, for the Me-porphyrins on which H* binds stronger than CO*, CO* readuction can be accomplished by cycling the

potential between positive values where hydrogen desorbs and CO adsorbes, and negative values where CO* is reduced. We note that, this scenario holds only if we assume CO* displacement by H* does not occur at the required overpotential for the reduction of CO*. As noted in for CO* reduction on binary bulk alloys in the previous chapter, CO* displacement by H* depends on the required overpotential for the reduction of CO*. We will return to this scenario in the next section where we consider catalytic activity of Me-porphyrins for CO* reduction.

In the course of potential cycling, water oxidation should also be taken into account. At positive potentials, water may oxidizes to OH*, and if it binds stronger than CO*, the active sites are blocked by OH*. To elucidate the possibility of OH* poisoning, we have plotted the binding free energies of CO* and OH* against each other at U = 0 V, as shown in Figure 5-4. For the Me-porphyrins below the diagonal, OH* poisoning does not occur. On the other hand, for Me-porphyrins above the diagonal such as Al, Ga, Mg and B, the active sites are already blocked at U = 0 V. By increasing the potential to the values above U = 0 V, OH* stabilizes and all the points would shift to left. In other word, for each Me-porphyrins below the diagonal, there is a potential window where H* would destabilizes and CO* adsorption occurs, while OH* poisoning does not occur. Such potential window is the biggest for Os and Ru-porphyrins.

5.3 **Scaling Relations**

Since only one adsorbate can bind to the active sites in Me-porphyrin structures, i.e. the transition metal at the center of porphyrin ring, the scaling relations between involved intermediates in the reduction of CO_2 could be different from pure metals. We note that on pure metals, generally the sites to which the adsorbates bind, are not the same for all adsorbates. Hence the scaling relations are a worthwhile issue to consider in Me-porphyrin systems. Additionally, we note that the presence of single active site reduces the number of possible intermediates, which in turn simplifies the calculations. In other word, methane and methanol are the only reaction products that can be formed. Formation of other reaction products, such as methane, is hindered, as more sites are needed for their formation.

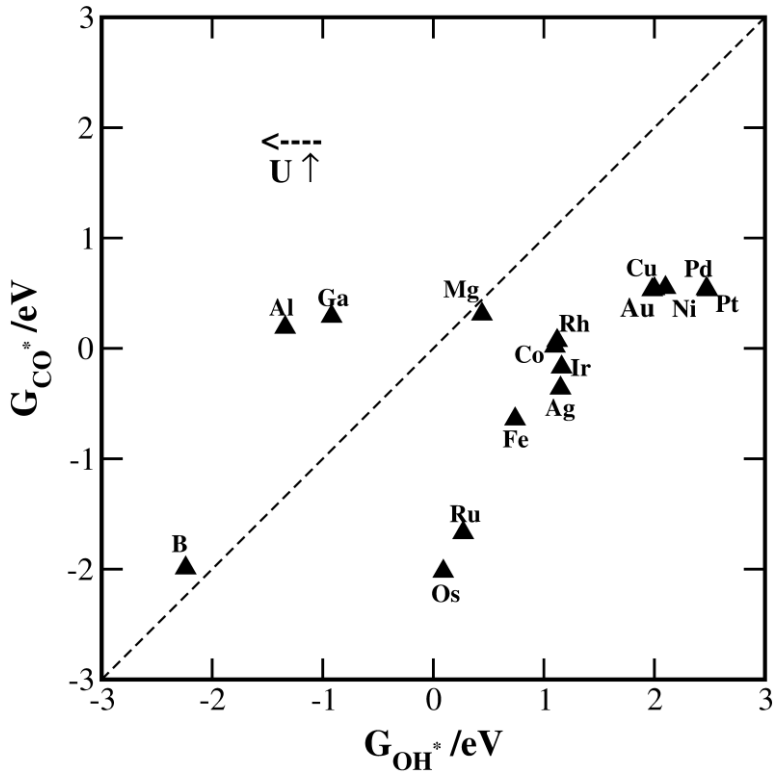

Figure 5-4: Free binding energies of CO* and OH* against each other, defining the OH* poisoning in the course of potential cycling. For the Me-porphyrins that are located above the diagonal, water dissociation occurs and the active sites are blocked by OH*. The horizontal arrow shows how the OH binding energies change with potential (vertical arrow).

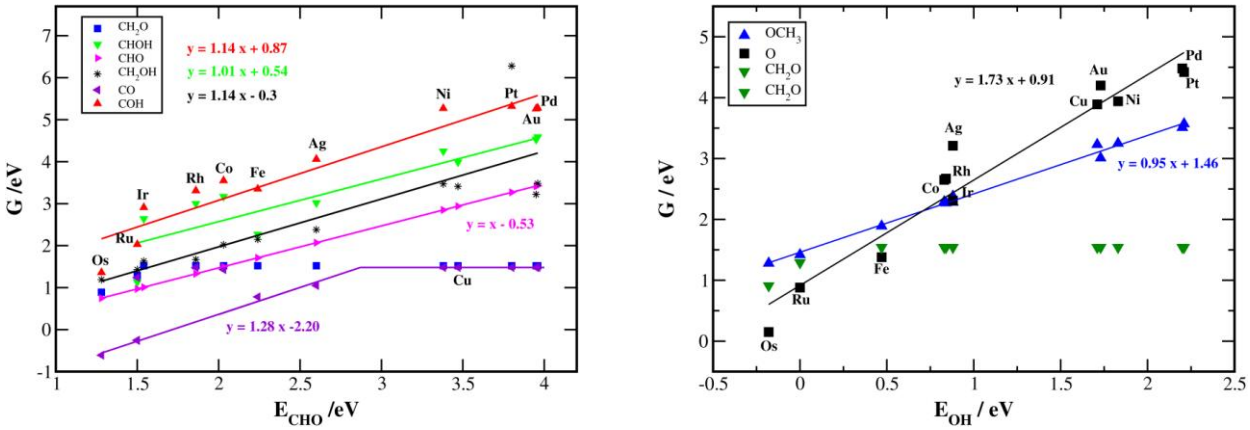

Figure 5-5: Scaling relation between involved intermediates in the reduction of CO2 that bind through carbon atom to the active sites versus CHO* binding energy (a) and the intermediates that bind through oxygen atoms versus OH* binding energy (b).

Figure 5-5 shows the scaling relations between different involved intermediates in the

reduction of CO_2 on Me-porphyrins. The free energy of binding of the intermediates that bind through carbon and oxygen atoms are plotted against the binding energies of CHO* and OH* respectively [19,66]. We note for the former that the binding energy of CHO* is used instead of CO*, because CO does not bind to some of the Me-porphyrins. This is not the case for metal catalysts where most of them bind CO [44]. Moreover, CHO was chosen because it is a common intermediate for CO reduction on all Me-porphyrins. As can be seen from Figure 5-5, CH_2O* is the only intermediate that does not bind to some Me-porphyrins, the only exceptions are Os and Ru. The constant value corresponding to CH_2O line is the chemical potential of CH_2O in the aqueous phase, i.e. CH_2O(aq). Moreover, we note that the slopes for the line in the scaling relation for the species that bind through carbon atoms are around 1.0. This is due to the fact that all of the species that bind through carbon atoms, would bind to atop site of the transition metal atoms in the center of the porphyrin rings as the surrounding nitrogen and graphitic carbon atoms are inactive in binding them. Hence, unlike transition metals the observation that the ratio between the slopes of lines for the adsorbates is proportional to the number of binds they make with the surface does not hold here [19]. This is because due to the lack of hollow sites, regardless of the number of unpaired bonds of the adsorbate, only a single bond can form which renders all the lines have the same slope. We note that this is not the case for the adsorbates that bind through oxygen atoms. It could be due to the fact that oxygen drains more charge from the transition metal owing to its high electronegativity.

5.4 **Volcano Plots**

To construct the two-dimensional volcano plots we follow the same approach as Peterson and co-workers [44]. In this approach the volcano plots is constructed by calculating limiting potential which is the potential at which all elementary steps become exergonic in free energy. If the corresponding successive intermediates in the elementary step have scaling relations with the same intermediates (they bind through same atom to the surface), the corresponding limiting potential can be defined as a function of the binding energy of the common intermediate with which they have scaling. Clearly, the line corresponding to the elementary step with highest distance from the equilibrium potential defines the potential determining step. In case of CO_2/CO reduction, since there is two

sets on intermediates that scale differently, two volcano plots are constructed for each set of intermediates (Figure 5-6). In this case, the line corresponding to the elementary step with the highest distance from the equilibrium potential in two volcanos, defines the potential determining step. We note that, this does not hold for the catalysts that do not follow the scaling relations, as will be seen in the following. For example, on Me-porphyrins that bind CO, both CO* and CHO* bind through carbon atom. Accordingly, their free energies of binding, i.e. ΔG_{CO*} and ΔG_{CHO*} scale linearly with the adsorption energy of CHO*, i.e. E_{CHO*}, through the following expression:

$$\Delta G_{CO*}(\Delta E_{CHO*}) = 1.28\ \Delta E_{CHO*} - 2.2 \quad (5\text{-}1)$$

$$\Delta G_{CHO*}(\Delta E_{CHO*}) = \Delta E_{CHO*} - 0.53 \quad (5\text{-}2)$$

The limiting potential corresponding to $CO^* + \left(H^+ + e^-\right) \rightarrow CHO^*$ elementary reaction step is given by the following relation:

$$U_L(\Delta E_{CHO*}) = -\frac{(\Delta G_{CHO*} - \Delta G_{CO*})}{e} = 0.28\ \Delta E_{CHO*} - 1.67 \quad (5\text{-}3)$$

Following this approach, we have constructed two volcano plots, i.e. CHO and OH volcanos, corresponding to two different sets of intermediates that bind through carbon and oxygen atoms, respectively. As can be seen form Figure 5-6, for most of the Me-porphyrins formation of adsorbed CHO from CO* is PDS, similar to transition metals. We would like to draw our attention to Ir, Rh and Co-porphyrins. CO does not bind to these Me-porphyrins. Hence, we expect them to be outlier in the CHO volcano and exhibit differently from the ones that follow scaling relations. For Rh and Ir, CO/CHO is PDS, while for Co, CH_2O(aq)/CH_2OH is PDS, as evidenced by the difference between CH_2O and CH_2OH lines.

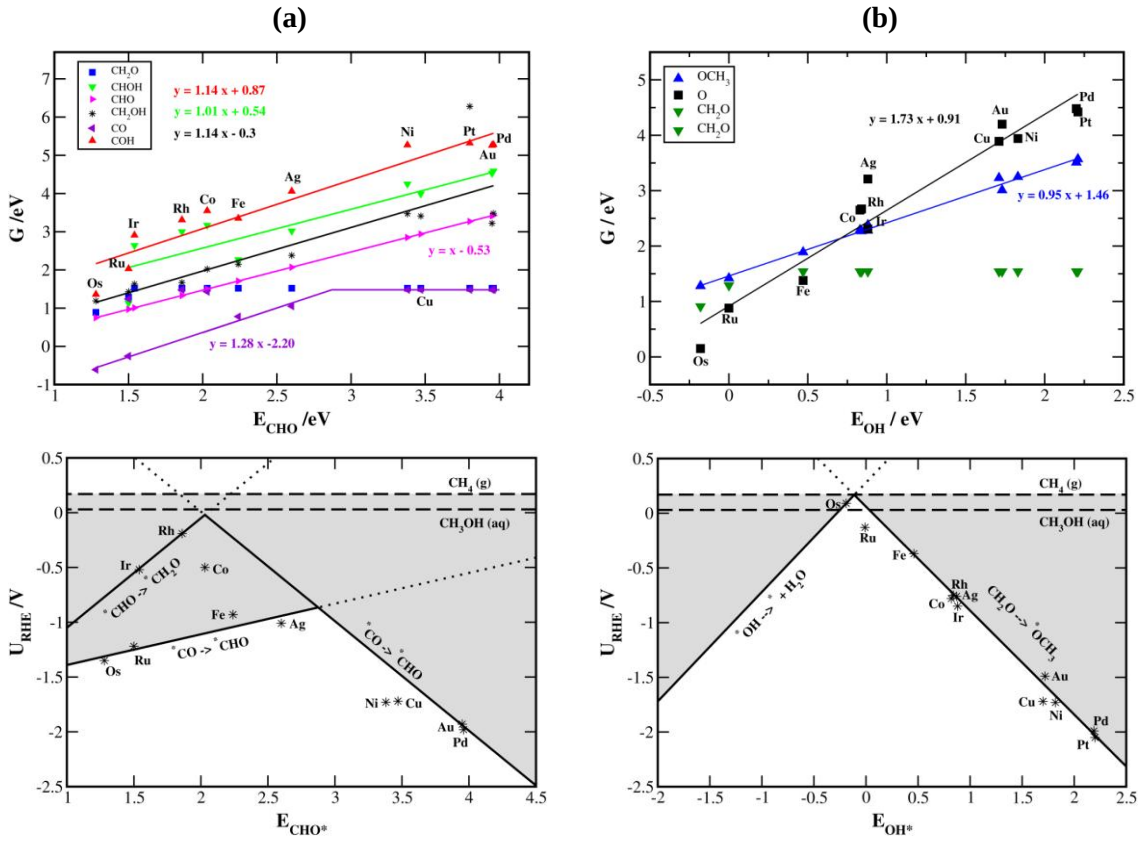

Figure 5-6: Volcano plots indicating the potential determining steps for CO electro-reduction on Me-porphyrins along with corresponding scaling relations have been used to construct the volcano plots. The vertical dashed lines define the equilibrium potential for methanol and methane production. The gray areas describe the overpotential. The minimum required for reduction of CO potentials and the corresponding potential determining steps, is defined by the line has highest distance from equilibrium potentials line two volcano plot, that are CO* → CHO* in CHO volcano or CH_2O*→OCH_3* and OH*→H_2O in OH volcano plot.

5.5 CO_2 reduction product

To define the final reaction product on each Me-porphyrin, we have examined all possible reaction pathways in the reduction of CO as depicted in Figure 5-7. The lowest-energy pathway for each Me-porphyrin is also defined. As can be seen, reduction of CO_2 results in the formation of three different products: formaldehyde, methane and mainly methanol. CO reduces to formaldehyde on most of the Me-porphyrins, because they can not bind formaldehyde, and formaldehyde is desorbed from the surface. However, we have not excluded the possibility that formaldehyde is being reduced further.

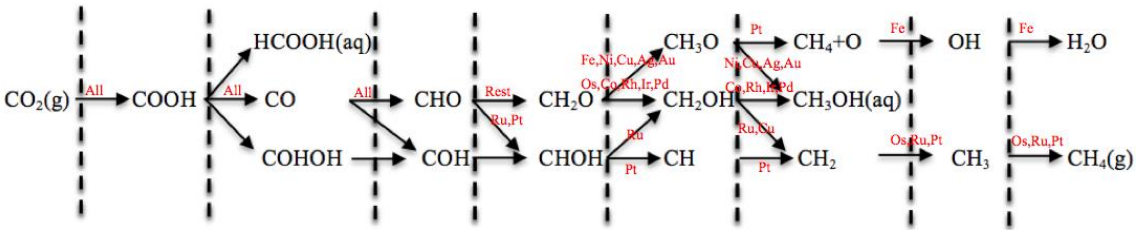

Figure 5-7: Reaction paths for electrochemical reduction of CO_2 on Me-porphyrins. "All'' and "Rest" indicate all and remaining Me-porphyrins, respectively.

The reaction product on each Me-porphyrin, (PDS) and the corresponding overpotential are shown in Table 5-1.

Table 5-1: Calculated potentials for CO reduction, main reaction product and PDS.

Me-porphyrin	Path	Potential (V)	PDS
Cu	CH_3OH	-1.72	$CH_2O(aq) \rightarrow CH_3O$
Ag	CH_3OH	-1.01	$CHO \rightarrow CH_2O(aq)$
Au	CH_3OH	-1.94	$CO \rightarrow CHO$
Ni	CH_3OH	-1.73	$CH_2O(aq) \rightarrow CH_3O$
Pd	CH_3OH	-1.99	$CH_2O(aq) \rightarrow CH_3O$
Pt	CH_4	-6.23	$COHO \rightarrow CH$
Co	CH_3OH	-0.20	$CH_2O(aq) \rightarrow CH_3O$
Rh	CH_3OH	-0.19	$CHO \rightarrow CH_2OH$
Ir	CH_4	-0.52	$CHO \rightarrow CH_2O(aq)$
Fe	CH_4	-0.93	$CO \rightarrow CHO$
Ru	CH_4	-1.22	$CO \rightarrow CHO$
Os	CH_4	-1.35	$CO \rightarrow CHO$
Mg	CH_3OH	-1.29	$CO \rightarrow CHO$
Al	CH_4	-1.17	$CH_3O \rightarrow CH_3O$
Ga	CH_4	-0.94	$CH_3O \rightarrow CH_3O$

It can be seen that the PDS are not the same on all Me-porphyrin: in the CHO volcano either CO/CHO or CHO/CH_2O elementary steps are the PDS, while in the OH volcano O/CH_3O and CH_2O/CH_3O are the PDS in OH volcano. Moreover, based on CHO and OH volcanos, the catalyst with lowest distance from the equilibrium potential of CO

reduction, is Rh-porphyrin. On Rh-porphyrin, reduction of CO results in methanol with CHO/CH_2O(aq) step as PDS, and the change in free energy corresponding to this step is -0.19 eV. Figure 5-8 shows the free energy diagram for the reduction of CO on Rh-porphyrin. Clearly, Rh-porphyrin exhibits higher activity than Cu, the most active metal for CO reduction. Moreover, the CO reduction product on Rh-porphyrin is methanol, different from the one on Cu, i.e. methane and ethane.

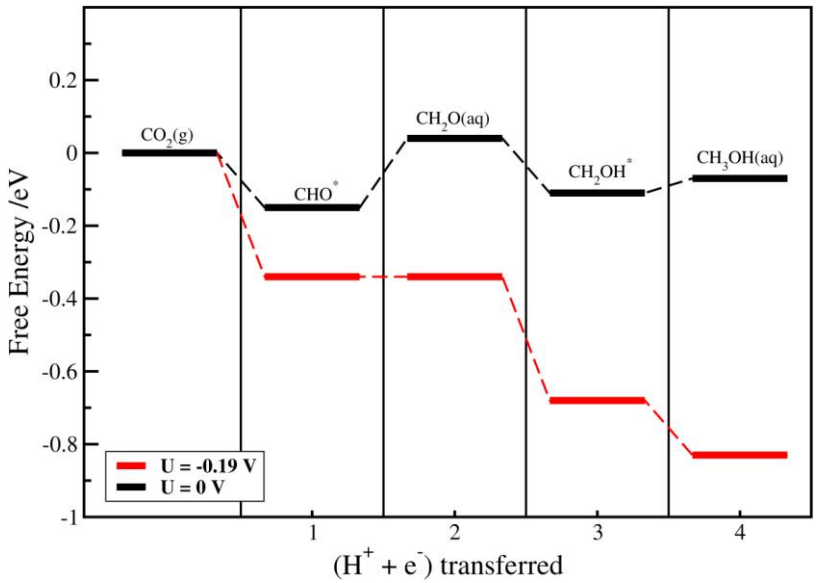

Figure 5-8: Free energy diagram for the lowest energy pathway for CO reduction on Rh-porphyrin. Black and red lines denote the free energy levels at 0 V and at the potential of -0.19 V, where all reaction steps become downhill in free energy.

5.6 Me-porphyrins for Hydrogen Oxidation/Evolution Reaction

So far, HER has been considered a competing reaction with CO_2/CO reduction. However, HER and its opposite reaction, i.e. HOR, are important reactions [2,74,75]. HER/HOR are the simplest electrochemical reactions, because they have only one intermediate that is the adsorbed hydrogen state. According to standard hydrogen electrode model, at equilibrium conditions, the chemical potentials of electron and proton (H^++e^-) are equal to that of hydrogen in the gas phase, i.e. $\frac{1}{2}\,H_2(g)$. This indicates the free energy of binding of hydrogen on the best catalyst for HER/HOR should be as close as possible to zero. The catalyst with zero free energy of binding will exhibit zero

overpotential. Platinum is the commonly used electrode material for HER/HOR, because the free energy of binding of hydrogen on Platinum is close to zero and hence exhibits lowest overpotential for HER/HOR when compared to other pure metals. However, the high cost of Platinum imposes the replacement of Platinum with other less scarce catalysts. We have considered catalytic activity of Me-porphyrins for HER/HOR. We would like to emphasize that the overpotential for both HER and HOR are the same. Table 5-2 shows the overpotential, i.e. the free binding energy of H*, for HER/HOR on all Me-porphyrins.

Table 5-2: Calculated overpotentials for HER/HOR on Me-porphyrins.

Me-porphyrin	Overpotential (V)
Cu	-1.70
Ag	-0.68
Au	-0.23
Ni	-1.67
Pd	-2.05
Pt	-1.77
Co	-0.26
Rh	0.15
Ir	0.28
Fe	-0.45
Ru	0.35
Os	0.57
Mg	-1.35
Al	0.38
Ga	0.77

The Me-porphyrins with the free binding energies of H* close to zero exhibit higher catalytic activity for HER/HOR. As can be seen, there are few candidates that exhibit low overpotential, among which Ir and Rh-porphyrins with the respective overpotentials of

0.28 and 0.15 V are the bests. We note that 0.15 overpotential for Rh-porphyrin is as good as the one for Pt for HER/HOR. Figure 5-9 shows the free energy diagram for HER/HOR on Rh-porphyrin at zero and the potential at which all reaction steps become downhill in free energy. Interestingly, Rh-porphyrin not only exhibits highest activity for CO reduction, but also it has highest activity for HER/HOR.

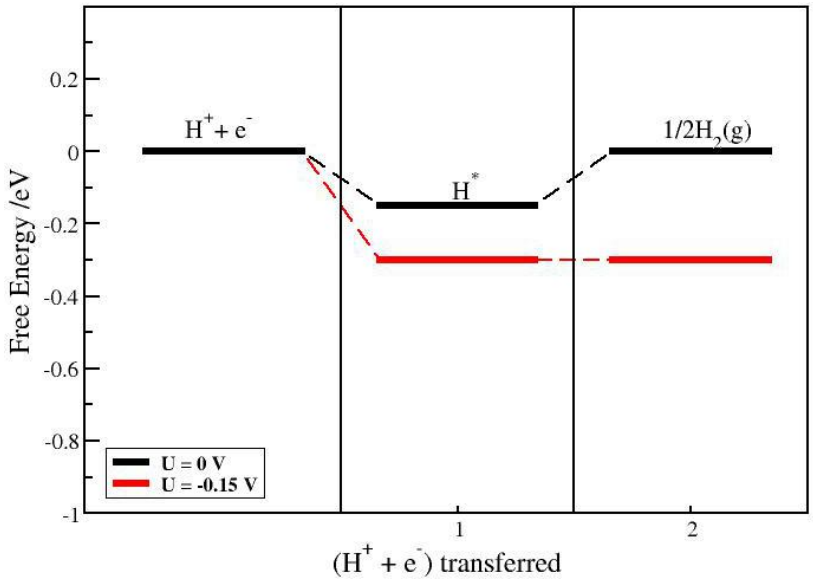

Figure 5-9: Free energy diagram for hydrogen evolution/oxidation reaction on Rh-porphyrin. The black and red lines denote the free energy levels at zero and the potential at which all reaction steps are downhill in free energy.

5.7 Summary and Outlook

We examined catalytic activity of the metal-functionalized porphyrin structures as catalyst with isolated active sites toward the electrochemical reduction of CO_2 and CO. We find that on all Me-porphyrins, H* binds stronger than COOH* on metal atom in the center of porphyrin ring. This causes all active sites are blocked by H* and HER dominates over CO_2 reduction. To avoid this problem CO was reduced instead of CO_2, as it competes better than COOH* with H* for occupying the active sites. Moreover, we constructed volcano plots using scaling relations between CO reduction intermediates to identify the best catalyst candidate. Our results showed that Rh-pophyrin exhibits the overpotential of 0.22 V for CO reduction to methanol. Finally, we examined the catalytic activity of the metal–porphyrins for HER/HOR, and found that Rh-porphyrin exhibits the overpotential of 0.15 V.

Chapter 6

Electrochemical Synthesis of H_2O_2

Hydrogen peroxide often reflected as a green and environmentally benign chemical oxidant is one of the world's most versatile inorganic chemicals possessing many industrial applications [76] such as water treatment and bleaching wood pulp, to name few. It can be applied as both energy carrier alternative to hydrogen (at anode side) and oxidant alternative to oxygen (at cathode side) for application in the fuel cells. As an alternative oxidant it is a powerful oxidizer over whole pH range with high oxidation potential and its electroreduction at the cathode of the fuel cell takes place at a solid/liquid interface with low activation barrier and fast kinetics, avoiding gas diffusion problem when compared to oxygen.

At present, H_2O_2 is produced via the anthraquinone process which is energy demanding. A simple and alternative way to produce H_2O_2 is direct synthesis of H_2O_2 from H_2 and O_2. However, the H_2 and O_2 mixture is explosive. One way to overcome this problem is to use fuel cells to electrochemically produce H_2O_2. This method has several advantages over anthraquinone process: 1) electrochemical production of H_2O_2 in an environmentally friendly process with small scale and simple production from constituent elements, H_2 and O_2, 2) it can be implemented at the point of use, 3) unlike the anthraquinone process, it can generate electricity at the same time [77]. These advantages have inspired researchers for direct electrochemical synthesis of H_2O_2 from H_2 and O_2.

6.1 Electrochemical Reduction of Oxygen

The electrochemical reduction of oxygen can occur via two- or four-electron transfer pathways with H_2O_2 and H_2O as final reaction products, respectively. Reactions (6-1)-(6-8) list possible reaction steps in the reduction of O_2:

$$* + O_2(g) + (H^+ + e^-) \rightarrow HOO^* \quad (6\text{-}1)$$

$$HOO^* + (H^+ + e^-) \rightarrow H_2O_2(l) + * \quad (6\text{-}2)$$

$$H_2O_2(l) + 2* \rightarrow 2HO^* \quad (6\text{-}3)$$

$$H_2O_2(l) \rightarrow O_2(g) + H_2(g) \quad (6\text{-}4)$$

$$HOO^* + (H^+ + e^-) \rightarrow O^* + H_2O(l) \quad (6\text{-}5)$$

$$O^* + (H^+ + e^-) \rightarrow HO^* \quad (6\text{-}6)$$

$$HO^* + (H^+ + e^-) \rightarrow H_2O(l) \quad (6\text{-}7)$$

$$2HO^* + 2(H^+ + e^-) \rightarrow 2H_2O(l) + 2* \quad (6\text{-}8)$$

$$O_2(g) + 2(H^+ + e^-) \rightarrow H_2O_2 \quad U = 0.7\ V\ (RHE) \quad (6\text{-}9)$$

$$O_2(g) + 4(H^+ + e^-) \rightarrow H_2O \quad U = 1.23\ V\ (RHE) \quad (6\text{-}10)$$

where * denotes the unoccupied sites. Reactions (6-9) and (6-10) show the overall electroreduction of O_2 to H_2O_2 and H_2O along with their equilibrium potentials, respectively. In the first electron-proton transfer, i.e. reaction (6-1), oxygen is reduced to HOO*. In the case of a two-electron reduction to hydrogen peroxide, the reaction is followed by reaction (6-2) that results in H_2O_2 as final product. On the other hand, for the four-electron process, the reaction can occur without H_2O_2 as intermediate, in which case, it proceeds through reactions (6-5), (6-6) and (6-7) or it can be proceed with H_2O_2 as intermediate, in which case, it proceeds through reactions (6-2),(6-3) and (6-8). We note that, reaction (6-3) and (6-4) display chemical decomposition of H_2O_2.

Four-electron reduction process occurs upon oxygen-oxygen bond breaking through chemical dissociation of HOO* to O* and HO*, or electrochemical reduction of HOO* to HO* and H_2O. On the other hand, in the two-electron process dissociation of OOH* does not occur and HOO* is the only intermediate that is present.

In the fuel cell design, H_2O_2 can be produced electrochemically via two-electron reduction of O_2 in acidic media and the process not only requires energy, but also is exergonic (reaction (6-9)), with a standard Gibbs free energy of formation, ΔG_f^0 = -120 kJ mol^{-1}. However, in practice, the main challenges that this process is facing are related to achieving simultaneous high selectivity and activity for H_2O_2 production. Selectivity towards H_2O and H_2O_2 is defined by the tendency of the catalyst towards O-O bond breaking and preserving in HOO* intermediate, respectively. The electroreduction of O_2 to H_2O_2 involves only one intermediate, namely HOO*. Therefore, activity towards H_2O_2 is defined by the binding energy of HOO* that, in turn, defines the overpotential [57]. For an optimal catalyst for electroreduction of O_2 to H_2O_2, i.e. with zero overpotential, the potential energy surface should be flat, meaning that all energy levels should be thermoneutral in which case the reaction would run as close as possible to it's equilibrium potential, i.e. 0.7 V versus RHE. For non-ideal catalysts, either activation of O_2 to form HOO* is potential limiting step, which is the case for the catalysts that bind HOO* weakly, or reduction of HOO* to form H_2O_2 is potential determining step, which is the case for the catalysts that bind HOO* strongly.

Large variety of catalysts has been tested for electrochemical production of H_2O_2 both experimentally and theoretically [78–80]. The most important challenge is related to the selectivity of catalyst towards H_2O_2 formation in the reduction of oxygen basically because all the active catalysts used for H_2O_2 synthesis are active for its decomposition and further reduction to water, which are thermodynamically favorable. In the following we explain the role of isolated sites in preventing further reduction of H_2O_2 to water and directing the selectivity towards H_2O_2.

6.2 **Catalysts with isolated active sites**

According to the above discussion, an efficient catalyst for hydrogen peroxide generation should fulfill three following characterization: 1) HOO* bond breaking, i.e. reaction (6-5), and also subsequent H_2O_2 dissociation, i.e. reactions (6-3) and (6-4) should be avoided, 2) the catalyst should selectively adsorb O_2 and preserve the O−O bond during H_2O_2 formation, and 3) H_2O_2 should be released right after it forms. These conditions can

be met on a catalyst with specific isolated sites serving as active sites towards ORR that are surrounded by inactive or less reactive elements towards ORR. On such a catalyst, the role of the active site is to activate O_2 adsorption and release H_2O_2 right after it forms. Moreover, O−O bond is preserved on the active sites as presence of contiguous active sites is required to activate HOO* dissociation. We note that O-O bond cleaving is mitigated on the less active O_2 adsorption, because they bind oxygen weakly.

Necessity of the existence of the isolated active sites at the catalyst surface for electrochemical production of H_2O_2 has been examined before and is supported by three successful examples tested and introduced in the literature [[71,78,81]]. First example is metalloporphyrins. As discussed in the previous chapter, these materials have isolated transition metal sites that are located of a ring composed of nitrogen and carbon atoms. In particular, porphyrins with cobalt center have been introduced for electrochemical production of H_2O_2 [[71,81]]. However, the catalyst is not stable in the electrochemical environment and stability and hence activity degrades over time. Another example of the systems with isolates active sites is graphitic materials doped with nitrogen catalyzing the two-electron pathway for electrochemical production of H_2O_2 [[82–84]]. In these systems, depending on the dispersion of nitrogen atoms into the graphene sheet, different carbon atoms located at the vicinity of the doped nitrogen are active sites. Another example that is related to creation of the isolated active sites on the surface of transition metals refers to the recent work of Jirkovsky et al. [[78]]. Using DFT calculations, they screened for selectivity and activity towards H_2O_2 production on Au(111) alloyed with isolated different transition metal atoms that form surface alloys. Their calculations predicted that Au(111) alloyed with isolated Pd atoms is selective towards H_2O_2 production with up to 90% selectivity, albeit at high overpotential of 0.4 V. To confirm the theoretical predictions and quantify the selectivity, they introduced $Au_{1-x}Pd_x$ nanoalloys with varying Pd content in a fuel cell cathode. These experiments demonstrated a noticeable increase in H_2O_2 formation for alloys with 8% Pd which is related to the presence of isolated Pd sites on the surface. This finding is in agreement with the recent study by Rankin and co-workers who carried out DFT calculations on twelve transition metals to predict the trend in selectivity and activity towards hydrogen peroxide [[85]]. By taking into account the kinetic barriers and constructing the volcano plot, they predicted that the binding energies

of oxygen and hydrogen on the catalysts with highest catalytic activity towards H_2O_2 production would fall near Pt and Pd. Moreover, their calculations predicted that the catalysts with simultaneous high activity and selectivity falls between Au and Pd in the descriptor space, in agreement with previous experimental findings that showed high activity and selectivity toward hydrogen peroxide synthesis on Au-Pd alloys.

Herein we have taken advantage of the isolated active site concept and screened for new catalysts for the electrochemical production of H_2O_2. We would like to emphasize that the screening span through not only surface alloys, but also bulk alloys constituting from different transition metals that can adsorb oxygen and the noble transition metals and non-noble metals that bind oxygen weakly. While the former group of metals is used to active O_2 adsorption, the latter group of metals is used to assure O-O bond breaking does not occur on the catalyst surface.

6.3 Alloys screened for electrochemical synthesis of H_2O_2

We consider catalytic activity and selectivity towards H_2O_2 for thirty different alloys including surface alloys and bulk alloys, which all retain the isolated active sites. The common feature of these alloys is that they all constitute from less active metals toward O-O bond cleaving and active metals for oxygen binding. These alloys can be categorized into three groups as depicted in Figure 6-1. First group of alloys include surface alloys of Au and active metals named X in in Figure 6-1, where X is Zn, Pt, Pd, Cu, Rh, Ru, Co and Ni. We note that for this group of alloys, the substrate is Au and the active site is X. Second group of alloys includes surface alloys of active metals named Y, where Y is Pt, Pd and Rh, and less active metals including Ag, Au and Hg. In this group of alloys, active metals form as substrate and the active sites on the surface are surrounded by less active metals. Finally, third group includes intermetallic compounds including Pt, Pd as active alloys and Au, Ag, Hg, In, Sn and Sb as less reactive ones, as depicted in Figure 6-1d-f. The bulk alloys of Pt and Pd with Ag and Au, i.e. Ag_3Pd, Au_3Pd and Au_3Pt have the same crystal structure as their constituents, i.e. face center cubic. Hence for these alloys, the most stable facet that is probably exposed under electrochemical condition is (111). On the other hand, for other bulk alloys, we assumed the facets that have isolated sites. Most

notably, for $PtHg_4$ alloy, given the crystal structure, (110) is the closest pack surface and is the facet that most probably exposed under electrochemical conditions, in agreement with experimental findings [60].

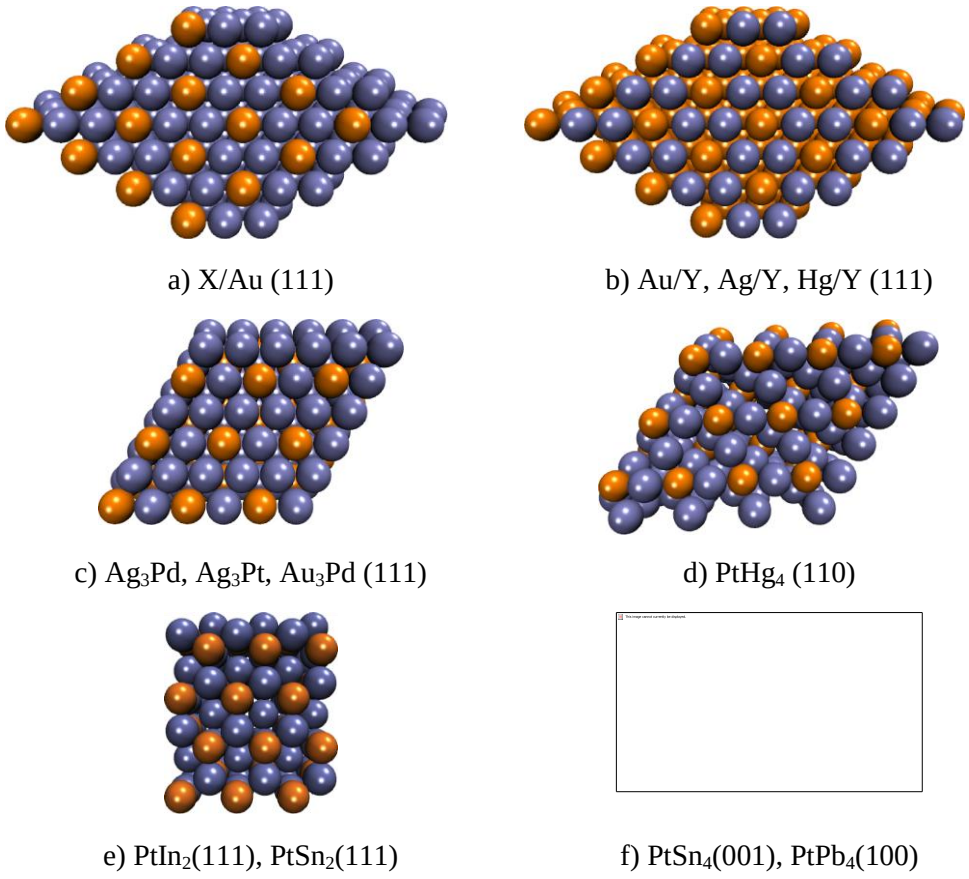

a) X/Au (111)

b) Au/Y, Ag/Y, Hg/Y (111)

c) Ag_3Pd, Ag_3Pt, Au_3Pd (111)

d) $PtHg_4$ (110)

e) $PtIn_2$(111), $PtSn_2$(111)

f) $PtSn_4$(001), $PtPb_4$(100)

Figure 6-1: Structure of different studied alloys. Common feature of all of the alloys is that the active transition metal (orange) is isolated within a surrounding inert transition metal (blue). Two different sets of surface alloys with gold and non-gold substrate are displayed in a) and b), respectively. Four categories of bulk alloys are displayed in (c), (d), (e), and (f).

6.4 **Volcano Plots**

To identify the selectivity as well as activity of the alloys, we construct two volcano plots for 2-electron and 4-electron pathways. For 2-electron pathway, since HOO* is the only intermediate that forms during electroreduction of O_2 to H_2O_2, the free energy of binding of HOO*, i.e. ΔG_{HOO*}, is used as descriptor. According to CHE model, the working potential, U_T, for the electroreduction of O_2 to H_2O_2 is the potential at which all reaction

steps become downhill or thermoneutral in free energy. Equivalently, the overpotential, η_{O_2/H_2O_2}, is defined as the difference between equilibrium potential, $U^0_{O_2/H_2O_2}$, and the limiting potential. The 2-electron volcano for electroreduction of O_2 to H_2O_2, blue line, shows a Sabatier analysis for H_2O_2 production [86]. Right side of the volcano is weak HOO* binding criteria, meaning that the activity is limited by activation of O_2 to form HOO*. Left side on the other hand, is strong HOO* binding where reduction of HOO* to form water is limiting step and hence defines the activity. The optimal catalyst with the free energy of binding energy of HOO* of 4.22+0.2 eV (similarly ΔG_{HO*} ~ 1.1 ± 0.2 eV) sits on top of the volcano and exhibits zero overpotential.

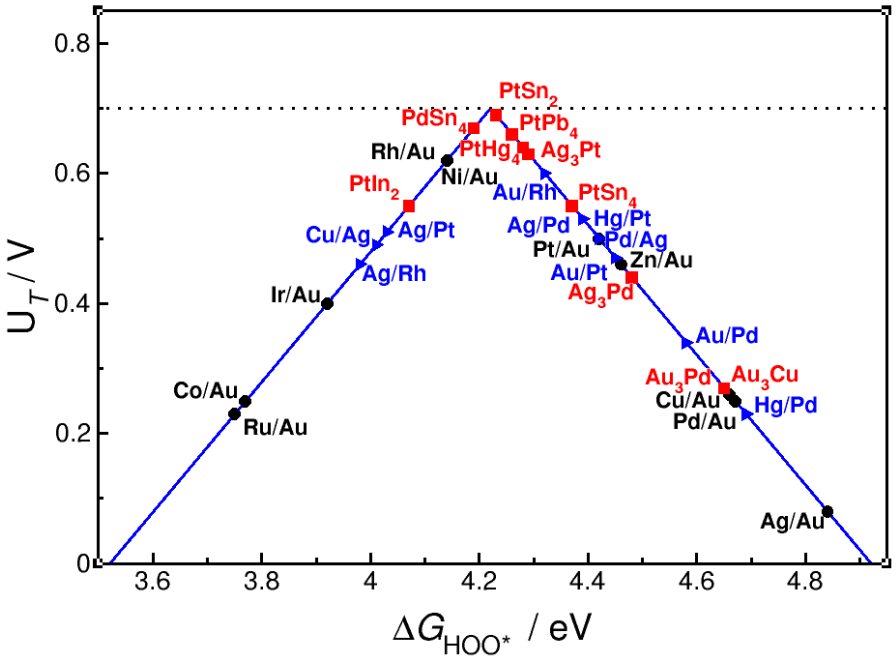

Figure 6-2: 2-electron activity volcano for electrochemical synthesis of H_2O_2. Three categories of alloys have been studied. Black circles are the surface alloys of Au(111). Blue triangles are the surface alloys of Pd, Pt and Rh. Bulk alloys of Pt, Pd and Cu are shown by red squares. All the alloys have isolated active sites. The equilibrium potential of two-electron reduction of O_2 to H_2O_2 is shown as a dotted line.

For the 4-electron pathway, as discussed above, there are two intermediates in the electro-reduction of O_2 to H_2O, namely HO* and HOO*. It is well known that either the activation of O_2 to form HOO*, or reduction of HO* to form H_2O is potential limiting step [17,87]. Moreover, it is also well known that the binding energies of HOO* and HO*, i.e. ΔG_{HOO*} and ΔG_{HO*} are correlated to each other [17,87]. This allows for construction of

the activity volcano using either ΔG_{HOO*} or ΔG_{HO*}.

Similar to 2-electron volcano, the 4-volcano establishes a Sabatier analysis for electroreduction of O_2 to H_2O [89]. To the left side of the volcano, i.e. strong binding of HO*, reduction of HO* is potential limiting step. On the other hand, to the right of the volcano, i.e. weak binding of HO*, activation of O_2 to form HOO*, is potential limiting step. This means that the catalytic activity is a compromise between weak and strong binding energy of HO* (or HOO*). Moreover, universal scaling between binding energies of HO* and HOO*, i.e. $\Delta G_{HOO*} = \Delta G_{HOO*} + 3.2 \pm 0.2$, establishes a 0.4 V difference between the top of the volcano and the equilibrium potential for the reduction of O_2 to H_2O, i.e. 1.23 V [[88]]. This is due to the fact that for an optimal catalyst all three intermediate steps should energetically be equally separated, which means at equilibrium potential, i.e. 1.23 V, for an ideal catalyst the free energy diagram will be flat and all the intermediate steps will be aligned. On the other hand, for the real catalysts, due to universal scaling relation between ΔG_{HO*} and ΔG_{HOO*}, i.e. $\Delta G_{HOO*} = \Delta G_{HOO*} + 3.2 \pm 0.2$, the difference between HOO* and HO* levels is fixed at 3.2 ± 0.2. Since, formation of HO* from HOO* involves two electron-proton transfer steps (reactions 4 and 5), even on the best catalyst, the difference of 3.2 eV is divided equally between these two steps, i.e. 3.2/2 = 1.6 eV. This means even on the best catalyst, an overptential of 0.4 V (1.6-1.23) exists, as evidenced by 0.4 V difference between the top of 4-electron volcano and the equilibrium potential of the reduction of O_2 to H_2O.

Before considering the selectivity and activity of the alloy candidates, the stability of the alloys under electrochemical conditions should be assessed. In the following we apply three different stability tests to examine the stability of the alloys.

6.5 Stability Tests for Screened Alloys

In addition to exhibiting high activity and selectivity, a successful catalyst for electrochemical reduction of O_2 to H_2O_2, should be stable under reaction conditions. To examine the stability of the alloys, three stability criteria are imposed: 1) metal dissolution, 2) thermodynamic stability, and 3) oxygen poisoning.

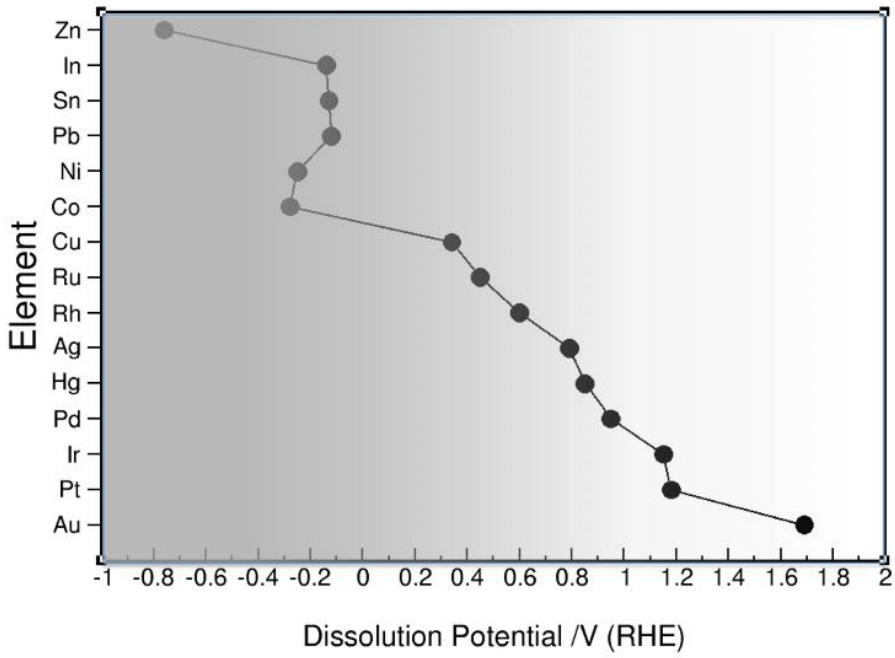

Figure 6-3: Dissolution potential of the constituent elements of the screened alloys. The grayscale gradient is used to represent the change in the dissolution potential of different elements as well as the limitation on the accuracy of the DFT calculations.

1-The constituents of the alloys should have higher dissolution potentials than the potentials at which the reduction of oxygen occurs. If the dissolution potential of the elements of the alloy is lower than the alloy potential of oxygen reduction reaction, the alloy dissolves into the solution and its activity degrades over time. Since reduction of oxygen on different alloys occurs at different potentials, it is not possible to specify a sharp potential limit above which the alloys with higher dissolution potential than that limit are excluded. However, to be on the safe side, we have assumed an upper limit of 0.5 V (RHE) for dissolution potential where an alloy is considered to be stable against the dissolution if its constituent elements have dissolution potential higher than 0.5 V (RHE). As can be seen from Figure 6-3, seven elements including Cu, Co, Ni, Pb, Sn, In and Zn are not stable and dissolve under the operating potentials [89]. Hence, ten alloys including these elements are excluded from further consideration based on dissolution criterion. This, in turn, means that even though $PtPb_4$ and $PtSn_2$ have optimal HOO* binding energies that put them very close to the top of 2-electron volcano, they are not stable at the experimental condition of H_2O_2 synthesis. We would like to emphasize that this

criterion might underestimate the stability of some elements in the alloys that could be potentially stable against dissolution at operating reaction conditions. This is due to the fact that, even though metals in their pure form dissolve, their stability might increase when they are alloyed with other elements. This is best illustrated by comparing the calculated dissolution potentials of $PtSn_2$ and $PtAg_3$ with the ones for their constituent elements, i.e. Sn and Ag, as shown in Table 6-1. Moreover, alloying might increase the kinetic stability of the alloy compared to its constituent elements.

Table 6-1: Calculated dissolution potentials for Ag and Sn elements in Ag_3Pt and $PtSn_2$ alloys. In the calculations, 1M concentrations were assumed for dissolved ions in the solution, i.e. Ag^+ and Sn^{4+}.

Bulk Alloy/Pure Metal	Calculated dissolution potential / V(RHE)
Ag_3Pt	0.77
$PtSn_2$	0.11
Ag	0.79
Sn	-0.13

2) The second stability test examines the thermodynamic stability: the free energy of formation from their constituent elements should be negative. The alloying energies were calculated for all surface and bulk alloys as below.

$$\Delta E_{Alloy} = E(Alloy) - E(constituents) \quad (6\text{-}11)$$

E(Alloy) and E(constituents) are the total energy of the alloy and its constituents elements in the metallic form respectively. Figure 6-4 shows the calculated ΔG_{HOO*} as a function of the formation energy to identify alloys that fulfill both stability and activity criteria. Red dashed line specifies the optimal HOO* free energy at 4.22 eV. The alloys with heat of formation above zero are not stable and should be excluded. However, due to uncertainty in DFT calculations and the fact that some alloys might form meta-stable phases, we have highlighted a wider range in free energy of formation to include such uncertainty. It is clear from Figure 6-4 that except Ru/Au and Rh/Au , all of the alloys are stable.

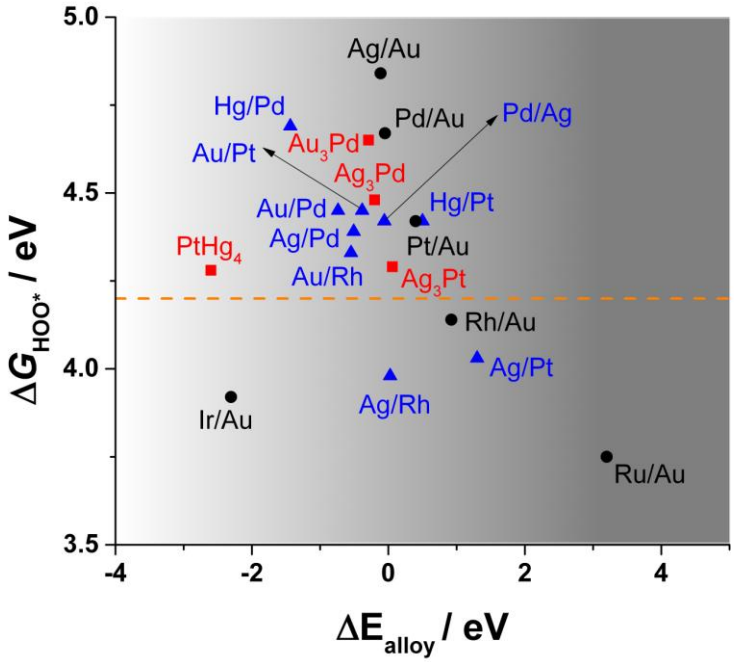

Figure 6-4: Energy of formation of the alloys passed from dissolution criterion. The grayscale gradient is used to represent the change in the alloying energy as well as the limitation on the accuracy of the DFT calculations.

3) As another important stability criterion, we considered the possibility of oxygen poisoning resulting from liquid water dissociation. In this case the active sites of the surface are poisoned and H_2O_2 synthesis is not preceded further. As shown in Figure 6-5, calculated binding energies of O* on the bulk alloys and surface alloys are positive meaning that the oxygen poisoning from dissociation of water on the surfaces of these alloys is avoided.

Figure 6-6 summarizes the stability assessment of the alloys candidates. In summary, after imposing stability criteria, 18 alloys remain stable in the electrochemical conditions.

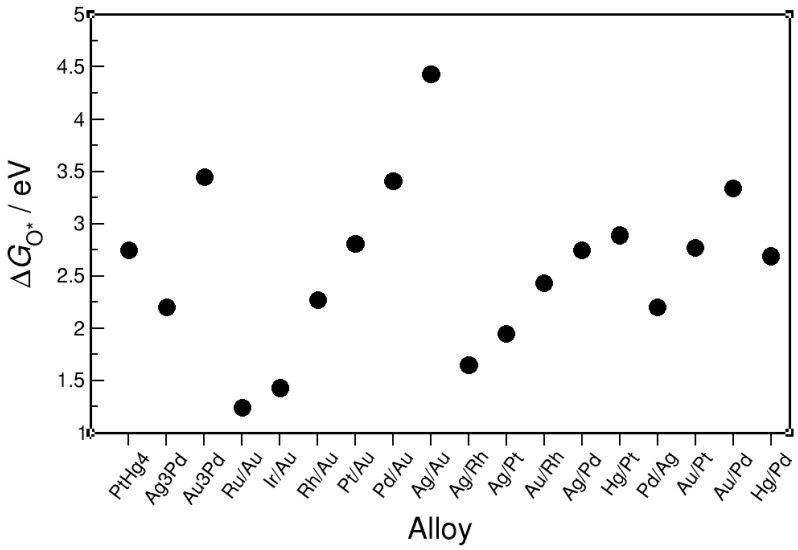

Figure 6-5: Oxygen poisoning in different alloy catalysts. As shown in the plot, all binding energies of O* are positive, meaning that oxygen poisoning from water dissociation is avoided.

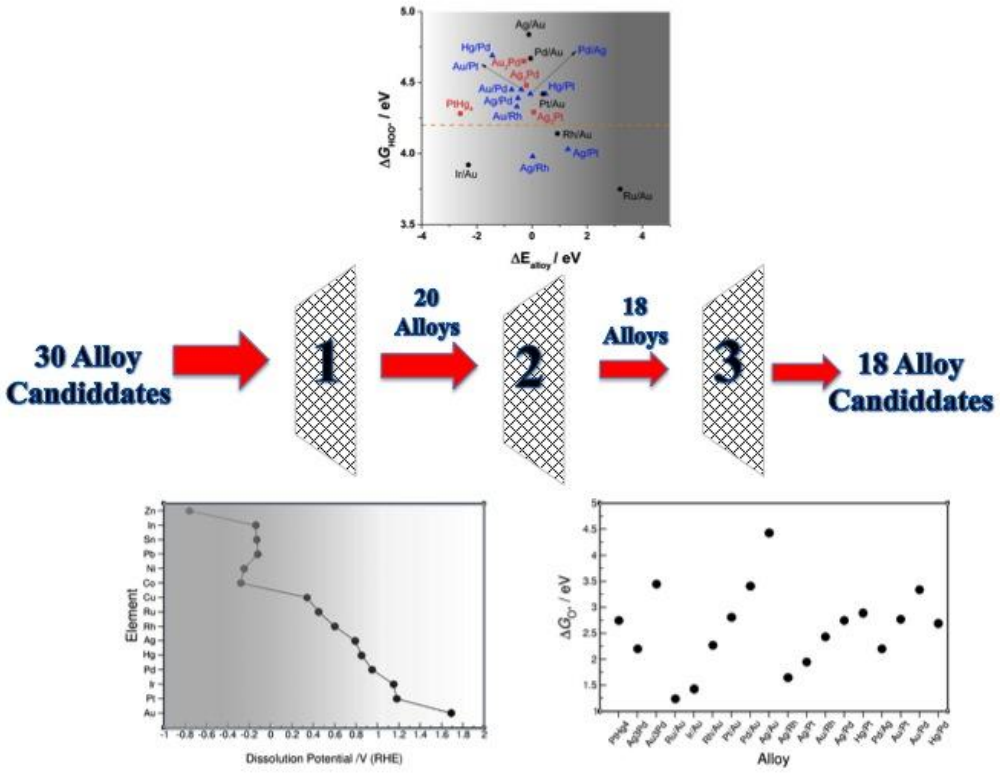

Figure 6-6: Schematic representation of three applied stability criteria for the alloys. After each stability test, the unstable alloys are excluded from further consideration. Eighteen alloys found to be stable under electrochemical reaction conditions.

6.6 Selectivity: Role of ensemble and electronic effects

In the part, we consider the selectivity and activity of stable alloys towards H_2O_2 production. Figure 6-7 shows 2-electron and 4-electron volcano plots for the sable alloys. To direct the selectivity of oxygen reduction towards H_2O_2, not only decomposition and further reduction of H_2O_2 to water should be avoided, but also the four electron reduction process of oxygen to water, i.e. chemical and electrochemical dissociation of OOH* should also be hindered. Therefore, to avoid O-O bond breaking, it is crucial to find a catalyst on which the barrier for dissociation of HOO* is higher than the one for protonation of HOO*. Under such circumstances, protonation of HOO* to form H_2O_2 will be favored over its dissociation. On the catalysts with strong binding energies of HO*, i.e. to the left side of both 2-electron and 4-electron volcanos, O-O bond dissociation is expected to promote over HOO* reduction to H_2O_2. We would like to emphasize the catalysts that locate on the left leg of 2-electron with binding energies of HO* weaker than 0.8 eV (top of 4-electron volcano) are also selective for 4-electron pathway. We predict 4-electron reduction dominates over 2-electron reduction owing to their strong binding energy of HO* on these catalysts. Similarly, this explains the tendency towards four-electron reaction on the transition metals, such as Pt and Pd that are very active in cleaving O-O bond and forming the next intermediates of four-electron path, i.e. O* and HO*. On the other hand, the catalysts with weak binding of HO*, i.e. the right side of 2-electron volcano, such as Au, that are not good catalysts in cleaving O-O bond, it is difficult to dissociate HOO*. Thus the activity increases by weakening HO* binding energy. This means to the right of the volcano, selectivity towards H_2O_2 increases at the cost of activity. Clearly to achieve high activity for H_2O_2 production, the catalyst should lie as close as possible to the top of 2-electron volcano where ΔG_{HOO*} = 4.22 eV and ΔG_{HO*} = 1.1 eV. The range of interesting HO* binding energy for high activity and selectivity in the volcano plot is highlighted.

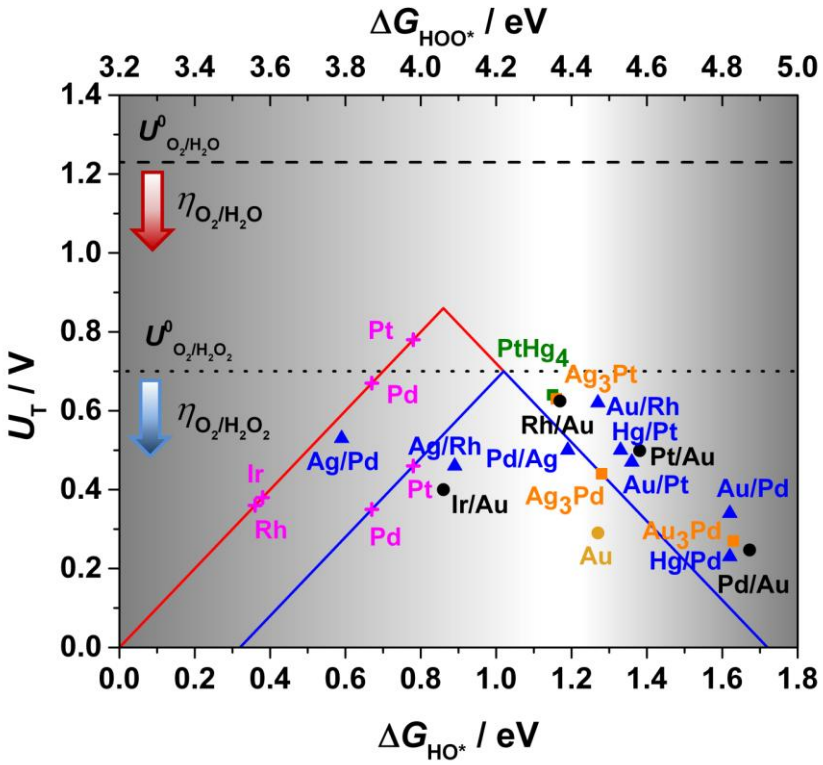

Figure 6-7: Theoretical volcano plot for 2-electron (blue) and 4-electron (red) reduction of O_2 including the potential stable alloys under electrochemical conditions. Three categories of alloys can be specified as black circles are the surface alloys of closely packed Au. Blue triangles are the surface alloys of Pd, Pt and Rh. Bulk alloys of Pt and Pd are shown by orange and green squares. The equilibrium potential of two-electron and four-electron reduction of O_2 are shown as dotted and dashed black lines, respectively.

Among the screened alloys, $PtHg_4$ stands out as the most active catalyst; it exhibits only 0.06 V theoretical overpotential. This is best illustrated by comparing the free energy diagrams for electro-reduction of O_2 to H_2O_2 (see Figure 6-8). The experimental results for ORR on $PtHg_4$, that will be presented later confirm the predicted high activity and selectivity towards H_2O_2. It is clear that the activity of $PtHg_4$ towards H_2O_2 production is distinctly different from pure platinum. The high activity of $PtHg_4$ can be attributed to electronic effect, which occurs when the electronic structure of the atoms sitting in the active site, i.e. Pt, is modified by surrounding inert element towards the 4-electron pathway, i.e. Hg. In fact, due to the presence of surrounding Hg atoms, HO* binds to Pt atoms on $PtHg_4$ by 0.37 eV weaker than on pure platinum, locating $PtHg_4$ in the weak binding side of the 2-electron volcano. It is important to note that high activity does not guarantee the selectivity towards H_2O_2. In other word, the catalysts on the right side of the 2-electron volcano are also active for 4-electron reduction.

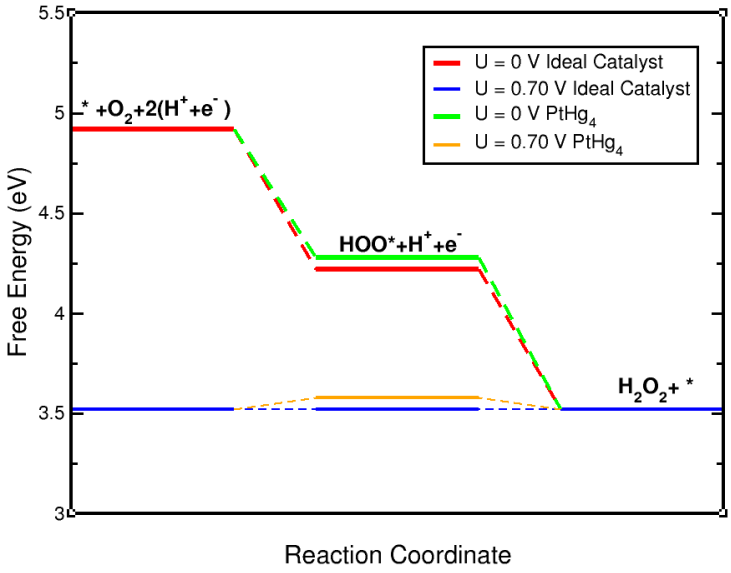

Figure 6-8: Free energy diagram for oxygen reduction to H_2O_2 on ideal catalyst and on $PtHg_4$(110) at U = 0 V and equilibrium potential.

High selectivity of $PtHg_4$, on the other hand, is attributed to ensemble As can be seen in Figure 6-9 shows the position of the Pt and Hg atoms on the surface of $PtHg_4$(110) structure.

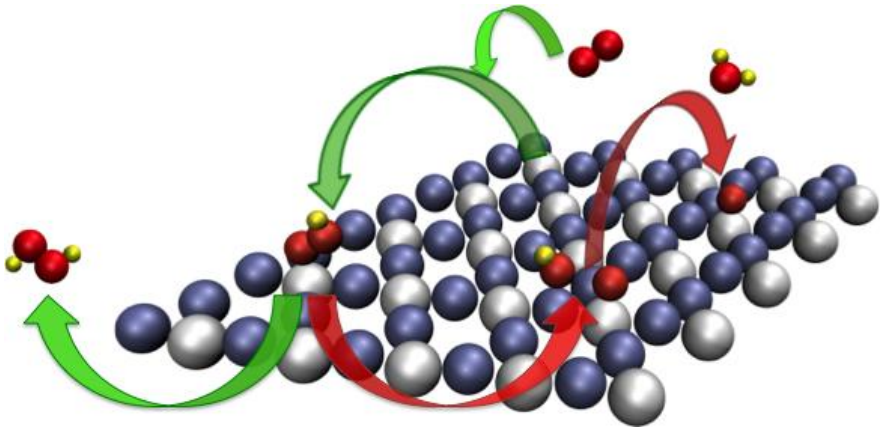

Figure 6-9: Schematic representing the single active site concept. Mercury, platinum, oxygen and hydrogen atoms are colored in blue, white, red and white, respectively. Green arrows denote the favorable reaction pathway that results in H_2O_2 as final product of the electroreuction of O_2. The red arrows show the unfavorable reaction pathways that result water as the final product of the electroreduction of O_2.

Each Pt atoms is isolated by Hg atoms. To direct the selectivity towards H_2O_2 production, both chemical and electrochemical dissociation of HOO* should be avoided. Chemical dissociation of HOO* to O* and HO* is highly prohibited due to the lack of hollow sites

and inability of the adjacent Hg atoms in binding O* and HO*. To elucidate electrochemical dissociation of HOO*, i.e. reduction of HOO* to O*+H_2O, we compare the free energy diagrams for ORR on $PtHg_4$ and Pt(111) (see Figure 6-10). As can be seen, even though, the binding energy of oxygen on $PtHg_4$ has become weaker than on Pt. Therefore, from thermodynamic point of view, reduction of HOO* to O* and H_2O is still more favourable over its reduction to H_2O_2. However, since the chemical environments of the two oxygen atoms of HOO* are different, that is one oxygen atom binds to Pt atom, while the other one does not, there could be two different kinetic barriers associated with their coupled proton-electron transfers. In other word, if the protonation of the oxygen atom bund to Pt in $PtHg_4$ has a smaller barrier than protonation of the other oxygen atom, the reduction product will be H_2O_2. We speculate that combination of both electronic effect and ensemble effects results in high activity and selectivity of H_2O_2 on $PtHg_4$.

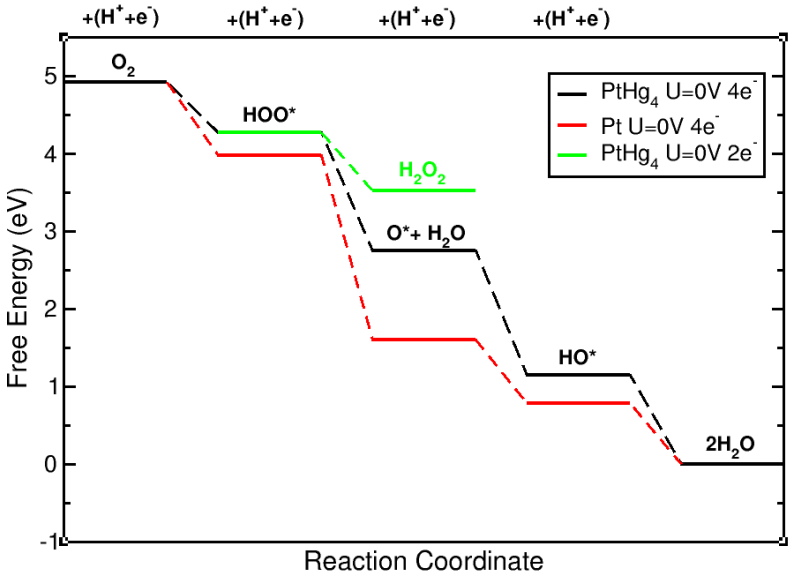

Figure 6-10: Free energy diagram for Pt and $PtHg_4$(110) for the 4-electron oxygen reduction at U = 0 V. For $PtHg_4$(110), the 2-electron pathway is also displayed by green color.

In the following the experimental results for the electrochemical measurements on $PtHg_4$ is presented. Arnau Verdaguer-Casadevall, from CINF, has done these experiments and related analysis.

6.7 Experimental Results

To synthesize $PtHg_4$, similar approach as Wu et al for Hg/Pt(111) followed, as described in chapter 2 [60]. The electrochemical activity for oxygen reduction to hydrogen peroxide is measured using the rotating ring disk electrode (RRDE) technique. Figure 6-11a shows the voltammograms in oxygen for Pt-Hg. The disk current increases exponentially with a decrease in potential from ~0.6 V, as kinetic barriers are lowered. To quantify the amount of hydrogen peroxide formed, the ring was potentiostated at 1.2 V, where oxygen reduction current is negligible while H_2O_2 oxidation is mass transport limited. This gives rise to a positive current at the ring as hydrogen peroxide is produced at the disk. The onset potential at the ring and the disk coincide at ~0.6 V, corresponding to an overpotential of ~0.1 V. Such low overpotential is in agreement with our theoretical predictions. As the overpotential increases, most of the current in the disk can be accounted for by the amount of H_2O_2 detected at the ring; the efficiency to hydrogen peroxide is as high as 96 % in the region between 0.2 and 0.4 V (Figure 6-11a). Within these potential limits, the hydrogen peroxide current density is 3 $mAcm^{-2}$, the theoretical mass transport limit for the 2-electron reduction of oxygen. It is only at potentials below 0.2 V that both selectivity and hydrogen peroxide current start to decrease, implying that water formation is favoured. Ultimately, should electrochemical hydrogen peroxide synthesis make a technological impact, it will require high surface area catalysts or thin films. It turns out that Pt-Hg/C nanoparticles are even more active than the extended surfaces.

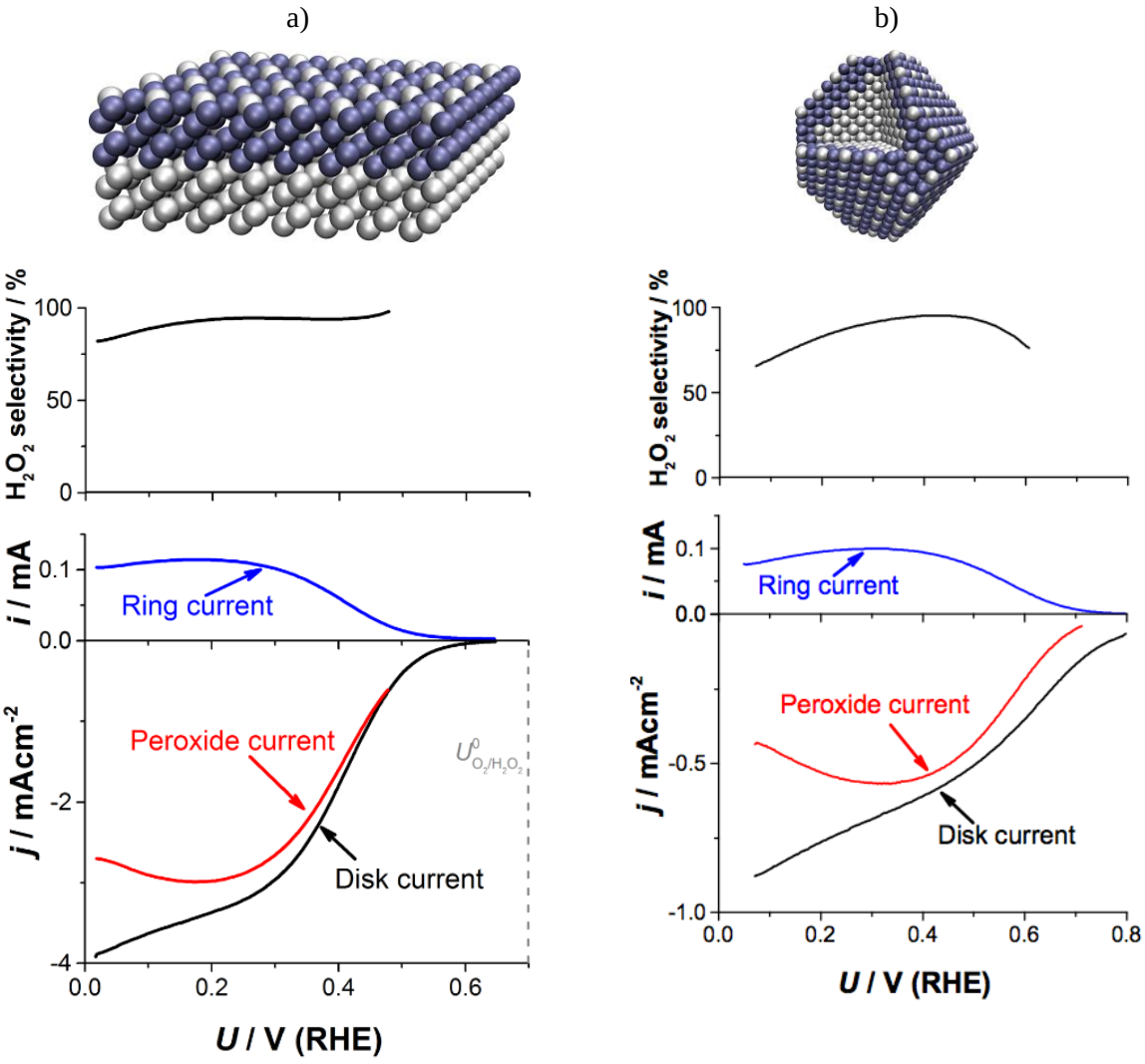

Figure 6-11: a) schematic representation of $PtHg_4$(110) extended surface along with the selectivity as a function of the applied potential and RRDE voltammograms at 1,600 r.p.m. in O_2-saturated electrolyte with the disc current (black), ring current (blue) and current corresponding to hydrogen peroxide (red). b) schematic representation of $PtHg_4$/C nanoparticle along with H_2O_2 selectivity as a function of applied potential and RRDE voltammograms of Pt-Hg/C at 1600 rpm in O_2-saturated electrolyte in 0.1 M $HClO_4$ and at 50 mVs^{-1} with the disk current (black), ring current (blue) and corresponding current to hydrogen peroxide (red).

An ink was prepared from commercial Pt/C and drop cast on a glassy carbon electrode. To prepare the Pt-Hg alloy the same electrodeposition procedure as for the polycrystalline surface was followed. The features of the base voltammograms were similar to those of polycrystalline Pt-Hg as depicted in the Figure 6-12.

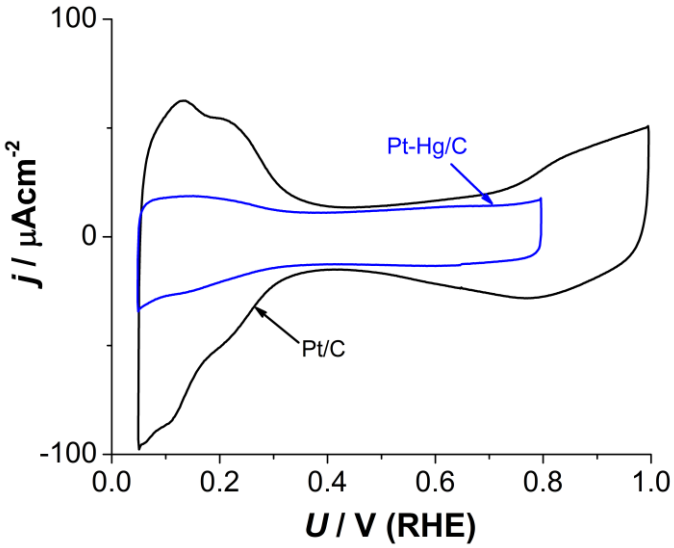

Figure 6-12: Voltammetries of Pt/C (black) and Pt-Hg/C nanoparticles in N_2 saturated solution. The flatter profile of Pt-Hg/C indicates that less contiguous Pt atoms exist. The charge in the H-upd region on Pt/C was used to calculate the surface area of both samples, corresponding to 1.07 ± 0.06 cm^2 (based on four independent measurements). Measurement taken at 50 mVs^{-1} in 0.1 M $HClO_4$ at room temperature.

Oxygen reduction on Hg-modified Pt nanoparticles is evaluated as shown in Figure 6-11b, where a similar current profile similar to the polycrystalline surfaces is observed. The ring current proved that a high yield of hydrogen peroxide was achieved, with over 90 % selectivity between 0.3 and 0.5 V. The catalyst is highly stable under reaction conditions. When cycling the potential between 0.05 and 0.8 V for 8000 cycles in an O_2-saturated electrolyte, there were no measureable losses in H_2O_2 production activity as shown in Figure 6-13.

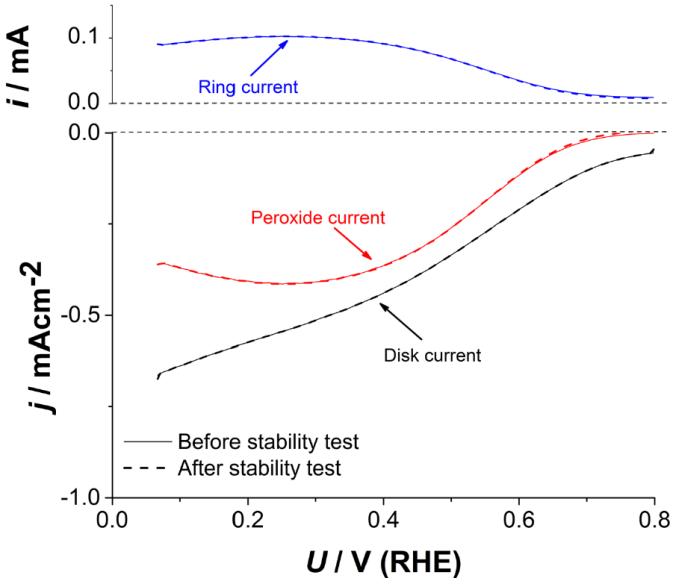

Figure 6-13: RRDE voltammograms of Pt-Hg/C at 1600 rpm in O_2-saturated electrolyte in 0.1 M $HClO_4$ and at 50 mVs^{-1} with the disk current (black), ring current (blue) and corresponding current to hydrogen peroxide (red) before and after stability test. The stability test consisted of 8000 cycles at 200 mVs^{-1} between 0.05 and 0.8 V in oxygen saturated electrolyte. The electrolyte was replaced with a fresh one after the stability test.

6.8 Summary and Outlook

In this chapter, we used the concept of isolated active sites to selectively reduce oxygen to hydrogen peroxide. The reaction mechanism in the reduction of oxygen was discussed, addressing the criteria that should be fulfilled by the catalysts to selectively reduce oxygen to H_2O_2 while maintaining high catalytic activity. By constructing activity volcano, we showed how high selectivity and activity could be achieved on the catalysts with isolated active sites. With these finding, we screened for new electrocatalysts preserving isolated active sites. We examined the stability of these catalysts under electrochemical reaction conditions. Interestingly, our screening results show that $PtHg_4$ alloy possesses exceptional combination of activity, selectivity and stability for H_2O_2 production. Moreover, $PtHg_4$ was examined experimentally and it turned out that it exhibits unprecedented activity, selectivity and stability. It shows 96 % H_2O_2 selectivity, one order of magnitude improvement over the best-known metallic catalyst for direct H_2O_2 production, i.e. Pd@Au.

Chapter 7

Electrochemical Reduction of CO_2 on RuO_2

The electrochemical reduction of CO_2 will be more attractive, if CO_2 is reduced to other products than hydrocarbons, in particular methanol. This is due to the fact that methanol is more convenient to be used for transportation applications. Unfortunately, methanol has not been reported to be a major product in CO_2 reduction on pure metals [8]. In chapter 5, the effort was to design new electrocatalysts to increase the selectivity to favorable products by creating isolated sites on the surface. Several binary alloys with lower overpotentials than the one for Cu and with methanol as a final product in the reduction of CO were suggested; however, the overpotentials are still high making the reduction of CO_2 far from being energy efficient. Another strategy to make CO_2 reduction an energy efficient process is to design/discover the catalysts on which CO_2 reduction proceeds through a different pathway than that on Cu. In this chapter we consider a electrochemical reduction of CO_2 on RuO_2 that experimentally has proven to be selective towards methanol at lower overpotentials than on Cu [90].

7.1 Previous experimental results for CO_2 reduction on RuO_2

Previous experimental studies provide evidences for selective reduction of CO_2 on other catalysts than pure metals, mainly on metal oxides catalysts such as RuO_2 and CuO_2 [90–95]. Spataru and co-workers reported electrochemical reduction of CO_2 on boron-doped diamond supported RuO_2. Table 7-1 shows the experimental results for CO_2 reduction on RuO_2-coated boron-doped diamond electrode at different pH values and different applied

potentials versus RHE. As can be seen, the reduction of CO_2 occurs at low overpotentials , i.e. < 0.4 V versus RHE. As can be seen, reduction of CO_2 on RuO_2 is distinctly different from Cu in the sense that: 1) methanol is not produced in the reduction of CO_2 on Cu, and 2) CO_2 reduction on Cu is accompanied with a very high overpotential, ca. -1V, on RuO_2 the overpotentials are lower, ca. -0.4 V. Even though, RuO_2 has been studied extensively for oxygen evolution reaction (OER) both from experimental and theoretical points of view, to the best of our knowledge there are no theoretical studies for the reduction of CO_2 on RuO_2 to the best of our knowledge. In fact, the key question to answer in this chapter is why RuO_2 exhibits distinct activity and selectivity compared to Cu and how the CO_2 reduction pathway on RuO_2 differs from the one for Cu. Moreover, given that the nature of active sites on metallic oxides are different from that of on pure metals, gaining insight about the nature of active sites and the mechanism through which the reduction of CO_2 proceeds on these sites can be used to develop new electrocatalyst that can selectively and efficiently catalyze the reduction of CO_2 to methanol. Additionally, RuO_2 has proven to have a high electrochemical stability and electrical conductivity that makes it an interesting system to study.

Table 7-1: Results of long time polarization experiments for CO_2 reduction on boron-doped diamond supported RuO_2 electrode at several pH values. (Adopted from Ref.[90])

pH	U / RHE	Product Efficiency / %				
		H_2	CO	CH_4	CH_3OH	HCOOH
2.4	-0.11	59.27	0.02	0.07	5.93	25.18
3.9	-0.12	25.25	0.01	1.7	7.73	40.58
5.9	-0.2	39.88	0.005	0.11	8.12	32.66
7.3	-0.32	44.85	0.003	0.12	4.77	37.45

7.2 Stable surface structure under reaction conditions

In this section, we try to identify the most stable surface structure under reaction conditions in the electrochemical environment. This is done by examining relative stability of the surface structures covered with different adsorbates that are directly or indirectly involved in the reduction of CO_2. We use RuO_2(110) as a model surface.

Previous in situ and ex situ spectroscopic studies at negative potentials after hydrogen evolution reaction on RuO_2 have shown that reduction to metallic Ru surface does not occur at negative potentials up to -0.25 V (RHE) as evidenced by the unchanged Ru 3d level characteristic of Ru^{4+} [96,97]. On the other hand, the same studies showed that RuO_2 surface is partially reduced [96]. To identify thermodynamically stable surface structures under reaction conditions as a function of voltage using DFT, first we consider the possibility of having a reduced surface under reaction condition. This is done by calculating relative stability of the reduced surface compared to stoichiometric RuO_2(110) surface [98]. Our calculations show that partial reduction of RuO_2(110), i.e the reduction of bridge oxygen atoms is thermodynamically favorable at $U \leq 0$ V versus RHE, in agreement with experimental findings [96]. In fact, -0.1 V versus RHE is the potential needed to reduce all bridge oxygen atoms (henceforth denoted as partially reduced surface). Further reduction of RuO2, i.e, reduction of atomic oxygen in the bulk of RuO_2 takes place at lower potentials, ca. -0.43 V (RHE). In the next step for defining the most stable surface structure, we investigate the relative stability of different adsorbates at various coverages present during reaction condition on partially reduced RuO_2(110) surface. We calculate the stability of surface adsorbates formed by proton reduction or water oxidation:

$$* + (H^+ + e^-) \rightarrow H* \quad (7\text{-}1)$$

$$* + H_2O \rightarrow OH* + (H^+ + e^-) \quad (7\text{-}2)$$

$$* + H_2O \rightarrow O* + 2(H^+ + e^-) \quad (7\text{-}3)$$

where * denotes a bridge or coordinately unsaturated site (CUS). We also consider the stability of intermediates formed by reduction of CO_2, such as carboxyl (COOH*), formate (OCHO*) and CO*:

$$* + CO_2 + (H^+ + e^-) \rightarrow COOH* \quad (7\text{-}4)$$

$$* + CO_2 + (H^+ + e^-) \rightarrow OCHO* \quad (7\text{-}5)$$

$$* + CO_2 + 2(H^+ + e^-) \rightarrow CO* + H_2O \quad (7\text{-}6)$$

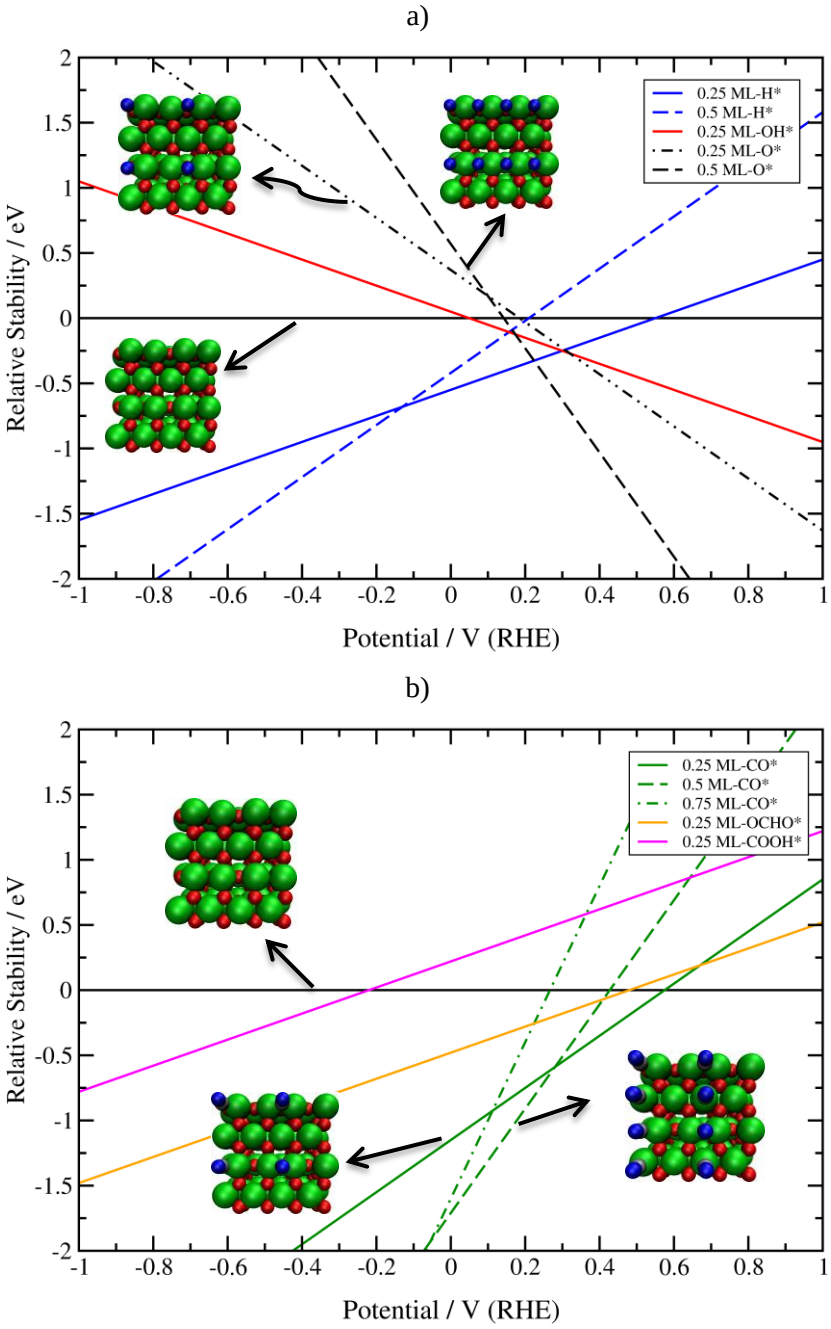

Figure 7-1: Relative stability of different adsorbates on RuO_2(110) formed by **(a)** proton reduction and water oxidation and **(b)** reduction of CO_2. The solid black line denotes partially reduced RuO_2(110) surface where all the bridge oxygen atoms are reduced, and the stoichiometric RuO_2(110) surface is denoted as 0.5 ML-O*.

Figure 7-1 shows the relative stability of the above adsorbates at different coverages on the partially reduced RuO_2(110) surface. According to our analysis, surfaces

with different coverages of CO* are the most stable surfaces at reducing conditions and CO* is therefore likely the most abundant reaction intermediate in CO_2 reduction. To verify this, we have calculated differential CO* coverage with reference to CO(g) and CO_2(g), H_2O(l) and H_2 (g).

As can be seen from Figure 7-2, when CO(g) is reduced, formation of higher coverages of CO* is favorable. This, in turn, means the surface is poisoned by CO* and CO reduction to CHO* will proceed at high overpotentials negative enough to reduce adsorbed CO* to CHO*. On the other hand, in the reduction of CO_2(g), according to Figure 7-2b, formation of 0.8 ML-CO* from CO_2(g) reduction on the reduced RuO_2 (110) surface is favorable.

However, some care should be taken regarding CO* coverage when defining the most stable surface structure. CO* is an inevitable intermediate that forms from CO_2 through COOH* intermediate with two electron-proton step. In fact, formation of CO* will not happen unless COOH* formation is kinetically possible. This mean in defining the coverage of CO*, formation of COOH* should be taken into account. On the reduced RuO_2(110) surface, formation of 0.25 ML of COOH* from CO_2 is associated with 0.22 eV change in the free energy. Once COOH* forms, formation of CO* from COOH* is exergonic. On the other hand formation of COOH* on 0.25 ML covered CO* is exergonic by 0.61 eV in free energy. According to the CHE model, this means that the formation of 0.25 and 0.5 ML of CO* are favorable at potentials of -0.22 and -0.61 V (RHE), respectively on the reduced RuO_2(110) surface. This, in turn, means at the potentials between -0.61 and -0.2 V (RHE), the most stable surface structures is 0.25 ML covered CO* (henceforth denoted as the low CO* coverage structure). Similarly, at potentials lower than -0.61 V (RHE) the most stable surface structure is 0.5 ML covered CO*(henceforth denoted as the high CO* coverage structure).

a)

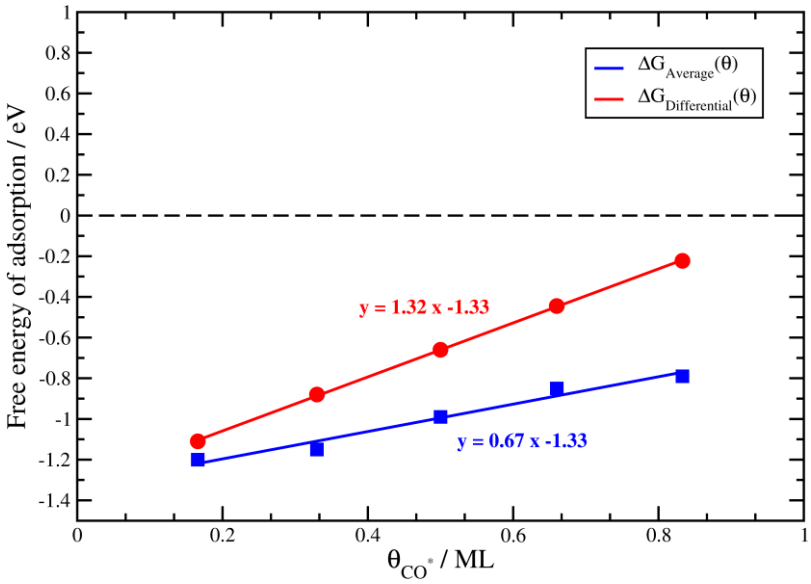

b)

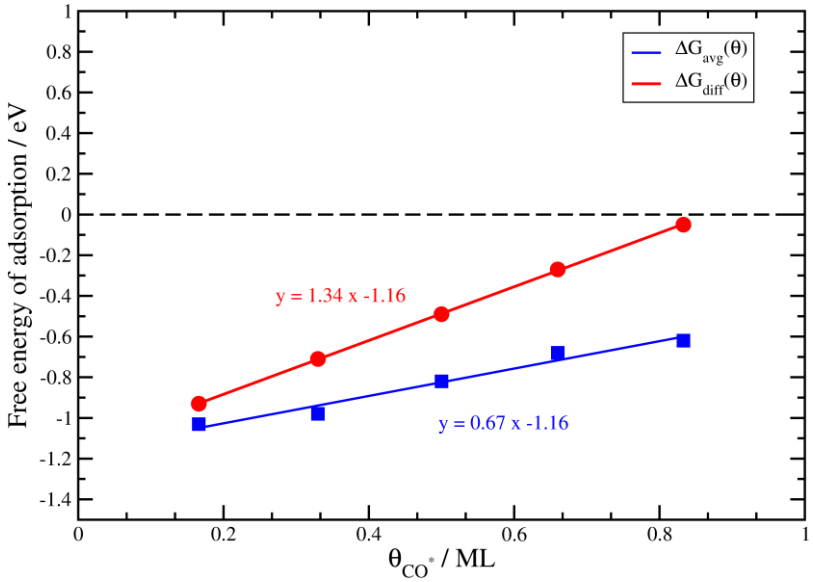

Figure 7-2: Differential and average free energies of adsorption of CO referenced to a) CO(a) and b) CO_2(g), H_2O(l) and H_2(g) on partially reduced RuO_2(110) surface. The blue points are calculated average free energies of adsorption of CO at different coverages and the blue lines are their linear fits. The red lines are the corresponding differential free energies of adsorption.

The electrochemical reduction of CO* may happens through a coupled proton electron transfer from CO* to either CHO* or COH*. As can be seen from Figure 7-3, the reduction of CO* goes through CHO* intermediate on low and high CO* coverage structures and is associated with 1.13 and 1.01 eV change in the free energies, respectively. CO* could also desorb through a chemical step; however, we find the enthalpy of desorption to be 2.09 and 1.49 eV for the low and high CO coverage

structures respectively. Therefore, the rate of CO desorption will be slow. This finding is consistent with the very low faradaic efficiency for CO production on RuO_2(110)[90]. In summary, the stable surface structures are always covered with CO*.

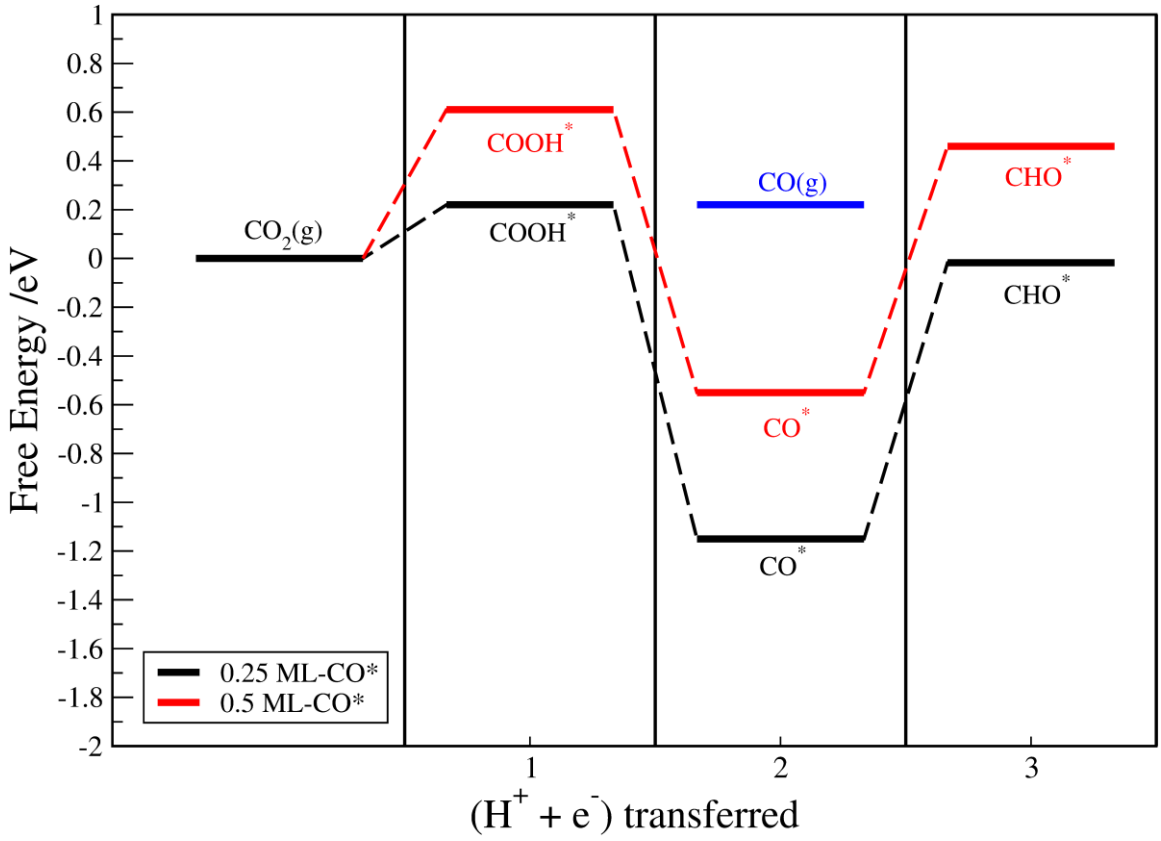

Figure 7-3: Free energy diagram for reduction of CO* to CHO* on RuO_2(110) surface at low (black) and high (red) CO* coverage structures. The chemical potential of CO(g) is also defined (blue).

7.3 CO_2 reduction on stable surface structures

Having identified the most stable surface structures at different potentials, we now aim to examine the electrocatalytic activity of CO_2 reduction on these surfaces at low and high CO* coverages. We inspect all possible reaction intermediates to construct free energy diagrams corresponding to different reactions. The free energy diagrams provide insight into the mechanistic pathways of CO_2 reduction on RuO_2 and its catalytic activity and selectivity. Here we focus on the lowest-energy pathways for the formation of HCOOH and CH_3OH, at both low and high CO* coverages.

7.3.1 Low CO* coverage structure

Figure 7-4 shows the possible reaction pathways for the reduction of CO_2 in the low CO* coverage structure. In the following we discuss in details the lowest-energy pathways for the formation of HCOOH and CH_3OH.

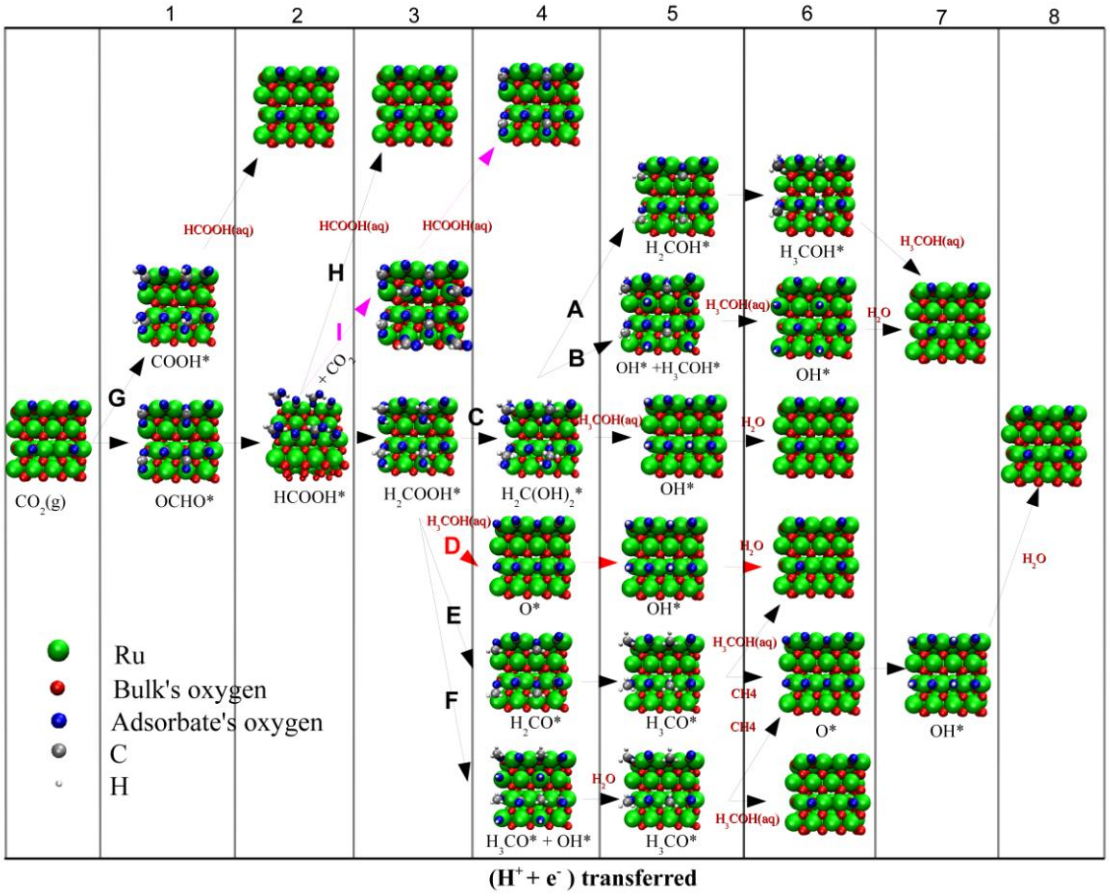

Figure 7-4: Possible pathways in the reduction of CO_2 on $RuO_2(110)$ surface at the low CO* coverage structure. The pink and red arrows (pathways I and D) denote the lowest free energy pathway for the reduction of CO_2 to formic acid and methanol, respectively.

7.3.1.1 CO_2 reduction to HCOOH(aq)

Pathways G,H and I, in **Figure 7-4**, show possible reaction pathways for formation of HCOOH on $RuO_2(110)$. Protonation of CO_2 results in the formation of OCHO* (formate) or COOH* (carboxyl). While formation of COOH* is endergonic by 0.61 eV, formation of OCHO* is exergonic by 0.46 eV. This, in turn, means that at potentials higher than -

0.46 V (RHE) formation of COOH* is not possible and thereby CO* coverage will not increase. The second electron-proton transfer results in the formation of formic acid, HCOOH*, that adsorbs on the bridge site. Since formation of OCHO* is exergonic and desorption of HCOOH* from the surface is endergonic by 0.63 eV, we speculate that HCOOH* may diffuse from a bridge site to neighboring CUS, followed by the adsorption of OCHO* on the freed bridge site and desorption of HCOOH* from the CUS into the solution (pathway I). Figure 7-5 shows the free energy diagram corresponding to pathway I. The change in free energy for to desorption of HCOOH* into the solution is 0.3 eV. This means this pathway is energetically more favorable than the direct desorption of HCOOH*. Moreover, we note that desorption of HCOOH* from the CUS is potential limiting step and since it is a non-electrochemical step, the change in free energy is not affected by the change in the potential.

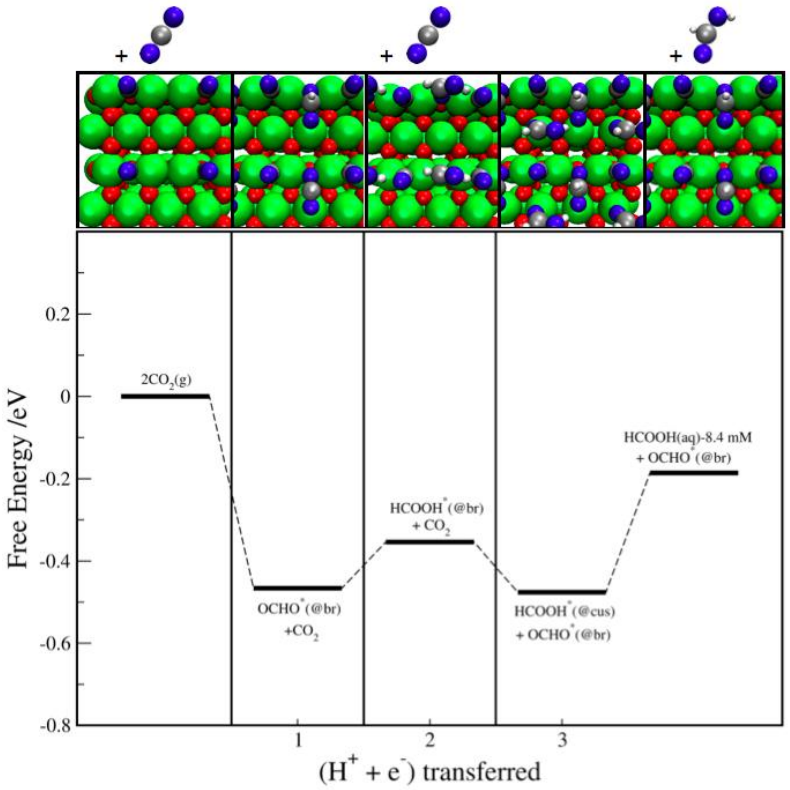

Figure 7-5: Calculated free energy diagram for the lowest energy pathway for the reduction of CO_2 to HCOOH(aq) at 0 V (RHE) on RuO_2(110) at low CO* coverage structure. The concentration of 8.4 and 1 mM was assumed for HCOOH(aq) according to Ref.[90].

7.3.1.2 CO_2 reduction to CH_3OH(aq)

Another reaction pathway that exists after formation of HCOOH*, is further electron-proton transfer to HCOOH* before breaking the oxygen-carbon bond and producing hydrocarbons or alcohols. We note that, transferring electron-proton pairs to HCOOH* could also take place after diffusion of HCOOH* from a bridge to a CUS. However, the calculations show this pathway is energetically less favorable in comparison with the one without diffusion. The first electron-proton pair transferring to HCOOH* results in the formation of H_2COOH* that adsorbs between the bridge site and CUS with the oxygen and hydroxyl ends binding to the bridge and CUS, respectively (cf. pathway D in Figure 7-6). For the next protonation step, we have examined all possible pathways and found out that pathway D is lowest-free energy pathway among all possible reaction pathways (see Figure 7-6). After second protonation step, methanol forms by leaving adsorbed oxygen behind. The adsorbed oxygen is reduced to water in the next two electron-proton transfer steps. The potential limiting step is the protonation of adsorbed formic acid, HCOOH* to form H_2COOH* and the change in free energy corresponding to this step is 0.35 eV at 0 V (RHE). We note that, the pathways that could result in the formation of CH_4 have higher energies compared to pathway D. This is in agreement with the experimental results that show very low faradaic efficiency for the CH_4 production on RuO_2(110).

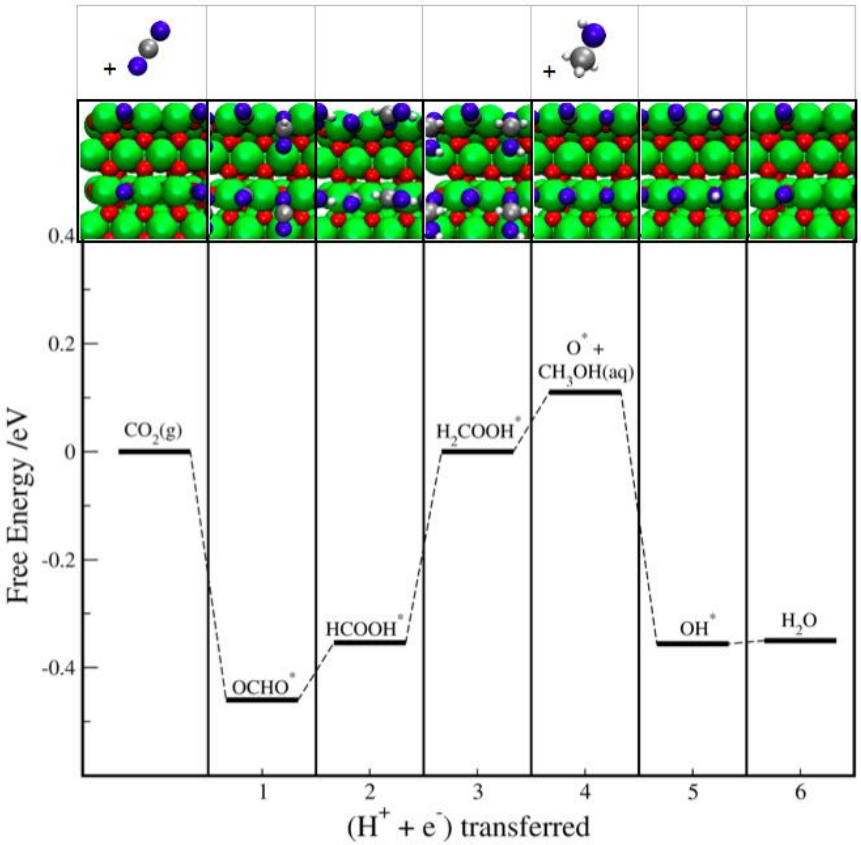

Figure 7-6: Calculated free energy diagram for the lowest energy pathway for the reduction of CO_2 to CH_3OH(aq) at 0 V (RHE) on RuO_2(110) at low CO* coverage structure. The concentration of 1 mM was assumed for CH_3OH(aq) according to Ref.[90].

7.3.2 High CO* coverage structure

At potentials below -0.61 V (RHE), the surface with 0.5ML-CO* is the most stable surface structure. Moreover, we would like to emphasize that even at the potentials higher than -0.61 V (RHE), where the low coverage structure surface is stable, there could be local fluctuations in the CO coverage with areas having coverages higher than the average CO coverage. Similar to the low CO*-coverage structure, we examined all possible reaction intermediates and pathways in the reduction of CO_2 (see **Figure 7-7**).

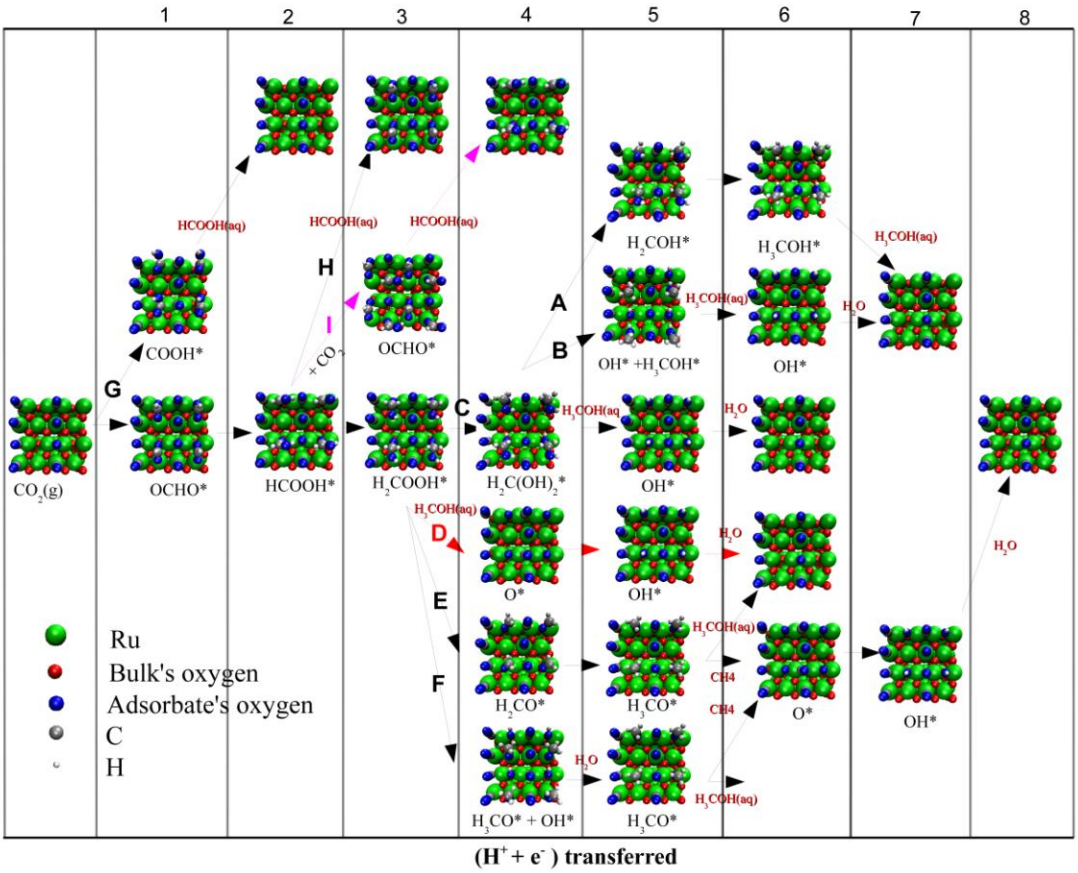

Figure 7-7: Possible pathways in the reduction of CO_2 on RuO_2(110) surface at high CO* coverage structure. The pink and red arrows (pathways I and D) denote the lowest free energy pathways for the reduction of CO_2 to formic acid and methanol respectively.

7.3.2.1 CO_2 reduction to HCOOH(aq)

Figure 7-8 shows the lowest free energy pathway to HCOOH on RuO_2(110) at high CO* coverage structure. The reduction of CO_2 to HCOOH follows the same reaction pathway as at the low CO* coverage. The first electron-proton transfer to CO_2 results in the formation of formate, OCHO, that is almost thermoneutral. On the other hand, the formation of COOH* is endergonic by 0.9 eV, hindering the formation of CO* and hence increasing the coverage of CO* at U > -0.9 V (RHE). The second electron-proton transfer results in the formation of formic acid, HCOOH*, adsorbed on the bridge site as in the case of low coverage structure. We also examined the possibility of HCOOH* diffusion from bridge to CUS. We find that the diffusion of HCOOH* from a bridge to a neighboring CUS, followed by the adsorption of OCHO* on the bridge site is thermodynamically equally favorable as direct HCOOH* desorption from the bridge site.

Therefore, it is expected that both mechanisms contribute in the formation of HCOOH(aq).

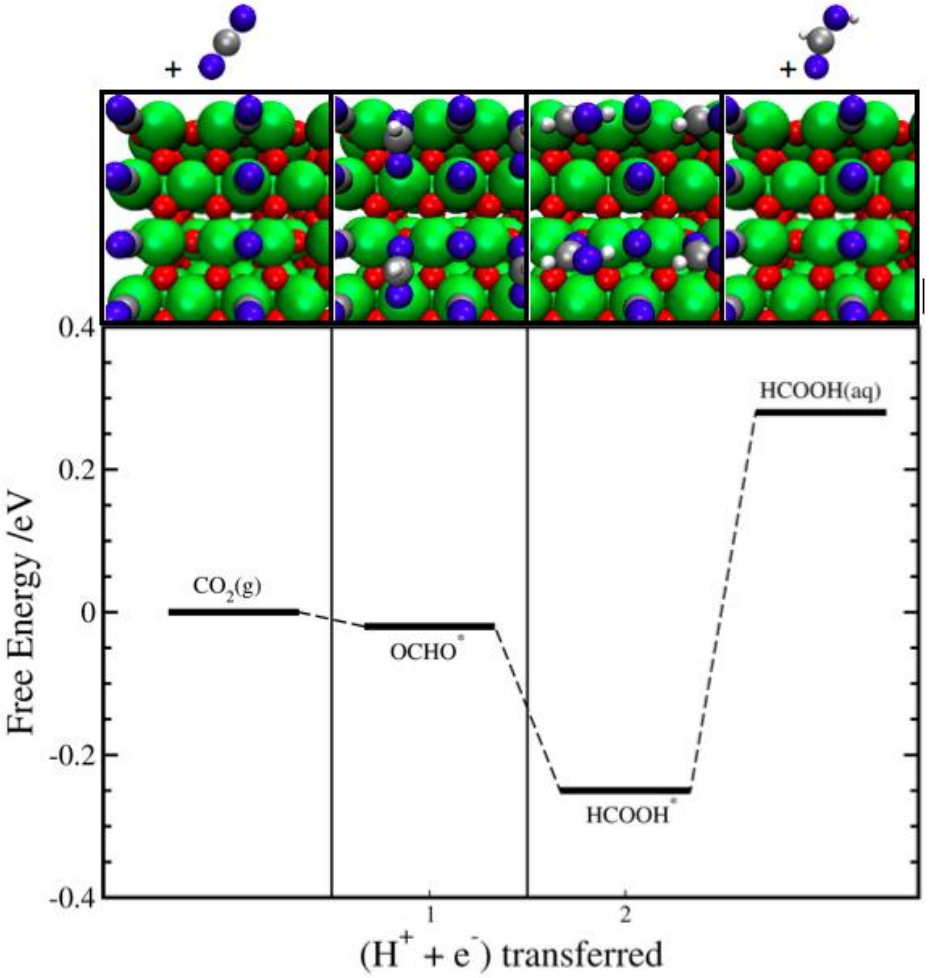

Figure 7-8: Calculated free energy diagram for the lowest energy pathway for the reduction of CO_2 to HCOOH(aq) at 0 V (RHE) on RuO_2(110) at high CO* coverage structure. The concentration of 8.4 mM was assumed for HCOOH(aq) according to Ref.[90].

7.3.2.2 CO_2 reduction to CH_3OH(aq)

Further protonation of HCOOH* could occur through different pathways as depicted in Figure 7-7. The lowest-energy pathway for further protonation of HCOOH*, follows the same reaction pathway as in the low CO* coverage structure. The first protonation step results in the formation of H2COOH* and the final reaction product is methanol (Figure 7-9). Additionally, similar to the low CO* coverage structure, the potential limiting step is the protonation of HCOOH* to H_2COOH*; however, the change in free energy

corresponding to this step is 0.65 eV at 0V (RHE) resulting in a more negative limiting potential of -0.65 V (RHE). This is ca. 0.3V higher than in the case of the low CO* coverage structure. We attribute the difference in the overpotential to the weaker repulsion from adsorbed CO on the neighboring sites.

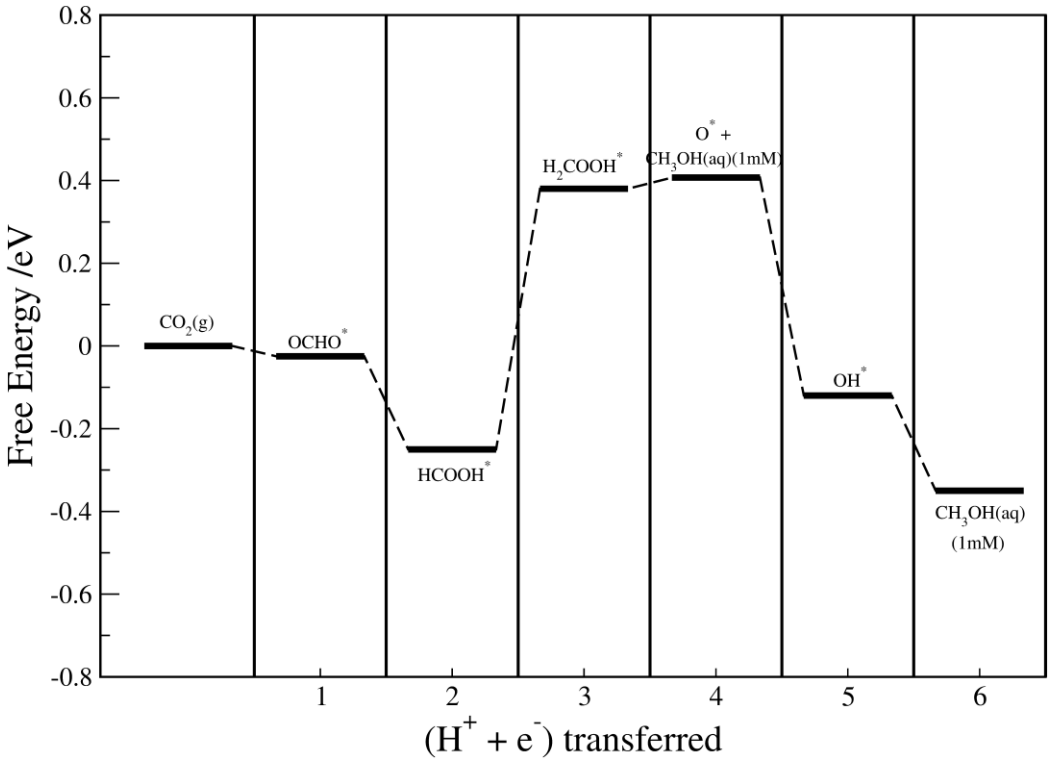

Figure 7-9: Calculated free energy diagram for the lowest energy pathway for the reduction of CO_2 to CH_3OH(aq) at 0 V (RHE) on RuO_2(110) at high CO* coverage structure. The concentration of 1 mM was assumed for CH_3OH(aq) according to Ref.[90].

7.4 CO_2 reduction: Cu(211) versus RuO_2(110)

Having determined the mechanisms for the reduction of CO_2 on RuO_2(110) at the low and high CO* coverage structures, in the following we will make comparison to the mechanism for CO_2 reduction of Cu(211). Figure 7-10 shows the calculated lowest-energy pathways for CO_2 reduction on Cu(211) (reproduced from Ref. [6]) and on RuO_2 (110) at low and high CO* coverages. Clearly the reduction of CO_2 on Cu and RuO_2 proceed through different pathways: On RuO_2, the reduction of CO_2 proceeds through a HCOOH* intermediate whose protonation to H_2COOH* is found out to be the potential limiting step. CO is a spectator species and not an intermediate. On the other hand, in the reduction of CO_2 on Cu, HCOOH* is not an intermediate, instead CO* is a key

intermediate whose protonation to CHO* is the potential limiting step for the formation of CH_4, C_2H_4. Most notably, different CO_2 products are produced on Cu and RuO_2; on Cu and methane and ethylene are the main reaction products, whereas methanol and formic acid are main products on RuO_2 apart from hydrogen.

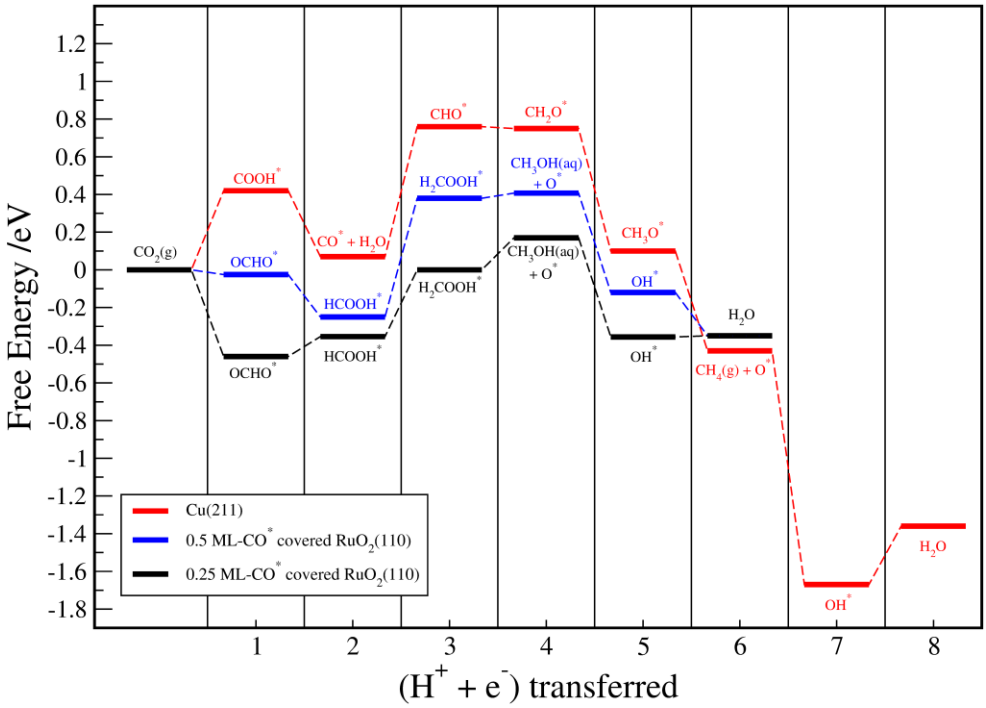

Figure 7-10: Calculated free energy diagram for the lowest energy pathways in the reduction of CO_2 on Cu(211), low and high CO* coverage structures on RuO_2(110) at 0 V (RHE).

The calculations predict higher catalytic activity for CO_2 reduction on RuO_2 than on Cu. The theoretical overpotentials for CO_2 reduction to methanol on RuO_2 for the low and high CO* coverage structures are 0.38 and 0.68 V, respectively, while the one for the CO_2 reduction to methane on Cu is around 1.0 V. The difference arises from the different mechanistic pathways for CO_2 reduction. Until now, a similar mechanism as on Cu has been assumed on metallic and non-metallic catalysts considered for the CO_2 reduction. The potential limiting step was the protonation of CO* to form CHO* or COH* [6,65,68]. However, current study shows that this is not the case at least for RuO_2.

Moreover, a comparison between reduction of CO_2 on RuO_2 surfaces at low and high CO* covered structures show that the CO_2 reduction mechanism is the same for both

surfaces, with similar potential determining steps and the same final product, i.e. methanol. This pinpoints the role of CO coverage in tuning the activity of CO_2 reduction on RuO_2.

7.5 Summary and Outlook

The electrochemical reduction of CO_2 on RuO_2 has been reported to produce methanol at low overpotentials. We used DFT to get insight into the mechanism for CO_2 reduction on RuO_2. RuO_2(110) was used as a model surface. The stable surface structures under electrochemical conditions were defined by examining the stability of different intermediates. Accordingly, two surface structures covered with 0.25 and 0.5 ML-CO*, corresponding to two different potential windows, were found to be most stable surface structures. We constructed the lowest free energy pathways for the reduction of CO_2 on both 0.25 and 0.5 ML-CO* covered surfaces by examining different reaction intermediates. Our results show stark difference between CO_2 reduction on Cu and CO* covered RuO_2(110) surfaces: 1) CO_2 is reduced to formic acid, which is further reduced on both CO* covered RuO_2(110) surfaces. 2) the reduction of formic acid to H_2COOH* is the thermodynamic potential determining step that becomes exergonic at potentials below -0.35 and -0.65 V versus RHE at 0.25 and 0.5 ML-CO* surfaces, respectively, 3) methanol and formic acid are the main reaction products apart from hydrogen.

The difference in the catalytic activities of 0.25 and 0.5 ML-CO* covered RuO_2(110) surface structures emphasizes the role of the CO coverage in controlling the activity. In this regard, surface functionalization with CO, can be used as a tool to tune the catalytic activity for CO_2 reduction.

Bibliography

1. *BP Statistical Review of World Energy June 2013, to be found under www.bp.com*.

2. Lewis, N. S. & Nocera, D. G. Powering the planet: chemical challenges in solar energy utilization. *Proc. Natl. Acad. Sci. U. S. A.* **103,** 15729–35 (2006).

3. Gattrell, M., Gupta, N. & Co, A. Electrochemical reduction of CO2 to hydrocarbons to store renewable electrical energy and upgrade biogas. *Energy Convers. Manag.* **48,** 1255–1265 (2007).

4. Hammer, B. & Nørskov, J. K. Electronic factors determining the reactivity of metal surfaces. *Surf. Sci.* **343,** 211–220 (1995).

5. Nørskov, J. K., Bligaard, T., Rossmeisl, J. & Christensen, C. H. Towards the computational design of solid catalysts. *Nat. Chem.* **1,** 37–46 (2009).

6. Peterson, A. A., Abild-Pedersen, F., Studt, F., Rossmeisl, J. & Nørskov, J. K. How copper catalyzes the electroreduction of carbon dioxide into hydrocarbon fuels. *Energy Environ. Sci.* **3,** 1311 (2010).

7. Vassilev, P. & Koper, M. T. M. Electrochemical Reduction of Oxygen on Gold Surfaces: A Density Functional Theory Study of Intermediates and Reaction Paths. *J. Phys. Chem. C* **111,** 2607–2613 (2007).

8. Hori, Y. in *Mod. Asp. Electrochem.* **42,** 89–189 (Springer New York, 2008).

9. Campos-Martin, J. M., Blanco-Brieva, G. & Fierro, J. L. G. Hydrogen peroxide synthesis: an outlook beyond the anthraquinone process. *Angew. Chem. Int. Ed. Engl.* **45,** 6962–84 (2006).

10. Martin, R. M. *Electronic Structure: Basic Theory and Practical Methods*. 647 (Cambridge University Press, 2008).

11. Hohenberg, P. Inhomogeneous Electron Gas. *Phys. Rev.* **136,** B864–B871 (1964).

12. Kohn, W. & Sham, L. J. Self-Consistent Equations Including Exchange and Correlation Effects. *Phys. Rev.* **140,** A1133–A1138 (1965).

13. Perdew, J. *et al.* Erratum: Atoms, molecules, solids, and surfaces: Applications of the generalized gradient approximation for exchange and correlation. *Phys. Rev. B* **48,** 4978–4978 (1993).

14. Perdew, J. P., Ernzerhof, M. & Burke, K. Rationale for mixing exact exchange with density functional approximations. *J. Chem. Phys.* **105,** 9982 (1996).

15. Zhang, Y. & Yang, W. Comment on "Generalized Gradient Approximation Made Simple."*Phys. Rev. Lett.* **80,** 890–890 (1998).

16. Hammer, B., Hansen, L. & Nørskov, J. Improved adsorption energetics within density-functional theory using revised Perdew-Burke-Ernzerhof functionals. *Phys. Rev. B* **59,** 7413–7421 (1999).

17. Nørskov, J. K. *et al.* Origin of the Overpotential for Oxygen Reduction at a Fuel-Cell Cathode. *J. Phys. Chem. B* **108,** 17886–17892 (2004).

18. Bligaard, T. & Nørskov, J. K. Ligand effects in heterogeneous catalysis and electrochemistry. *Electrochim. Acta* **52,** 5512–5516 (2007).

19. Abild-Pedersen, F. *et al.* Scaling properties of adsorption energies for hydrogen-containing molecules on transition-metal surfaces. *Phys. Rev. Lett.* **99,** 016105 (2007).

20. Hammer, B. & Norskov, J. K. Why gold is the noblest of all the metals. *Nature* **376,** 238–240 (1995).

21. Hammer, B. Theoretical Surface Science and Catalysis — Calculations and Concepts. **45,** (2000).22. Greeley, J. *et al.* Alloys of platinum and early transition metals as oxygen reduction electrocatalysts. *Nat. Chem.* **1,** 552–6 (2009).

23. Greeley, J., Jaramillo, T. F., Bonde, J., Chorkendorff, I. B. & Nørskov, J. K. Computational high-throughput screening of electrocatalytic materials for hydrogen evolution. *Nat. Mater.* **5,** 909–13 (2006).

24. Kitchin, J., Nørskov, J., Barteau, M. & Chen, J. Role of Strain and Ligand Effects in the Modification of the Electronic and Chemical Properties of Bimetallic Surfaces. *Phys. Rev. Lett.* **93,** 156801 (2004).

25. Mavrikakis, M., Hammer, B. & Nørskov, J. Effect of Strain on the Reactivity of Metal Surfaces. *Phys. Rev. Lett.* **81,** 2819–2822 (1998).

26. Strasser, P. *et al.* Lattice-strain control of the activity in dealloyed core-shell fuel cell catalysts. *Nat. Chem.* **2,** 454–60 (2010).

27. Kowal, A., Skompska, M., Wieckowski, A., Bligaard, T. & Nørskov, J. K. Ligand effects in heterogeneous catalysis and electrochemistry. *Electrochim. Acta* **52,** 5512–5516 (2007).

28. Gasteiger, H. A., Markovic, N. M. & Ross, P. N. H2 and CO Electrooxidation on Well-Characterized Pt, Ru, and Pt-Ru. 1. Rotating Disk Electrode Studies of the Pure Gases Including Temperature Effects. *J. Phys. Chem.* **99,** 8290–8301 (1995).

29. Giorgi, L., Pozio, A., Bracchini, C., Giorgi, R. & Turtù, S. H2 and H2/CO oxidation mechanism on Pt/C, Ru/C and Pt–Ru/C electrocatalysts. *J. Appl. Electrochem.* **31,** 325–334 (2001).

30. Stephens, I. E. L. *et al.* Tuning the activity of Pt(111) for oxygen electroreduction by subsurface alloying. *J. Am. Chem. Soc.* **133,** 5485–91 (2011).

31. Knudsen, J. *et al.* A Cu/Pt near-surface alloy for water-gas shift catalysis. *J. Am. Chem. Soc.* **129,** 6485–90 (2007).32. Andersson, K. J., Calle-Vallejo, F., Rossmeisl, J. & Chorkendorff, I. Adsorption-driven surface segregation of the less reactive alloy component. *J. Am. Chem. Soc.* **131,** 2404–7 (2009).

33. Markovic, N. Surface science studies of model fuel cell electrocatalysts. *Surf. Sci. Rep.* **45,** 117–229 (2002).

34. Skúlason, E. *et al.* Modeling the Electrochemical Hydrogen Oxidation and Evolution Reactions on the Basis of Density Functional Theory Calculations. *J. Phys. Chem. C* **114,** 18182–18197 (2010).

35. Shan, B. *et al.* Coverage-Dependent CO Adsorption Energy from First-Principles Calculations. *J. Phys. Chem. C* **113,** 6088–6092 (2009).

36. Lai, S. C. S., Lebedeva, N. P., Housmans, T. H. M. & Koper, M. T. M. Mechanisms of Carbon Monoxide and Methanol Oxidation at Single-crystal Electrodes. *Top. Catal.* **46,** 320–333 (2007).

37. Beden, B., Lamy, C., de Tacconi, N. R. & Arvia, A. J. The electrooxidation of CO: a test reaction in electrocatalysis. *Electrochim. Acta* **35,** 691–704 (1990).

38. Koper, M. T. M. Introductory Lecture : Electrocatalysis: theory and experiment at the interface. *Faraday Discuss.* **140,** 11 (2009).

39. Lebedeva, N. P., Koper, M. T. M., Feliu, J. M. & van Santen, R. A. Mechanism and kinetics of the electrochemical CO adlayer oxidation on Pt(111). *J. Electroanal. Chem.* **524,** 242–251 (2002).

40. Shubina, T. . & Koper, M. T. . Quantum-chemical calculations of CO and OH interacting with bimetallic surfaces. *Electrochim. Acta* **47,** 3621–3628 (2002).

41. Gattrell, M., Gupta, N. & Co, A. A review of the aqueous electrochemical reduction of CO2 to hydrocarbons at copper. *J. Electroanal. Chem.* **594,** 1–19 (2006).42. Hori, Y., Murata, A. & Takahashi, R. Formation of hydrocarbons in the electrochemical reduction of carbon dioxide at a copper electrode in aqueous solution. *J. Chem. Soc. Faraday Trans. 1* **85,** 2309 (1989).

43. Fernández, E. M. *et al.* Scaling relationships for adsorption energies on transition metal oxide, sulfide, and nitride surfaces. *Angew. Chem. Int. Ed. Engl.* **47,** 4683–6 (2008).

44. Peterson, A. A. & Nørskov, J. K. Activity Descriptors for CO 2 Electroreduction to Methane on Transition-Metal Catalysts. *J. Phys. Chem. Lett.* **3,** 251–258 (2012).

45. Pourbaix, M. *Atlas of electrochemical equilibria in aqueous solutions*. 644 (National Association of Corrosion Engineers, 1974).

46. Maroun, F., Ozanam, F., Magnussen, O. M. & Behm, R. J. The role of atomic ensembles in the reactivity of bimetallic electrocatalysts. *Science* **293,** 1811–4 (2001).

47. Strmcnik, D. *et al.* The role of non-covalent interactions in electrocatalytic fuel-cell reactions on platinum. *Nat. Chem.* **1,** 466–72 (2009).

48. Cuesta, A. At least three contiguous atoms are necessary for CO formation during methanol electrooxidation on platinum. *J. Am. Chem. Soc.* **128,** 13332–3 (2006).

49. Greeley, J. *et al.* Alloys of platinum and early transition metals as oxygen reduction electrocatalysts. *Nat. Chem.* **1,** 552–6 (2009).

50. Liu, P., Logadottir, A. & Nørskov, J. K. Modeling the electro-oxidation of CO and H2/CO on Pt, Ru, PtRu and Pt3Sn. *Electrochim. Acta* **48,** 3731–3742 (2003).

51. Wang, K., Gasteiger, H. A., Markovic, N. M. & Ross, P. N. On the reaction pathway for methanol and carbon monoxide electrooxidation on Pt-Sn alloy versus Pt-Ru alloy surfaces. *Electrochim. Acta* **41,** 2587–2593 (1996).52. EscuderoEscribano, M. *et al.* Cyanide-modified Pt(111): Structure, stability and hydrogen adsorption. *Electrochim. Acta* **82,** 524–533 (2012).

53. Strmcnik, D. *et al.* Enhanced electrocatalysis of the oxygen reduction reaction based on patterning of platinum surfaces with cyanide. *Nat. Chem.* **2,** 880–5 (2010).

54. Neurock, M., Janik, M. & Wieckowski, A. A first principles comparison of the mechanism and site requirements for the electrocatalytic oxidation of methanol and formic acid over Pt. *Faraday Discuss.* **140,** 363–78; discussion 417–37 (2008).

55. Neurock, M. Perspectives on the first principles elucidation and the design of active sites. *J. Catal.* **216,** 73–88 (2003).

56. Bandarenka, A. S. *et al.* Design of an Active Site towards Optimal Electrocatalysis: Overlayers, Surface Alloys and Near-Surface Alloys of Cu/Pt(111). *Angew. Chemie* **124,** 12015–12018 (2012).

57. Kornyshev, A. A., Tsirlina, G. A., Ulstrup, J. & Koper, M. T. M. Thermodynamic theory of multi-electron transfer reactions: Implications for electrocatalysis. *J. Electroanal. Chem.* **660,** 254–260 (2011).

58. Trasatti, S. Work function, electronegativity, and electrochemical behaviour of metals. *J. Electroanal. Chem. Interfacial Electrochem.* **39,** 163–184 (1972).

59. Guminski, C. The Hg-Pt (Mercury-Platinum) system. *Bull. Alloy Phase Diagrams* **11,** 26–32 (1990).

60. Wu, H. L., Yau, S. & Zei, M. S. Crystalline alloys produced by mercury electrodeposition on Pt(111) electrode at room temperature. *Electrochim. Acta* **53,** 5961–5967(2008).

61. Greeley, J., Jaramillo, T. F., Bonde, J., Chorkendorff, I. B. & Nørskov, J. K. Computational high-throughput screening of electrocatalytic materials for hydrogen evolution. *Nat. Mater.* **5,** 909–13 (2006).

62. Kibler, L. A. Cover Picture: Hydrogen Electrocatalysis (ChemPhysChem 5/2006). *ChemPhysChem* **7,** 973–973 (2006).

63. *ASM Handbook, Alloy Phase Diagrams*. (1992).

64. Bandarenka, A. S. *et al.* Design of an active site towards optimal electrocatalysis: overlayers, surface alloys and near-surface alloys of Cu/Pt(111). *Angew. Chem. Int. Ed. Engl.* **51,** 11845–8 (2012).

65. Tripkovic, V. *et al.* Electrochemical CO 2 and CO Reduction on Metal-Functionalized Porphyrin-like Graphene. *J. Phys. Chem. C* **117,** 9187–9195 (2013).

66. Calle-Vallejo, F., Martínez, J. I., García-Lastra, J. M., Abad, E. & Koper, M. T. M. Oxygen reduction and evolution at single-metal active sites: Comparison between functionalized graphitic materials and protoporphyrins. *Surf. Sci.* **607,** 47–53 (2013).

67. Maroun, F., Ozanam, F., Magnussen, O. M. & Behm, R. J. The role of atomic ensembles in the reactivity of bimetallic electrocatalysts. *Science* **293,** 1811–4 (2001).

68. Peterson, A. & Nørskov, J. Activity Descriptors for CO2 Electroreduction to Methane on Transition-Metal Catalysts. *J. Phys. Chem. Lett.* **3,** 251– 258 (2012).

69. Calle-Vallejo, F., Martínez, J. I. & Rossmeisl, J. Density functional studies of functionalized graphitic materials with late transition metals for Oxygen Reduction Reactions. *Phys. Chem. Chem. Phys.* **13,** 15639–43 (2011).

70. Ziegelbauer, J. M. *et al.* Direct Spectroscopic Observation of the Structural Origin of Peroxide Generation from Co-Based Pyrolyzed Porphyrins for ORR Applications. *J. Phys. Chem. C* **112,** 8839–8849 (2008).

71. Siahrostami, S., Björketun, M. E., Strasser, P., Greeley, J. & Rossmeisl, J. Tandem cathode for proton exchange membrane fuel cells. *Phys. Chem. Chem. Phys.* **15,** 9326–34 (2013).

72. Lefèvre, M., Proietti, E., Jaouen, F. & Dodelet, J.-P. Iron-based catalysts with improved oxygen reduction activity in polymer electrolyte fuel cells. *Science* **324,** 71–4 (2009).

73. Gupta, S., Tryk, D., Bae, I., Aldred, W. & Yeager, E. Heat-treated polyacrylonitrile-based catalysts for oxygen electroreduction. *J. Appl. Electrochem.* **19,** 19–27 (1989).

74. Jacobson, M. Z., Colella, W. G. & Golden, D. M. Cleaning the air and improving health with hydrogen fuel-cell vehicles. *Science* **308,** 1901–5 (2005).

75. Hamann, C. H., Hamnett, A. & Vielstich, W. *Electrochemistry*. (Wiley-VCH, Weinheim, 1998).

76. Samanta, C. Direct synthesis of hydrogen peroxide from hydrogen and oxygen: An overview of recent developments in the process. *Appl. Catal. A Gen.* **350,** 133–149 (2008).

77. Yamanaka, I., Onizawa, T., Takenaka, S. & Otsuka, K. Direct and continuous production of hydrogen peroxide with 93 % selectivity using a fuel-cell system. *Angew. Chem. Int. Ed. Engl.* **42,** 3653–5 (2003).

78. Jirkovský, J. S. *et al.* Single atom hot-spots at Au-Pd nanoalloys for electrocatalytic H2O2 production. *J. Am. Chem. Soc.* **133,** 19432–41 (2011).

79. Viswanathan, V., Hansen, H. A., Rossmeisl, J. & Nørskov, J. K. Unifying the 2e – and 4e – Reduction of Oxygen on Metal Surfaces. *J. Phys. Chem. Lett.* **3,** 2948–2951 (2012).

80. Yamanaka, I., Hashimoto, T., Ichihashi, R. & Otsuka, K. Direct synthesis of H2O2 acid solutions on carbon cathode prepared from activated carbon and vapor-growing-carbon-fiber by a H2/O2 fuel cell. *Electrochim. Acta* **53,** 4824–4832 (2008).

81. Koper, M. *et al.* Selectivity of cobalt-based catalysts towards hydrogen peroxide formation during the reduction of oxygen. *Catal. Today* **202,** 135–143 (2013).

82. Sidik, R. A., Anderson, A. B., Subramanian, N. P., Kumaraguru, S. P. & Popov, B. N. O2 reduction on graphite and nitrogen-doped graphite: experiment and theory. *J. Phys. Chem. B* **110,** 1787–93 (2006).

83. Kurak, K. A. & Anderson, A. B. Nitrogen-Treated Graphite and Oxygen Electroreduction on Pyridinic Edge Sites. *J. Phys. Chem. C* **113,** 6730–6734 (2009).

84. Fellinger, T.-P., Hasché, F., Strasser, P. & Antonietti, M. Mesoporous nitrogen-doped carbon for the electrocatalytic synthesis of hydrogen peroxide. *J. Am. Chem. Soc.* **134,** 4072–5 (2012).

85. Rankin, R. B. & Greeley, J. Trends in Selective Hydrogen Peroxide Production on Transition Metal Surfaces from First Principles. *ACS Catal.* **2,** 2664–2672 (2012).

86. Chorkendorff, I. & Niemantsverdriet, J. W. *Concepts of Modern Catalysis and Kinetics*. (Wiley-VCH, 2003).

87. Rossmeisl, J., Karlberg, G. S., Jaramillo, T. & Nørskov, J. K. Steady state oxygen reduction and cyclic voltammetry. *Faraday Discuss.* **140,** 337 (2009).

88. Man, I. C. *et al.* Universality in Oxygen Evolution Electrocatalysis on Oxide Surfaces. *ChemCatChem* **3,** 1159–1165 (2011).

89. *CRC Handbook of Chemistry and Physics* . (CRC Press , 1996).

90. Spataru, N., Tokuhiro, K., Terashima, C., Rao, T. N. & Fujishima, A. Electrochemical reduction of carbon dioxide at ruthenium dioxide deposited on boron-doped diamond. *J. Appl. Electrochem.* **33,** 1205–1210 (2003).

91. Le, M. *et al.* Electrochemical Reduction of CO2 to CH3OH at Copper Oxide Surfaces. *J. Electrochem. Soc.* **158,** E45 (2011).

92. Frese, K. W. Electrochemical Reduction of C02 at Intentionally Oxidized Copper Electrodes. **138,** 3338–3344 (1991).

93. Bandi, A. Electrochemical Reduction of Carbon Dioxide on Conductive Metallic Oxides. *J. Electrochem. Soc.* **137,** 2157 (1990).

94. Popić, J. P., Avramov-Ivić, M. L. & Vuković, N. B. Reduction of carbon dioxide on ruthenium oxide and modified ruthenium oxide electrodes in 0.5 M NaHCO3. *J. Electroanal. Chem.* **421,** 105–110 (1997).

95. Qu, J., Zhang, X., Wang, Y. & Xie, C. Electrochemical reduction of CO2 on RuO2/TiO2 nanotubes composite modified Pt electrode. *Electrochim. Acta* **50,** 3576–3580 (2005).

96. Kötz, E. R. & Stucki, S. Ruthenium dioxide as a hydrogen-evolving cathode. *J. Appl. Electrochem.* **17,** 1190–1197 (1987).

97. Rochefort, D., Dabo, P., Guay, D. & Sherwood, P. M. A. XPS investigations of thermally prepared RuO2 electrodes in reductive conditions. *Electrochim. Acta* **48,** 4245–4252 (2003).

98. Su, H.-Y. *et al.* Identifying active surface phases for metal oxide electrocatalysts: a study of manganese oxide bi-functional catalysts for oxygen reduction and water oxidation catalysis. *Phys. Chem. Chem. Phys.* **14,** 14010–22 (2012).

Included Papers

Paper I

Electrocatalysis

DOI: 10.1002/anie.201205314

Design of an Active Site towards Optimal Electrocatalysis: Overlayers, Surface Alloys and Near-Surface Alloys of Cu/Pt(111)**

*Aliaksandr S. Bandarenka, Ana Sofia Varela, Mohammedreza Karamad, Federico Calle-Vallejo, Lone Bech, Francisco J. Perez-Alonso, Jan Rossmeisl, Ifan E. L. Stephens, and Ib Chorkendorff**

Electrochemical devices hold promise as a sustainable route for energy conversion to meet the requirements of future generations. Their development is contingent upon improvements to the functionality of their electrodes.[1] The catalytic performance of these materials is controlled by the atomic and electronic structure of their active sites.[1b,2] Therefore, the design of the appropriate active site is crucial to obtain high catalytic activity, especially where multi-functionality is needed. However, the control of a given surface on an atom-by-atom basis is particularly challenging.

The electrochemical oxidation of CO is the prototypical bifunctional reaction.[3] The active site needs to be reactive towards both oxygen and carbon atoms. Because Pt is reactive towards carbon atoms and Cu is reactive towards oxygen atoms,[4] these are two obvious candidates for the construction of a bifunctional catalyst for electrochemical CO oxidation.

Fundamental studies have shown that overlayers (OLs), near-surface alloys (NSAs), and surface alloys (SAs) of Cu/Pt show markedly different characteristics from pure Cu or Pt surfaces.[5] Herein, we present a study of how to control the reactivity of the Cu/Pt(111) system by modifying the atomic structure in an electrochemical environment. We employ electrochemical measurements, angle-resolved X-ray photoelectron spectroscopy (AR-XPS), and density functional theory (DFT) calculations. This has allowed us to make a detailed comparison between experimental results and theoretical simulations on identical systems.

The Cu/Pt(111) OL, SA, and NSA were prepared according to the general method shown in Figure 1. The resulting AR-XPS depth profiles in Figure 1 confirm that the desired structures were formed.[5c]

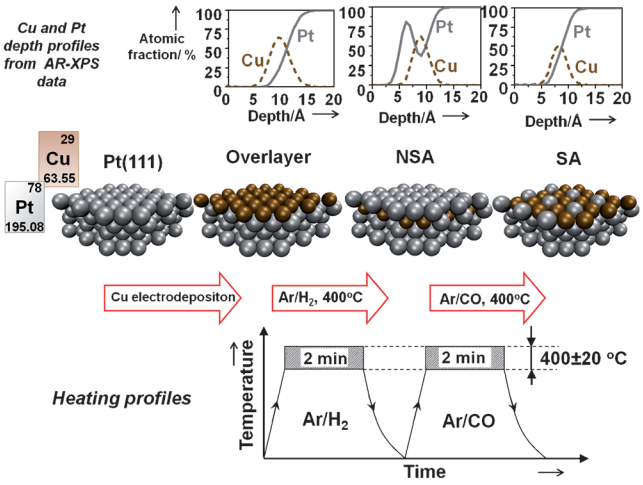

Figure 1. General scheme used to prepare Cu/Pt(111) OL, NSA, and SA. The corresponding depth profiles, obtained using AR-XPS, are shown at the top.

There are considerable differences between the voltammograms of the surfaces in 0.1 M $HClO_4$, as shown in Figure 2. On Pt(111), from 0.05 V to 0.4 V there is a reversible peak arising from the adsorption/desorption of *H (herein * denotes a free site and *X an adsorbed species, X); from 0.6 V to 0.9 V there is a reversible peak arising from the adsorption of *OH.[6] On the NSA, the *H peak is shifted negatively and the *OH peak is shifted positively, suggesting that both *H and *OH are destabilized,[5c] consistent with our DFT calculations, described in the Supporting Information. On the other hand, the Cu/Pt(111) overlayer exhibits a featureless voltammogram between 0.05 V and 0.38 V (the potential was limited to this range because above 0.38 V there was a small oxidation current, prior to the main peak at 0.7 V, as shown in the inset in Figure S5a of the Supporting Information; this could be attributed to Cu dissolution). According to our *CO-displacement measurements (see

[*] Dr. A. S. Bandarenka, A. S. Varela, Dr. L. Bech, Dr. F. J. Perez-Alonso, Dr. I. E. L. Stephens, Prof. I. Chorkendorff
Center for Individual Nanoparticle Functionality
Technical University of Denmark, Building 312
DK-2800 Lyngby (Denmark)
E-mail: ibchork@fysik.dtu.dk
Homepage: http://www.cinf.dtu.dk
M. Karamad, Dr. F. Calle-Vallejo, Dr. J. Rossmeisl
Center for Atomic-Scale Material Design
Technical University of Denmark, Building 307
DK-2800 Lyngby (Denmark)
Dr. A. S. Bandarenka
Center for Electrochemical Sciences, Ruhr Universität Bochum
Universitätsstrasse 150 NC 4/73, 44801 Bochum (Germany)

[**] Funding by the Danish Strategic Research Council's (DSRC) HyCycle program and SERC project (grant no. 2104-06-0011), the Spanish Government's, "Programa Nacional de Movilidad de Recursos Humanos del PN de I-D + I 2008-2011", the PSO-financed ForskEL/ELgrant (HighPerformanceMEA's, project 010076) from energinet.dk and Catalysis for Sustainable Energy research initiative, funded by the Danish Ministry of Science Technology and Innovation is acknowledged. A.S.B. acknowledges additional financial support from the European Union and the MWIFT-NRW (Hightech.NRW competition). The Center for Atomic-scale Materials Design is supported by the Lundbeck Foundation. The Center for Individual Nanoparticle Functionality is supported by the Danish National Research Foundation.

Supporting information (experimental details) for this article is available on the WWW under http://dx.doi.org/10.1002/anie.201205314.

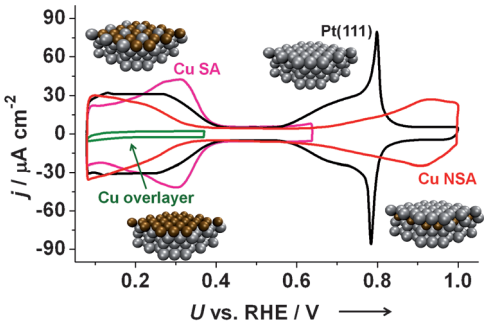

Figure 2. Cyclic voltammograms in 0.1 M $HClO_4$ of: Pt(111), Cu OL on Pt(111), Cu/Pt(111) NSA, and Cu/Pt(111) SA. $dU/dt = 50\ mV s^{-1}$.

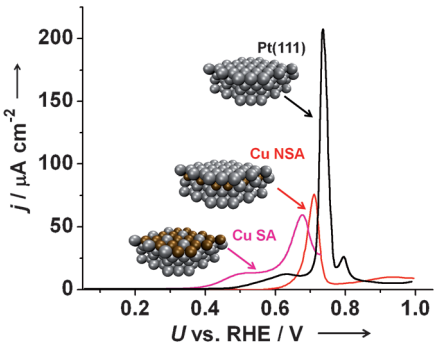

Figure 3. *CO stripping voltammograms for Pt(111), Cu/Pt(111) SA, and Cu/Pt(111) NSA, in $HClO_4$, $dU/dt = 20\ mV s^{-1}$. The CO was adsorbed at 0.05 V, whereas the voltammogram was carried out in a CO-free solution.

Supporting Information), the surface is covered with anionic species in this potential range, which our DFT calculations suggest should be *OH. Within the short time required for a voltammogram, no further anion adsorption takes place, explaining the absence of any peaks. On the other hand, the Cu/Pt(111) SA voltammogram has a reversible peak centered at 0.3 V. The DFT calculations would suggest that this is due to the adsorption of *OH on the Cu sites: *OH binds the SA 0.6 eV stronger than Pt(111), in good agreement with the approximate shift of 0.5 V between the peak on the SA and that of *OH adsorption on Pt(111).

Our results confirm that the trends observed previously for the gas-phase adsorption of *CO[5a,b] also persist for the electrochemical adsorption of *H and *OH (consistent with similar investigations by others,[7] there is a linear correlation between the binding energies of *CO and *H, as shown in Figure S4). Placing Cu in the first atomic layer, as in the SA, results in stronger interactions with *H and *OH, whereas placing Cu in the second layer, as in the NSA, weakens the interaction with the same adsorbates. Having established the relationship between the position of Cu and the reactivity of the surface, we will now use this relationship to control the activity for an electrocatalytic reaction: CO adlayer oxidation.

The *CO electro-oxidation voltammogram for Pt(111), Cu/Pt(111) SA, and NSA is shown in Figure 3. The observed area of the CO electro-oxidation peaks can be used to estimate the CO coverage of each surface. For Pt(111), the charge of $328\ \mu C cm^{-2}$ corresponds to a coverage of 0.68 monolayers (ML), consistent with 0.7 ML obtained by DFT calculations (Supporting Information) and with previous results.[8] In contrast, the charge of $164\ \mu C cm^{-2}$ on the NSA corresponds to a coverage of 0.34 ML, which is in good agreement with the sharp change in CO differential free energy of adsorption at a coverage of 0.33 ML predicted by DFT (Figure S1 b). Because both consist of pure Pt atoms in the outer layer, the difference in *CO coverage can only be attributed to the modified electronic properties of the Pt surface atoms. It is interesting to compare the Cu/Pt(111) NSA with $Pt_3Ni(111)$ and $Pt_3Co(111)$, both of which also have first layers of pure Pt atoms.[9] On these bulk alloys, the coverage of *CO approximates that of Pt(111). This is clearly not the case for the NSA, suggesting that the CO electro-oxidation charge may not always provide a one-to-one correlation with the surface area of nanocatalysts with a Pt overlayer.

For the SA, there is also an abrupt change in the calculated CO differential free energy of adsorption when the coverage reaches 1/3 ML, suggesting that this is the equilibrium coverage (Figure S1 a). This is consistent with a CO molecule covering each platinum surface atom. However, the rigorous experimental determination of the *CO coverage is challenging; the charge owing to CO electro-oxidation is convoluted with the charge arising from *OH adsorption and Cu dissolution (which starts above 0.7 V).

We compare the catalytic activity of the different surfaces towards CO electro-oxidation by taking into account the position of the main peak, corresponding to terrace-bound *CO.[8] The potential required to oxidize CO increases in the following order: SA < NSA < Pt(111).

To understand this reaction, we consider the following mechanism [Eq. (1)–(3)]:

$$CO(g) + * \rightarrow *CO \quad (1)$$

$$H_2O(l) + * \rightarrow *OH + H^+(aq) + e \quad (2)$$

$$*OH + *CO \rightarrow CO_2 + H^+(aq) + e^- + 2* \quad (3)$$

Applying a Sabatier analysis,[10] the optimal catalyst for the electrochemcial oxidation of CO must have an intermediate binding energy towards both *CO and *OH.[9]

Figure 4 shows the 3D volcano plot for CO electro-oxidation as a function of the free energies of adsorption of *CO and *OH. In agreement with our experiments, the overpotential required to oxidize CO increases in the following order: SA < NSA < Pt(111). The SA exhibits a lower overpotential for CO oxidation by virtue of its bifunctional nature: *OH binds to Cu sites and *CO binds to Pt.

Strikingly, the volcano plot suggests that the Cu/Pt(111) OL should exhibit optimal activity for *CO electro-oxidation. However, this theoretical prediction could not be realized, since the Cu overlayer is destabilized by the presence of CO.[11] This caused the oxidation of *CO to be accompanied by the dissolution of the Cu (see Supporting Information).

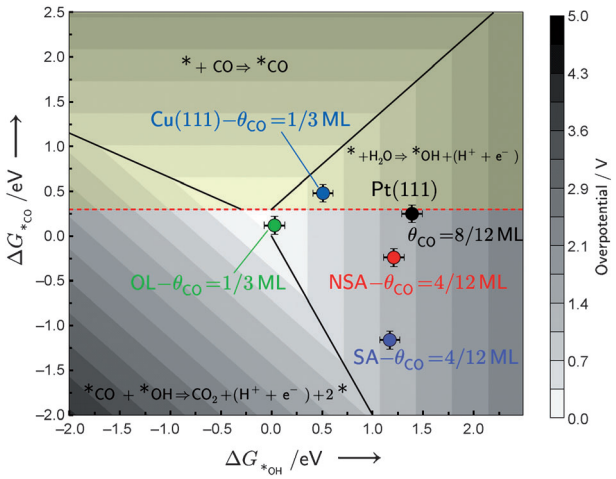

Figure 4. Volcano plot for CO electro-oxidation as a function of the differential free energies of adsorption of CO and OH on different surfaces: Pt(111), Cu(111), Cu/Pt(111) NSA, Cu/Pt(111) SA, and Cu/Pt(111) OL. ΔG_{*CO} is the differential free energy of adsorption of CO when the surfaces are pre-adsorbed with CO, near the corresponding saturation coverage. ΔG_{*OH} is the differential free energy of adsorption of OH co-adsorbed with *CO. The coverage of CO is depicted for each surface. The potential determining step for each region is also defined. The dashed horizontal line denotes the chemical potential of CO in the gas phase, above which CO does not bind to the surface (yellow region).

This illustrates that optimal binding to the intermediates is a necessary but insufficient criterion for an effective catalyst: it must also be stable.[12]

In the NSA, subsurface Cu is kinetically stable below 1.15 V. However, both the SA and the OL are unstable at potentials more positive than 0.7 V, as shown in Figure S5; this observation is consistent with the DFT-calculated dissolution potentials, which are roughly equal for the SA and the OL, as documented in Table S1. Thus the position of the solute metal determines its stability. Less noble metals, which are often alloyed with Pt, such as Ni, Co, Fe, La, or Y, have much lower dissolution potentials than Cu.[13] On the basis of our results, we would not expect these reactive metals to be stable at high potentials in the first surface layer, in contrast to some reports in the literature.[14] The kinetic stability of the solute metal is contingent upon a protective Pt overlayer.

In conclusion, our results demonstrate an unprecedented degree of agreement between electrochemical experiments and first-principle calculations. The location of Cu atoms in Pt(111) controls its interaction with *H, *OH, and *CO. Weakening the binding of CO, by forming a subsurface alloy, can decrease the saturation coverage of CO; thus the CO oxidation charge may not always be a reliable method for the determination of the surface area of nanocatalysts with Pt overlayers. In contrast, Cu atoms in the first layer strengthen the Pt binding energy towards *H, *OH, and *CO. Using this knowledge, we tailored the configuration of Cu atoms in Pt(111) for the electro-oxidation of CO. A large number of electrochemical processes for sustainable fuel production and utilization are controlled by the binding to these adsorbates.[5c,10b,15] Our general approach, outlined here, could enable further progress to be made to the catalysis of these all-important reactions.

Received: July 5, 2012
Published online: October 22, 2012

Keywords: Cu/Pt alloy · cyclic voltammetry · density functional calculations · electrocatalysis · electrochemistry

[1] a) H. A. Gasteiger, J. Garche in *Handbook of Heterogeneous Catalysis*, 2nd ed. (Eds.: G. Ertl, H. Knoezinger, F. Schueth, J. Weitkamp), Wiley-VCH, Chichester, **2008**, pp. 3081–3120; b) D. V. Esposito, S. T. Hunt, A. L. Stottlemyer, K. D. Dobson, B. E. McCandless, R. W. Birkmire, J. G. G. Chen, *Angew. Chem.* **2010**, *122*, 10055–10058; *Angew. Chem. Int. Ed.* **2010**, *49*, 9859–9862; c) Y. C. Lu, H. A. Gasteiger, Y. Shao-Horn, *J. Am. Chem. Soc.* **2011**, *133*, 19048–19051; d) I. E. L. Stephens, A. S. Bondarenko, U. Grønbjerg, J. Rossmeisl, I. Chorkendorff, *Energy Environ. Sci.* **2012**, *5*, 6744–6762.

[2] a) H. E. Hoster, M. J. Janik, M. Neurock, R. J. Behm, *Phys. Chem. Chem. Phys.* **2010**, *12*, 10388–10397; b) L. A. Kibler, A. M. El-Aziz, R. Hoyer, D. M. Kolb, *Angew. Chem.* **2005**, *117*, 2116–2120; *Angew. Chem. Int. Ed.* **2005**, *44*, 2080–2084; c) D. S. Strmcnik, D. V. Tripkovic, D. van der Vliet, K. C. Chang, V. Komanicky, H. You, G. Karapetrov, J. Greeley, V. R. Stamenkovic, N. M. Markovic, *J. Am. Chem. Soc.* **2008**, *130*, 15332–15339; d) J. L. Zhang, M. B. Vukmirovic, Y. Xu, M. Mavrikakis, R. R. Adzic, *Angew. Chem.* **2005**, *117*, 2170–2173; *Angew. Chem. Int. Ed.* **2005**, *44*, 2132–2135; e) F. J. Perez-Alonso, D. McCarthy, A. Nierhoff, P. Hernandez-Fernandez, C. Strebel, I. E. L. Stephens, J. H. Nielsen, I. Chorkendorff, *Angew. Chem.* **2012**, *124*, 4719–4721; *Angew. Chem. Int. Ed.* **2012**, *51*, 4641–4643; f) T. F. Jaramillo, K. P. Jorgensen, J. Bonde, J. H. Nielsen, S. Horch, I. Chorkendorff, *Science* **2007**, *317*, 100–102; g) P. Strasser, S. Koh, T. Anniyev, J. Greeley, K. More, C. F. Yu, Z. C. Liu, S. Kaya, D. Nordlund, H. Ogasawara, M. F. Toney, A. Nilsson, *Nat. Chem.* **2010**, *2*, 454–460.

[3] a) S. C. S. Lai, N. P. Lebedeva, T. H. M. Housmans, M. T. M. Koper, *Top. Catal.* **2007**, *46*, 320–333; b) K. J. J. Mayrhofer, M. Arenz, B. B. Blizanac, V. Stamenkovic, P. N. Ross, N. M. Markovic, *Electrochim. Acta* **2005**, *50*, 5144–5154; c) I. Kanezashi, S. Nohara, J. Omura, M. Watanabe, H. Uchida, *J. Electroanal. Chem.* **2011**, *662*, 123–129.

[4] J. Rossmeisl, P. Ferrin, G. A. Tritsaris, A. U. Nilekar, S. Koh, S. Brankovic, P. Strasser, M. Mavrikakis, *Energy Environ. Sci.* **2012**, DOI: 10.1039/C2EE21455E.

[5] a) J. Knudsen, A. U. Nilekar, R. T. Vang, J. Schnadt, E. L. Kunkes, J. A. Dumesic, M. Mavrikakis, F. Besenbacher, *J. Am. Chem. Soc.* **2007**, *129*, 6485–6490; b) K. J. Andersson, F. Calle-Vallejo, J. Rossmeisl, I. Chorkendorff, *J. Am. Chem. Soc.* **2009**, *131*, 2404–2407; c) I. E. L. Stephens, A. S. Bondarenko, F. J. Pérez-Alonso, F. Calle-Vallejo, L. Bech, T. P. Johansson, A. K. Jepsen, R. Frydendal, B. P. Knudsen, J. Rossmeisl, I. Chorkendorff, *J. Am. Chem. Soc.* **2011**, *133*, 5485–5491.

[6] a) A. S. Bondarenko, I. E. L. Stephens, H. A. Hansen, F. J. Pérez-Alonso, V. Tripkovic, T. P. Johansson, J. Rossmeisl, J. K. Nørskov, I. Chorkendorff, *Langmuir* **2011**, *27*, 2058–2066; b) A. Berna, V. Climent, J. M. Feliu, *Electrochem. Commun.* **2007**, *9*, 2789–2794.

[7] a) J. Greeley, M. Mavrikakis, *Catal. Today* **2006**, *111*, 52–58; b) M. P. Humbert, J. G. G. Chen, *J. Catal.* **2008**, *257*, 297–306.

[8] A. Lopez-Cudero, A. Cuesta, C. Gutierrez, *J. Electroanal. Chem.* **2005**, *579*, 1–12.

[9] D. F. van der Vliet, C. Wang, D. G. Li, A. P. Paulikas, J. Greeley, R. B. Rankin, D. Strmcnik, D. Tripkovic, N. M. Markovic, V. R. Stamenkovic, *Angew. Chem.* **2012**, *124*, 3193 – 3196; *Angew. Chem. Int. Ed.* **2012**, *51*, 3139 – 3142.

[10] a) H. Falsig, B. Hvolbaek, I. S. Kristensen, T. Jiang, T. Bligaard, C. H. Christensen, J. K. Nørskov, *Angew. Chem.* **2008**, *120*, 4913 – 4917; *Angew. Chem. Int. Ed.* **2008**, *47*, 4835 – 4839; b) P. Ferrin, A. U. Nilekar, J. Greeley, M. Mavrikakis, J. Rossmeisl, *Surf. Sci.* **2008**, *602*, 3424 – 3431.

[11] C. A. Lucas, N. M. Markovic, P. N. Ross, *Surf. Sci.* **2000**, *448*, 77 – 86.

[12] a) J. Greeley, J. K. Nørskov, *J. Phys. Chem. C* **2009**, *113*, 4932 – 4939; b) K. J. J. Mayrhofer, K. Hartl, V. Juhart, M. Arenz, *J. Am. Chem. Soc.* **2009**, *131*, 16348 – 16349; c) S. Chen, H. A. Gasteiger, K. Hayakawa, T. Tada, Y. Shao-Horn, *J. Electrochem. Soc.* **2010**, *157*, A82 – A97; d) F. J. Perez-Alonso, C. F. Elkjær, S. S. Shim, B. L. Abrams, I. E. L. Stephens, I. Chorkendorff, *J. Power Sources* **2011**, *196*, 6085 – 6091.

[13] M. Pourbaix, *Atlas of Electrochemical Equilibria in Aqueous Solutions*, 2nd ed., National Association of Corrosion Engineers, Houston, TX, **1974**.

[14] a) S. J. Yoo, S. J. Hwang, J. G. Lee, S. C. Lee, T. H. Lim, Y. E. Sung, A. Wieckowski, S. K. Kim, *Energy Environ. Sci.* **2012**, *5*, 7521 – 7525; b) S. J. Yoo, S.-K. Kim, T.-Y. Jeon, S. J. Hwang, J.-G. Lee, S.-C. Lee, K.-S. Lee, Y.-H. Cho, Y.-E. Sung, T.-H. Lim, *Chem. Commun.* **2011**, *47*, 11414 – 11416; c) X. F. Yang, J. Hu, J. Fu, R. Q. Wu, B. E. Koel, *Angew. Chem.* **2011**, *123*, 10364 – 10367; *Angew. Chem. Int. Ed.* **2011**, *50*, 10182 – 10185.

[15] a) A. A. Peterson, F. Abild-Pedersen, F. Studt, J. Rossmeisl, J. K. Nørskov, *Energy Environ. Sci.* **2010**, *3*, 1311 – 1315; b) J. K. Nørskov, J. Rossmeisl, A. Logadottir, L. Lindqvist, J. R. Kitchin, T. Bligaard, H. Jonsson, *J. Phys. Chem. B* **2004**, *108*, 17886 – 17892; c) J. K. Nørskov, T. Bligaard, A. Logadottir, J. R. Kitchin, J. G. Chen, S. Pandelov, U. Stimming, *J. Electrochem. Soc.* **2005**, *152*, J23 – J26; d) I. C. Man, H.-Y. Su, F. Calle-Vallejo, H. A. Hansen, J. I. Martínez, N. G. Inoglu, J. Kitchin, T. F. Jaramillo, J. K. Nørskov, J. Rossmeisl, *ChemCatChem* **2011**, *3*, 1159 – 1165.

Angewandte Chemie
Eine Zeitschrift der Gesellschaft Deutscher Chemiker

Supporting Information

69451 Weinheim, Germany

Design of an Active Site towards Optimal Electrocatalysis: Overlayers, Surface Alloys and Near-Surface Alloys of Cu/Pt(111)**

*Aliaksandr S. Bandarenka, Ana Sofia Varela, Mohammedreza Karamad, Federico Calle-Vallejo, Lone Bech, Francisco J. Perez-Alonso, Jan Rossmeisl, Ifan E. L. Stephens, and Ib Chorkendorff**

anie_201205314_sm_miscellaneous_information.pdf

DFT calculations

The total energies of the different adsorbates on each surface were calculated with density functional theory (DFT) using the DACAPO code in the ASE simulation environment with the RPBE exchange-correlation functional. [1] Ion-electron interactions were described by ultrasoft pseudopotentials. The Kohn-Sham one-electron states were expanded in series of plane waves with a converged energy cutoff of 450 eV and a density cut off of 500 eV. The electron density was determined by iterative diagonalization of the Kohn–Sham Hamiltonian using Pulay mixing of electronic densities at an electronic temperature of 0.1 eV and all total energies were extrapolated to K_BT = 0 eV. The (111) facet of the face-centered cubic (fcc) metals was considered for all calculations: near surface alloy (NSA), surface alloy (SA), Cu-overlayer (OL), Pt(111) and Cu(111).

For the NSA, we assumed a subsurface concentration of 2/3 ML Cu. This is on the basis of our earlier experiments that show that when 1 ML is deposited initially, 0.6 ML reside in the subsurface, following the annealing.[2] For the SA, a surface concentration of 2/3 ML Cu was assumed, also on the basis of our earlier investigations.[3] For the OL. a complete pseudomorphic monolayer was assumed.

The surfaces were modeled using four-layer $\left(2\sqrt{3}\times 2\sqrt{3}\right)R30^{\circ}$ and $\left(\sqrt{3}\times\sqrt{3}\right)R30^{\circ}$ slabs repeated in a super cell geometry with 14 Å of vacuum between successive slabs. Moreover, adsorption was allowed only on one of the exposed surfaces and dipole corrections were used. All *OH and *H adsorption calculations were performed at a coverage of 1/3 ML, whereas the coverage of 1/3ML was assumed for *CO on all surfaces except for Pt(111) where 2/3ML of *CO was considered.

In all calculations, the bottom two layers were fixed in their bulk structure while the top two layers and adsorbates on them were allowed to relax in all directions until the maximum force on any atom was below 0.05 eV $Å^{-1}$. Monkhorst-Pack grids with dimensions $3\times3\times1$ and $6\times6\times1$ were used for sampling the Brillouin zones of the surface $\left(2\sqrt{3}\times2\sqrt{3}\right)R30^{\circ}$ and $\left(\sqrt{3}\times\sqrt{3}\right)R30^{\circ}$ structures respectively. All adsorption sites (atop, bridge and hollow) were

considered and only the most stable ones are used here. Lattice constants of 4.02 and 3.71 Å were used for Pt and Cu respectively, and the lattice constants of the alloys and OL were assumed to be the same as that of the substrate metal. All free energies are calculated relative to $H_2O(l)$, $CO_2(g)$ and $H_2(g)$. Zero-point energies and entropies were included in energetic calculations.[4] We considered solvation effects on all surfaces by assuming that *OH and *CO exposed to liquid water are stabilized by approximately 0.5 and 0.1 eV respectively, as suggested by Peterson el al.[4a] We would like to emphasize that the stabilization of *OH by water in the bilayer depends on the coverage of *CO. When Pt(111) is at its saturation coverage of 2/3 ML of *CO, we do not anticipate any stabilization of the *OH by the water in the bilayer.[5] However, when the surface is pre-dosed with *CO, *CO electrooxidation initiates at the step sites, where *OH adsorption is more favorable than on terrace sites.[6] When the first few CO molecules are oxidized, they leave behind free sites where water can be adsorbed and hence stabilize adsorbed *OH. Thus, the reaction of terrace-bound *CO and *OH is unlikely until the potential where a significant amount of *OH is able at the terraces in the absence of *CO, ~0.7V (see Figure 2 of the main text), which corresponds to the onset of the main peak for *CO oxidation. We note that this is not the case for NSA and SA. On these alloys, due to the lower coverage of *CO, there are already free sites between adsorbed *CO molecules where water can be adsorbed before *CO oxidation takes place. The free energy of gas-phase CO_2 was also corrected by 0.45 eV, accounting for the inaccurate description of gas-phase CO_2 within the RPBE formalism.[4b] We have used the computational hydrogen electrode approach introduced by Nørskov et al.[4, 7] In this model, the electrode potential, U (versus the reversible hydrogen electrode), is taken into account by shifting the electron energy by $-eU$ when an electron is transferred. The overpotential is defined as the maximum positive free energy difference ~~among~~ between each two successive reaction steps.

Equilibrium coverage calculations

The equilibrium CO coverages for the Cu/Pt(111) SA and NSA were calculated using the integral and differential free energies of adsorption. The integral energy is the total adsorption energy of all adsorbed CO molecules on the surface (relative to CO in the gas phase) per surface metal atom. It can also be calculated as the product between the average free energy and the CO coverage. The differential free energy of adsorption is calculated by differentiating the integral free energy with respect to CO coverage.[8] It defines the most stable CO coverage (assuming negligible co-adsorption of other species, the CO coverage should be potential independent, as CO adsorption is not an electrochemical step). Eq(1) shows the relation between average and differential free adsorption energy of CO :

$$G_{diff}(\theta)=d(G_{int})/d(\theta)=d(G_{avg}\theta)/d(\theta) \quad (1)$$

Where θ, G_{diff}, G_{int} and G_{avg} are the coverage, differential, integral and average free energies of adsorption of CO, respectively.

Figure S1 shows the differential free energy of adsorption on Cu/Pt(111) SA, NSA and Pt(111). For the SA and NSA, there is a an abrupt discontinuity at θ = 0.33 ML . In the case of the SA, this is due to a change in the adsorption site. For CO coverages below 0.33 ML, CO molecules adsorb on atop sites of Pt atoms on the SA. However, when the coverage exceeds 0.33 ML, additional CO starts occupying atop sites of Cu atoms, explaining the discontinuity observed at this coverage for the Cu/Pt(111) SA (figure S1.*a*). On the contrary, for the NSAs, the adsorption sites do not change upon increasing the coverage of CO above 0.33 ML. Consequently, the abrupt change in the differential free energy on the NSAs could be explained as a change in adsorbate-adsorbate interactions. Below 0.33 ML, there would be negligible interaction between neighboring CO molecules, whereas above 0.33 ML there would be repulsive interactions. For Pt(111), starting at very low coverage of CO, both the adsorption sites and the number of CO molecules occupying specific adsorption sites change upon continuously increasing the coverage of CO. For example, while at θ = 0.12 ML both atop and fcc hollow sites are occupied, upon increasing the coverage to 0.19 ML just fcc hollow sites are occupied and at θ = 0.5 ML there is an equal mix of atop and bridge sites. At θ = 0.5 ML, the lateral interactions increase significantly, causing an abrupt discontinuity, but the adsorption of CO is still energetically favorable up to θ = 0.7 ML.

The equilibrium coverage of CO should be set at the point where G_{diff} = 0. According to the plots in Figure S1, this takes place at θ = *0.33* ML for the SA and θ = 0.44 ML for the NSA and θ = 0.7ML for Pt(111). In the case of the NSA, this value is comparable, albeit slightly higher than the experimental value. However, given the uncertainty in the DFT calculations of ~ 0.3 eV , it is quite plausible that the coverage at which G_{diff}=*0* would actually correspond to the discontinuity, i.e. at 0.33 ML, explaining the experimentally determined CO coverage.[9] A similar analysis would also be applicable for the SA, where it was not possible to accurately determine the experimental value of θ.

The equilibrium coverage of *O and *OH on the Cu/Pt(111)OL were also calculated following the same scheme used for *CO, except that we assumed 0.5 eV stabilization for *OH due to solvation effect. On the OL, the *O coverage is not influenced by the presence of co-adsorbed water. While the coverage of *OH is 0.3 ML, the coverage of *O is very low at *U*=0 V.

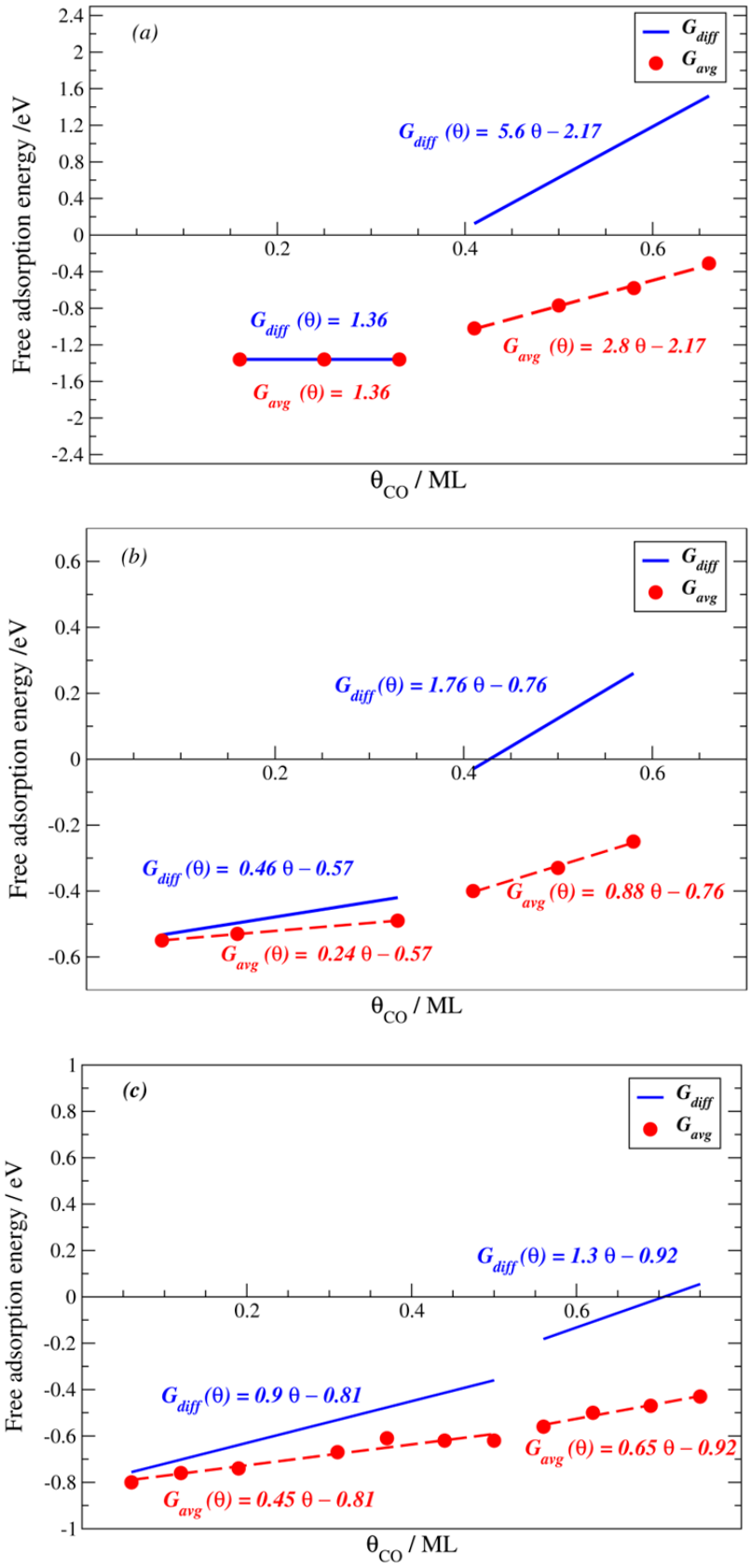

Figure S1. Differential free energy of adsorption of CO on (*a*) surface alloy, (*b*) near surface alloy, and (*c*) Pt(111). The red points are the calculated average adsorption energy at different coverages of CO and the red dashed lines are the fit to them at different coverage regimes.

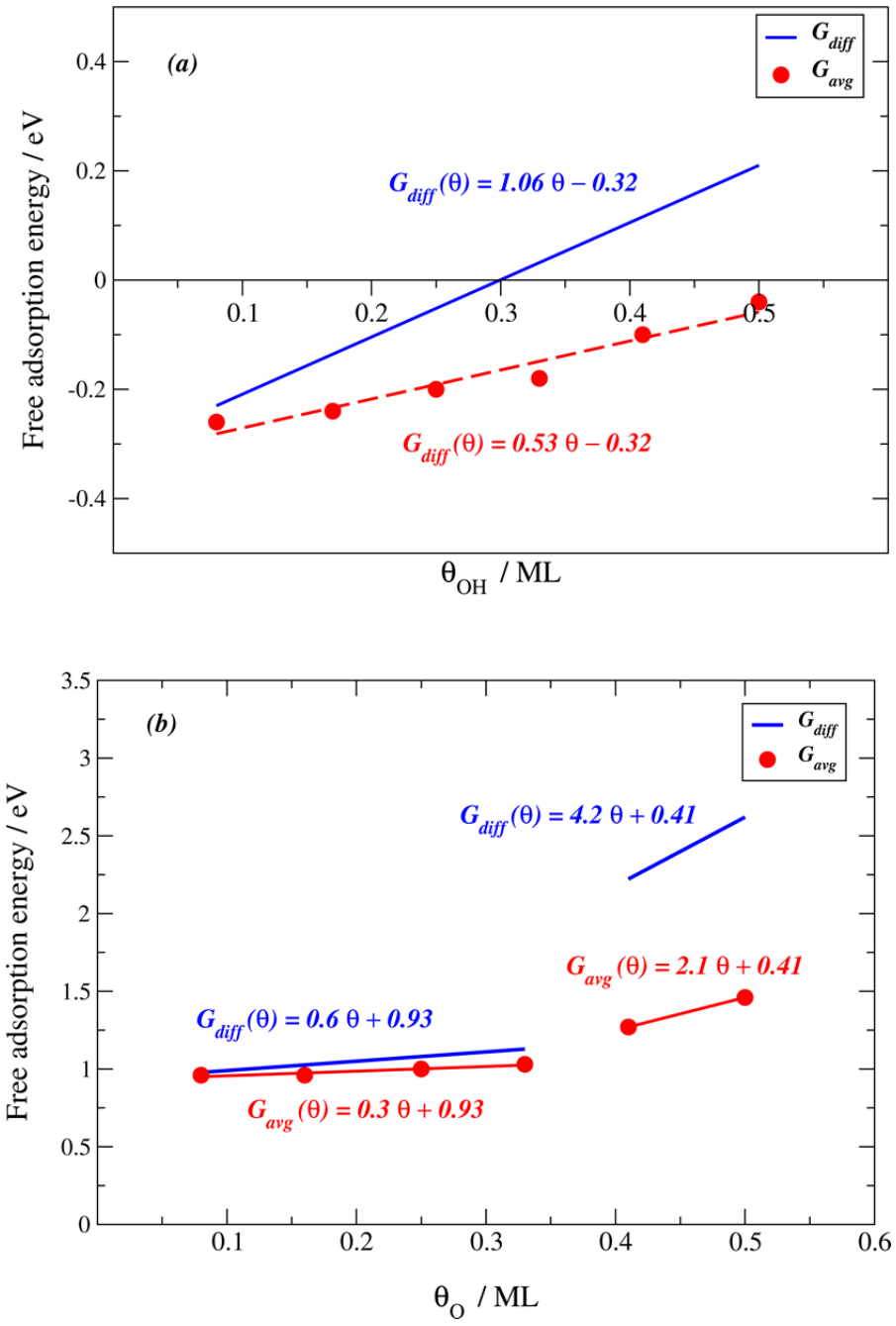

Figure S2. Differential free energy of adsorption of OH (a) and O (b) on the Cu-overlayer at U = 0 V. For OH, the solvation effects have been taken into account.

Binding energy calculations

The calculated binding energies of *H, *OH and *CO on different surfaces are shown in Figure S3. Consistent with experimental results, the binding energies of the different adsorbates are

strongly dependent on the location of the Cu atoms. On the NSA, OL and Cu(111), the binding energies of *OH and *H and *CO are weaker than on Pt(111), when compared at a given coverage. However, on the Cu/Pt(111) SA, the binding energies for the same adsorbates are stronger than on Pt(111). Somewhat counterintuitively, for Pt(111), at the experimentally determined CO coverage of 0.66 ML, the integral CO adsorption energy is weaker than on the NSA. However, at 0.33 ML, the CO binding energy is stronger on Pt(111) than on the NSA.

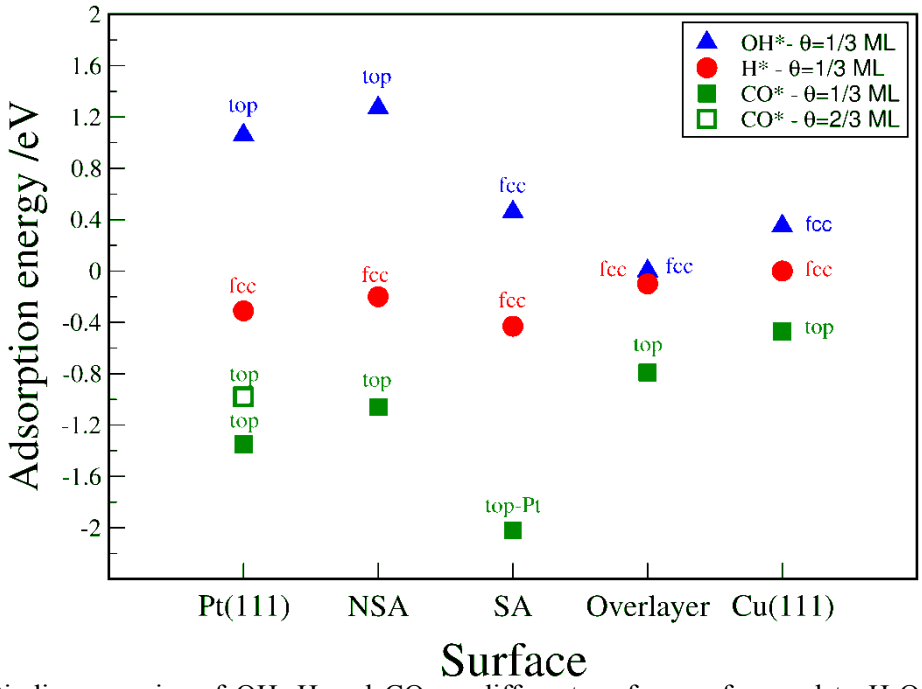

Figure S3. Binding energies of OH, H and CO on different surfaces referenced to $H_2O(l)$, $H_2(g)$ and CO(g) respectively. The adsorption site for each adsorbate is provided.

We note that, the trend in H adsorption correlates well with that of CO on all of the Cu/Pt(111) systems under study, as shown on Figure S4, consistent with the literature.[10]

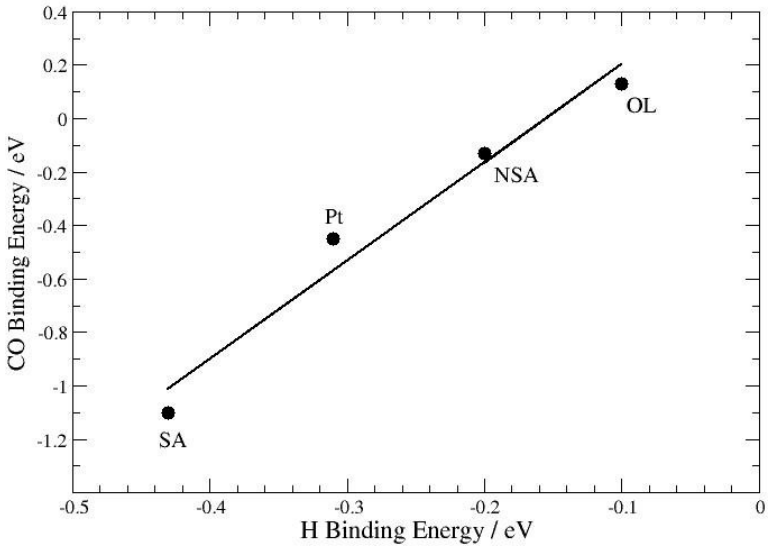

Figure S4: Correlation between hydrogen and CO binding energies on different Cu/Pt(111) systems referenced to H_2(g) and CO(g) respectively.

Volcano plot for CO adlayer electro-oxidation

In order to study the electrochemical oxidation of a CO adlayer we have considered the following steps:

$$CO(g) + * \rightarrow *CO \quad (2)$$

$$H_2O(l) + {}^{*}*CO \rightarrow *CO + {}^{*}OH + H^{+}(aq) + e^{-} \quad (3)$$

$$*OH + *CO \rightarrow CO_2\,(g) + H^{+}(aq) + e^{-} + 2* \quad (4)$$

The first two are elementary reaction steps whereas the last involves both the recombination and the charge transfer step. We assume that CO desorption is irreversible, i.e. that there is no readsorption of CO, via (2) during the course of the oxidation experiment. This assumption is only appropriate for the electo-oxidation of pre-adsorbed *CO when CO is absent from the solution. However, it is not appropriate for the electo-oxidation of CO when CO is dissolved in the solution. The * refers to free sites onto which *CO and *OH can bind, located on a surface which has been preadsorbed with CO to near-saturation CO coverage. It is important to note that these sites can be different, which makes it possible to design bifunctional sites on the catalyst surface, as it is the case of the surface alloy. In addition, there is no direct scaling between the OH and CO binding energies. This means that the two reactivities can be varied more or less independently, making it possible to have surface sites at which both the OH and CO reactivities are optimal.

A good catalyst for the electrochemical CO oxidation has to be able to effectively catalyze the three reaction steps given above. It has to bind CO(g), it has to activate water and form *OH, and it has to bind CO and OH not so strongly that it becomes difficult to form CO_2. The free energies of the three reaction steps gives are the following:[9]

$$\Delta G_1 = \Delta G_{*_{CO}} = G(CO^*) - G(CO(g)) - G(*) \quad (5)$$

$$\Delta G_2 = \Delta G_{*_{OH}} = G(*OH+*CO) + \tfrac{1}{2}G(H_2) - G(H_2O(l)) - G(*CO) - eU - kT\ln(a_{H^+}) \quad (6)$$

$$\Delta G_3 = G(CO_2(g)) + \tfrac{1}{2}G(H_2) + 2G(*) - G(^*OH) - G(^*CO) - eU - kTln(a_{H^+}) \quad (7)$$

Where the term $(1/2\,G(H_2) - eU - kT\ln(a_{H^+}))$ is the chemical potential of electrons and protons using the computational standard hydrogen electrode.[7] ΔG_1, ΔG_2 and ΔG_3 have to simultaneously be as close to zero as possible. We note that, while these are necessary criteria for good catalysts,

there could easily be additional criteria other than those considered here. For example, step 3 involves two elementary steps,[6b] which could mean that ΔG_3 could be more accurately described if further deconvoluted. Only two parameters are catalyst dependent and they are the free energy adsorption of CO, $\Delta G_{*_{CO}}$ ~~$G(^*CO)$~~ and the free energy of adsorption of OH, $\Delta G_{*_{OH}}$ ~~$G(^*OH)$~~.This means that we can plot the overpotential ~~catalyst activity~~ as a function of these two parameters.[7] As discussed above, the overpotential is defined as the maximum positive energy difference between each two successive reaction steps. Mathematically, it can be written as below:

$$U_{\text{Overpotential}} = Max\left[\Delta G_1, \Delta G_2^\circ, \Delta G_3^\circ\right]/e$$

Where ΔG_{2-3}° are the changes in free energies of the respective ΔG_{2-3} reactions at $U = 0$ vs Reversible Hydrogen Electrode (RHE). Since the first step of the reaction, the adsorption of CO is potential independent, when $\Delta G_1 > 0$ CO does not bind to the surface, regardless of the potential and the reaction will simply not take place.

The activity of the surface toward electrochemical CO oxidation can be related to the overpotential in a simple way without taking into account the kinetics details. We assume that the activation barrier for each electron-proton transfer step is equal to corresponding free energy change and that the trends in the overpotential represent the trends in the activity.[7]

We would like to emphasize that the trends in the overpotential do not go hand-in-hand to experimental measured activity as the kinetics details are not taken into accounts. However, this approach gives us an important insight in understanding the trend in the catalytic activity of electrochemical CO oxidation on different surfaces. The volcano plot for the electrochemical CO oxidation is plotted in Fig. S5 against the free energies of the involved intermediates, *CO and *OH.

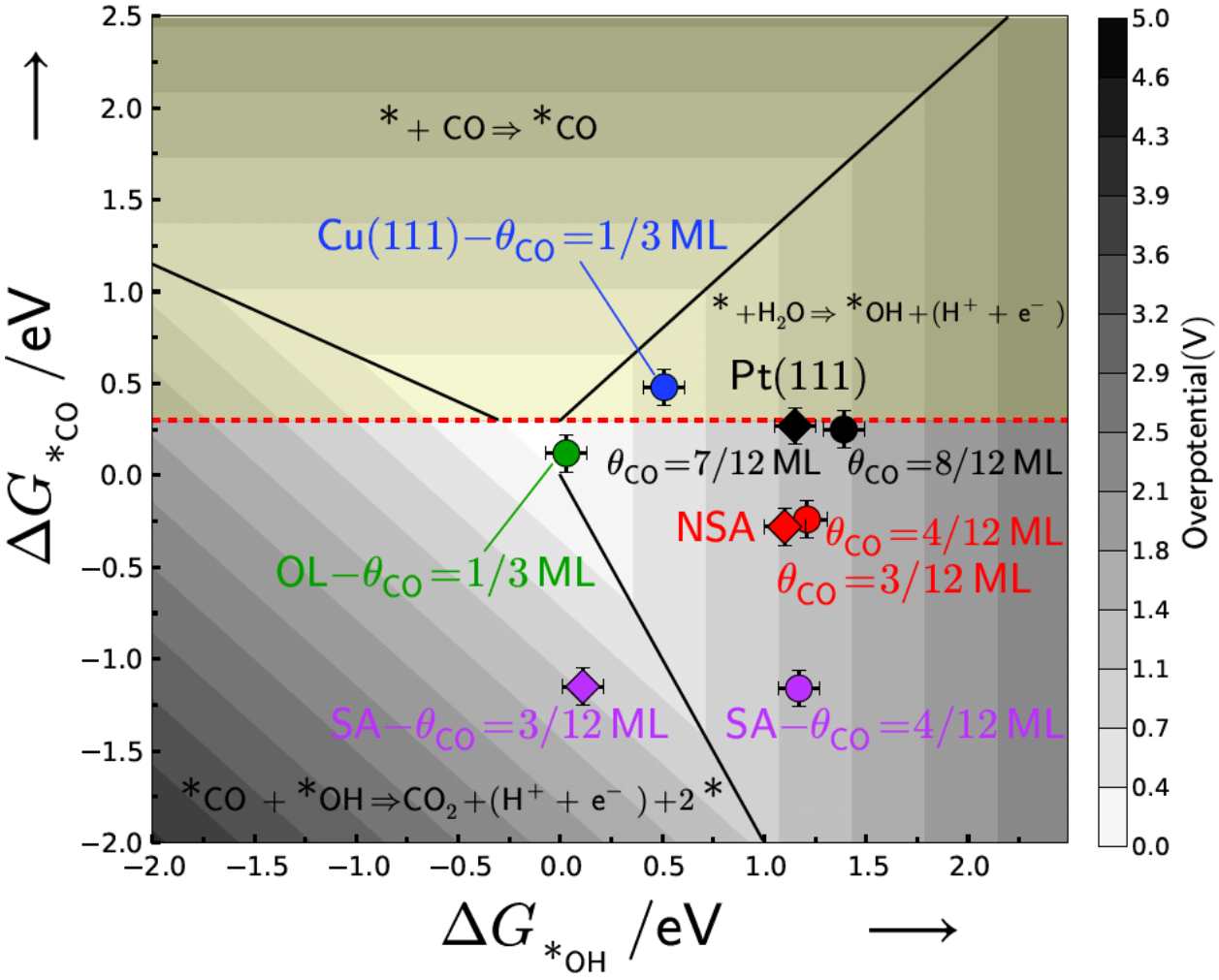

Figure S5. Volcano plot for CO electro-oxidation as a function of the differential free energies of adsorption of CO and OH on different surfaces: Pt(111), Cu(111), Cu/Pt(111) NSA, Cu/Pt(111) SA and Cu-overlayer. $\Delta G_{*_{CO}}$ is the differential free energy of adsorption of CO when the surfaces are pre-adsorbed with CO, near the corresponding saturation coverage. $\Delta G_{*_{OH}}$ is the differential free energy of adsorption of OH coadsorbed with CO. The CO coverages are provided for each surface. The circles show the overpotential for CO electro-oxidation when the CO coverage is 2/3 and 1/3 ML on Pt(111) and all the other surfaces, respectively. Diamonds show the overpotential for CO electro-oxidation on NSA, SA and Pt(111) when the CO coverage is 1/12 ML lower than the corresponding saturation coverages. The potential determining step for each region is also provided. The dashed horizontal line denotes the chemical potential of CO in the gas phase, above which value CO does not bind to the surface (yellow region).

Figure S5 shows the volcano plot of the overpotential towards the electrochemical CO oxidation as a function of the free energies for its intermediates, *CO and *OH. The *CO binding energy has been plotted (a) at the most stable coverage of *CO, and (b) at a *CO coverage 1/12 of a monolayer lower than the most stable coverage for the respective structures. This slightly lower coverage would more accurately model the effect of the change in coverage during the course of the voltammogram. The same trends persist at both coverages, i.e. that the overpotential for the reaction increases in the following order: Cu/Pt(111) overlayer < Cu/Pt(111) SA < Cu/Pt(111)

NSA < Pt(111). The figure also shows that Cu(111) is unable to activate *CO, as its binding energy is too weak in comparison to the chemical potential of gas-phase CO.

For all structures, the activity towards *CO electro-oxidation is slightly improved when the *CO coverage is lower, meaning that when *CO starts to be oxidized the reaction becomes more favourable [6b], in agreement with earlier experimental studies. Furthermore, Figure S5 shows that that by lowering the *CO coverage on the Cu/Pt(111) SA, the limiting step changes from the *OH adsorption to CO2 desorption, since at a lower *CO coverages there are more available sites where *OH binds more strongly. In other words, for the lower coverages of *CO on the Cu/Pt(111) SA , *OH binds to the fcc site formed from Cu and Pt atoms. This site is more stable than atop Cu, which is the most stable adsorption site for the equilibrium coverage of *CO of 1/3 ML.

It is worth perusing upon the effect of defects upon the CO-electroxidation activity of the catalysts under study. We do not know what exact form the defects would take on the alloy surfaces under investigation. Nonetheless, we know from earlier surface science studies of these single crystal alloys that the (111) terraces are well ordered.[3, 11]

For Pt(111), there is a general consensus in the literature that the pre-peak, starting at ~0.5 V, is due to CO oxidation facilitated by defects in the crystal whereas the main peak, whose onset starts at 0.7 V and reaches a maximum at ~0.75 V, is primarily due to the reaction of terrace-bound *CO and *OH.[6] According to Figure S5, *OH activation is potential determining for Pt(111), consistent with the literature.[6b] The effect of the defects on the position of the main peak would be related to the decrease in total coverage of *CO, relative to the saturation coverage, that occurs during the pre-peak. As shown in the figure, decreasing the local coverage of CO, where the reaction takes place, from 2/3 ML to 7/12 ML results in a slight decrease of the theoretical overpotential. The local coverage would be primarily determined by the total coverage of CO and its surface diffusivity or mobility.[6b] If we were to assume that the CO is immobile, and that *OH nucleates and grows from the step, the local coverage of *CO would be high at the sites where the reaction takes place. On the other hand, if we were to assume that the CO is highly mobile, then the local coverage of *CO would be slightly lower than the saturation coverage, due to the amount oxidized in the pre-peak. As the voltammogram proceeds beyond the onset of the main peak, the coverage of *CO would decrease and the coverage of *OH would increase, bringing about an autocatalytic effect to the reaction.

In the case of the NSA, there is only a single peak in the stripping voltammogram shown on Figure 3 of the main article text, starting at ~0.6 V and reaching a maximum at ~0.7 V. This absence of a pre-peak is consistent with the notion that the oxidation only occurs at one site, presumably the terrace, and that the role of defects may be less important. Consequently, to model the onset of the peak, it would be appropriate to consider that the coverage is equal to the saturation coverage.

On the CO stripping voltammogram of the SA, shown in Figure 3 of the main body text, there is a pronounced pre-peak, starting at ~0.4 V. The main peak starts at ~0.6 V and reaches a maximum at ~0.65 V. We propose that the pre-peak corresponds to *CO oxidation, facilitated by defects, similar to Pt(111). As shown in the Figure, at the saturation coverage of 1/3 ML *CO, *OH activation is potential determining. However, it can be deduced from Figure S5 that decreasing the coverage of *CO from 1/3 ML to 3/12 ML strengthens the *OH binding by ~1 eV. Therefore, the removal of a small amount of *CO would significantly facilitate the adsorption of *OH; this would mean that the CO oxidation current in the pre-peak would be concomitant with that of *OH adsorption (in the absence of *CO, *OH would be adsorbed at ~0.3 V, as shown in Fig 2 of the main body text). Assuming that amount of *CO oxidized in the pre-peak brings about a lower local *CO coverage where the reaction takes place, at the onset of the main peak, it would be more appropriate to model the reaction at 3/12 ML coverage. At this lower local coverage the reaction rate or overpotential would be limited by the electrochemical recombination of *CO and *OH.

To summarize the above, we anticipate that the pre-peaks exhibited by Pt(111) and the SA are due to defects. The effect of the defects would be to decrease the total *CO coverage on these surfaces at the onset of the main peak, where terrace bound *CO and *OH react. However, as discussed earlier, the reaction overpotential, or catalytic activity, is only slightly sensitive to the *CO coverage for the surfaces under study. At both saturation coverages and slightly lower coverages of *CO, the theoretical model is able to describe the experimental data, where the overpotential increases in the following order: SA < NSA < Pt(111).

Cu dissolution potentials:

In order to calculate the dissolution potential of Cu in different Cu/Pt(111) systems, we consider following derivation.[12] By assuming standard hydrogen electrode as the reference state, electrode reaction that describes the dissolution potential of the metal A in the alloy constituting from A and B atoms, A/B, $\mathrm{A/B} \rightarrow \mathrm{B/B} + \mathrm{A^{n+}} + \mathrm{ne^-}$,can be written as follows:

$$\mathrm{A/B} + \mathrm{nH^+} \rightarrow \mathrm{B/B} + \mathrm{A^{n+}} + \frac{1}{2}\mathrm{H_2}$$

The dissolution potential of metal A in the alloy is related to the chemical potentials through the following equation:

$$U_{diss-A} = (E_{B/B} - E_{A/B} + NE_{A-Bulk} - NE_{B-Bulk} + NnU_{diss-A,Bulk})/n$$

Where $\mathrm{U_{diss-A}}$ is the dissolution potential of metal A in the alloy (from DFT), $\mathrm{E_{B/B}}$ is the total energy of the pure B metal slab (from DFT), $\mathrm{E_{A/B}}$ is the total energy of the alloy slab (from DFT), N is the number of alloying metal atoms (A) per unit cell in the alloy slab, $NE_{\mathrm{A-Bulk}}$ is the total energy of bulk A atoms (from DFT), $\mathrm{NE_{B-Bulk}}$is the total energy of bulk B atoms (from DFT), n is the number of electrons involved in the dissolution of A atoms (n = 2 in the case of Cu dissolution) and $\mathrm{U_{diss-A,Bulk}}$ is the dissolution potential of bulk A atoms. In

the calculations for dissolution potential of Cu in different Cu/Pt(111) systems, the value of $U_{diss-Cu,Bulk}$ was taken for a pH of 1 and a Cu concentration of 10^{-6} M.[13] Table 1 shows the dissolution potentials of the Cu in different Cu/Pt(111) systems. It should be noted that the experimentally observed dissolution potentials may be significantly more positive, due to additional kinetic barriers.

Cu/Pt(111) System	Dissolution Potential / V (RHE)
NSA	0.48
SA	0.29
Overlayer	0.28

Table S1: Dissolution potentials of Cu in different Cu/Pt(111) systems.

Preparation of Cu/Pt(111) monolayer, NSA and SA

Pt(111) single crystals, with a diameter of 5mm oriented to < 0.1° and polished to the surface roughness 30nm were used (Mateck, Julich, Germany). Before experiments, the Pt(111) crystals were annealed at 850±20°C in a H_2(5%)+Ar atmosphere for 6 min, followed by annealing in a CO(0.1%)+Ar atmosphere for 2 min at 850±20°C.

The Cu/Pt(111) monolayer was prepared by Cu underpotential deposition (UPD) on Pt(111). The deposition of 1 ML of Cu was performed in 0.1 M $HClO_4$ with 2 mM Cu^{2+}, at 0.4V RHE, for 3 minutes, under which conditions a pseudomorphic Cu overlayer on Pt(111) should be formed.[14] The deposited amount of Cu was controlled by the charge required for the anodic dissolution of the Cu overlayer.

The Cu/Pt(111) NSA was obtained by annealing the Cu/Pt(111) monolayer during 2 minutes at 400°C in Ar/H_2 atmosphere (5% of H_2 in Ar). The SA was subsequently obtained by annealing the Cu-Pt(111) NSA for 2 minutes in Ar/CO atmosphere (0.1% of CO in Ar) and afterwards cooling in the same atmosphere. Adsorbed CO was then electrochemically oxidized in 0.1M $HClO_4$ at 0.57V RHE. The temperature during annealing was controlled with a K-type (Ni/Cr+Ni/Al) thermocouple attached to the back side of the crystal. In-depth surface composition information for the Cu/Pt(111) NSA and SA samples was extracted from angle resolved X-ray photoelectron spectroscopy (AR-XPS) spectra recorded using a Theta Probe instrument from Thermo Scientific. The procedure is described in detail elsewhere.[15]

The system used to prepare the near-surface alloy and surface alloy consists of a custom made electrochemical cell with an induction heater directly attached. The electrochemical component consisted of a Pt counter electrode, a mercury/mercury sulfate reference electrode, and the Pt(111) single crystal as the working electrode, in a hanging meniscus configuration. The atmosphere was controlled through gas inlet and outlet ports. The counter electrode was attached to the cell via a port connecting to a separate purging compartment, with its own gas inlet. This compartment allowed the electrolyte (or rinsing water) to be purged of air, prior to its entry into the working compartment of the cell.

The position of the single crystal could be controlled vertically so it could be lifted up and annealed by the induction heater without the need to expose it to air.

After the experiments, the SA- and NSA-samples were the subject for a special treatment in order to remove surface and subsurface Cu and restore the initial Pt(111) surface. For that, the samples were cycled in 0.1M $HClO_4$ between 0.05V and 1.45V(RHE) for few hours at the scan rate 50 mV/s. Afterwards, the crystals were annealed in Ar/H_2 and Ar/CO atmosphere. Cyclic voltammetry, X-ray photoelectron spectroscopy, and low-energy electron diffraction, ion scattering spectroscopy were used to ensure that the Pt(111) surface was restored and no Cu was present close to the surface.

Electrochemical measurements

A Biologic Instruments SP-150 potentiostat was used to control the measurements.

Before the experiments, the cell was cleaned for 24 hours in a "piranha" solution consisting of a mixture of 96% H_2SO_4 and 30% H_2O_2 (3:1), followed by multiple heating/rinsing with Millipore water (18.2 MΩ cm) to remove sulfates. Swagelok stainless steel tubes were used to supply CO, Ar, Ar/H_2 and Ar/CO pure gases and gas mixtures into the cell. Plastic tubing was avoided to minimise outgassing of organic contamination.

Each experiment was conducted in 0.1 M $HClO_4$ (Merck, Suprapur) in ultrapure water (Millipore Synergy Pak UV >18.2 M Ω cm, 22±2°C).

For the Cu UPD, 0.1M CuO (Aldrich, 99.9999%) was dissolved in a solution of 0.3M $HClO_4$, before adding an aliquot of this solution to the electrolyte to obtain a Cu^{2+} concentration of 2mM.

Stability measurments

DFT calculations predict that Cu in the first layer is oxidized at the same potential on the Cu/Pt(111) OL and on Cu/Pt(111) SA. Experimentally we observed the onset potential for Cu

oxidation from the Cu/Pt(111) SA to be around 0.75V (figure S5*a*), which is similar to the stripping potential of copper from the Cu/Pt(111) ML (shown as an insert in figure S5*a*). However, the shape of the oxidation peak is significantly different for these two surfaces. The sharp oxidation peak observed on the Cu/Pt(111) ML indicates strong attractive interactions between copper atoms so when a copper atom is removed, the whole copper monolayer becomes unstable.[16] On the other hand, the broad Cu oxidation peak on the SA could be because the Pt atoms are not dissolved at these potentials. Consequently, Cu dissolution from the SA would result in vacancy or Pt island formation in the surface, which would be less energetically favourable [17] than the simultaneous removal of the first surface layer which occurs in the case of the OL structure. [12],[18]). After Cu stripping from the SA, the voltammogram is drastically different (Fig. S5*b*) compared to that for the initial Pt(111) surface and the corresponding voltammogram for the NSA (see Figs in the manuscript). The voltammogram shown in Fig. S1*b* is rather a fingerprint of a markedly defective surface (peaks in H* adsorption/desorption region and a broader and less reversible OH* adsorption/desorption peaks) [19]. This behavior is expected after Cu removal from the first platinum layer. Notably, after Cu overlayer oxidation from the Pt(111) and subsequent rinsing with 0.1M $HClO_4$ under potential control to remove Cu^{2+}, it was not possible to restore the surface to the initial cyclic voltammogram characteristic of a well ordered Pt(111) surface. The voltammogram of Pt(111) could only be restored if the Cu stripping from the surface alloy was followed by high temperature annealing.

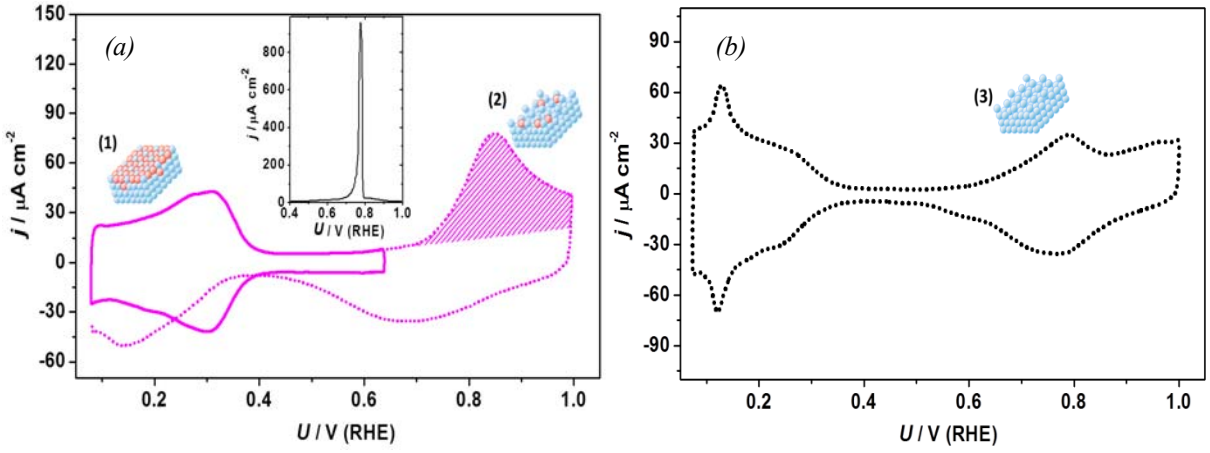

Figure S5: Cyclic voltammograms taken in 0.1M $HClO_4$ characterizing *(a)* (*1*) Cu-Pt(111) SA, (*2*) oxidation of Cu from the Cu-Pt(111) SA and *(b)* (*3*) defective platinum surface remaining after Cu atoms were stripped out from the surface alloy (20^{th} cycle is shown in *b*). Dashed line in *a* also shows the first cycle after Cu oxidation from the SA-surface. d*E*/dt = 50 mV/s

CO displacement and adlayer oxidation on the Cu/Pt(111) overlayer

According to the volcano plot shown in Figure S5, the Cu/Pt(111) overlayer structure should have the very high activity for CO adlayer oxidation, because of its optimal binding to *CO and *OH. However, experiments by Markovic, Ross and co-workers suggest that this structure should be unstable in the presence of CO. [20] They reported that when CO was adsorbed at 0.35V on a Cu/Pt(111) overlayer in perchloric acid solution, the CO displaced the *Cu, leading to its dissolution as Cu^{2+}. Their results suggest that it should not be possible to carry out CO adlayer oxidation on this structure, as the *CO oxidation would instead take place on a clean Pt(111) surface. To clarify this issue, we carried out CO displacement and adlayer oxidation experiments on the Cu/Pt(111) overlayer. In particular, we aimed to answer the following questions (a) does the adsorption of CO result in the displacement of *Cu or the displacement of O* or OH*? (b) do the observed phenomena observed show any potential dependence? (c) if the *Cu is stable, what is its activity for *CO oxidation?

The CO displacement experiments were conducted in accordance to the procedure described by Clavilier and co-workers. [21] Once the Cu monolayer was deposited, the potential was fixed at a given value while the current was recorded. CO was dosed to the cell trough a gas inlet situated 1 cm away from the meniscus, generating a current response.[21] (Figure S6) Once the measured current reached a stable value, the CO flux was stopped. Subsequently, the cell was purged with Ar for 30 minutes under potential control. Finally, the potential was swept to positive values to electrooxidize the adsorbed *CO.

For this study we selected four different potential (0V, 0.1V 0.22V and 0.32V) and repeated the measurements at least two times per selected potential. We observed that there is a strong dependence between the adsorption potential and the obtained charge. (Figure S7). The charge generated during CO adsorption is due to the displacement of charged species in the interphase. For the Cu/Pt(111) overlayer, we expect these displaced species to be *O, *OH, *Cu, either separately or in combination.

In agreement with Ross and coworkers' results,[20] at sufficiently positive potentials, in this case 0.32V (RHE), CO adsorption results in a positive current, consistent with the displacement of a positively charged species, i.e. the dissolution of *Cu. The observed charge of 140μC/cm^2 is smaller than 480μC/cm^2 expected for the oxidation of a full Cu monolayer, since the displacement of copper is accompanied by *OH and *O displacement that produce a negative charge. Furthermore, the cyclic voltammogram for CO electrooxidation, after holding the potential at 0.32V resembles CO electrooxidation on Pt(111). These results confirm that when the CO is adsorbed at 0.32 V, the *Cu is displaced from the surface.

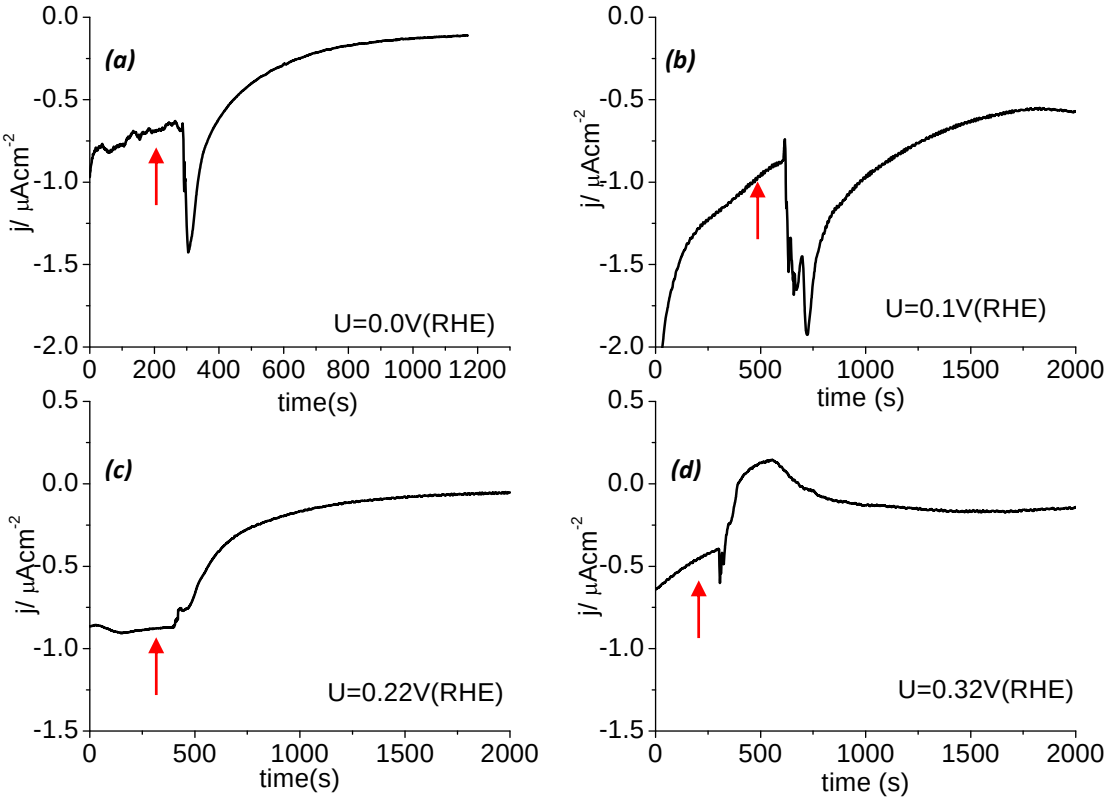

Figure S6: Measured current during the CO adsorption at a fixed potential (*U*=0.0V (*a*), *U*=0.1V (*b*) *U*=0.22V (*c*) and *U*=0.32V (*d*)) The red arrow indicates the time at which CO was dosed into the cell.

On the contrary, when the potential is held at 0.1V and at 0 V (RHE) a negative charge is observed, suggesting the dissolution of a negatively charged species, such as *OH or *O. This confirms the output of the theoretical calculations, which suggested that *O or *OH desorb from the surface. The negative charge of 213µC/cm^2 observed at 0.1V would correspond to close to 1 monolayer of *OH or 1/2 a monolayer *O, while the coverage predicted by DFT are only 0.3 ML for *OH and nearly zero for *O (figure S2). This discrepancy suggests that the measured charge may not only be attributable to chemisorption but also to dipole rearrangements at the interphase.[22] It is also worth noticing that the charge obtained at 0V is considerable different from that obtained at 0.1V, this could be attributed to the adsorption of *H close to 0V. When the CO was adsorbed at 0.22 V, there is no measurable charge. This indicated that at this potential, CO adsorption results in desorption of both positive and negative species, resulting in a net displacement charge of zero.

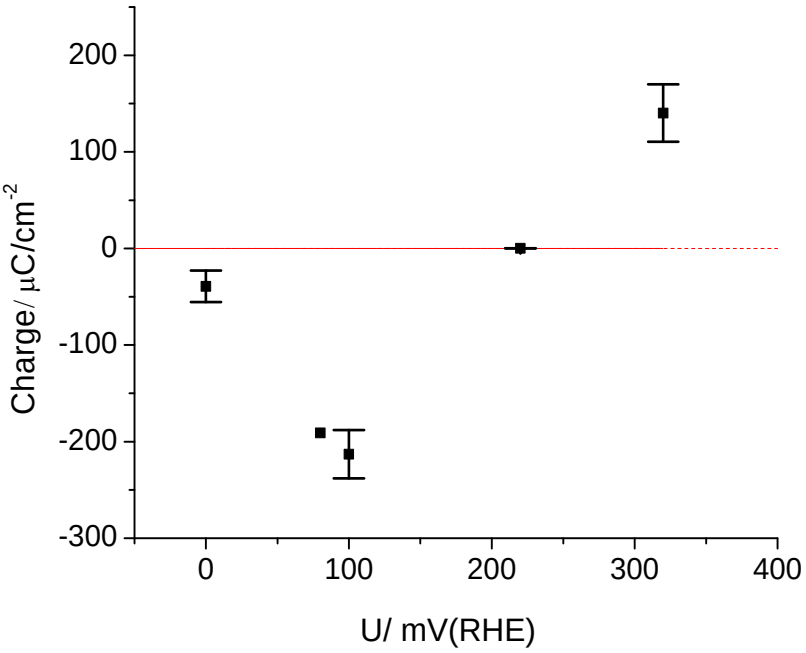

Figure S7: Charge generated during the CO displacement as a function of the adsorption potential.

In summary, the CO displacement experiments confirm that the Cu/Pt(111) overlayer is stable below 0.1 V. At more positive potentials, *Cu is displaced by *CO. This instability of *Cu makes it challenging to obtain reproducible results for the electrochemical oxidation of *CO on the Cu/Pt(111) overlayer. Figure S8 shows the *CO stripping voltammogram on Cu/Pt(111) overlayer after adsorbing CO at a 0.1V (RHE). We interpret the peak at 0.6 V to be *CO oxidation. Consistent with the predictions from theory (see Figure S5), it seems to occur at lower overpotentials that for the other surfaces. We attribute the peak starting at ~0.7 V to be *Cu dissolution. However, the peak is not as sharp as for Cu/Pt(111) overlayer in the absence of *CO, as shown in the inset in Figure S5a. This suggests that some structural changes have occurred to the overlayer during the course of *CO adsorption and oxidation. It is also conceivable that there could be some residual *CO at the surface above ~0.7 V, and that its oxidation would be concomitant with that of Cu in this potential range.

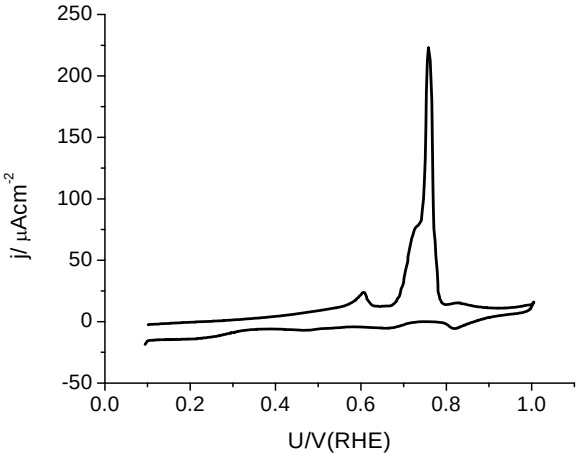

Figure S8: Anodic stripping voltammograms for CO electro-oxidation on Cu/Pt(111) monolayer at 20mV/s

REFERENCES

[1] S. R. Bahn, K. W. Jacobsen, *Comput. Sci. Eng.* **2002**, *4*, 56-66.

[2] I. E. L. Stephens, A. S. Bondarenko, F. J. Pérez-Alonso, F. Calle-Vallejo, L. Bech, T. P. Johansson, A. K. Jepsen, R. Frydendal, B. P. Knudsen, J. Rossmeisl, I. Chorkendorff, *J. Am. Chem. Soc.* **2011**, *133*, 5485-5491.

[3] K. J. Andersson, F. Calle-Vallejo, J. Rossmeisl, I. Chorkendorff, *J. Am. Chem. Soc.* **2009**, *131*, 2404-2407.

[4] aA. A. Peterson, F. Abild-Pedersen, F. Studt, J. Rossmeisl, J. K. Nørskov, *Energy Environ. Sci.* **2010**, *3*, 1311-1315; bP. Ferrin, A. U. Nilekar, J. Greeley, M. Mavrikakis, J. Rossmeisl, *Surf. Sci.* **2008**, *602*, 3424-3431.

[5] D. S. Strmcnik, D. V. Tripkovic, D. van der Vliet, K. C. Chang, V. Komanicky, H. You, G. Karapetrov, J. Greeley, V. R. Stamenkovic, N. M. Markovic, *J. Am. Chem. Soc.* **2008**, *130*, 15332-15339.

[6] aA. Lopez-Cudero, A. Cuesta, C. Gutierrez, *J. Electroanal. Chem.* **2005**, *579*, 1-12; bS. C. S. Lai, N. P. Lebedeva, T. H. M. Housmans, M. T. M. Koper, *Top. Catal.* **2007**, *46*, 320-333; cH. S. Wang, Z. Jusys, R. J. Behm, H. D. Abruna, *J. Phys. Chem. C* **2012**, *116*, 11040-11053.

[7] J. K. Nørskov, J. Rossmeisl, A. Logadottir, L. Lindqvist, J. R. Kitchin, T. Bligaard, H. Jonsson, *Journal of Physical Chemistry B* **2004**, *108*, 17886-17892.

[8] E. Skulason, V. Tripkovic, M. E. Bjorketun, S. Gudmundsdottir, G. Karlberg, J. Rossmeisl, T. Bligaard, H. Jonsson, J. K. Nørskov, *J. Phys. Chem. C* **2010**, *114*, 18182-18197.

[9] B. Hammer, L. B. Hansen, J. K. Norskov, *Physical Review B* **1999**, *59*, 7413-7421.

[10] aJ. Greeley, M. Mavrikakis, *Catal. Today* **2006**, *111*, 52-58; bM. P. Humbert, J. G. G. Chen, *J. Catal.* **2008**, *257*, 297-306.

[11] J. Knudsen, A. U. Nilekar, R. T. Vang, J. Schnadt, E. L. Kunkes, J. A. Dumesic, M. Mavrikakis, F. Besenbacher, *J. Am. Chem. Soc.* **2007**, *129*, 6485-6490.

[12] J. Greeley, J. K. Nørskov, *Electrochimica Acta* **2007**, *52*, 5829-5836.

[13] M. Pourbaix, *Atlas of Electrochemical Equilibria in Aqueous Solutions*, Second ed., National Association of Corrosion Engineers, Houston, Texas, **1974**.

[14] E. Herrero, L. J. Buller, H. D. Abruna, *Chem. Rev.* **2001**, *101*, 1897-1930.

[15] A. S. Bondarenko, I. E. L. Stephens, I. Chorkendorff, *Electrochemistry Communications* **2012**, *in press DOI: 10.1016/j.elecom.2012.06.030*.

[16] J. Greeley, *Electrochimica Acta* **2010**, *55*, 5545-5550.

[17] R. Jinnouchi, E. Toyoda, T. Hatanaka, Y. Morimoto, *J. Phys. Chem. C* **2010**, *114*, 17557-17568.

[18] P. Strasser, S. Koh, J. Greeley, *Physical Chemistry Chemical Physics* **2008**, *10*, 3670-3683.

[19] J. Clavilier, A. Rodes, K. Elachi, M. A. Zamakhchari, *Journal De Chimie Physique Et De Physico-Chimie Biologique* **1991**, *88*, 1291-1337.

[20] aC. A. Lucas, N. M. Markovic, B. N. Grgur, P. N. Ross, *Surf. Sci.* **2000**, *448*, 65-76; bC. A. Lucas, N. M. Markovic, P. N. Ross, *Surf. Sci.* **2000**, *448*, 77-86.

[21] J. Clavilier, R. Albalat, R. Gomez, J. M. Orts, J. M. Feliu, A. Aldaz, *J. Electroanal. Chem.* **1992**, *330*, 489-497.

[22] R. Guidelli, W. Schmickler, in *Modern Aspects of Electrochemistry, Vol. 38* (Ed.: B. E. Conway), Kluwer Academic-Plenum Publishers, New York, **2005**, pp. 303-371.

Paper II

THE JOURNAL OF PHYSICAL CHEMISTRY C

Article

pubs.acs.org/JPCC

Electrochemical CO_2 and CO Reduction on Metal-Functionalized Porphyrin-like Graphene

Vladimir Tripkovic, Marco Vanin, Mohammedreza Karamad, Mårten E. Björketun, Karsten W. Jacobsen, Kristian S. Thygesen, and Jan Rossmeisl*

Center for Atomic-scale Materials Design, Department of Physics, Technical University of Denmark, DK-2800 Kongens Lyngby, Denmark

Supporting Information

ABSTRACT: Porphyrin-like metal-functionalized graphene structures have been investigated as possible catalysts for CO_2 and CO reduction to methane or methanol. The late transition metals (Cu, Ag, Au, Ni, Pd, Pt, Co, Rh, Ir, Fe, Ru, Os) and some p (B, Al, Ga) and s (Mg) metals comprised the center of the porphyrin ring. A clear difference in catalytic properties compared to extended metal surfaces was observed owing to a different electronic nature of the active site. The preference to bind hydrogen, however, becomes a major obstacle in the reaction path. A possible solution to this problem is to reduce CO instead of CO_2. Volcano plots were constructed on the basis of scaling relations of reaction intermediates, and from these plots the reaction steps with the highest overpotentials were deduced. The Rh−porphyrin-like functionalized graphene was identified as the most active catalyst for producing methanol from CO, featuring an overpotential of 0.22 V. Additionally, we have also examined the hydrogen evolution and oxidation reaction, and in their case, too, Rh−porphyrin turned out to be the best catalyst with an overpotential of 0.15 V.

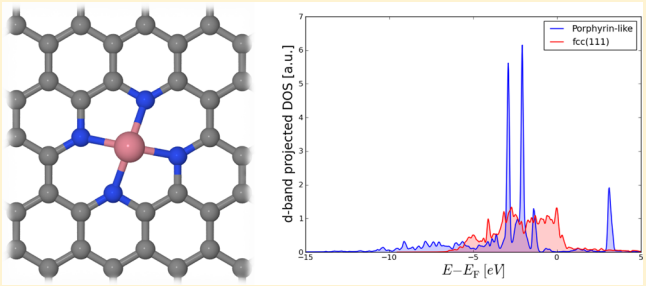

I. INTRODUCTION

The intermittency of renewable energy sources calls for a practical energy storage solution.[1,2] This can be accomplished by finding an efficient way to store energy in the form of chemical fuels, which would be particularly appealing if combined with CO_2 capture. For that reason, the electrochemical reduction of CO_2 to chemical fuels has spurred huge interest in recent years.[1−20] Copper is the only metal that has been experimentally shown to produce significant quantities of hydrocarbons, mostly CH_4 and C_2H_4, albeit at a huge voltage cost and with a low faradaic efficiency due to the competing hydrogen evolution reaction.[3−5,7,21,22] Furthermore, none of the metals was able to produce methanol. The origin of the overpotential remained elusive until recently, when a complete reaction mechanism was mapped out by employing density functional theory (DFT) calculations in conjunction with the computational hydrogen electrode method.[18,19,23]

The lack of efficient metallic catalysts for the electrochemical reduction of CO_2 necessitates scrutiny of other types of materials. We have studied a new class of materials consisting of a metal atom coordinated to a porphyrin ring embedded in graphene (cf. Figure 1a). The term "porphyrin-like" has been used in order to emphasize that our structure differs from the usual porphyrin structure: the central metal atom is coordinated to four nitrogen atoms and with neighboring carbon atoms forms five- and six-atom-long rings. This particular 4-fold coordination was chosen because it was found to be the most stable binding configuration for metal and nitrogen atoms in graphene.[24−26]

Recent advances in experiments have made it possible to synthesize nanostructured graphene. Graphene sheets can be readily doped and modified for catalytic and energy conversion purposes.[27−29] The porphyrin type of functionalization has already been realized experimentally on carbon nanotubes and other graphitic materials. Some of these systems have been shown to possess high catalytic activities for oxygen reduction and methanol oxidation reaction.[24,25,30−33]

The choice of catalysts was inspired by two facts: first, some porphyrin-based catalysts are known to be active for electrochemical reduction of CO_2;[34−37] second, the versatility and relatively low cost of graphene render the studied system a very good catalyst candidate.

The sine qua non condition to make CO_2/CO reduction cost efficient is to find a suitable catalyst. A good catalyst should fulfill three criteria: (1) it should be active in reducing CO_2/CO, i.e. have a low reduction overpotential, (2) it should have a high faradaic efficiency toward CH_4/CH_3OH, and (3) it should be stable, i.e., not poisoned by adsorbed H or OH. The aim of this work is to investigate if any of the studied systems fulfills these three basic conditions.

Received: June 22, 2012
Revised: April 10, 2013
Published: April 10, 2013

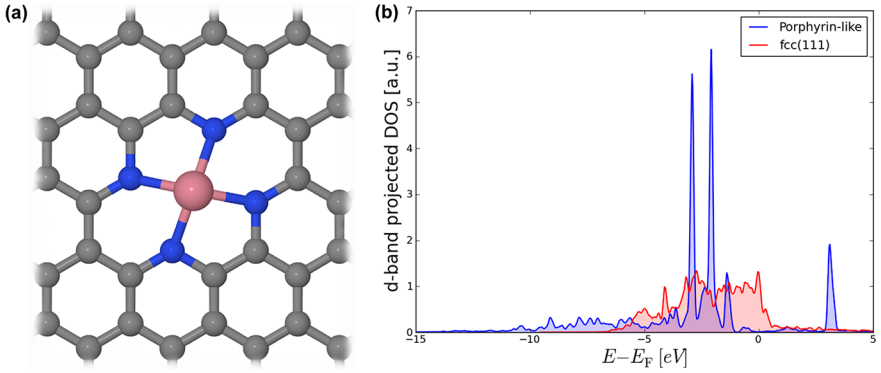

Figure 1. (a) Atomic structure of porphyrin-like functionalized graphene. The central metal atom is coordinated to four nitrogen atoms, forming the porphyrin ring that is embedded in a graphene matrix. (b) Comparison of density of states projected onto the d orbitals of the Pt atom located at the center of the porphyrin ring and the Pt surface atom in Pt(111) surface.

Electronically, a single, isolated, active site is in stark contrast to traditional metal-based catalysts where often many active sites are available for intermediates to bind. This difference is visualized in Figure 1b, in which the total density of states (DOS) is projected onto the d orbitals of Pt in the porphyrin-like graphene and the d orbitals of Pt in the Pt(111) surface, respectively. As can be seen, the graphene system exhibits more atomic-like, sharp peaks compared to the broad d-band features of the extended metal surface. The huge disparity in the DOS could have a significant impact on the catalytic activity. Distinct features offered by an individual active site can be seen as a bridge between a metal-based catalyst and a molecular catalyst, and it can open up an ample spectrum of possibilities in terms of engineering and controlling the active site.

II. COMPUTATIONAL METHODS

The electronic structure calculations were carried out with use of DFT based on the projector augmented wave method and the revised Perdew–Burke–Ernzerhof (RPBE)[38] functional. The calculations were performed spin polarized with the use of the real space GPAW software package[39,40] integrated with the Atomic Simulation Environment (ASE).[41] The functionalized porphyrin-like structures were modeled in a 4 × 4 graphene unit cell using periodic boundary conditions and sufficient vacuum in the direction perpendicular to the graphene plane (at least 12 Å). A grid spacing of 0.18 Å and a (8 × 8 × 1) *k*-point sampling grid were employed. All the structures were relaxed until the force on each atom was lower than 0.01 eV/Å. We have used the computational hydrogen electrode (CHE) method to calculate the free energy levels of all the intermediate states and to construct the potential energy diagrams.

The rationale behind the CHE method is to calculate electrochemical reactions as if they were chemical using the definition of the standard hydrogen electrode (SHE, $H^+ + e^- = \frac{1}{2}H_2$), and then afterward to correct for conditions other than standard. In this manner, the cumbersome problem of calculating charges and ions in solution is neatly replaced by a much simpler problem of computing hydrogen in the gas phase. Conceptually, the CHE method can only deal with concerted electron–proton transfer. The systems are computed at $U = 0$, and afterward, all the states are tuned to a desired voltage by changing the free energy by eU, where U is the electrode potential. Similarly, the pH effects are not directly taken into account (values are given on the reversible hydrogen electrode (RHE) scale), but they can be accounted for a posteriori by changing the chemical potential of protons. Applying the CHE method assumes an aqueous environment as, by definition of the SHE, protons are solvated in water and not in some other medium. To include solvation effects, we use a simple thermodynamic correction of 0.3 eV[55] for all species that contain an OH group (OH, COOH, COH, CHOH, CH_2OH). We have not probed the influence of the electric field on the binding energies because previous studies have shown that it has a very limited effect on the overall results.[56−58] For more details about this approach we refer to ref 23, in which the method was initially outlined. Also, we would like to emphasize that this is a purely thermodynamic study: charge transfer kinetics have not been taken into account. However, according to previous studies on metals,[59] the kinetics should not play a significant role. Additionally, knowing how water adheres on the surface is a prerequisite for studying kinetics, but this has yet to be ascertained.

Discussion about the Method. In this section we present arguments why we deem our method suitable for studying these systems.

Porphyrin molecules are well-known to the organometallic community, and they have been the main targets for photocatalytic application for decades. However, the methods they used are inherently different from the one employed here because they all reside in the fact that electron–proton transfer is treated independently. For molecular catalysts solvated in water or some other medium, the only way to activate the metal center toward CO_2/CO reduction is to lower the potential in order to allow the electrons from the neighboring ligand groups to occupy the lowest unoccupied molecular orbital (LUMO) state of the molecule. Since, usually their LUMO state lies far from the Fermi level, the overvoltage requirement is significant, and the electron transfer becomes a major obstacle.[42−44] Therefore, the electron transfer is considered independently from the proton transfer, which is seen to be a more facile step. The metal atom in the porphyrin ring can undergo only discrete changes from one valence state to another, which is usually handled by calculating the redox potentials. In contrast, our systems should be considered as a whole, in which porphyrin motifs are part of a larger graphene electrode. There is no need to look at decoupled proton–electron transfer as there are always available graphene or/and metal states just above the Fermi level (see Supporting Information, Figure 4) that can be readily occupied at negative potentials. In other words, while the charge in molecular catalysts is centered on the porphyrin ring, in our systems it is spread out all over the

dx.doi.org/10.1021/jp306172k | J. Phys. Chem. C 2013, 117, 9187−9195

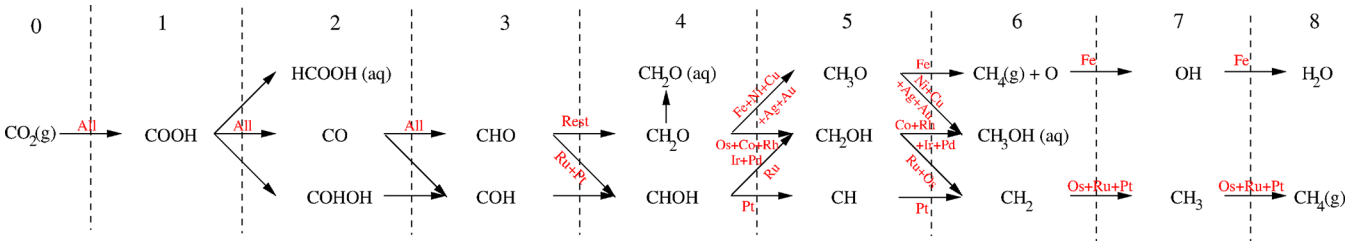

Figure 2. Reaction paths for electrochemical CO_2 reduction on a range of d metals. "All" and "Rest" labels stand for all and remaining metals.

graphene−porphyrin electrode. By changing the potential, one would change not the oxidation state of the atom, but rather the surface dipole of the electrode. The surface dipole would change continuously in the same way as the chemical potential—the variable it depends on. Consequently, the binding energies would also change linearly with potential. Since there are no experimental results for CO_2/CO reduction to support this claim, we will refer to another reaction, that is, the oxygen reduction reaction extensively studied on the same/similar type of catalysts.[45,46] The continuous current−potential curves without any abrupt features in cyclic voltammograms give evidence that the graphene−porphyrin system behaves as one electrode.

We have chosen the RPBE functional because it gives good oxidation states for metal atoms in the porphyrin ring, assuming square-planar geometry and corresponding splitting of the d states.[47,55] However, this functional is also known to favor low spin states for transition metals with partially filled 3d orbitals.[48−51] To get the right spin state, one would need to employ a hybrid GGA functional; however, this is out of the scope of this paper. We believe that the chosen functional is sufficiently accurate for the purpose of this study, which is to report activity trends, although we do not exclude the possibility that some of the 3d metals might shift on the volcano plots. Furthermore, all the calculations are performed spin polarized, assuming the porphyrin motifs to be ferromagnetic. This might not always be true: a recent study has shown that two adjacent porphyrin motifs can have opposite spins;[26] i.e., the overall system can become antiferromagnetic. Nevertheless, the energy differences were too minute (on the order of millielectronvolts) to add any significant error bar to our calculations. The binding energies will also be affected by the choice of the exchange-correlation functional;[52] however, as almost all the species have very similar electronic structures with the highest occupied molecular orbital (HOMO) state at nearly the same position (see the Supporting Information Figures 6 and 7 for more details), the binding energies will change proportionally, having little or no effect on the volcano plots.

Additionally, we would like to emphasize that we used a correction for the DFT-RPBE value of CO_2(g) in GPAW. It has previously been established that the RPBE functional does not yield good reaction energies for reactions that contain CO_2(g) or gas phase molecules with a CO_2 group.[18] Analyzing the same set of gas phase reactions as in ref 18, we arrived at a CO_2/CO correction of 0.43/0.04 eV (see the Supporting Information for detailed information). Subsequently, all the CO_2(g) energies were corrected by this amount, while the CO(g) correction was neglected.

Finally, we have just looked at thermodynamic barriers; for calculating charge transfer barriers one needs to explicitly include water in the system.[53,54]

III. RESULTS AND DISCUSSION

The electrochemical CO_2 reduction reaction (CRR) is a many proton−electron transfer step process that entails a lot of different reaction intermediates with several possible reaction outcomes. The final product depends on the number of reduction steps, which is in general determined by the strength of the CO binding.[2] The most common reactions and their equilibrium potentials vs RHE are listed below.

$$CO_2 + 2H^+ + 2e^- \rightarrow HCOOH(aq) \qquad (U = -0.20\ V)$$

$$CO_2 + 2H^+ + 2e^- \rightarrow CO + H_2O \qquad (U = -0.12\ V)$$

$$CO_2 + 4H^+ + 4e^- \rightarrow CH_2O(aq) \qquad (U = -0.07\ V)$$

$$CO_2 + 6H^+ + 6e^- \rightarrow CH_3OH(aq) \qquad (U = 0.03\ V)$$

$$CO_2 + 8H^+ + 8e^- \rightarrow CH_4 \qquad (U = 0.17\ V)$$

The two most valuable products are methanol and methane; however, as mentioned in the Introduction, only Cu is able to reduce CO/CO_2 to hydrocarbons, whereas none of the metals was seen to produce methanol in significant amounts. We have systematically analyzed, based on DFT simulations, all possible reaction pathways (cf. Figure 2) for CRR on a range of different metals in the porphyrin ring (Cu, Ag, Au, Ni, Pd, Pt, Co, Rh, Ir, Fe, Ru, Os, B, Al, Ga, and Mg).

The number of possible intermediates and reactions is reduced compared to metal surfaces as the single active site can only bind one intermediate at a time. Accordingly, methane and methanol are the only hydrocarbon and alcohol that can be produced. Making larger hydrocarbon chains would require a Langmuir−Hinshelwood reaction in which two adsorbed species join together to form a C−C bond.

Selectivity Criteria. As already discussed, in this class of materials catalytic sites are isolated from each other. Their distribution is uniform owing to the imposed periodic boundary conditions. The existence of only one active site simplifies the theoretical analysis because no coverage effects need to be taken into account. On the other hand, the competition for the active site, i.e., selectivity, enters as a key parameter that determines the overall performance of the catalyst. Similarly, if some of the intermediates that are not directly involved in CRR path would bind stronger to the surface, they would poison the active site and thus terminate the reaction. All potential reaction pathways, except for the hydrogen evolution reaction (HER), proceed through the COOH* intermediate, and therefore the competition between H* and COOH* binding will determine the outcome of the reaction. Moreover, as both the H* and the COOH* formation steps involve transfer of one proton−electron pair, the difference between the H* and COOH* binding energies is not affected by the change in voltage.

dx.doi.org/10.1021/jp306172k | J. Phys. Chem. C 2013, 117, 9187−9195

To further investigate the impact of HER, the binding energies of the first intermediates in HER and CRR, H* and COOH*, were plotted against each other in Figure 3a. Ideally, the points should fall in the lower part of the graph, in which the H* blockage would not impede CRR ($G_{COOH^*} < G_{H^*}$). However, from the figure it is clear that CRR would be completely suppressed by hydrogen adsorption in almost all the systems.

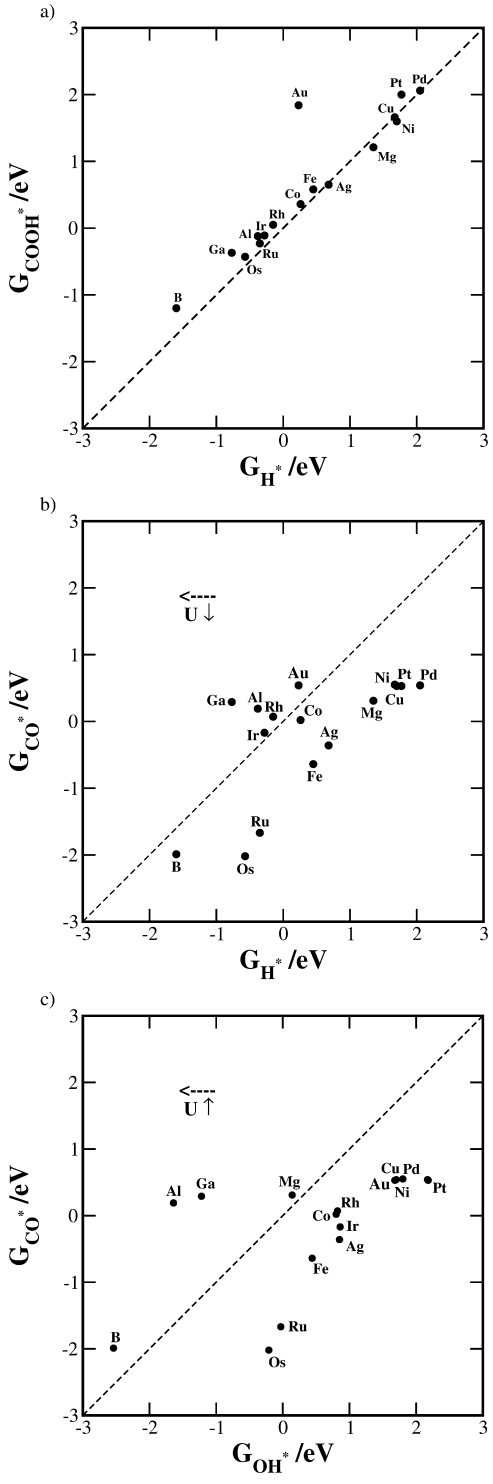

Figure 3. Selectivity criteria defining preference toward HER or CRR. The COOH* and CO* binding energies are calculated with respect to $H_2O(l)$, $H_2(g)$, and the energy of the C-containing molecule they originate from, that is, $CO_2(g)$ for COOH* and CO(g) for CO*, respectively. The horizontal arrows show how the binding energies of H* and OH* species change with respect to a change in potential (vertical arrows).

The reaction diagram in Figure 2 suggests a way to overcome the hydrogen poisoning problem. If one would reduce CO instead of CO_2, then the weak COOH* binding might no longer present a hindrance. Moreover, CO can be used as a viable alternative to CO_2 because it is a product of many industrial processes such as gasification of biomass, cracking of hydrocarbons, or metal oxide reduction. Alternatively, CO could be produced from CO_2 by a process opposite to the water gas shift reaction or, perhaps, even electrochemically using some other catalyst to reduce CO_2 to CO. The CO reduction follows the same path as the CO_2 reduction apart from the first two steps that are missing. CO* is expected to bind stronger than COOH* and, thus, to better compete with H*. It is clear from Figure 3b that the CO* binding is stronger on most of the metal atoms at $U = 0$ V vs RHE. The CO* binding is potential independent, while the free energy of the $H^+ + e^- \rightarrow H^*$ reaction changes as a function of the applied voltage. When the potential is reduced, the points will shift accordingly to the left in Figure 3b. For the points that lie close to the diagonal, at negative potentials the selectivity will change toward HER. A way to work around this problem could be to cycle the cell potential. To better explain this approach, let us take an example, for instance Rh−porphyrin. The Rh point is located slightly on the left side of the diagonal, meaning that at a very small positive potential the selectivity will turn toward the CO reduction products. However, as CO cannot be reduced at positive potentials, the voltage needs to be lowered to enable CO reduction. Hence, the CO reduction could be accomplished by periodically cycling the potentials in the cell between the potentials at which CO adsorbs and the potentials at which it reduces.

Brief excursions to positive potentials can bring another problem: water oxidation and subsequent OH* poisoning of the active site. To elucidate this possibility, we have plotted the CO* vs OH* binding energies for all the metals in Figure 3c. When the potential is increased above $U = 0$ V, the OH* binding shifts to the left; i.e., the OH* species become more stable on the surface. According to Figure 3c, the OH* poisoning presents a problem only for Ga, B, Mg, and Al as all the other metals lie at a safe distance from the diagonal.

In the following discussion we will restrict our analysis to the transition metals, although we show results for all the metals used in this study.

Scaling Relations and Volcano Plots. For a multielectron transfer reaction, it is usually difficult to find a good catalyst that can perform the overall reaction at a small voltage cost. This is best illustrated by comparing electrochemical reactions that involve different numbers of proton−electron transfer steps. Complete reductions of hydrogen, oxygen, and CO_2 proceed through two, four, and eight charge transfer steps; at the same time their smallest predicted overpotentials change from 0, to 0.4, to 0.9 V.[18,23,59,60] The large differences in overpotentials can be understood in terms of the intermediates' binding energies, which are commonly found to scale linearly against each other.[61] The scaling relations are not only limited to metallic surfaces, but as was recently shown also hold on graphene, at least for oxygen reduction intermediates.[47,55] The linearity in binding energies on transition metals is usually rationalized through the d-band model and the position of the

dx.doi.org/10.1021/jp306172k | J. Phys. Chem. C 2013, 117, 9187−9195

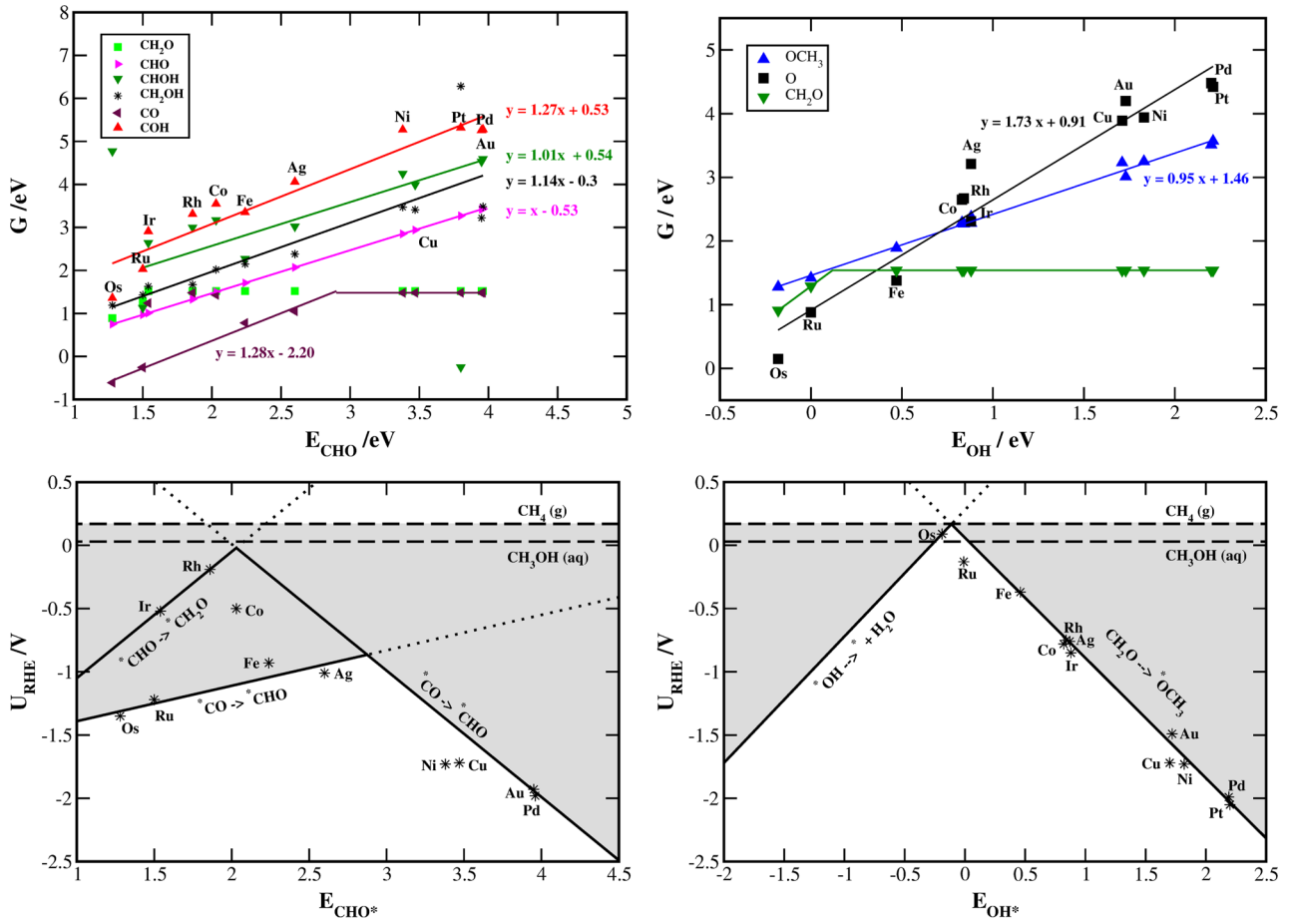

Figure 4. Scaling relations and volcano plots indicating potential determining steps for CO electroreduction. The gray areas designate the overpotentials for this class of catalysts. They stretch from the equilibrium potentials for methanol and methane production, 0.03 and 0.17 V, respectively, to the minimum potential required to drive the reaction at different CHO* and OH* values (solid black lines). The overpotential for CO reduction is the bigger value in the two volcano plots.

d-band center.[62] It is impossible to change the binding energy of one intermediate without simultaneously affecting the binding of others in a proportional manner. Tuning an eight electron transfer reaction such as CRR is therefore a cumbersome task.

Reduction of CO results in three possible products: formaldehyde, methanol, and methane. Most of the metal-functionalized porphyrin-like catalysts produce formaldehyde, CH_2O. As CH_2O is just an intermediate product in the full reduction path, it could be easily further reduced to methanol or methane.

In Figure 4 all the intermediates appearing in the main reaction path are plotted versus either CHO* or OH* binding energies, depending on whether the species bind through carbon or oxygen atoms. It is important to stress, here, why we have chosen to scale the intermediates' binding energies against CHO* and not against CO*, which is commonly used as a descriptor in reactions containing C_xO_y species. The problem with CO* is that it does not bind on all the metals, and consequently, those metals will not show up in the scaling relations. This is not the case on extended metal surfaces because most of the metals bind CO. CHO* is the most obvious choice, not just because it binds on all the metals, but also because all reaction paths lead through this intermediate.

The scaling relation for CH_2O* is a broken line, since on most metals CH_2O* desorbs from the surface (exceptions are Ru and Os). A few metals that substantially deviate from other points were not included in the fits (e.g., Pt in CHOH and CH_2OH scalings). Another important observation is that the slopes of the lines in the CHO* scaling plot fall close to 1.00 (1.01−1.27). This result is different from what could be expected if the bond counting rule established on metal surfaces is applied.[61] According to this simple rule, the expected slopes for the CH_2OH*, CHOH*, and COH* scalings against the CHO* should be 1, 2, and 3 because they should in principle form one, two, and three bonds to the metal atom, whereas CHO* should bind through a single bond. The reason why the slopes defy the bond counting rule is because the species can just bind to a single atom. The intermediates cannot satisfy their unpaired electrons as there are no metal aggregates available on the surface. This interpretation is corroborated by the DOS analysis reported in the Supporting Information. The only exception is the oxygen intermediate, most likely because oxygen has the highest electronegativity, so it can drain more charge from the metal atom.

By using linear relationships, we have constructed volcano plots, shown as well in Figure 4. All energies were corrected by free energy corrections calculated on the Cu(211) surface.[18] Although the geometries of the intermediates might vary between those on Cu(211) and metal-functionalized porphyrin-like graphene, the zero point energies and entropies will not be appreciably affected. For more details on the construction of

dx.doi.org/10.1021/jp306172k | J. Phys. Chem. C 2013, 117, 9187−9195

volcano plots, we refer to ref 63. In most systems the potential determining step (PDS) is found in the CHO volcano. Notice also that the CO* reduction to CHO* gives rise to both the left and right leg of the volcano. The difference between the CO (brown) and CHO (magenta) trend lines in the CHO scaling plot is in fact what yields the CHO volcano. The CHO volcano describes well the overpotentials for all the points except for Rh, Ir, and Co. These metals deviate substantially from the linear trend because either they do not bind CO (Co, Rh) or they bind it very weekly (Ir). Consequently, these metals exhibit different PDS: for Rh and Ir it is the CHO* reduction to CH_2O, whereas for Co it is the CH_2O reduction to CH_2OH*. Owing to relatively large deviations Rh, Ir, and Co seem to be very good catalysts for CO reduction. This result corroborates, once again, the claim that one of the ways to beat large overpotentials is to have points that do not obey general trends.

The early transition metals were not included in the study because shifting to stronger binding energies would only increase the overpotential in the CHO volcano.

Whether the final product of the reaction is methane or methanol depends on the central metal atom in the porphyrin ring. Table 1 shows what the most stable product on different metals is, the potential at which the reduction takes place, and PDS. As seen, two-thirds of the metals produce methanol and one-third produce methane. PDS are either the CO/CHO reduction to CHO/CH_2O in the CHO volcano or the CH_2O reduction to CH_3O in the OH volcano. The exceptions are the p-metals B, Al, and Ga, presumably because they follow different trends.

Table 1. Calculated Potentials for the CO_2 Reduction Reaction, Main Reaction Product, and PDS[a]

metal	path	potential (V)	PDS
Cu	CH_3OH	−1.72	$CH_2O(aq) \rightarrow CH_3O$
Ag	CH_3OH	−1.01	$CHO^* \rightarrow CH_2O(aq)$
Au	CH_3OH	−1.94	$CO^* \rightarrow CHO^*$
Ni	CH_3OH	−1.73	$CH_2O(aq) \rightarrow CH_3O$
Pd	CH_3OH	−1.99	$CH_2O(aq) \rightarrow CH_3O^*$
Pt	CH_4	−6.32	$CHOH^* \rightarrow CH^*$
Co	CH_3OH	−0.20	$CH_2O(aq) \rightarrow CH_2OH^*$
Rh	CH_3OH	−0.19	$CHO^* \rightarrow CH_2O(aq)$
Ir	CH_3OH	−0.52	$CHO^* \rightarrow CH_2O(aq)$
Fe	CH_4	−0.93	$CO^* \rightarrow CHO^*$
Ru	CH_4	−1.22	$CO^* \rightarrow CHO^*$
Os	CH_4	−1.35	$CO^* \rightarrow CHO^*$
Mg	CH_3OH	−1.29	$CO^* \rightarrow CHO^*$
Al	CH_4	−1.17	$CH_3O^* \rightarrow O^*$
Ga	CH_4	−0.94	$CH_3O^* \rightarrow O^*$

[a]The overpotential for methanol or methane formation is obtained by adding the reactions' equilibrium potentials to the absolute potentials in the table.

The best catalyst for the reaction is the system with the lowest max(U_{RHE}(CO), U_{RHE}(OH)). In our case this is Rh, which exhibits only 0.19 + 0.03 = 0.22 V overpotential (0.19 V is the potential at which CO reduces and 0.03 V is the equilibrium potential for the CO reduction to methanol). As a comparison, on the most active metal surface, Pt(111), the requirement for CO reduction to methanol is 0.46 V,[64] and on the most active step surface, Cu(211), it is 0.77 V.[18] Figure 5 shows the free energy diagram for the CO reduction on Rh together with snapshots of the most stable structures in each electrochemical step.

Hydrogen Oxidation/Evolution Reaction. So far we have considered HER only in terms of hydrogen poisoning and its implications on the CRR; however, HER is an important reaction in itself. This reaction, for instance, takes place at the cathode of a water electrolyzer—a device that is able to convert solar into chemical energy by splitting water into its constituents.[1] The opposite reaction to HER, the hydrogen oxidation reaction (HOR), is perhaps even more important because it is a major reaction in fuel cells. Pt is the state-of-the-art catalyst for HER/HOR. Although Pt loading on the anode is 4 times less than it is on the cathode,[65] its amount still contributes significantly to the current noncompetitive prices of proton exchange membrane fuel cells. The overpotential requirements for HER and HOR are identical because they involve only one electrochemical step (intermediate), and hence, the potential energy profile is symmetrical. In other words, the same catalyst could, in principle, be used for both reactions. In this last section we will discuss if some of the catalysts reported in this study could be potentially used as viable replacements for platinum for HER/HOR.

A good HER/HOR catalyst should have G(H*) as close as possible to 0 eV. Looking at Table 2, there are quite a few candidates with promising H* binding energies (Rh, Ir, Au, and Co). The Rh-functionalized porphyrin-like graphene appears to be the best candidate with a G(H*) binding of 0.15 eV. It is important to note that since a single metal atom cannot simultaneously bind two hydrogen atoms, the hydrogen evolution reaction would be forced through the Heyrovsky step. The Heyrovsky step has a 2 times higher barrier than the Tafel step, assuming that the same water bilayer structure would form at the graphene/water interface as on metal surfaces.[59] Kinetic limitations might therefore make these catalysts less active than the metals with similar thermodynamic barriers. HER would proceed unhindred at the potentials relevant for CRR as the charge transfer barriers would become smaller.[59] Finally, it is important to stress that Rh, Co, and Ir seem to be the best porphyrin catalysts for a range of electrochemical reactions, not just for the ones investigated in this work, but also, for instance, for the oxygen reduction reaction.[55]

IV. CONCLUSIONS

In summary, we have assessed the catalytic activity of the metal-functionalized porphyrin-like structures toward the electrochemical reduction of CO_2 and CO. This study was prompted by recent findings on Cu(211).[18] The major obstacle preventing efficient CO_2 reduction was hydrogen poisoning of the active site. This turned out to be a general setback regardless of the metal atom in the porphyrin ring. We suggest a way to circumvent this problem, namely, reducing CO rather than CO_2, as CO* competes better than COOH* with H* for the active sites. Moreover, on the basis of the linear relationships among the reaction intermediates, we have constructed volcano plots which helped us identify the best catalyst candidate: Rh-functionalized pophyrin-like graphene featuring an overpotential of 0.22 V for CO reduction to methanol. This is much lower than the overpotential on the extended metal surfaces; however, the potential needs to be cycled so that CO can be adsorbed in one potential range and reduced in another, making sure water does not dissociate when the potential is cycled positively. Finally, we have also

dx.doi.org/10.1021/jp306172k | J. Phys. Chem. C 2013, 117, 9187−9195

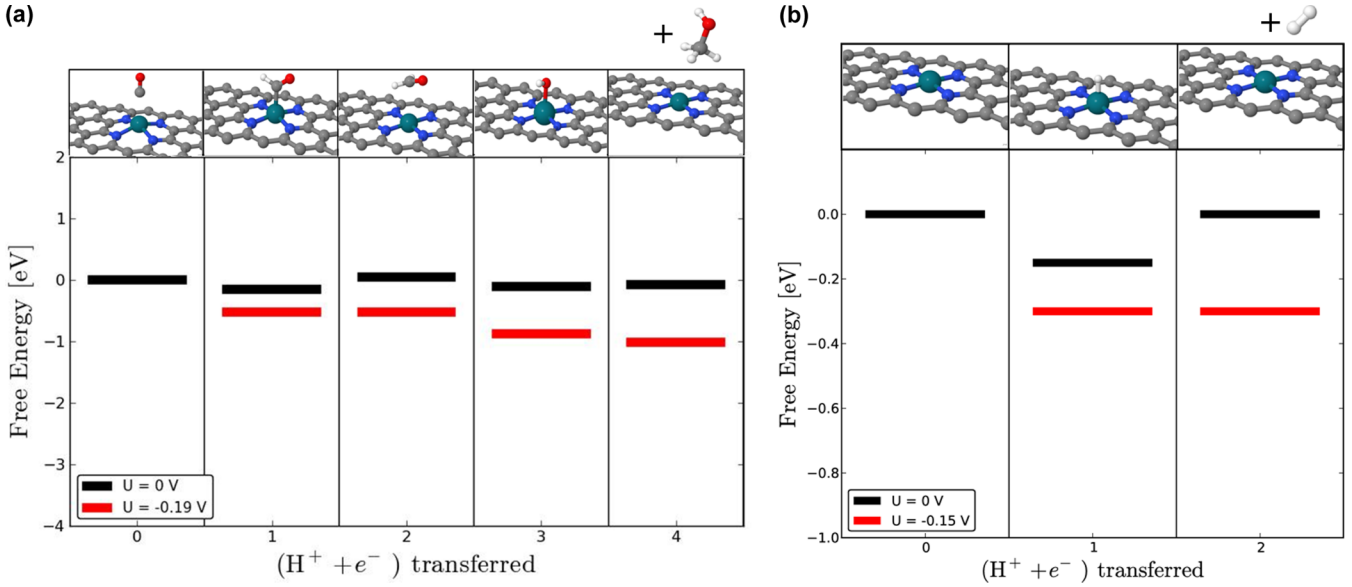

Figure 5. Free energy diagrams for (a) the CO_2 reduction reaction and (b) hydrogen evolution/oxidation reaction on Rh−porphyrin-like functionalized graphene, respectively. The black and red lines denote the free energy levels at 0 V and at the potentials at which all the reaction steps are downhill in free energy.

Table 2. Calculated Overpotentials for the Hydrogen Evolution/Oxidation Reaction

metal	overpotential (V)
Cu	−1.70
Ag	−0.68
Au	−0.23
Ni	−1.67
Pd	−2.05
Pt	−1.77
Co	−0.26
Rh	0.15
Ir	0.28
Fe	−0.45
Ru	0.35
Os	0.57
Mg	−1.35
B	1.60
Al	0.38
Ga	0.77

briefly examined the catalytic activity of the metal−porphyrins for HER/HOR. Even though there are a few candidates with promising overpotentials, it is still unclear whether these systems would, in reality, be that active due to severe kinetic limitations.

■ ASSOCIATED CONTENT

Supporting Information

Sensitivity analysis of CO_2 and CO corrections derived from a set of reactions containing CO and CO_2 molecules. Tables with the most stable spin states and free binding energies for different intermediates. DOS analysis. This material is available free of charge via the Internet at http://pubs.acs.org.

■ AUTHOR INFORMATION

Corresponding Author

*E-mail: jross@fysik.dtu.dk. Phone: (+45) 45-253-166. Fax: (+45) 45-932-399.

Notes

The authors declare no competing financial interest.

■ ACKNOWLEDGMENTS

The Catalysis for Sustainable Energy initiative is funded by the Danish Ministry of Science, Technology and Innovation. Support from the Danish Center for Scientific Computing, the Danish Council for Technology and Innovation's FTP program, and the Strategic Electrochemistry Research Center is gratefully acknowledged. We also acknowledge Juan Maria Garcia Lastra for fruitful discussions.

■ ABBREVIATIONS

DFT, density functional theory; DOS, density of states; CRR, CO_2 reduction reaction; HER, hydrogen evolution reaction; HOR, hydrogen oxidation reaction; PDS, potential determining step

■ REFERENCES

(1) Lewis, N. S.; Nocera, D. G. Powering the Planet: Chemical Challenges in Solar Energy Utilization. *Proc. Natl. Acad. Sci. U. S. A.* **2006**, *103*, 15729−15735.

(2) Gattrel, M.; Gupta, N.; Co, A. A Review of the Aqueous Electrochemical Reduction of CO_2 to Hydrocarbons at Copper. *J. Electroanal. Chem.* **2006**, *594*, 1−19.

(3) Hori, Y.; Kikuchi, K.; Murata, A.; Suzuki, S. Production of Methane and Ethylene in Electrochemical Reduction of Carbon-Dioxide at Copper Electrode in Aqueous Hydrogencarbonate Solution. *Chem. Lett.* **1986**, *15*, 897−898.

(4) Hori, Y.; Murata, A.; Takahashi, R.; Suzuki, S. Electroreduction of CO to CH_4 and C_2H_4 at a Copper Electrode in Aqueous Solutions at Ambient Temperature and Pressure. *J. Am. Chem. Soc.* **1987**, *109*, 5022−5023.

(5) Hori, Y.; Murata, A.; Takahashi, R. Formation of Hydrocarbons in the Electrochemical Reduction of Carbon-Dioxide at a Copper Electrode in Aqueous-Solution. *J. Chem. Soc., Faraday Trans.* **1989**, *85*, 2309−2326.

(6) Hori, Y.; Wakebe, H.; Tsukamoto, T.; Koga, O. Electrocatalytic Process of CO Selectivity in Electrochemical Reduction of CO_2 at

Metal-Electrodes in Aqueous-Media. *Electrochim. Acta* **1994**, *39*, 1833−1839.
(7) Hori, Y.; Takahashi, R.; Yoshinami, Y.; Murata, A. Electrochemical Reduction of CO at a Copper Electrode. *J. Phys. Chem. B* **1997**, *101*, 7075−7081.
(8) Hori, Y. *Modern Aspects of Electrochemistry*; Springer: New York, 2008; Vol. 42, Chapter 3, pp 89−189.
(9) Benson, E. E.; Kubiak, C. P.; Sathrum, A. J.; Smieja, J. M. Electrocatalytic and Homogeneous Approaches to Conversion of CO2 to Liquid Fuels. *Chem. Soc. Rev.* **2009**, *38*, 89−99.
(10) Roy, S. C; Varghese, O. K.; Paulose, M.; Grimes, C. A. Toward Solar Fuels: Photocatalytic Conversion of Carbon Dioxide to Hydrocarbons. *ACS Nano* **2010**, *4*, 1259−1278.
(11) Darensbourg, D. J. Chemistry of Carbon Dioxide Relevant to Its Utilization: A Personal Perspective. *Inorg. Chem.* **2010**, *49*, 10765−10780.
(12) Barton Cole, E.; Lakkaraju, P. S.; Rampulla, D. M.; Morris, A. J.; Abelev, E.; Bocarsly, A. B. Using a One-Electron Shuttle for the Multielectron Reduction of CO_2 to Methanol: Kinetic, Mechanistic, and Structural Insights. *J. Am. Chem. Soc.* **2010**, *132*, 11539−11551.
(13) Le, M.; Ren, M.; Zhang, Z.; Sprunger, P. T.; Kurtz, R. L.; Flake, J. C. Electrochemical Reduction of CO_2 to CH_3OH at Copper Oxide Surfaces. *J. Electrochem. Soc.* **2011**, *158*, E45−E49.
(14) Whipple, D. T.; Kenis, P. J. A. Prospects of CO_2 Utilization via Direct Heterogeneous Electrochemical Reduction. *J. Phys. Chem. Lett.* **2010**, *1*, 3451−3458.
(15) Schouten, K. J. P.; Kwon, Y.; van der Ham, C. J. M.; Qin, Z.; Koper, M. T. M. A New Mechanism for the Selectivity to C-1 and C-2 Species in the Electrochemical Reduction of Carbon Dioxide on Copper Electrodes. *Chem. Sci.* **2011**, *2*, 1902−1909.
(16) Schouten, K. J. P.; Qin, Z.; Gallent, E. P.; Koper, M. T. M. Two Pathways for the Formation of Ethylene in CO Reduction on Single-Crystal Copper Electrodes. *J. Am. Chem. Soc.* **2012**, *134*, 9864−9867.
(17) Chaplin, R. P. S; Wragg, A. A. Effects of Process Conditions and Electrode Material on Reaction Pathways for Carbon Dioxide Electroreduction with Particular Reference to Formate Formation. *J. Appl. Electrochem.* **2003**, *33*, 1107−1123.
(18) Peterson, A. A.; Abild-Pedersen, F.; Studt, F.; Rossmeisl, J.; Nørskov, J. K. How Copper Catalyzes the Electroreduction of Carbon Dioxide into Hydrocarbon Fuels. *Energy Environ. Sci.* **2010**, *3*, 1311−1315.
(19) Peterson, A. A.; Nørskov, J. K. Activity Descriptors for CO_2 Electroreduction to Methane on Transition-Metal Catalysts. *J. Phys. Chem. Lett.* **2012**, *3*, 251−258.
(20) Durand, W. J.; Peterson, A. A.; Studt, F.; Abild-Pedersen, F.; Nørskov, J. K. Structure Effects on the Energetics of the Electrochemical Reduction of CO_2 by Copper Surfaces. *Surf. Sci.* **2011**, *605*, 1354−1359.
(21) Kim, J. J.; Summers, D. P., Jr.; Frese, K. W. Reduction of CO_2 and CO to Methane on Cu Foil Electrodes. *J. Electroanal. Chem.* **1988**, *245*, 223−244.
(22) DeWulf, D. W.; Jin, T.; Baard, A. J. Electrochemical and Surface Studies of Carbon-Dioxide Reduction to Methane and Ethylene at Copper Electrodes in Aqueous-Solutions. *J. Electrochem. Soc.* **1989**, *136*, 1686−1691.
(23) Nørskov, J. K.; Rossmeisl, J.; Logadottir, A.; Lindqvist, L.; Kitchin, J. R.; Bligaard, T.; Jonsson, H. Origin of the Overpotential for Oxygen Reduction at a Fuel-Cell Cathode. *J. Phys. Chem. B* **2004**, *108*, 17886−17892.
(24) Lee, D. H.; Lee, W. J.; Lee, W. J.; Kim, S. O.; Kim, Y.-H. Theory, Synthesis, and Oxygen Reduction Catalysis of Fe-Porphyrin-Like Carbon Nanotube. *Phys. Rev. Lett.* **2011**, *106*, 175502.
(25) Titov, A.; Zapol, P.; Král, P.; Liu, D.-J.; Iddir, H.; Baishya, K.; Curtiss, L. A. Catalytic Fe-xN Sites in Carbon Nanotubes. *J. Phys. Chem. C* **2009**, *113*, 21629−21634.
(26) Kattel, S.; Atanassov, P.; Kiefer, B. Stability, Electronic and Magnetic Properties of In-Plane Defects in Graphene: A First-Principles Study. *J. Phys. Chem. C* **2012**, *116*, 8161−8166.
(27) Kamat, P. V. Graphene-Based Nanoassemblies for Energy Conversion. *J. Phys. Chem. Lett.* **2011**, *2*, 242−251.
(28) Qu, L.; Liu, Y.; Baek, J.-B.; Dai, L. Nitrogen-Doped Graphene as Efficient Metal-Free Electrocatalyst for Oxygen Reduction Reaction. *ACS Nano* **2010**, *4*, 1321−1326.
(29) Kamat, P. V. Graphene-Based Nanoarchitectures. Anchoring Semiconductor and Metal Nanoparticles on a Two-Dimensional Carbon Support. *J. Phys. Chem. Lett.* **2010**, *1*, 520−527.
(30) Feng, H.; Ma, J.; Hu, Z. Nitrogen-Doped Carbon Nanotubes Functionalized by Transition Metal Atoms: A Density Functional Study. *J. Mater. Chem.* **2010**, *20*, 1702−1708.
(31) Ziegelbauer, J. M.; Olson, T. S.; Pylypenko, S.; Alamgir, F.; Jaye, C.; Atanassov, P.; Mukerjee, S. Direct Spectroscopic Observation of the Structural Origin of Peroxide Generation from Co-Based Pyrolyzed Porphyrins for ORR Applications. *J. Phys. Chem. C* **2008**, *112*, 8839−8849.
(32) Olson, T. S.; Pylypenko, S.; Fulghum, J. E.; Atanassov, P. Bifunctional Oxygen Reduction Reaction Mechanism on Non-Platinum Catalysts Derived from Pyrolyzed Porphyrins. *J. Electrochem. Soc.* **2010**, *157*, B54−B63.
(33) Li, Y.; Zhou, W.; Wang, H.; Xie, L.; Liang, Y.; Wei, F.; Idrobo, J.-C.; Pennycook, S. J.; Dai, H. An Oxygen Reduction Electrocatalyst Based on Carbon Nanotube-Graphene Complexes. *Nat. Nanotechnol.* **2012**, *7*, 394−400.
(34) Ramirez, G.; Ferraudi, G.; Chen, Y.-Y.; Trollund, E.; Villagra, D. Enhanced Photoelectrochemical Catalysis of CO(2) Reduction Mediated by a Supramolecular Electrode of Packed Co(II)-(tetrabenzoporphyrin). *Inorg. Chim. Acta* **2009**, *362*, 5−10.
(35) Ogura, K.; Yoshida, I. Electrocatalytic Reduction of CO_2 to Methanol. 9. Mediation with Metal Porphyrins. *J. Mol. Catal.* **1988**, *47*, 51−57.
(36) Bhugun, I.; Lexa, D.; Saveant, J. M. Catalysis of the Electrochemical Reduction of Carbon Dioxide by Iron(0) Porphyrins: Synergystic Effect of Lewis Acid Cations. *J. Phys. Chem.* **1996**, *100*, 19981−19985.
(37) Bhugun, I.; Lexa, D.; Saveant, J. M. Catalysis of the Electrochemical Reduction of Carbon Dioxide by Iron(0) Porphyrins: Synergystic Effect of Weak Bronsted Acids. *J. Am. Chem. Soc.* **1996**, *118*, 1769−1776.
(38) Hammer, B.; Hansen, L. B.; Nørskov, J. K. Improved Adsorption Energetics within Density-Functional Theory Using Revised Perdew-Burke-Ernzerhof Functionals. *Phys. Rev. B* **1999**, *59*, 7413−7421.
(39) Mortensen, J. J.; Hansen, L. B.; Jacobsen, K. W. Real-Space Grid Implementation of the Projector Augmented Wave Method. *Phys. Rev. B* **2005**, *71*, 035109.
(40) Enkovaara, J.; Rostgaard, C.; Mortensen, J. J.; Chen, J.; Dulak, M.; Ferrighi, L.; Gavnholt, J.; Glinsvad, C.; Haikola, V.; Hansen, H. A.; et al. Electronic Structure Calculations with GPAW: A Real-Space Implementation of the Projector Augmented-Wave Method. *J. Phys.: Condens. Matter* **2010**, *22*, 253202.
(41) Atomic Simulation Environment (ASE); Center for Atomic-scale Materials Design (CAMD), Technical University of Denmark, Lyngby. https://wiki.fysik.dtu.dk/ase.
(42) Dhanasekaran, T.; Grodkowski, J.; Neta, P.; Hambright, P.; Fujita, E. *p*-Terphenyl-Sensitized Photoreduction of CO_2 with Cobalt and Iron Porphyrins. Interaction between CO and Reduced Metalloporphyrins. *J. Phys. Chem. A* **1999**, *103*, 7742−7748.
(43) Grodkowski, J.; Dhanasekaran, T.; Neta, P.; Hambright, P.; Brunschwig, B. S.; Shinozaki, K.; Fujita, E. Reduction of Cobalt and Iron Phthalocyanines and the Role of the Reduced Species in Catalyzed Photoreduction of CO_2. *J. Phys. Chem. A* **2000**, *104*, 11332−11339.
(44) Kadish; K. M.; Royal, G.; Van Caemelbecke, E.; Gueletti, L. In *The Porphyrin Handbook*; Kadish, K. M., Smith, K. M., Guilard, R., Eds.; Academic Press: Boston, 2000; Vol. 9, pp 1−219.
(45) Lefévre, M.; Proietti, E.; Jaouen, F.; Dodelet, J.-P. Iron-Based Catalysts with Improved Oxygen Reduction Activity in Polymer Electrolyte Fuel Cells. *Science* **2009**, *324*, 71−74.

(46) Gupta, S.; Tryk, D.; Bae, I.; Aldred, W.; Yeager, E. Heat-Treated Polyacrylonitrile-Based catalysts for Oxygen Reduction Reaction. *J. Appl. Electrochem.* **1989**, *19*, 19−27.
(47) Calle-Vallejo, F.; Martínez, J. I.; García-Lastra, J. M.; Abad, E.; Koper, M. T. M. Oxygen Reduction and Evolution at Single-Metal Active Sites: Comparison between Functionalized Graphitic Materials and Protoporphyrins. *Surf. Sci.* **2013**, *607*, 47−53.
(48) Leung, K.; Rempe, S. B.; Schultz, P. A.; Sproviero, E. M.; Batista, V. S.; Chandross, M. E.; Medforth, C. J. Density Functional Theory and DFT+U study of Transition Metal Porphines Adsorbed on Au(111) Surfaces and Effects of Applied Electric Fields. *J. Am. Chem. Soc.* **2006**, *128*, 3659−3668.
(49) Leung, K. Transition-Metal Ion Impurities in $KTaO_3$. *Phys. Rev. B* **2002**, *65*, 012102.
(50) Reiher, M.; Salomon, O.; Hess, B. A. Dinuclear Diazene Iron and Ruthenium Complexes as Models for Studying Nitrogenase Activity. *Theor. Chem. Acc.* **2001**, *107*, 48.
(51) Reiher, M. Theoretical Study of the $Fe(phen)_2(NCS)_2$ Spin-Crossover Complex with Reparametrized Density Functionals. *Inorg. Chem.* **2002**, *41*, 6928.
(52) Cramer, C. J.; Truhlar, D. G. Density Functional Theory for Transition Metals and Transition Metal Chemistry. *Phys. Chem. Chem. Phys.* **2009**, *11*, 10757−10816.
(53) Nielsen, I. M. B.; Leung, K. Cobalt-Porphyrin Catalyzed Electrochemical Reduction of Carbon Dioxide in Water. 1. A Density Functional Study of Intermediates. *J. Phys. Chem. A* **2010**, *114*, 10166−10173.
(54) Leung, K.; Nielsen, I. M. B.; Sai, N.; Medforth, C.; Shelnutt, J. A. Cobalt-Porphyrin Catalyzed Electrochemical Reduction of Carbon Dioxide in Water. 2. Mechanism from First Principles. *J. Phys. Chem. A* **2010**, *114*, 10174−10184.
(55) Calle-Vallejo, F.; Martínez, J. I.; Rossmeisl, J. Density Functional Studies of Functionalized Graphitic Materials with Late Transition Metals for Oxygen Reduction Reaction. *Phys. Chem. Chem. Phys.* **2011**, *13*, 15639−15643.
(56) Karlberg, G. S.; Rossmeisl, J.; Nørskov, J. K. Estimations of Electric Field Effects on the Oxygen Reduction Reaction based on the Density Functional Theory. *Phys. Chem. Chem. Phys.* **2007**, *9*, 5158−5161.
(57) Karlberg, G. S.; Jaramillo, T. F.; Skúlason, E.; Rossmeisl, J.; Bligaard, T.; Nørskov, J. K. Cyclic Voltammograms for H on Pt(111) and Pt(100) from First Principles. *Phys. Rev. Lett.* **2007**, *99*, 126101.
(58) Tripkovic, V.; Skúlason, E.; Siahrostami, S.; Nørskov, J. K.; Rossmeisl, J. The Oxygen Reduction Reaction Mechanism on Pt(111) from Density Functional Theory Calculations. *Electrochim. Acta* **2010**, *55*, 7975−7981.
(59) Skúlason, E.; Tripkovic, V.; Björketun, M. E.; Gudmundsdóttir, S.; Karlberg, G.; Rossmeisl, J.; Bligaard, T.; Jónsson, H.; Nørskov, J. K. Modeling the Electrochemical Hydrogen Oxidation and Evolution Reactions on the Basis of Density Functional Theory Calculations. *J. Phys. Chem. C* **2010**, *114*, 18182−18197.
(60) Koper, M. T. M. Thermodynamic Theory of Multi-Electron Transfer Reactions: Implications for Electrocatalysis. *J. Electroanal. Chem.* **2011**, *660*, 254−260.
(61) Abild-Pedersen, F.; Greeley, J.; Studt, F.; Rossmeisl, J.; Munter, T. R.; Moses, P. G.; Skúlason, E.; Bligaard, T.; Nørskov, J. K. Scaling Properties of Adsorption Energies for Hydrogen-Containing Molecules on Transition-Metal Surfaces. *Phys. Rev. Lett.* **2007**, *99*, 016105.
(62) Hammer, B.; Nørskov, J. K. Electronic Factors Determining the Reactivity of Metal Surfaces. *Surf. Sci.* **1995**, *343*, 211−220.
(63) Rossmeisl, J.; Qu, Z.-W.; Zhu, H.; Kroes, G.-J.; Nørskov, J. K. Electrolysis of Water on Oxide Surfaces. *J. Electroanal. Chem.* **2007**, *607*, 83−89.
(64) Ferrin, P.; Nilekar, A. U; Greeley, J.; Mavrikakis, M.; Rossmeisl, J. Reactivity Descriptors for Direct Methanol Fuel Cell Anode Catalysts. *Surf. Sci.* **2008**, *602*, 3424−3431.
(65) Gasteiger, H. A.; Kocha, S. S.; Sompalli, B.; Wagner, F. T. Activity Benchmarks and Requirements for Pt, Pt-Alloy, and Non-Pt Oxygen Reduction Reaction Catalysts for PEMFCs. *Appl. Catal., B* **2005**, *56*, 9−35.

Supplementary information for Electrochemical CO_2 and CO Reduction on Metal-functionalized Porphyrin-like Graphene

Vladimir Tripkovic, Marco Vanin, Mohammedreza Karamad, Mårten E. Björketun, Karsten W. Jacobsen, Kristian S. Thygesen, and Jan Rossmeisl
Center for Atomic-scale Materials Design, Department of Physics, Technical University of Denmark, DK-2800 Kgs. Lyngby, Denmark

I. CO_2 AND CO CORRECTION

To arrive at the CO_2 and CO corrections we have analyzed the same set of reactions as in the supplementary material of ref. 18 in the paper, albeit using a somewhat different approach. We divided all the reactions into three groups. First group included reactions that contained only CO_2, either free or within a more complex molecule such as HCOOH or CH_3COOH. Similarly, the second group comprised all the reactions having CO. Finally, the third group had both CO and CO_2. The first two groups were used to calculate CO_2 and CO correction, while the third group was used to check the accuracy of both corrections. The reactions in the three respective groups are listed below.

First group:

$$4H_2 + CO_2 \rightarrow CH_4 + 2H_2O \quad (1)$$
$$CO_2 + H_2 \rightarrow HCOOH \quad (2)$$
$$3H_2 + CO_2 \rightarrow CH_3OH + H_2O \quad (3)$$
$$3H_2 + CO_2 \rightarrow 1/2CH_3CH_2OH + 3/2H_2O \quad (4)$$
$$10/3H_2 + CO_2 \rightarrow 1/3C_3H_8 + 2H_2O \quad (5)$$
$$7/2H_2 + CO_2 \rightarrow 1/2C_2H_6 + 2H_2O \quad (6)$$
$$3H_2 + CO_2 \rightarrow 1/2C_2H_4 + 2H_2O \quad (7)$$
$$11/4H_2 + CO_2 \rightarrow 1/4CH_2 = CHCH = CH_2 + 2H_2O \quad (8)$$
$$2H_2 + CO_2 \rightarrow 1/2CH_3COOH \quad (9)$$
$$2H_2 + CO_2 \rightarrow 1/2HCOOCH_3 + H_2O \quad (10)$$

Second group:

$$3H_2 + CO \rightarrow CH_4 + H_2O \quad (11)$$
$$2H_2 + CO \rightarrow CH_3OH \quad (12)$$
$$2H_2 + CO \rightarrow 1/2CH_3CH_2OH + 1/2H_2O \quad (13)$$
$$7/3H_2 + CO \rightarrow 1/3C_3H_8 + H_2O \quad (14)$$
$$5/2H_2 + CO \rightarrow 1/2C_2H_6 + H_2O \quad (15)$$
$$2H_2 + CO \rightarrow 1/2C_2H_4 + H_2O \quad (16)$$
$$7/4H_2 + CO \rightarrow 1/4CH_2 = CHCH = CH_2 + H_2O \quad (17)$$

Third group:

$$CO_2 + H_2 \rightarrow CO + H_2O \quad (18)$$
$$CO + H_2O \rightarrow HCOOH \quad (19)$$
$$CO + H_2 \rightarrow 1/2CH_3COOH \quad (20)$$
$$CO + H_2 \rightarrow 1/2HCOOCH_3 \quad (21)$$

To get an estimate of the CO_2/CO correction, we have performed the sensitivity analysis on the reaction group 1 and 2. The results are shown in Fig. 1. The minimum in the diagram gives 0.43 eV correction for CO_2 and 0.04 eV for CO.

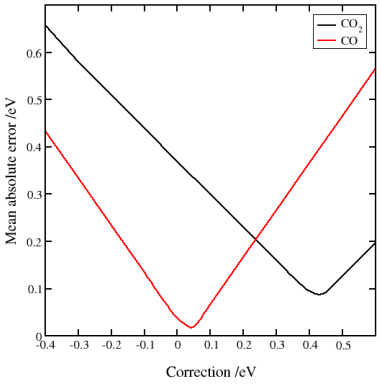

FIG. 1: The CO_2 and CO enthalpy corrections obtained from the sensitivity analysis. The corrections are found in the minima of the mean absolute error curves and amount to 0.43/0.04 eVs for CO_2(g)/CO(g).

The experimental, theoretical uncorrected, and theoretical corrected reaction enthalpies are listed in Tables I and II, along with the absolute errors before and after the correction is applied. As seen in Table I, the deduced

TABLE I: The first three columns denote the experimental reference enthalpies, theoretical calculated enthalpies and their absolute differences, whilst the last two columns stand for the CO_2 corrected theoretical values and the absolute differences with respect to the reference values in the first column. All the values are given in eVs.

ΔH_{ref}	ΔH_{unc}	abs error	ΔH_{cor}	abs error
-1.71	-1.27	0.44	-1.70	0.01
-0.55	-0.12	0.43	-0.55	0.00
-0.89	-0.45	0.44	-0.88	0.01
-1.30	-0.85	0.45	-1.28	0.02
-1.37	-0.94	0.43	-1.37	0.00
-0.66	-0.29	0.37	-0.72	0.06
-0.65	-0.25	0.40	-0.68	0.03

TABLE II: The first three columns denote the experimental reference enthalpies, theoretical calculated enthalpies and their absolute differences, whilst the last two columns stand for the CO corrected theoretical values and the absolute differences with respect to the reference values in the first column. All the values are given in eVs.

ΔH_{ref}	ΔH_{unc}	abs error	ΔH_{cor}	abs error
-2.14	-2.09	0.05	-2.13	0.01
-0.98	-0.94	0.04	-0.98	0.00
-1.32	-1.26	0.06	-1.30	0.02
-1.72	-1.67	0.05	-1.71	0.01
-1.80	-1.76	0.04	-1.80	0.00
-1.09	-1.10	0.01	-1.14	0.05
-1.08	-1.07	0.01	-1.11	0.03

CO_2 correction improves considerably the reaction enthalpies containing CO_2 molecule. On the other hand, the CO correction is very small and therefore, it can be neglected. The CO_2 correction does not improve the reaction enthalpies for the reactions in Table III, except for the first reduction reaction in which case the error reduces significantly. All the other reactions have CO_2 group within a more complex molecule. Hence, it is straightforward to conclude that the CO_2 correction holds only for the CO_2(g) and not when CO_2 group forms part of larger assemblies, such as $HCOOCH_3$ or CH_3COOH.

In Fig. 2 we show the most stable spin states for the clean metal-poprhyrins and when different intermediates are adsorbed on the central metal atoms. We considered 4 different spin states 0,1,2 and 3 such that for the metals that

TABLE III: The first three columns denote the experimental reference enthalpies, theoretical calculated enthalpies and their absolute differences, whilst the last two columns stand for the CO_2 corrected theoretical values and the absolute differences with respect to the reference values in the first column. All the values are given in eVs.

ΔH_{ref}	ΔH_{unc}	abs error	ΔH_{cor}	abs error
0.43	0.82	0.39	0.39	0.04
-0.27	-0.49	0.22	-0.06	0.21
-1.10	-1.13	0.03	-0.70	0.40
-0.60	-0.79	0.19	-0.36	0.24

have one unpaired electron we performed calculations for spin 1 and 3 and for the metals with no unpaired electrons we used spin 0 and 2. For the states with the adsorbed reaction intermediates we inferred the spin states by looking at how many bonds a species makes to the porphyrine metal atom. For instance CHO^* has one free bond which adds one extra electron to the metal atom and hence, the spin should become opposite to the spin value on the clean metal-funcionalized porphyrine-like graphene. The computed binding energies are compiled in Table. 3. For all the species that contain the OH group, a correction of 0.3 eV for solvation effects was used.

Element	Clean	OH*	O*	OCH3*	CO*	COOH*	CHO*	COH*	CH2O*	CHOH*	CH2OH*	CH2*	H*	CH*	CH3*
Fe	2	1	2	1	0	1	1	1	0	0	1	0	1	1	1
Ru	2	1	2	1	0	1	1	1	0	0	1	0	1	1	1
Os	0	1	0	1	0	1	1	1	0	2	1	0	1	1	1
Co	1	0	1	0	1	0	0	0	1	1	0	1	0	-	0
Rh	1	0	1	0	1	0	0	0	1	1	0	1	0	-	0
Ir	1	0	1	0	1	0	0	0	1	1	0	1	0	0	0
Ni	0	1	2	1	0	1	1	1	0	0	1	0	1	-	-
Pd	0	1	2	1	0	1	1	1	0	0	1	0	1	-	1
Pt	0	1	2	1	0	1	1	1	0	0	1	0	1	1	1
Cu	1	0	1	0	1	0	0	0	1	1	0	1	0	-	-
Ag	1	0	1	0	1	0	0	0	1	1	0	1	0	-	0
Au	1	0	1	0	1	0	0	0	1	1	0	-	0	-	-
B	1	0	1	0	1	0	0	0	1	1	0	1	0	0	0
Al	1	0	1	0	1	0	0	0	1	1	0	1	0	-	-
Ga	1	0	1	0	1	0	0	0	1	1	0	1	0	-	-
Mg	0	1	2	1	0	1	1	0	0	0	1	-	1	-	-

FIG. 2: The most stable spin states used for different intermediates.

We have performed detailed density of states (DOS) analysis in this study. The total DOS, the projected density of states onto the d states of the d metals and the distribution of the intermediates' molecular states are summarized in Figs. 4, 5 and 6. Additionaly, we have also analyzed using the same means the bonding of different intermediates on Rh-porphyrin - the best catalyst we have found (see Fig. 7).

From Fig. 4 it is obvious that there are always occupied states at the Fermi level available to donate the charge needed for reduction. From Fig. 5 we see that different intermediates, especially the C species are isoelectronic. Fig. 7 shows that the intermediates bind in a similar way to the metal atom - the peaks are located at nearly the same positions. This is the reason why the binding energies will change similarly regardless of the Exchange-Correlation Functional. The observation that they have virtually the same electronic structure with the HOMO level close to the Fermi level explains why the slopes of the scaling relations in Figure 4 in the paper are all close to 1.0. If more electrons were exchanged than the slope would have a value other than 1. The second observation that the peaks are not broadened much is an indication of weak interactions, much weaker than in metals, which can be also ascertained by comparing the respective binding energies.

Element	COOH*	CO*	CHO*	CH_2O*	OCH_3*	O*	OH*	COH*	CHOH*	CH_2OH*	CH	CH_2	CH_3
Fe	1.82	0.78	1.71	1.52	1.89	1.38	0.44	4.04	1.97	1.85	3.43	2.18	1.13
Ru	1.01	-0.25	0.97	1.29	1.42	0.88	-0.03	1.81	0.83	1.13	2.11	0.9	0.38
Os	0.8	-0.61	0.74	0.91	1.28	0.15	-0.21	1.06	4.47	0.89	0.87	0.31	0.13
Co	1.6	1.43	1.5	1.52	2.3	2.65	0.8	3.24	2.87	1.72	-	2.89	1.06
Rh	1.28	1.48	1.33	1.52	2.27	2.66	0.82	3	2.7	1.37	-	2.54	0.7
Ir	1.12	1.25	1	1.52	2.37	2.31	0.86	2.61	2.34	1.33	3.42	2.24	0.6
Ni	2.9	1.48	2.84	1.52	3.25	3.94	1.8	4.96	3.95	3.17	-	-	-
Pd	3.3	1.48	3.43	1.52	3.51	4.48	2.17	4.98	4.29	3.18	-	4.64	2.68
Pt	3.15	1.48	3.27	1.52	3.57	4.42	2.18	5.02	-0.55	5.98	5.7	4.46	2.5
Cu	2.84	1.48	2.94	1.52	3.24	3.89	1.68	6.87	3.69	3.11	-	-	-
Ag	1.89	1.05	2.06	1.52	2.28	3.21	0.85	3.76	2.72	2.08	-	3.16	1.17
Au	3.07	1.48	3.42	1.52	3.01	4.2	1.7	4.96	4.23	2.92	-	-	-

FIG. 3: Free energy values of different intermediates. All energies are given in eVs.

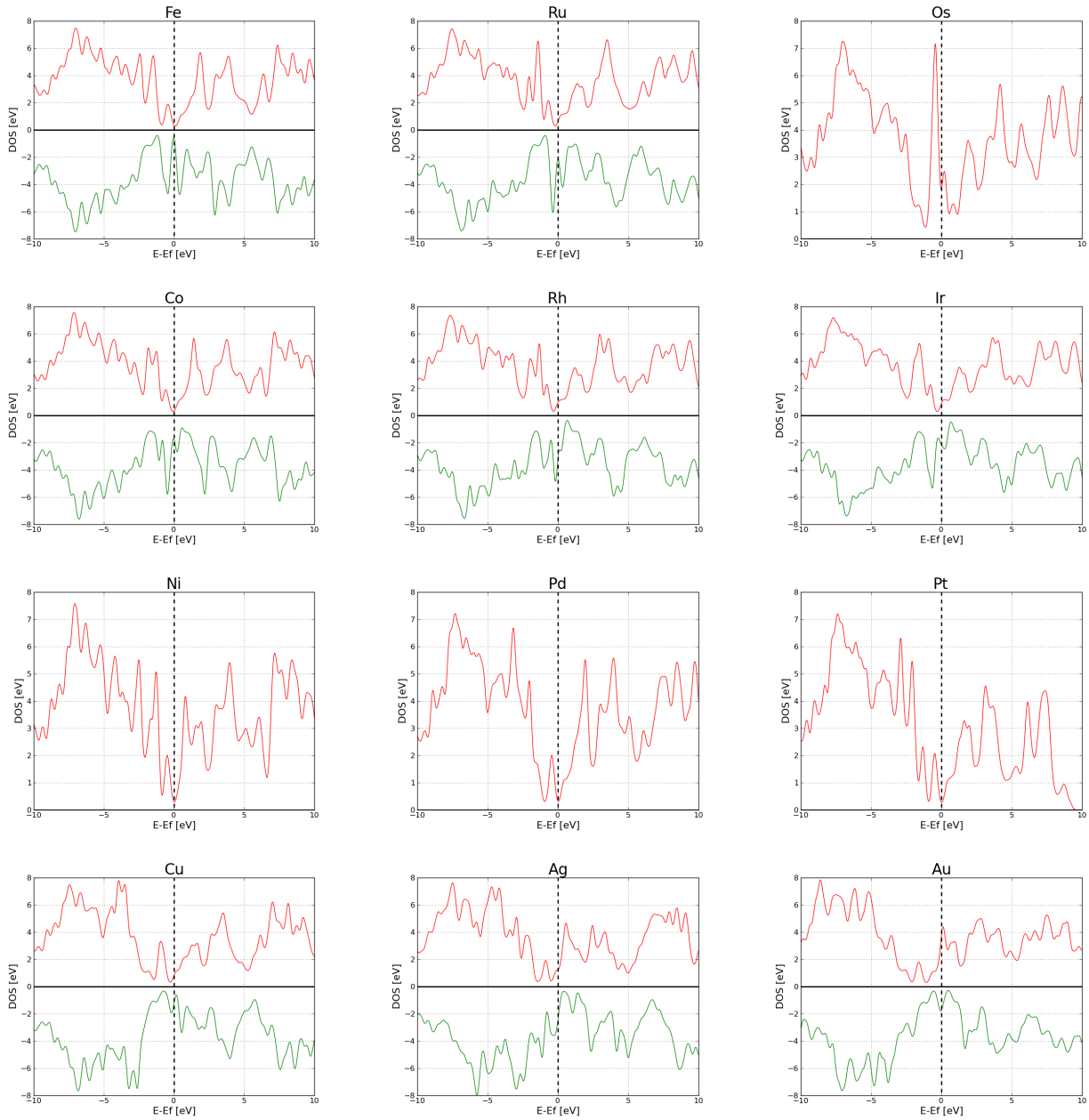

FIG. 4: Total density of states.

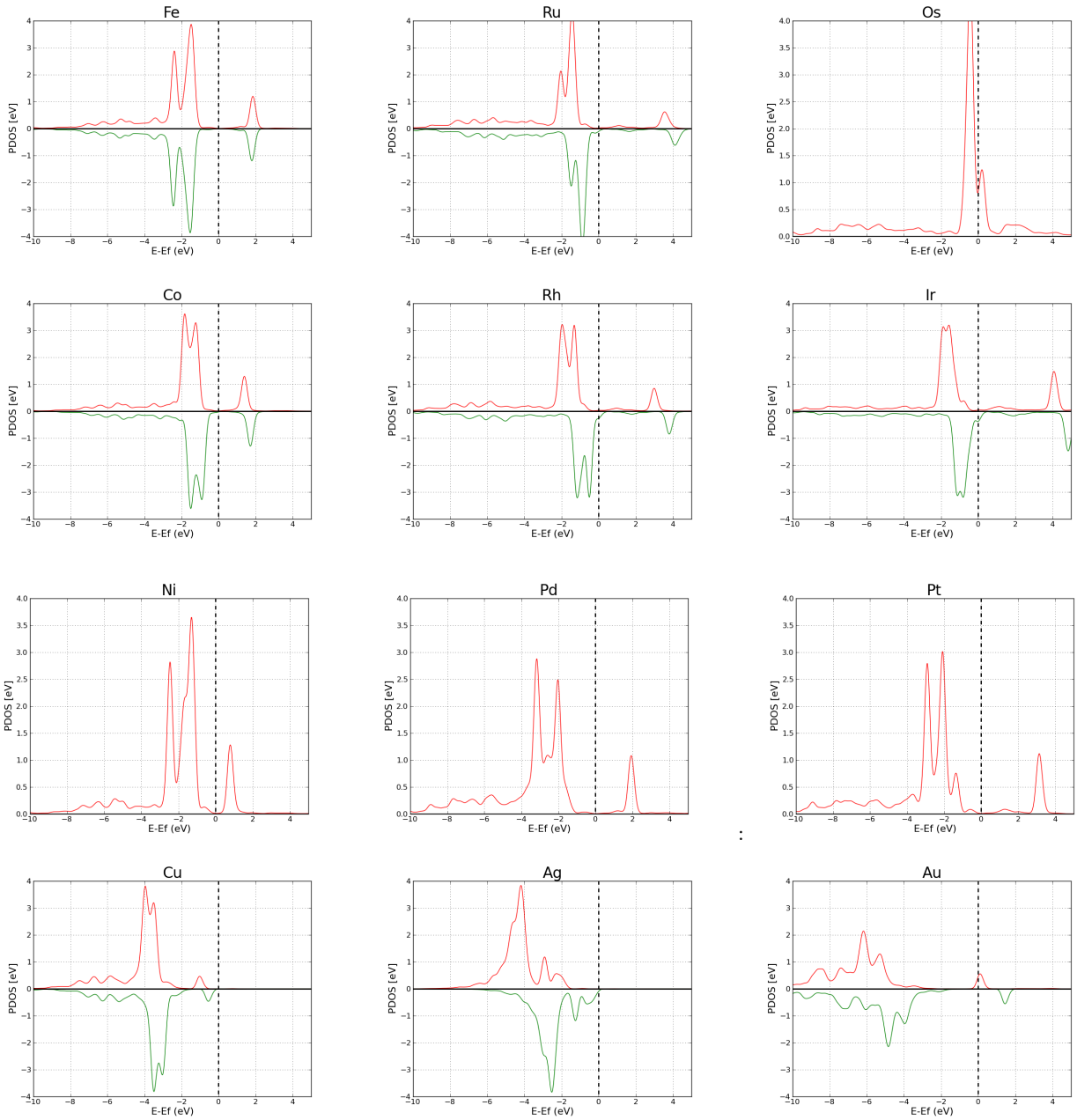

FIG. 5: Projected density of states onto the d-orbitals of the d-metals in the porphyrin ring.

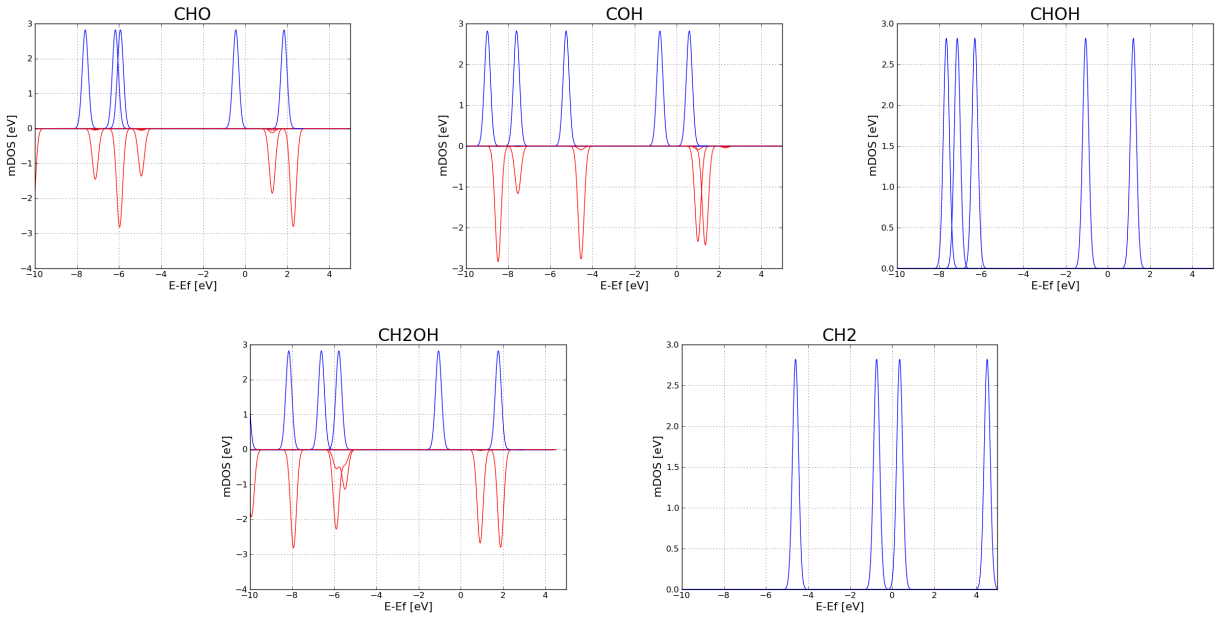

FIG. 6: Molecular density of states for different intermediates.

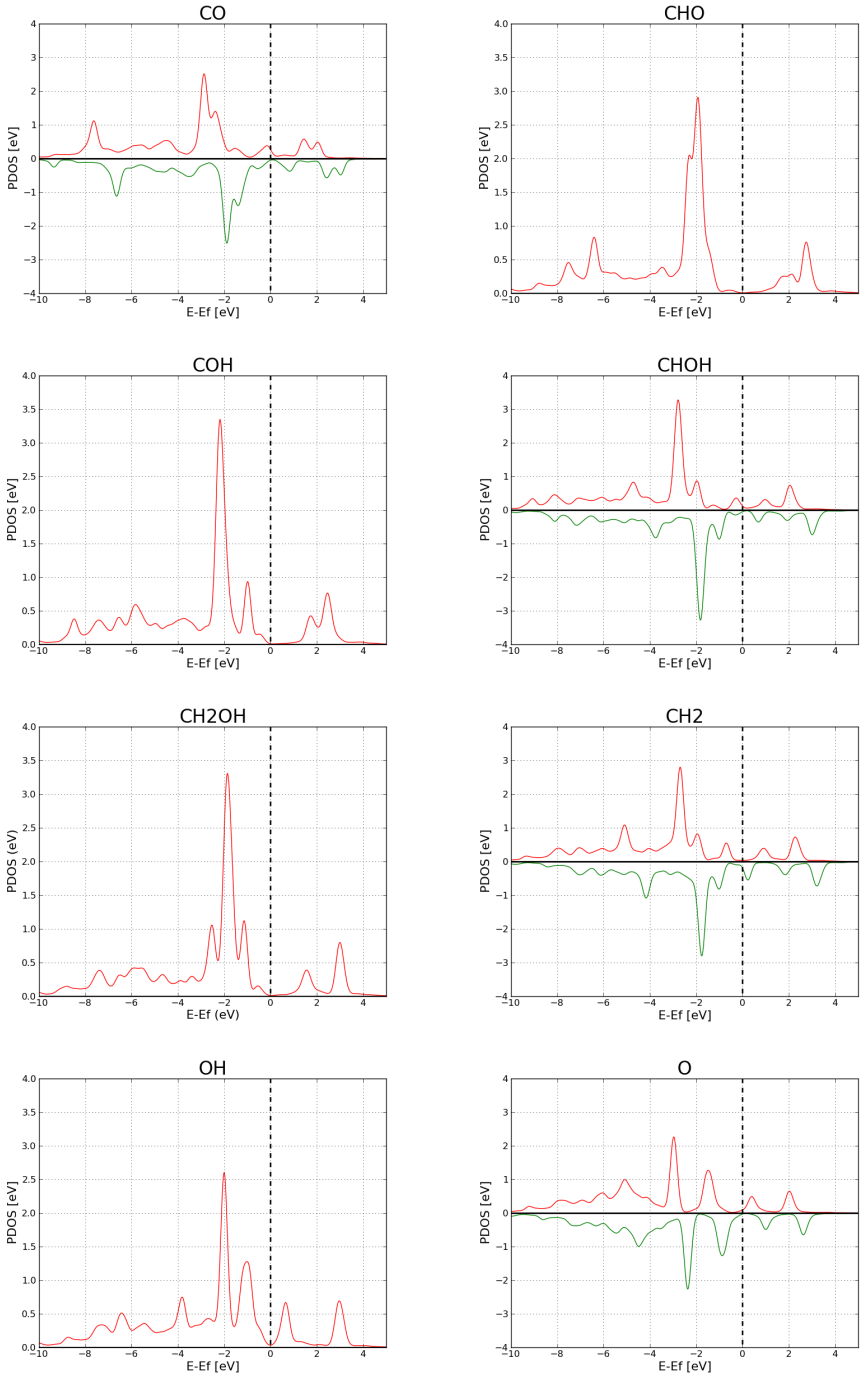

FIG. 7: Projected density of states on Rh d orbitals for the bare Rh-porphyrin and Rh-porphyrin with different intermediates.

Paper III

nature materials

ARTICLES

PUBLISHED ONLINE: 17 NOVEMBER 2013 | DOI: 10.1038/NMAT3795

Enabling direct H_2O_2 production through rational electrocatalyst design

Samira Siahrostami[1†], Arnau Verdaguer-Casadevall[2†], Mohammadreza Karamad[1], Davide Deiana[3], Paolo Malacrida[2], Björn Wickman[2,4], María Escudero-Escribano[2], Elisa A. Paoli[2], Rasmus Frydendal[2], Thomas W. Hansen[3], Ib Chorkendorff[2], Ifan E. L. Stephens[2*] and Jan Rossmeisl[1*]

Future generations require more efficient and localized processes for energy conversion and chemical synthesis. The continuous on-site production of hydrogen peroxide would provide an attractive alternative to the present state-of-the-art, which is based on the complex anthraquinone process. The electrochemical reduction of oxygen to hydrogen peroxide is a particularly promising means of achieving this aim. However, it would require active, selective and stable materials to catalyse the reaction. Although progress has been made in this respect, further improvements through the development of new electrocatalysts are needed. Using density functional theory calculations, we identify Pt–Hg as a promising candidate. Electrochemical measurements on Pt–Hg nanoparticles show more than an order of magnitude improvement in mass activity, that is, A g^{-1} precious metal, for H_2O_2 production, over the best performing catalysts in the literature.

At present, the most commonly produced chemicals, such as ammonia, hydrogen, methanol and hydrogen peroxide are produced in centralized reactors on a very large scale. There is a general call[1,2] for a more decentralized infrastructure where both energy conversion and chemical synthesis are conducted closer to the point of consumption. Electrochemical devices are set to play an increasingly important role in reaching this goal; they can be operated under ambient conditions, at variable rates and require little auxiliary plant[3]. They can also be coupled with intermittent renewable power sources, such as solar or wind, providing a means to store electricity and level out demand. Herein, we focus on the electrochemical production of hydrogen peroxide.

Copious amounts of H_2O_2 are produced globally; its annual production exceeds 3 million tons (ref. 4). It is both an environmentally benign chemical oxidant, used for chemical synthesis, the pulp and paper industry and in water treatment[5,6], and a potential energy carrier[7]. When produced from H_2 and O_2, H_2O_2 production is exergonic, with a standard Gibbs free energy of formation, $\Delta G_f^0 = -120\,\mathrm{kJ\,mol^{-1}}$. At present, H_2O_2 is produced using the anthraquinone process, a batch method conducted in large-scale facilities, with an average yield of 50 thousand tons per year per plant[4]. It involves the sequential hydrogenation and oxidation of anthraquinone molecules, and it is energy intensive[8].

The inherent complexity of the anthraquinone process has motivated many researchers towards developing a direct synthesis of H_2O_2 from its elements,[9,10] aiming at: small-scale, continuous production through a catalytic process[6]. Pd-modified Au nanoparticles (henceforth denoted as Pd/Au) are the most active catalysts for this process[9]. The electroreduction of oxygen to H_2O_2 in a fuel cell or electrolyser holds significant advantages over the above processes. It would enable on-site production of hydrogen peroxide, and unlike the direct synthesis route, it would not be constrained by the need to maintain the hydrogen and oxygen outside the explosive regime. Moreover, when produced in a fuel cell, it should, in principle, be possible to recover most of the ΔG_f^0, 120 kJ mol^{-1}, as electrical energy. Alternatively, one could do away with H_2 altogether, and synthesize H_2O_2 at the cathode of an electrolyser; with oxygen evolution occurring at its anode, the energy input would be ~200 kJ mol^{-1} (see Supplementary Information). Nonetheless, industrially viable, electrochemical production of H_2O_2 requires a catalyst that is stable, active and selective for the electroreduction of oxygen[6,11–14].

The most active and selective catalysts found for this reaction, thus far, are based on porphyrins containing 3*d* transition metals such as Co (ref. 15). However, the nitrogen ligands of these catalysts degrade in the presence of H_2O_2, resulting in rapid performance losses[16,17]. On the other hand, catalysts based on noble metals provide adequate stability under the harsh reaction conditions. Au nanoparticles have a modest activity for H_2O_2 production, ~1 mA at 0.4 V overpotential, but with a selectivity of only ~80%. On the other hand, Pd/Au nanoparticles show similar activity to Au and up to ~90% selectivity[13]. An overview of different electrocatalysts for H_2O_2 production is shown in Fig. 1, compiled from the literature.

Here, our goal is to discover new alloys for the electrochemical generation of H_2O_2, exhibiting an unprecedented combination of activity, selectivity and stability. We specifically focus our attention on catalysts that function under ambient conditions, containing elements that are stable in acidic, rather than basic electrolytes. This is because H_2O_2 decomposes at high temperatures or alkaline conditions[6], and devices based on hydroxide-conducting polymeric electrolytes exhibit low membrane stability, poor water management and low hydrogen oxidation activity[18,19].

We identify the catalysts using density functional theory (DFT) calculations, synthesize and test them electrochemically and characterize their composition and structure *ex situ*.

[1]Center for Atomic-scale Materials Design, Department of Physics, Technical University of Denmark, DK-2800 Kongens Lyngby, Denmark, [2]Center for Individual Nanoparticle Functionality, Department of Physics, Technical University of Denmark, DK-2800 Kongens Lyngby, Denmark, [3]Center for Electron Nanoscopy, Technical University of Denmark, DK-2800 Kongens Lyngby, Denmark, [4]Department of Applied Physics, Chalmers University of Technology, SE-41296 Göteborg, Sweden. †These authors contributed equally to this work. *e-mail: ifan@fysik.dtu.dk; jross@fysik.dtu.dk

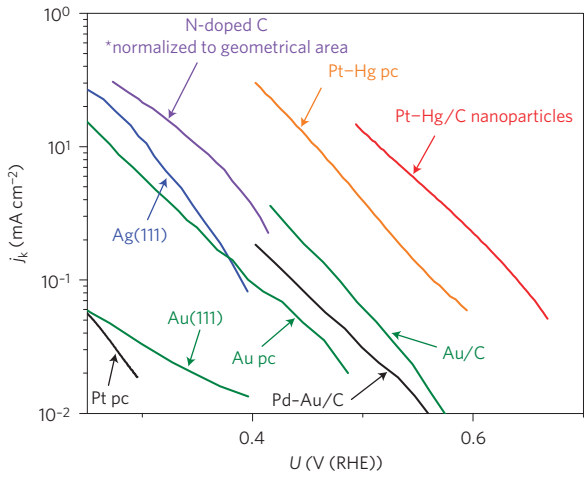

Figure 1 | Overview of different electrocatalysts for H_2O_2 production from the literature and from the present work. For the comparison, the kinetic current has been derived by correcting the partial current density for H_2O_2 production for mass transport limitations. Further details are available in the Methods and in the Supplementary Information. Data adapted from: ref. 46 for Pt polycrystalline (pc); ref. 47 for Au(111); ref. 48 for Au pc; ref. 49 for Ag(111); ref. 14 for N-doped C; ref. 13 for Pd–Au/C and Au/C. Data for Pt–Hg pc and Pt–Hg/C is from the present study.

Computational screening

The electroreduction of O_2 to H_2O_2 involves two coupled electron and proton transfers[20]:

$$O_2 + * + (H^+ + e^-) \rightarrow HOO^* \quad (1)$$

$$HOO^* + (H^+ + e^-) \rightarrow H_2O_2 + * \quad (2)$$

where $*$ denotes an unoccupied active site, and HOO* denotes the single adsorbed intermediate for the reaction. The catalyst provides high activity, by minimizing kinetic barriers for (1) and (2), and selectivity, by maximizing the barrier for HOO* reduction or dissociation to O* and OH*, the intermediates of the four-electron reduction of O_2 to H_2O.

The catalytic activity and selectivity, in turn, are determined by an interplay between two effects: ensemble effects and electronic effects. The binding of the reaction intermediates is controlled by electronic effects[21,22]. Varying the catalyst material allows one to tune the binding of HOO* to the surface. This means that the key parameter, or descriptor, in controlling the catalyst activity is the HOO* binding energy, ΔG_{HOO^*}. As the binding energy of HOO* scales linearly with that of HO*, ΔG_{HO^*} by a constant amount of 3.2 ± 0.2 eV (ref. 23), ΔG_{HO^*} can also be used as a descriptor. In Fig. 2e, the thermodynamic limiting potential, U_T, which is the most positive potential at which both (1) and (2) are downhill in free energy, is plotted, in blue, as a function of ΔG_{HO^*}; the HOO* binding energy is also shown on the upper horizontal axis for comparison. The thermodynamic overpotential for the two-electron reaction, η_{O_2/H_2O_2}, is denoted by the blue arrow, and is defined as the distance from the Nernstian potential for H_2O_2 production, $U^0_{O_2/H_2O_2} = 0.7$ V, to the U_T. Applying a bias equivalent to η_{O_2/H_2O_2} would allow the catalyst to sustain appreciable kinetic rates for H_2O_2 production, due to low charge transfer barriers[24–26].

Figure 2e establishes that there is a volcano-type relationship between η_{O_2/H_2O_2} (and hence the catalytic activity), and ΔG_{HO*}. Catalysts on the right-hand side of the volcano are limited by HOO* formation. For Au(211) it is 0.41 eV uphill to form HOO* at $U^0_{O_2/H_2O_2}$, as shown in the free-energy diagram in Fig. 2b. Accordingly, a thermodynamic overpotential of 0.41 V is required to drive the reaction. Catalysts on the left-hand side, such as Pt or Pd, bind HOO* too strongly, and the overpotential for the two-electron pathway is due to the reduction of HOO* to H_2O_2. The ideal catalyst, at the peak of the volcano, has a $\Delta G_{HOO*} \sim 4.2 \pm 0.2$ eV and $\eta_{O_2/H_2O_2} = 0$; its free-energy diagram is flat at the equilibrium potential, as shown in Fig. 2b. This means that the ideal catalyst would exhibit high current densities at negligible overpotentials.

In Fig. 2e, the U_T for the four-electron reduction of O_2 to H_2O is also plotted, in red, as a function of ΔG_{HO*} and ΔG_{HOO*}. In this case, there is an extra step contributing to the overpotential for the reaction, HO* reduction (where HO* is an adsorbed hydroxyl group, formed from the dissociation or reduction of HOO*; ref. 27):

$$HO^* + (H^+ + e^-) \rightarrow H_2O + * \quad (3)$$

The thermodynamic overpotential for equation (3), H_2O formation, η_{O_2/H_2O}, is indicated by the red arrow. Strikingly, in contrast to the two-electron volcano, even on the optimal catalyst, a minimum η_{O_2/H_2O} of ~0.4 V is required to drive H_2O formation.

The high value of η_{O_2/H_2O} is typical for reactions involving more than two electrons[20,22,23,26,28,29]; this is to overcome the large difference in adsorption energies between the intermediates, HO* and HOO*, whose binding energies scale linearly with each other[26]. On the other hand, the negligible overpotential required to drive O_2 reduction to H_2O_2 is characteristic of two-electron reactions, where the criterion for finding the ideal catalyst is relatively trivial: the adsorption of the sole reaction intermediate should be thermoneutral at the equilibrium potential[30].

The selectivity towards H_2O_2 or H_2O is determined by its propensity to break the O–O bond. This is, in turn, set by the binding strengths of the intermediates of the four-electron pathway, O* and HO*. To the left side of the peak (strong HO* binding) of both the four- and two-electron volcanoes (Fig. 2e), it is more downhill in free energy to form H_2O from HO*; this means the selectivity towards the four-electron pathway will dominate over the two-electron pathway, as is the case for Pt and Pd. The right side (weak HO* binding) of both two- and four-electron volcanoes overlap each other. In other words, at the peak of the two-electron volcano, there is a high activity for both H_2O_2 and H_2O formation, and both pathways will occur in tandem. Moving further right, beyond the peak of the two-electron volcano, towards Au it becomes more difficult to break the O–O bond and form HO* and O*, either through the chemical dissociation of HOO* or its electrochemical reduction. In summary, moving rightwards from the peak of the two-electron volcano weakens the interaction with O* and HO*, increasing the selectivity, but lowering the activity.

Apart from electronic effects, selectivity can also be controlled by geometric (or ensemble) effects; these are associated with the geometric arrangement of atoms on the catalyst surface[31,32]. On a selective catalyst, both the chemical dissociation to HO* and O* and the electrochemical reduction of HOO* to $O^* + H_2O$ should be avoided. Therefore, destabilizing O*, relative to HOO*, improves the selectivity. This can be achieved by controlling the geometry of the binding site: HOO* normally binds onto atop sites whereas O* binds onto hollow sites[33]. Eliminating hollow sites will specifically destabilize O*, without necessarily changing the activity. Catalysts such as Co-porphyrins[34] lack hollow sites whereas catalysts such as Pd/Au (ref. 13) contain hollow sites that interact weakly with oxygen; their active sites consist of single atoms, isolated by elements, such as Au, N or C (see Supplementary Information). This explains why Pd/Au is also an effective catalyst for the direct gas-phase synthesis of H_2O_2 from H_2 and O_2 (ref. 9).

Taking into account the above trends, using DFT, we screened for new alloy catalysts for the electrochemical generation of H_2O_2, which had not previously been tested. Our main criteria are that: for optimal activity, $\Delta G_{HOO*} \sim 4.2 \pm 0.2$ eV; each of the constituent

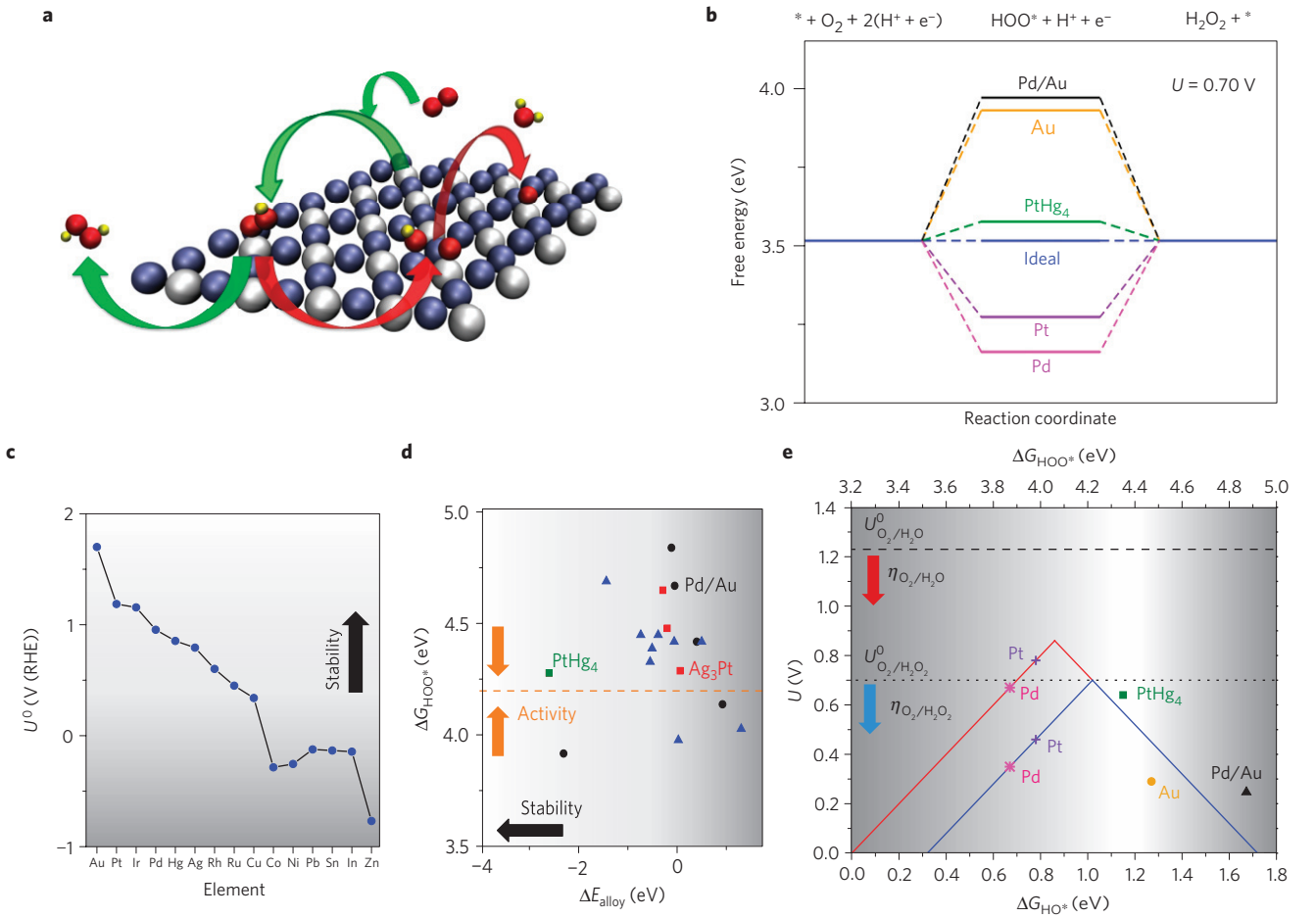

Figure 2 | Theoretical modelling of oxygen reduction to H_2O and H_2O_2. a, Representation of the $PtHg_4$(110) surface, based on the investigation of Hg/Pt(111) in ref. 35. The green arrows represent the reaction path to H_2O_2, whereas the red arrows the path to H_2O. Mercury, blue; platinum, grey; oxygen, red; hydrogen, yellow. **b**, Free-energy diagram for oxygen reduction to H_2O_2. The ideal catalyst is compared with $PtHg_4$(110), Pd/Au and closely packed pure metals Pd(111) and Au(211), all calculated for this work, and Pt(111), adapted from ref. 27. **c**, Dissolution potential for various elements under standard conditions[50]. **d**, Formation energy (per formula unit) ΔE_{alloy}, as a function of ΔG_{HOO*}. The optimal value for HOO binding is plotted as the orange dashed line. Bulk alloys are shown by red and green squares, surface alloys with a Au substrate are shown as black circles and surface alloys with non-Au substrate are shown by blue triangles. For **c**,**d** the colour gradient scales with stability, with the most stable areas highlighted in white. **e**, Theoretically calculated oxygen reduction volcano plot for the two-electron (blue) and four-electron (red) reduction of O_2, with the limiting potential plotted as a function of ΔG_{HO*} (lower horizontal axis) and ΔG_{HOO*} (upper horizontal axis). The equilibrium potential for the two-electron pathway, $U^0_{O_2/H_2O_2}$, is shown as the dotted line, and the equilibrium potential for the four-electron pathway, $U^0_{O_2/H_2O}$, is shown as the dashed line. The range of interesting HO* free energy for high selectivity and activity is highlighted with the greyscale gradient at its edges, recognizing limitations to the accuracy of DFT. Extensive details of the alloys included in the DFT screening are included in the Supplementary Information.

elements should be stable against dissolution or oxidation under reaction conditions; and the alloy should have as negative a heat of formation as possible (this provides a driving force to form the required monatomic ensembles). Each of the alloys has an active site where isolated atoms of the reactive metal, for example Pt, Pd, Rh or Ir, are surrounded by more inert elements, such as Au and Hg. A total number of 30 alloys were screened. An outline for the screening process is given in Fig. 2, (further details are available in the Supplementary Information).

Our attention was focused on the use of Hg as a means of forming the isolated reactive atoms. Hg is catalytically inactive. It is stable against dissolution up to 0.80 V at pH 0 (at standard conditions), and according to both our calculations (see Supplementary Information) and experiments[35] it forms stable alloys. The negative enthalpy of formation of the formed phase, $PtHg_4$, will stabilize the Hg, relative to pure Hg, meaning that it will be stable against dissolution. Hg can be easily electrodeposited onto Pt (ref. 36); on Pt(111) it forms a self-organized surface structure at room temperature[35]; each Pt atom is surrounded by Hg, as shown in Fig. 2a, thus forming the monatomic ensembles required for high selectivity. Figure 2b also shows that $PtHg_4$ has a close to optimal binding energy, with a thermodynamic overpotential smaller than 0.1 V. Alloying evidently induces electronic effects, as the binding of HOO* is ~0.37 eV weaker than pure Pt. Indeed, we emphasize that $PtHg_4$ is the only catalyst identified in the screening that fulfils all of our criteria for activity, selectivity and stability.

Although Hg is toxic, only monolayer quantities of Hg would be required to produce the required atomic ensembles; its present industrial applications, for example, lighting or the cathode for chlorine synthesis, require much larger amounts[4]. In the following we show that $PtHg_4$ is indeed highly selective and active for the two-electron pathway.

Experimental results

To synthesize $PtHg_4$, we modified a polycrystalline Pt disc following the procedure of ref. 35 for Hg/Pt(111). About 10 monolayers

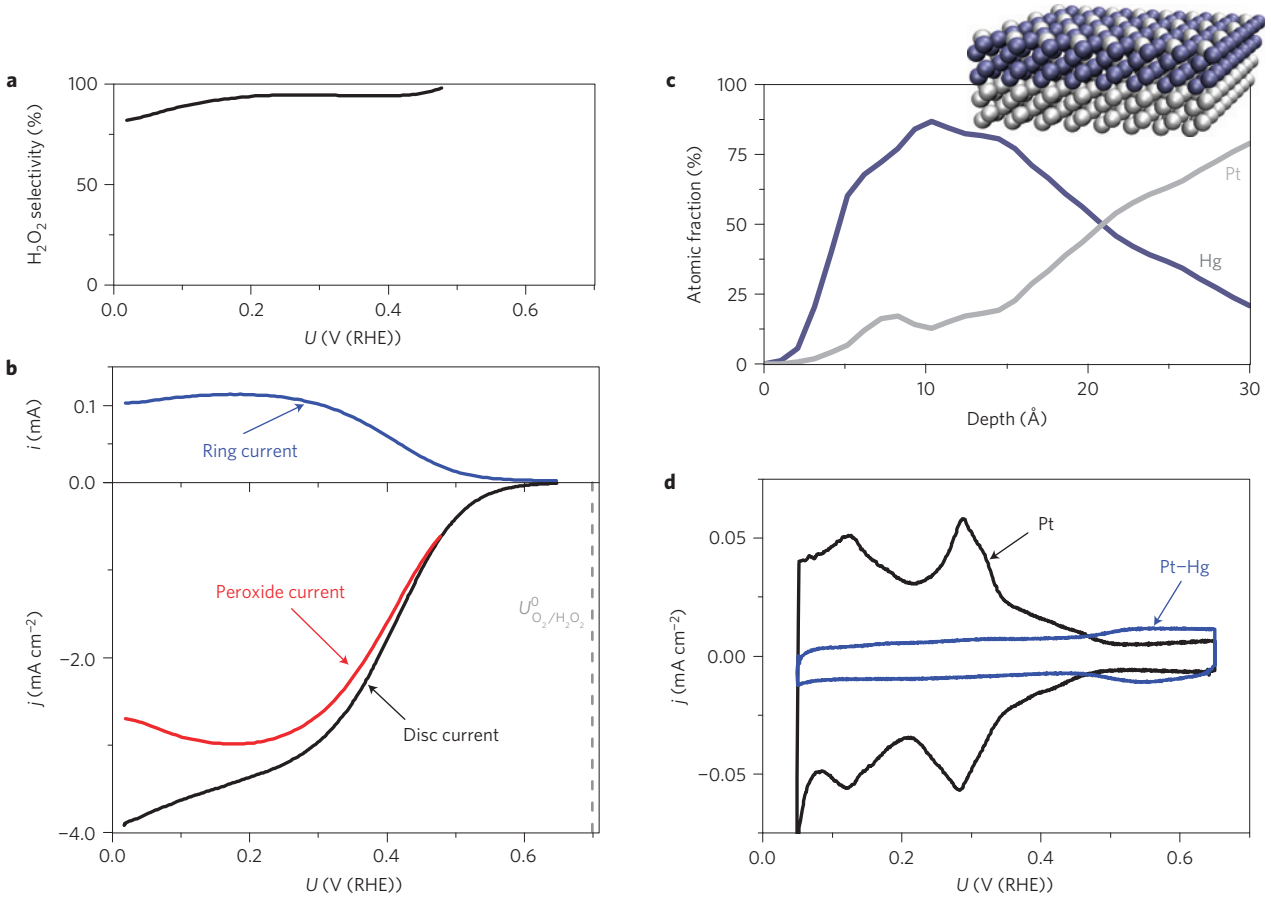

Figure 3 | Experimental characterization of Pt–Hg on extended surfaces. a, H_2O_2 selectivity as a function of the applied potential. **b**, RRDE voltammograms at 1,600 r.p.m. in O_2-saturated electrolyte with the disc current, ring current and current corresponding to hydrogen peroxide obtained from the ring current (only the anodic cycle is shown). **c**, Angle-resolved XPS depth profile of Pt–Hg. The adventitious C and O traces have been omitted for clarity. The inset shows a schematic representation of the structure revealed by the angle-resolved depth profile, with a Pt–Hg alloy above a Pt substrate. **d**, Voltammograms in N_2-saturated electrolyte of Pt and Pt–Hg. All electrochemical measurements were taken in 0.1 M $HClO_4$ and at 50 mV s^{-1} at room temperature.

of Hg were electrodeposited from $HgClO_4$. *Ex situ* angle-resolved X-ray photoelectron spectroscopy (XPS) of the sample at this stage revealed that the surface is composed of ~20% Pt and ~80% Hg, in agreement with a $PtHg_4$ structure (Fig. 3c). Figure 3d shows a cyclic voltammogram in N_2-saturated solution for Pt and Hg-modified Pt. The voltammogram for Pt shows the typical hydrogen adsorption/desorption peaks at 0.05–0.5 V, whereas Pt–Hg has a flat profile, suggesting a negligible amount of hydrogen adsorption. This is consistent with our DFT calculations (see Supplementary Information), which show that H is destabilized on $PtHg_4$(110), relative to Pt(111). Moreover, isolated Pd atoms on Au exhibit similar voltammograms[13]. We understand this phenomenon on the basis that on pure Pt and Pd, H usually adsorbs at hollow sites, with three Pt or Pd nearest neighbours[37]; isolated Pt or Pd atoms would lack such sites. The negative alloying energy of $PtHg_4$ provides a driving force to maximize the coordination of Hg to Pt and minimize the number of Pt–Pt nearest neighbours. Further evidence for the surface composition can be found in the Supplementary Information. In summary, our observations support the notion that isolated Pt atoms are formed at the surface of Pt–Hg, consistent with earlier experiments on Hg/Pt(111) (ref. 35).

We measure the electrochemical activity for oxygen reduction to hydrogen peroxide, using the rotating ring disc electrode (RRDE) technique[38]. Figure 3b shows the voltammograms in oxygen for Pt–Hg. The disc current increases exponentially with a decrease in potential from ~0.6 V, as kinetic barriers are lowered. To quantify the amount of hydrogen peroxide formed, the ring was potentiostated at 1.2 V, where the oxygen reduction current is negligible and H_2O_2 oxidation is mass transport limited. This gives rise to a positive current at the ring as hydrogen peroxide is produced at the disc (Fig. 3b). The onset potential at the ring and the disc coincide at ~0.6 V, corresponding to an overpotential of ~0.1 V. Such low overpotential is in agreement with our theoretical predictions. As the overpotential increases, most of the current in the disc can be accounted for by the amount of H_2O_2 detected at the ring; the efficiency of hydrogen peroxide production is as high as 96% in the region between 0.2 and 0.4 V (Fig. 3a). Within these potential limits, the hydrogen peroxide current density is 3 mA cm^{-2}, the theoretical mass transport limit for the two-electron reduction of oxygen. It is only at potentials below 0.2 V that both selectivity and hydrogen peroxide current start to decrease, implying that water formation is favoured.

To validate the stability criteria for our computational screening (Fig. 2), we also tested Pt–Sn and Ag_3Pt as catalysts for H_2O_2 production. As described in the Supplementary Information, we predict that both of these catalysts would, in principle, have optimal H_2O_2 activity. However, they fail to meet our stability criteria. Consequently, the less noble component, Sn or Ag, dissolved under reaction conditions. These examples illustrate the importance of stability in the corrosive electrochemical environment, which is both acidic and oxidizing.

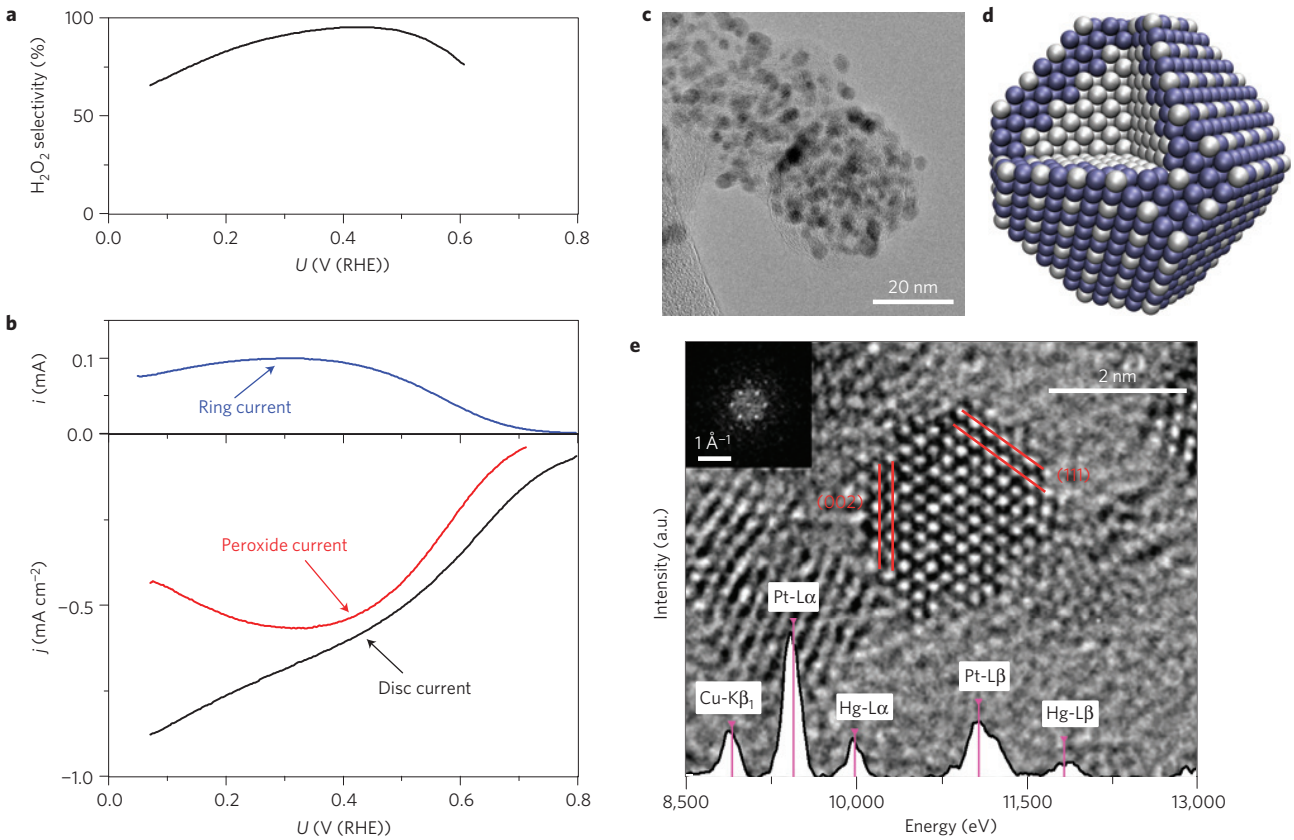

Figure 4 | Experimental characterization of Pt–Hg/C nanoparticles. a, H_2O_2 selectivity as a function of the applied potential. **b**, RRDE voltammograms at 1,600 r.p.m. in O_2-saturated electrolyte with the disc current, ring current and current corresponding to hydrogen peroxide obtained from the ring current (only the anodic cycle is shown). All electrochemical measurements were taken in 0.1 M $HClO_4$ and at 50 mV s^{-1} at room temperature. The disc current is normalized to the surface area of Pt nanoparticles (from H-upd) before deposition of Hg. **c**, TEM image of Pt–Hg/C nanoparticles. **d**, Schematic representation of a Pt–Hg/C nanoparticle. Mercury, blue; platinum, grey. **e**, HRTEM image of a single Pt–Hg nanoparticle, with the corresponding EDS spectrum of the particle superimposed on top, with peaks corresponding to Pt and Hg from the nanoparticle, and Cu, from the TEM grid; the {111} and {002} planes are shown in red; the corresponding diffractogram is shown in the inset.

Ultimately, should electrochemical hydrogen peroxide synthesis make a technological impact, it will require high-surface-area catalysts or thin films[26,39]. It turns out that Pt–Hg/C nanoparticles are even more active than the extended surfaces.

An ink was prepared from commercial Pt/C and drop-cast on a glassy carbon electrode (details in the Supplementary Information). To prepare the Pt–Hg alloy we followed the same electrodeposition procedure as for the polycrystalline surface. The features of the base voltammograms were similar to those of polycrystalline Pt–Hg (see Supplementary Information).

Transmission electron microscopy (TEM) analysis showed well-distributed nanoparticles on the carbon support (Fig. 4c). A high-resolution TEM (HRTEM) image of a single nanoparticle and its Fourier transform are shown in Fig. 4e. By positioning the scanning TEM probe on an individual nanoparticle, an energy-dispersive X-ray spectroscopy (EDS) spectrum as shown in Fig. 4e was acquired. Both Pt and Hg peaks are present in the spectrum. XPS analysis, which is sensitive to the first few atomic layers, confirmed the presence of both elements. However, the lattice parameters from the HRTEM are consistent with the structure of Pt. Together, the HRTEM and XPS data suggest a core of Pt and a shell of Pt–Hg (see Supplementary Information).

We then evaluated oxygen reduction on Hg-modified Pt nanoparticles (Fig. 4b), where we observed a similar current profile to the polycrystalline surfaces. The ring current proved that a high yield of hydrogen peroxide was achieved, with over 90% selectivity between 0.3 and 0.5 V (Fig. 4a). The catalyst is highly stable under reaction conditions. When cycling the potential between 0.05 and 0.8 V for 8,000 cycles in an O_2-saturated electrolyte, there were no measurable losses in H_2O_2 production activity (see Supplementary Information).

The viability of an electrochemical device producing H_2O_2 will require it to be efficient, safe and that the cost of its constituent materials is minimal. Given that the most viable catalysts for H_2O_2 production are based on precious metals, it is essential that the loading of these metals is minimized, that is, that the current density per gram of precious metal is maximized.

State-of-the-art fuel cells and electrolysers are engineered to avoid losses due to the transport of oxygen. Thus, to yield a quantitative comparison of catalyst performance, we have corrected the data in Figs 3 and 4 for mass transport losses. The results are shown in Fig. 1. In terms of specific activity (normalized to the surface area of Pt), nanoparticulate Pt–Hg/C exhibits 4–5 times the activity of polycrystalline Pt–Hg. The higher activity of the nanoparticles compared with extended surfaces indicates that undercoordinated sites, which are more prevalent on nanoparticulate surfaces[40], could play an important role in the reaction. Notably, Pt–Hg/C shows more than one order of magnitude improvement in mass activity over previously reported Pd–Au/C or Au/C (ref. 13). To the best of our knowledge, Pt–Hg nanoparticles present the best activity reported in the literature for hydrogen peroxide synthesis on a metallic catalyst, with a selectivity of up to 96% and a mass activity of $26 \pm 4\ A\ g^{-1}_{noble\ metal}$ at 50 mV overpotential.

In this work, we have taken advantage of the isolated active site concept to tune the activity and selectivity for oxygen reduction. Our theoretical model successfully predicted Pt–Hg as an active, selective and stable catalyst for hydrogen peroxide synthesis.

Comparing the activity reported here with that reported for other two-electron reactions, we anticipate that it should be possible to discover even more active catalysts for electrochemical H_2O_2 production[23,30,37,41,42]. Nonetheless, as our theoretical model shows, improved activity may come at the cost of selectivity. The rational approach used here to tune activity and selectivity can be extended to other, more complex reactions for sustainable energy conversion, in particular the electroreduction of CO_2 and N_2 (refs 28,29).

Methods

Computational details. The computational analysis was carried out using grid-based projector-augmented wave (GPAW) method, a DFT code based on a projected augmented wave (all-electron frozen core approximation) method integrated with the atomic simulation environment[43,44]. The revised Perdew–Burke–Ernzerhof functional was used as an exchange correlation functional[45]. An eight-layer 2×2 slab with 17.5 Å vacuum between successive slabs was used to model the $PtHg_4(110)$ surface. Monkhorst–Pack grids with dimensions of $4 \times 4 \times 1$ were used to sample the Brillouin zone. The bottom four layers were fixed in the bulk structure whereas the upper layers and adsorbates were allowed to relax in all directions until residual forces were less than 0.05 eV $Å^{-1}$. Further details on DFT calculations are provided in the Supplementary Information.

Extended surface electrode preparation. A platinum polycrystalline electrode was mirror polished to <0.25 μm before every experiment and prepared by flame annealing as previously reported[46]. Several voltammograms in nitrogen-saturated 0.1 M $HClO_4$ were recorded to ensure a reproducible surface, and then the electrode was moved to an electrodeposition cell containing 0.1 M $HClO_4$ + 1 mM $HgClO_4$. The potential was swept from open circuit (about 1 V) at 50 mV s^{-1} to 0.2 V, where the potential was stopped for 2 min to electrodeposit mercury following the procedure detailed in ref. 35. The potential was scanned to 0.65 V at 50 mV s^{-1} and stopped there while removing the electrode from the cell. We immediately moved the Hg-modified Pt electrode back into the RRDE cell, where it was inserted under potential control of about 0.1 V in N_2-saturated 0.1 M $HClO_4$. Then the potential was swept between 0.05 and 0.65 V until a stable cyclic voltammogram was obtained. As we observed mercury traces at the ring, we cleaned it electrochemically by cycling it between 0.05 and 1.6 V while rotating the electrode to avoid mercury redeposition. Once the ring and disc voltammetries became stable, we saturated the cell with O_2 to record voltammetries at the disc while keeping the ring at 1.2 V to detect H_2O_2.

High-surface-area catalysts. To prepare the Pt/C nanoparticles, a simple synthesis method was employed. First, 5.75 mg of 60% wt Pt supported on C was mixed with 9.5 ml of Millipore water, 3 ml of isopropanol and 50 μl of 1:100 Nafion. To facilitate dispersion of the nanoparticles, 20 μl of 2% wt solution of polyvinylpyrrolidone was used. The nanoparticles had a nominal size of 3 nm. The mixture was sonicated for 20 min at about 25 °C and 10 μl of it was drop-casted on top of a glassy carbon disc of 0.196 cm^2. The sample was then left to dry before embedding into a RRDE set-up. To ensure a good dispersion of the film, oxygen reduction was carried out on the Pt/C nanoparticles (see Supplementary Information). The same procedure adopted for the polycrystalline sample was followed to electrodeposit mercury. All data relative to nanoparticles were normalized to the underpotential deposition of hydrogen (H-upd; that is, assuming that the voltammetric charge between 0.5 and 0.05 V is equivalent to 210 μC cm^{-2} of Pt surface area[18]) before Hg deposition, and the corresponding capacitance was subtracted from all oxygen reduction measurements.

Chemicals. Concentrated $HClO_4$ was obtained from Merck and diluted to 0.1 M. $HgClO_4$ was obtained from Sigma Aldrich and diluted in 0.1 M $HClO_4$ to reach 1 mM $HgClO_4$. All gases were of 5N5 quality and purchased from AGA.

Electrochemical measurements. A typical three-electrode cell was used for the RRDE experiments. Another three-electrode cell was used to electrodeposit mercury. In both cells the counter electrodes were Pt wires and Hg/Hg_2SO_4 electrodes were used as a reference, separated from the working electrode compartment using a ceramic frit. All potentials are quoted with respect to the reversible hydrogen electrode, and are corrected for ohmic losses. All experiments were performed using a Bio-Logic Instruments' VMP2 potentiostat, controlled by a computer. The RRDE assembly was provided by Pine Instruments Corporation. The ring was made of platinum and its collection efficiency, N, was of 20 ± 1%. To compute H_2O_2 selectivity, η, we made use of the following equation[38]: $\eta = 2(I_r/N/I_d + I_r/N)$, where I_r and I_d are ring and disc currents, respectively. H_2O_2 selectivity is not calculated below ~0.2 mA of disc current, owing to a poorer signal to background ratio at low currents.

To correct the current for mass transport losses, the equation $1/j = 1/j_d + 1/j_k$ was used, where j is the total current, j_d is the mass-transport-limited current to hydrogen peroxide (obtained from the ring), and j_k is the kinetic current to hydrogen peroxide. Further details are given in the Supplementary Information.

Received 27 June 2013; accepted 1 October 2013; published online 17 November 2013; corrected after print 21 November 2013

References

1. Perlo, P. *et al. Catalysis for Sustainable Energy Production* 89–105 (Wiley, 2009).
2. Armaroli, N. & Balzani, V. The future of energy supply: challenges and opportunities. *Angew. Chem. Int. Ed.* **46,** 52–66 (2007).
3. Kotrel, S. & Brauninger, S. in *Handbook of Heterogeneous Catalysis* 2nd edn (eds Ertl, G., Knoezinger, H., Schueth, F. & Weitkamp, J.) 1963 (Wiley, 2008).
4. *Ullmann's Encyclopedia of Industrial Chemistry* (Wiley, 1999–2013).
5. Samanta, C. Direct synthesis of hydrogen peroxide from hydrogen and oxygen: An overview of recent developments in the process. *Appl. Catal. A* **350,** 133–149 (2008).
6. Campos-Martin, J. M., Blanco-Brieva, G. & Fierro, J. L. G. Hydrogen peroxide synthesis: An outlook beyond the anthraquinone process. *Angew. Chem. Int. Ed.* **45,** 6962–6984 (2006).
7. Fukuzumi, S., Yamada, Y. & Karlin, K. D. Hydrogen peroxide as a sustainable energy carrier: Electrocatalytic production of hydrogen peroxide and the fuel cell. *Electrochim. Acta* **82,** 493–511 (2012).
8. Hâncu, D., Green, J. & Beckman, E. J. H_2O_2 in CO_2/H_2O biphasic systems: Green synthesis and epoxidation reactions. *Ind. Eng. Chem. Res.* **41,** 4466–4474 (2002).
9. Edwards, J. K. *et al.* Switching off hydrogen peroxide hydrogenation in the direct synthesis process. *Science* **323,** 1037–1041 (2009).
10. Ford, D. C., Nilekar, A. U., Xu, Y. & Mavrikakis, M. Partial and complete reduction of O_2 by hydrogen on transition metal surfaces. *Surf. Sci.* **604,** 1565–1575 (2010).
11. Yamanaka, I., Hashimoto, T., Ichihashi, R. & Otsuka, K. Direct synthesis of H_2O_2 acid solutions on carbon cathode prepared from activated carbon and vapor-growing-carbon-fiber by a H_2/O_2 fuel cell. *Electrochim. Acta* **53,** 4824–4832 (2008).
12. Lobyntseva, E., Kallio, T., Alexeyeva, N., Tammeveski, K. & Kontturi, K. Electrochemical synthesis of hydrogen peroxide: Rotating disk electrode and fuel cell studies. *Electrochim. Acta* **52,** 7262–7269 (2007).
13. Jirkovský, J. S. *et al.* Single atom hot-spots at Au–Pd nanoalloys for electrocatalytic H_2O_2 Production. *J. Am. Chem. Soc.* **133,** 19432–19441 (2011).
14. Fellinger, T-P., Hasché, F., Strasser, P. & Antonietti, M. Mesoporous nitrogen-doped carbon for the electrocatalytic synthesis of hydrogen peroxide. *J. Am. Chem. Soc.* **134,** 4072–4075 (2012).
15. Gouérec, P. & Savy, M. Oxygen reduction electrocatalysis: Ageing of pyrolyzed cobalt macrocycles dispersed on an active carbon. *Electrochim. Acta* **44,** 2653–2661 (1999).
16. Bezerra, C. W. B. *et al.* A review of Fe–N/C and Co–N/C catalysts for the oxygen reduction reaction. *Electrochim. Acta* **53,** 4937–4951 (2008).
17. Schulenburg, H. *et al.* Catalysts for the oxygen reduction from heat-treated iron(III) tetramethoxyphenylporphyrin chloride: Structure and stability of active sites. *J. Phys. Chem. B* **107,** 9034–9041 (2003).
18. Sheng, W., Gasteiger, H. A. & Shao-Horn, Y. Hydrogen oxidation and evolution reaction kinetics on platinum: Acid vs alkaline electrolytes. *J. Electrochem. Soc.* **157,** B1529–B1536 (2010).
19. Ayers, K. E., Dalton, L. T. & Anderson, E. B. Efficient generation of high energy density fuel from water. *ECS Trans.* **41,** 27–38 (2012).
20. Viswanathan, V., Hansen, H. A., Rossmeisl, J. & Nørskov, J. K. Unifying the 2e– and 4e– reduction of oxygen on metal surfaces. *J. Phys. Chem. Lett.* **3,** 2948–2951 (2012).
21. Norskov, J. K., Bligaard, T., Rossmeisl, J. & Christensen, C. H. Towards the computational design of solid catalysts. *Nature Chem.* **1,** 37–46 (2009).
22. Greeley, J. *et al.* Alloys of platinum and early transition metals as oxygen reduction electrocatalysts. *Nature Chem.* **1,** 552–556 (2009).
23. Koper, M. T. M. Thermodynamic theory of multi-electron transfer reactions: Implications for electrocatalysis. *J. Electroanal. Chem.* **660,** 254–260 (2011).
24. Janik, M. J., Taylor, C. D. & Neurock, M. First-principles analysis of the initial electroreduction steps of oxygen over Pt(111). *J. Electrochem. Soc.* **156,** B126–B135 (2009) doi:10.1149/1.3008005.
25. Tripković, V., Skúlason, E., Siahrostami, S., Nørskov, J. K. & Rossmeisl, J. The oxygen reduction reaction mechanism on Pt(111) from density functional theory calculations. *Electrochim. Acta* **55,** 7975–7981 (2010).
26. Stephens, I. E. L., Bondarenko, A. S., Gronbjerg, U., Rossmeisl, J. & Chorkendorff, I. Understanding the electrocatalysis of oxygen reduction on platinum and its alloys. *Energy Environ. Sci.* **5,** 6744–6762 (2012).
27. Rossmeisl, J., Karlberg, G. S., Jaramillo, T. & Norskov, J. K. Steady state oxygen reduction and cyclic voltammetry. *Faraday Discuss.* **140,** 337–346 (2009).

28. Peterson, A. A. & Nørskov, J. K. Activity descriptors for CO_2 electroreduction to methane on transition-metal catalysts. *J. Phys. Chem. Lett.* **3,** 251–258 (2012).
29. Skulason, E. *et al.* A theoretical evaluation of possible transition metal electro-catalysts for N_2 reduction. *Phys. Chem. Chem. Phys.* **14,** 1235–1245 (2012).
30. Hansen, H. A. *et al.* Electrochemical chlorine evolution at rutile oxide (110) surfaces. *Phys. Chem. Chem. Phys.* **12,** 283–290 (2010).
31. Maroun, F., Ozanam, F., Magnussen, O. M. & Behm, R. J. The role of atomic ensembles in the reactivity of bimetallic electrocatalysts. *Science* **293,** 1811–1814 (2001).
32. Strmcnik, D. *et al.* Enhanced electrocatalysis of the oxygen reduction reaction based on patterning of platinum surfaces with cyanide. *Nature Chem.* **2,** 880–885 (2010).
33. Viswanathan, V. *et al.* Simulating linear sweep voltammetry from first-principles: Application to electrochemical oxidation of water on Pt(111) and Pt3Ni(111). *J. Phys. Chem. C* **116,** 4698–4704 (2012).
34. Siahrostami, S., Bjorketun, M. E., Strasser, P., Greeley, J. & Rossmeisl, J. Tandem cathode for proton exchange membrane fuel cells. *Phys. Chem. Chem. Phys.* **15,** 9326–9334 (2013).
35. Wu, H. L., Yau, S. & Zei, M. S. Crystalline alloys produced by mercury electrodeposition on Pt(111) electrode at room temperature. *Electrochim. Acta* **53,** 5961–5967 (2008).
36. Angerstein-Kozlowska, H., MacDougall, B. & Conway, B. E. Origin of activation effects of acetonitrile and mercury in electrocatalytic oxidation of formic acid. *J. Electrochem. Soc.* **120,** 756–766 (1973).
37. Skuílason, E. *et al.* Modeling the electrochemical hydrogen oxidation and evolution reactions on the basis of density functional theory calculations. *J. Phys. Chem. C* **114,** 18182–18197 (2010).
38. Paulus, U. A., Schmidt, T. J., Gasteiger, H. A. & Behm, R. J. Oxygen reduction on a high-surface area Pt/Vulcan carbon catalyst: A thin-film rotating ring-disk electrode study. *J. Electroanal. Chem.* **495,** 134–145 (2001).
39. Van der Vliet, D. F. *et al.* Mesostructured thin films as electrocatalysts with tunable composition and surface morphology. *Nature Mater.* **11,** 1051–1058 (2012).
40. Perez-Alonso, F. J. *et al.* The effect of size on the oxygen electroreduction activity of mass-selected platinum nanoparticles. *Angew. Chem. Intl Ed.* **51,** 4641–4643 (2012).
41. Wesselmark, M., Wickman, B., Lagergren, C. & Lindbergh, G. Hydrogen oxidation reaction on thin platinum electrodes in the polymer electrolyte fuel cell. *Electrochem. Commun.* **12,** 1585–1588 (2010).
42. Wolfschmidt, H., Weingarth, D. & Stimming, U. Enhanced reactivity for hydrogen reactions at Pt nanoislands on Au(111). *ChemPhysChem* **11,** 1533–1541 (2010).
43. Mortensen, J. J., Hansen, L. B. & Jacobsen, K. W. Real-space grid implementation of the projector augmented wave method. *Phys. Rev. B* **71,** 035109 (2005).
44. Atomic Simulation Environment (ASE), available at https://wiki.fysik.dtu.dk/ase, Center for Atomic Scale Material Design (CAMD), Technical University of Denmark, Lyngby.
45. Hammer, B., Hansen, L. B. & Nørskov, J. K. Improved adsorption energetics within density-functional theory using revised Perdew-Burke-Ernzerhof functionals. *Phys. Rev. B* **59,** 7413–7421 (1999).
46. Verdaguer-Casadevall, A., Hernandez-Fernandez, P., Stephens, I. E. L., Chorkendorff, I. & Dahl, S. The effect of ammonia upon the electrocatalysis of hydrogen oxidation and oxygen reduction on polycrystalline platinum. *J. Power Sources* **220,** 205–210 (2012).
47. Alvarez-Rizatti, M. & Jüttner, K. Electrocatalysis of oxygen reduction by UPD of lead on gold single-crystal surfaces. *J. Electroanal. Chem. Interfacial Electrochem.* **144,** 351–363 (1983).
48. Jirkovsky, J. S., Halasa, M. & Schiffrin, D. J. Kinetics of electrocatalytic reduction of oxygen and hydrogen peroxide on dispersed gold nanoparticles. *Phys. Chem. Chem. Phys.* **12,** 8042–8053 (2010).
49. Blizanac, B. B., Ross, P. N. & Markovic, N. M. Oxygen electroreduction on Ag(111): The pH effect. *Electrochim. Acta* **52,** 2264–2271 (2007).
50. *CRC Handbook of Chemistry and Physics* (CRC Press, 1996).

Acknowledgements

The authors gratefully acknowledge financial support from the Danish Ministry of Science's UNIK initiative, Catalysis for Sustainable Energy and The Danish Council for Strategic Research's project NACORR (12-132695). M.E-E. acknowledges financial support from EU PF7's initiative Fuel Cell and Hydrogen Joint Undertaking's project CathCat (GA 303492). B.W. thanks Formas (project number 219-2011-959) for financial support. The Center for Individual Nanoparticle Functionality is supported by the Danish National Research Foundation (DNRF54).

Author contributions

J.R. and S.S. conceived the DFT calculations. S.S. and M.K. performed the DFT calculations. A.V. and I.E.L.S. designed the experiments. A.V. performed the electrochemical experiments, D.D. the TEM, P.M. the XPS and B.W. the EQCM and SEM-EDS. E.A.P. and R.F. prepared the Ag_3Pt sample and performed its XRD. S.S., A.V. and I.E.L.S. co-wrote the first draft of the paper. A.V. designed the figures. All authors discussed the results and commented on the manuscript.

Additional information

Supplementary information is available in the online version of the paper. Reprints and permissions information is available online at www.nature.com/reprints. Correspondence and requests for materials should be addressed to I.E.L.S. or J.R.

Competing financial interests

Patent application EP 13165265.3 'Alloy catalyst material' has been filed.

CORRIGENDUM

Enabling direct H_2O_2 production through rational electrocatalyst design

Samira Siahrostami, Arnau Verdaguer-Casadevall, Mohammadreza Karamad, Davide Deiana, Paolo Malacrida, Björn Wickman, María Escudero-Escribano, Elisa A. Paoli, Rasmus Frydendal, Thomas W. Hansen, Ib Chorkendorff, Ifan E. L. Stephens and Jan Rossmeisl

Nature Materials **12,** 1137–1143 (2013); published online 17 November 2013; corrected after print 21 November 2013.

In the version of this Article originally published, the middle initials of the penultimate author were missing; the name should have read Ifan E. L. Stephens. In the Author contributions and Additional information sections 'I.S.' should have read 'I.E.L.S.' These errors have now been corrected in the online versions of the Article.

nature materials

SUPPLEMENTARY INFORMATION

DOI: 10.1038/NMAT3795

Enabling direct H_2O_2 production through rational electrocatalyst design

Samira Siahrostami[1a], Arnau Verdaguer-Casadevall[2a], Mohammadreza Karamad[1], Davide Deiana[3], Paolo Malacrida[2], Björn Wickman[2,4], Maria Escudero-Escribano[2], Elisa A. Paoli[2], Rasmus Frydendal[2], Thomas W. Hansen[3], Ib Chorkendorff[2], Ifan Stephens[2]*, Jan Rossmeisl[1]*

[1]Center for Atomic-scale Materials Design, Department of Physics, Technical Univ. of Denmark, DK-2800 Kongens Lyngby, Denmark

[2]Center for Individual Nanoparticle Functionality, Department of Physics, Technical Univ. of Denmark, DK-2800 Kongens Lyngby, Denmark

[3]Center for Electron Nanoscopy, Technical Univ. of Denmark, DK-2800 Kongens Lyngby, Denmark

[4]Department of Applied Physics, Chalmers University of Technology, SE-41296 Göteborg, Sweden

[a] These authors contributed equally to this work.
*Corresponding authors.

DOI: 10.1038/NMAT3795

Energy cost for H_2O_2 synthesis technologies

The reaction $H_2(g) + O_2(g) \rightarrow H_2O_2(l)$ is highly exothermic, with a standard Gibbs free energy of -120 kJ mol^{-1}.

The method which is currently used industrially to synthetize H_2O_2 is based on the anthraquinone process, which is very energy intensive[1]. The main reason for that is that the anthraquinone process needs to work at low temperatures (45-60 C). Given that hydrogen peroxide synthesis is an exothermic reaction, a significant amount of energy has to be used in cooling the reactor.

A fuel cell based device producing hydrogen peroxide and operating at 0.5 V of potential difference between anode and cathode would generate 96 kJ mol^{-1}. Alternatively, one could use an electrolyser with water oxidation at the anode and oxygen reduction to hydrogen peroxide at the cathode. Accounting for a potential difference of 1 V, this means that the energy cost would be 192 kJ mol^{-1}.

Alloys screened for electrochemical synthesis of H_2O_2

Fig. S1 displays a two-electron volcano activity for all the alloys screened in this work. We use HOO* calculated free energy (ΔG) as a descriptor to construct the activity volcano. Slothful reaction steps involving a positive ΔG_{HOO*} are either activation of O_2 to form HOO* or reduction of HOO* to form H_2O_2. We studied thirty different alloys, which all include single active sites. They can be summarized in three different categories. In the first category (black circles), less active closely packed Au surface is applied to make single site of active metals named X in Fig. S2a, where, X: Zn, Pt, Pd, Cu, Rh, Ru, Co, Ni. The second category embraces closely packed surfaces of active metals Y: Pt, Pd and Rh to make a surface alloy of less active Au, Ag and Hg to isolate surface atoms of the active metals (blue triangles) (Fig. S2b). Intermetallic compounds (bulk alloys) of Pt and Pd with Hg, Ag and non-noble metals such as In, Sn and Pb is the last studied category (red squares) (Fig. S2c, S2d, S2e, S2f).

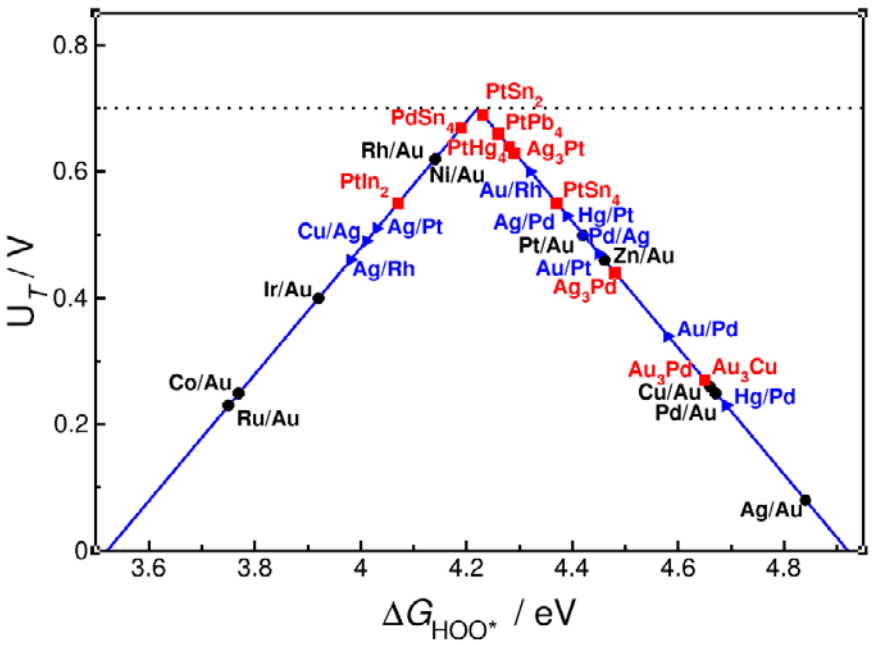

Figure S1. 2-electron activity volcano for electrochemical synthesis of H_2O_2. Three categories of alloys have been studied. Black circles are the surface alloys of Au(111). Blue triangles are the surface alloys of Pd, Pt and Rh. Bulk alloys of Pt, Pd and Cu are shown by red squares. All the alloys have isolated active sites. The equilibrium potential of two-electron reduction of O_2 to H_2O_2 is shown as a dotted line.

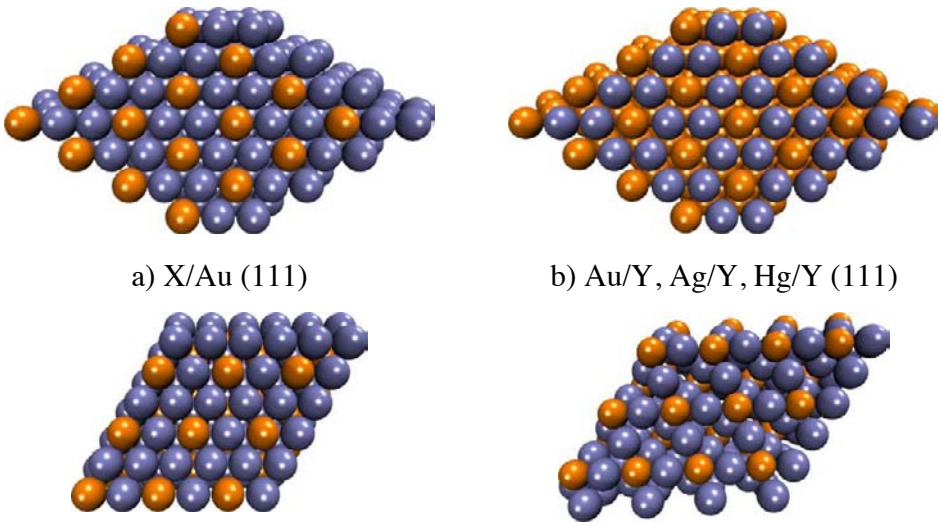

a) X/Au (111)

b) Au/Y, Ag/Y, Hg/Y (111)

DOI: 10.1038/NMAT3795

c) Ag_3Pd, Ag_3Pt, Au_3Pd (111)

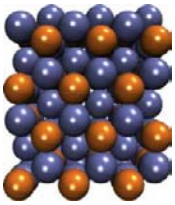

d) $PtHg_4$ (110)

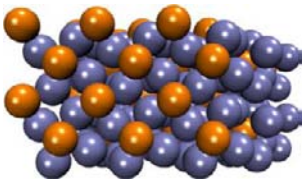

e) $PtIn_2$(111), $PtSn_2$(111)

f) $PtSn_4$(001), $PtPb_4$(100)

Figure S2. Structure of different studied alloys. Common feature of all of the alloys is that the active transition metal (orange) is isolated within a surrounding inert transition metal (blue). Two different sets of surface alloys with gold and non-gold substrate are displayed in a) and b), respectively. Four categories of bulk alloys (see the text above) are displayed in (c), (d), (e), and (f).

Electronic structure calculations

The total energies of different adsorbates on each surface were calculated with Density Functional Theory (DFT) using grid-based projector-augmented wave method (GPAW) code [3,4]. The calculations were performed using RPBE as exchange-correlation functional [5]. For all alloys, their lattice constant(s) were optimized for their crystal systems. Extended model slabs were constructed for all surfaces considered in this study including surface alloys and bulk alloys. In the surface alloys, the slabs were constructed to face center cubic structure (fcc) with closed packed (111) surfaces. For all surface alloys, the lattice constants were assumed to be the same as host metal. The surface alloys were modeled using a four-layer $(\sqrt{3} \times \sqrt{3})R30^{\circ}$ slab corresponding to guest atoms coverage of 1/3 ML. Very similar adsorption energies obtained with lower coverage of guest atoms suggests that the results are independent of the coverage of the guest atoms. Brillouin zones were sampled using $6 \times 6 \times 1$ Monkhorst-Pack k-points. The bottom two layers were fixed in their bulk structure while the upper layers and adsorbates were allowed to relax.

In the case of the bulk alloys of Ag_3Pt, Ag_3Pd and Au_3Pd with face-centered cubic (fcc) crystal structure, closed packed (111) surfaces were assumed and the surfaces were

modeled using four-layer 2×2 slabs. Brillouin zones were sampled using $6 \times 6 \times 1$ Monkhorst-Pack k-points and the bottom two layers were fixed while the upper layers and adsorbates were allowed to relax.

The bulk alloy of $PtHg_4(110)$ structure was modeled using an eight-layer 2×2 slab size. The corresponding Brillouin zones were sampled using $4 \times 4 \times 1$Monkhorst-Pack k-points. The bottom four layers were kept fixed while the upper layers and adsorbates were allowed to relax. Other bulk alloys, including $PtPb_4(100)$, $PtSn_4(001)$, $PtSn_2(111)$, and $PtIn_2(111)$, were modeled using 7-, 8-, 10- and 10-layer slabs with 4-, 4-, 5- and 5-layer fixed respectively. At least 16 Å of vacuum was set to separate the successive slabs in all calculations. Adsorption was only allowed on one side of the slabs. All structures were allowed to relax in all direction until residual forces were less than 0.05 $eV/Å$. Moreover, in all cases, convergence of total energy with respect to grid spacing and k-point set were considered.

All adsorption sites (atop, bridge and hollow) were considered and only the most stable ones are used here. All free energies are calculated relative to $H_2O(l)$ and $H_2(g)$. Zero point energies and entropies were included in energetics calculations[6]. We assume that HO* and HOO* exposed to liquid water are stabilized similarly on all alloys. Hence we did not apply any correction for solvation effect on considered alloys.

We have used computational hydrogen electrode (CHE) approach to calculate the free energy levels of all intermediate states[6]. In this model, the electrode potential, U (versus the reversible hydrogen electrode), is taken into account by shifting the electron energy by $-eU$ when an electron is transferred. The overpotential is defined as the maximum positive free energy difference between successive intermediate states.

Stability Test for Screened Alloys

In addition to exhibiting high activity and selectivity, a successful catalyst for electrochemical reduction of O_2 to H_2O_2, should be stable under reaction conditions. To examine the stability of the alloys, three stability criteria as shown in the following are imposed: 1) metal dissolution, 2) thermodynamic stability, 3) oxygen poisoning.

DOI: 10.1038/NMAT3795

1- The constituents of the alloys should have more positive dissolution potentials than the potentials at which the reduction of oxygen occurs. Otherwise, there would be a driving force for the catalyst to dissolve into the solution and for its activity to degrade over time. We have chosen an upper limit of 0.5 V (RHE) for the standard dissolution potential. As shown in Fig. 2c in the main text, seven elements including Cu, Co, Ni, Pb, Sn, In and Zn are unstable against dissolution under the operating potentials. On this basis, we exclude twelve alloys from further consideration. This, in turn, means that even though $PtPb_4$ and $PtSn_2$ have optimal OOH* binding energies that put them very close to the top of activity volcano, they would not be stable experimentally.

2- The alloys should be thermodynamically stable, i.e. the free energy of formation from their constituent elements should be negative. The alloying energies were calculated for all surface and bulk alloys as below:

$$\Delta E_{Alloy} = E(Alloy) - E(constituents)$$

$E(Alloy)$ and $E(constituents)$ are the total energy of the alloy and its constituent elements in the metallic form respectively.

Fig. S3 shows the calculated ΔG_{HOO*} as a function of the formation energy to identify alloys that fulfill both stability and activity criteria. The orange dashed line specifies the optimal HOO* free energy at 4.22 eV. The alloys with heat of formation above zero are not stable and should be excluded. However, due to uncertainty in DFT calculations and the fact that some alloys might form metastable phases, we have highlighted a wider range in free energy of formation to include such uncertainty. It is clear from Fig. S3 that all the alloys should be stable on the basis of this criterion, with the exception of Ag/Pt, Ru/Au and Rh/Au.

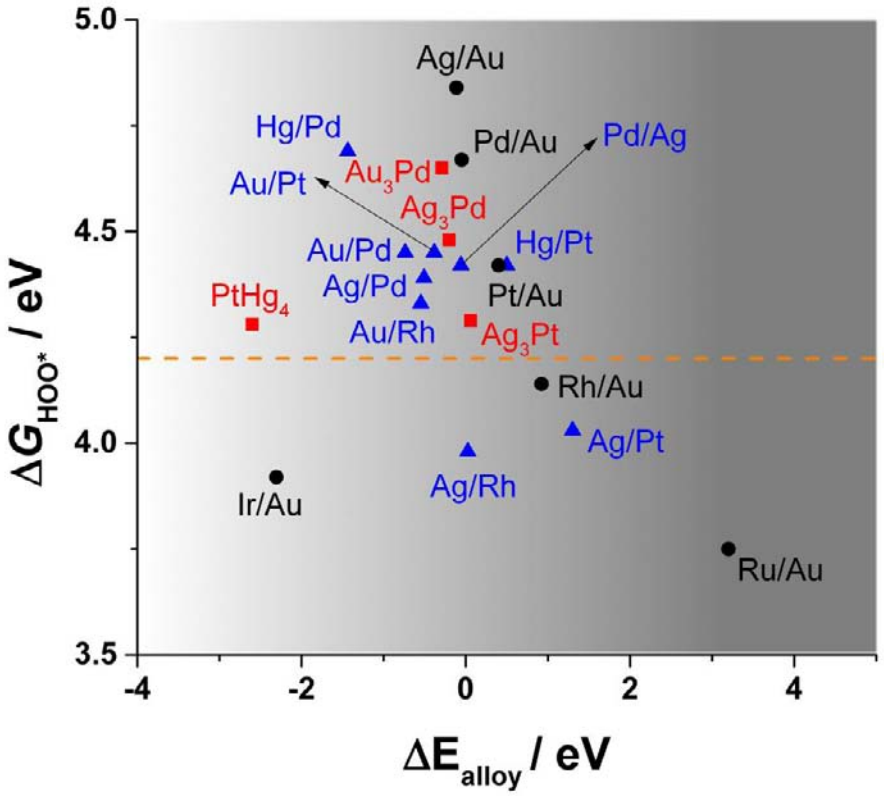

Figure S3: (a) Energy of formation and (b) dissolution potential of the constituent elements of the screened alloys as displayed in figure 2 in the main text.

3- As another important stability criterion, we considered the possibility of oxygen poisoning resulting from liquid water dissociation. In this case the active sites of the surface are poisoned and H_2O_2 synthesis is not preceded further. As shown in Fig.S4, calculated binding energies of O* on the bulk alloys and surface alloys are positive meaning that the oxygen poisoning from dissociation of water on the surfaces of these alloys is avoided.

DOI: 10.1038/NMAT3795

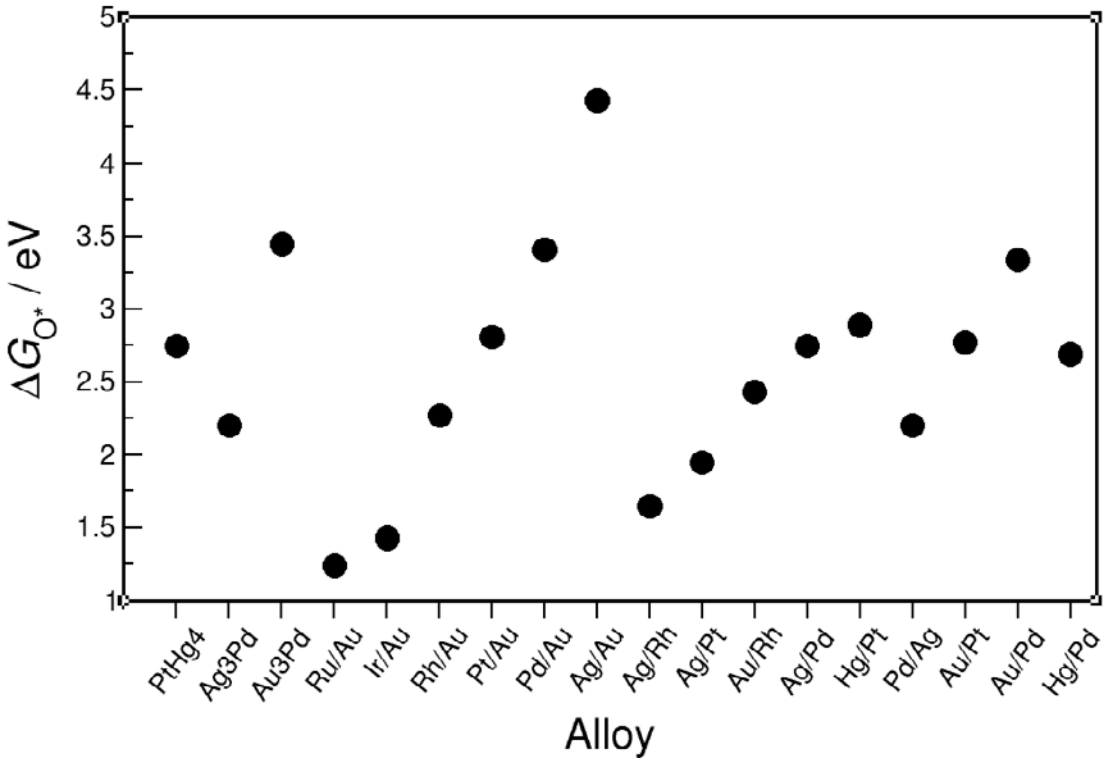

Figure S4: Oxygen poisoning in different alloy catalysts. As shown in the plot, all binding energies of O* are positive, meaning that oxygen poisoning from water dissociation is avoided.

Hydrogen binding energy on Pt(111) and $PtHg_4$ (110)

Calculated free energy of adsorption of hydrogen on Pt(111) and $PtHg_4$(111) are given in Table S1. Hydrogen binding on $PtHg_4$(110) is destabilized by 0.07 eV compared to Pt(111). This is due to the fact that on Pt(111) hydrogen binds to three-fold hollow sites while on $PtHg_4$(110) it binds to atop sites of Pt atoms. This difference is manifested qualitatively in the difference in voltammograms for Pt and Pt-Hg. While Pt-Hg does not exhibit any hydrogen adsorption/desorption peaks, Pt shows hydrogen adsorption/desorption features (see Figure 2d of the main text).

Surface	ΔG_{H^*}/eV
Pt(111)	-0.15
$PtHg_4$ (110)	-0.09

Table S1. Free energy of adsorption of hydrogen on Pt(111) and $PtHg_4$(110).

Selectivity

To identify selective alloys towards the 2-electron path, we constructed a 2-electron volcano and a 4-electron volcano in Fig. S5, where all the unstable alloys have been excluded. The position of closely packed pure metals, adapted from ref. [6] , such as Pt, Pd, Rh, Ir and Au are indicated for comparison. $PtHg_4$ stands out as the most active catalyst for 2-electron path presenting a theoretical overpotential 0.06 V away from the optimal. In fact, as can be seen from Fig. S5, $PtHg_4$ behaves differently from a pure Pt surface. Presence of surrounding Hg atoms weakens the binding energy of HO* by 0.37 eV compared to pure Pt and locates the alloy of $PtHg_4$ in the weak binding side of the 2-electron volcano (*electronic effect*). Fig. S6 compares the free energy diagram for 4-electron pathways of Pt and $PtHg_4$. As can be seen the oxygen binding energy in the case of Pt is stronger than that of $PtHg_4$. This in turn shows that the 4-electron pathway is dominant in the case of Pt and only small amounts of H_2O_2 can be formed. Even though

DOI: 10.1038/NMAT3795

the oxygen binding energy in the case of $PtHg_4$ is significantly weaker than Pt, it is still below the H_2O_2 free energy level. This means that the possibility of 4-electron pathway cannot be excluded and it is thermodynamically possible to dissociate $H_2O_2 \rightarrow O^*+H_2O$ or $HOO^* \rightarrow O^*+H_2O$. However, we found 96% of H_2O_2 in our experimental results on $PtHg_4$. On this basis, it seems that the kinetics of H_2O_2 or HOO* transformation to O^*+H_2O are very slow, even though they are thermodynamically possible [8]. This approach is reasonable since the two oxygen atoms of HOO* have different chemical environments and one would expect that the proton transfer barrier for each of these oxygen atoms would be different. The protonation of the oxygen atom bound to the isolated active site, i.e. Pt in $PtHg_4$, would result in H_2O_2. If the proton transfers to the other oxygen atom, on the other hand, it leaves a bound oxygen atom attached to the metal center and $H_2O(l)$ is released. Based on experimental evidence one can conclude that the kinetic barrier is higher in the latter case on $PtHg_4$ which results in H_2O_2 formation.

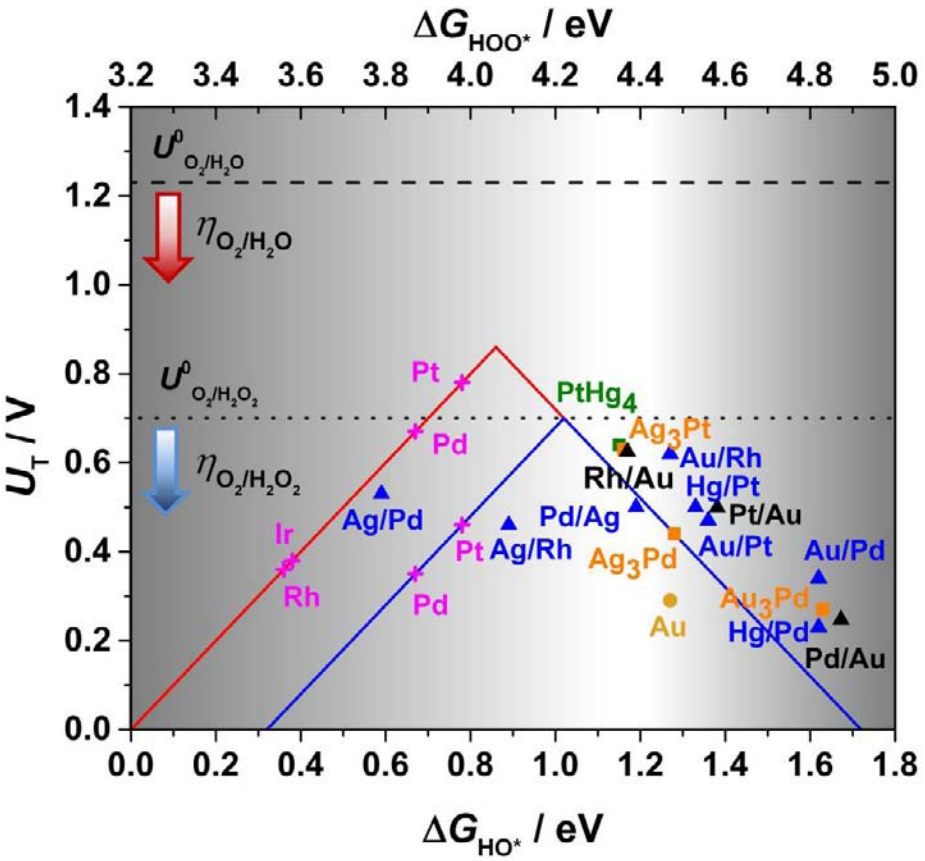

Figure S5. Theoretical volcano plot for 2-electron (blue) and 4-electron (red) reduction of O_2 including the potential stable alloys under ambient conditions. Three categories of alloys can be specified as black circles are the surface alloys of closely packed Au. Blue triangles are the surface alloys of Pd, Pt and Rh. Bulk alloys of Pt and Pd are shown by orange and green squares. The equilibrium potential of two-electron and four-electron reduction of O_2 are shown as dotted and dashed black lines, respectively.

DOI: 10.1038/NMAT3795

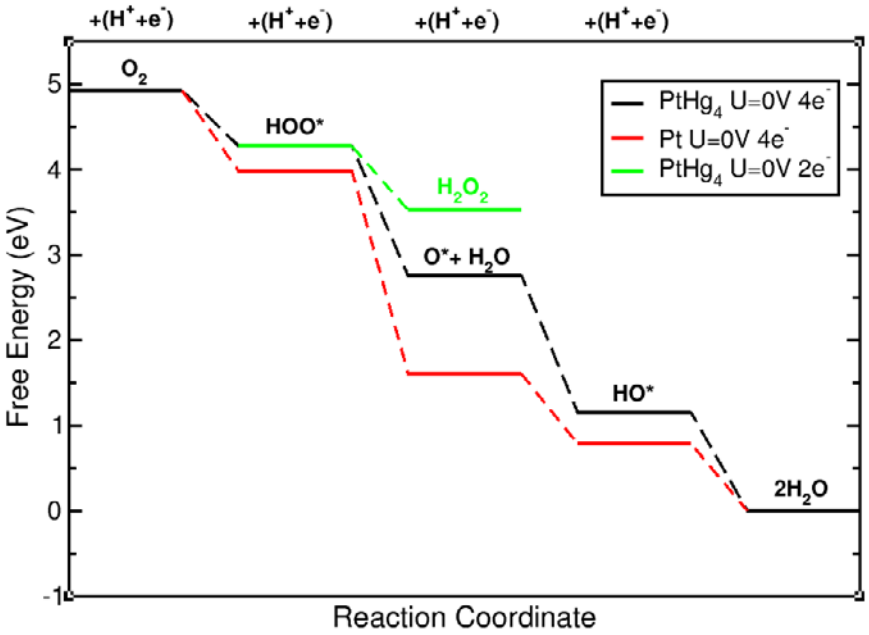

Figure S6. Free energy diagram for Pt as opposed to $PtHg_4(110)$ for the 4-electron oxygen reduction at $U = 0$ V. For $PtHg_4(110)$, the 2-electron pathway is also displayed by green color.

Ag_3Pt experimental characterization

To validate the stability criteria used in the theoretical screening, we synthetized and tested Ag_3Pt. While DFT calculations predicted such sample to be active, its negligible energy of formation should hinder the formation of the monoatomic ensembles required for high selectivity. Ag_3Pt was sputter deposited on a glassy carbon following the procedure outline below. XRD (X-ray diffraction) confirmed the presence of an ordered intermetallic in agreement with the literature, as presented in Fig. S7 [9]. The voltammogram in nitrogen (Fig. S8) did not show hydrogen adsorption and desorption features, consistent with the absence of contiguous Pt sites (see main article text) or that the surface is completely covered with Ag. Figure S9 shows the oxygen reduction activity. In agreement with our calculations, Ag_3Pt shows current to hydrogen peroxide at low overpotentials, albeit its selectivity is not as high as that of Pt-Hg. This could be due to the presence of islands of one or two contiguous Pt atoms, owing to an energy of formation close to zero for this alloy. It could also be attributed to the fact that Ag in itself is a more reactive material than Hg and not completely inert for oxygen reduction to

water [10]. However, after leaving the sample at open circuit (0.7 V) for about ten seconds, we observed a completely different behavior (Fig. S10). The total current at the disk was much higher, while currents to hydrogen peroxide became lower. This shows that the sample was active for the four-electron reduction of oxygen to water.

We can rationalize the poor performance of the catalyst on the basis that it is thermodynamically unstable against dissolution. According to Fig. 2c, the standard dissolution potential for silver is 0.79 V. Consequently, the corrosion potential for Ag deposition at pH 0 is 0.61 V (assuming a concentration of 10^{-6} M Ag^{2+} in solution). Since Ag_3Pt has a negligible energy of formation, the dissolution potential of the Ag would be the same as the bulk dissolution potential. These experiments demonstrate the importance of eliminating unstable alloys in the catalyst screening.

DOI: 10.1038/NMAT3795

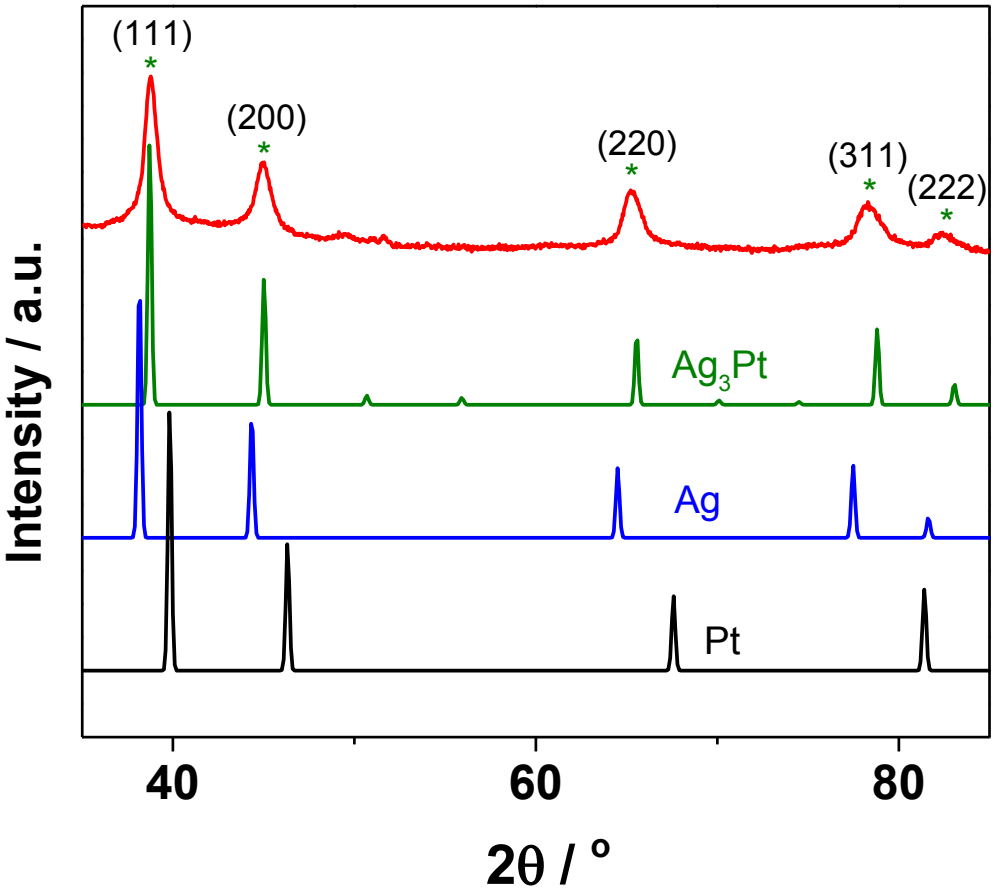

Figure S7. Grazing angle XRD for sputter deposited Ag_3Pt (red), together with reference patterns for Ag_3Pt (green) [9], Ag (blue) [11] and Pt (black) [9]. The five primary peaks of the sputter deposited sample can be identified as originating from planes of the Ag_3Pt alloy, as indicated by the green stars.

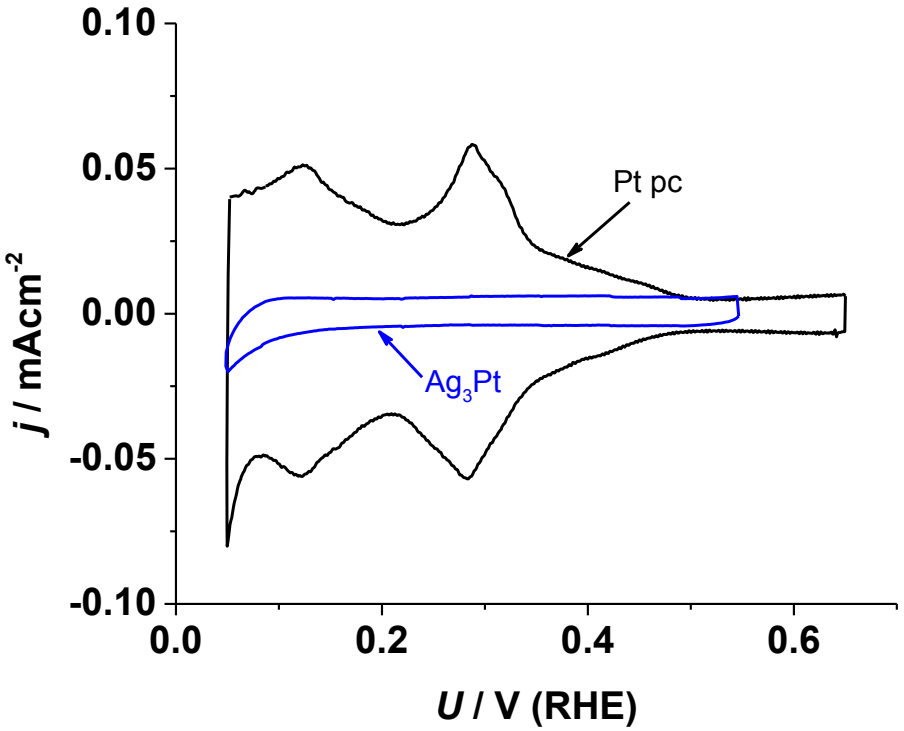

Figure S8. Cyclic voltammograms at 50 mVs^{-1} in N_2-saturated 0.1 M $HClO_4$ of Pt pc and Ag_3Pt. Interestingly, Ag_3Pt presents a flat profile, consistent with the absence of hollow Pt sites.

DOI: 10.1038/NMAT3795

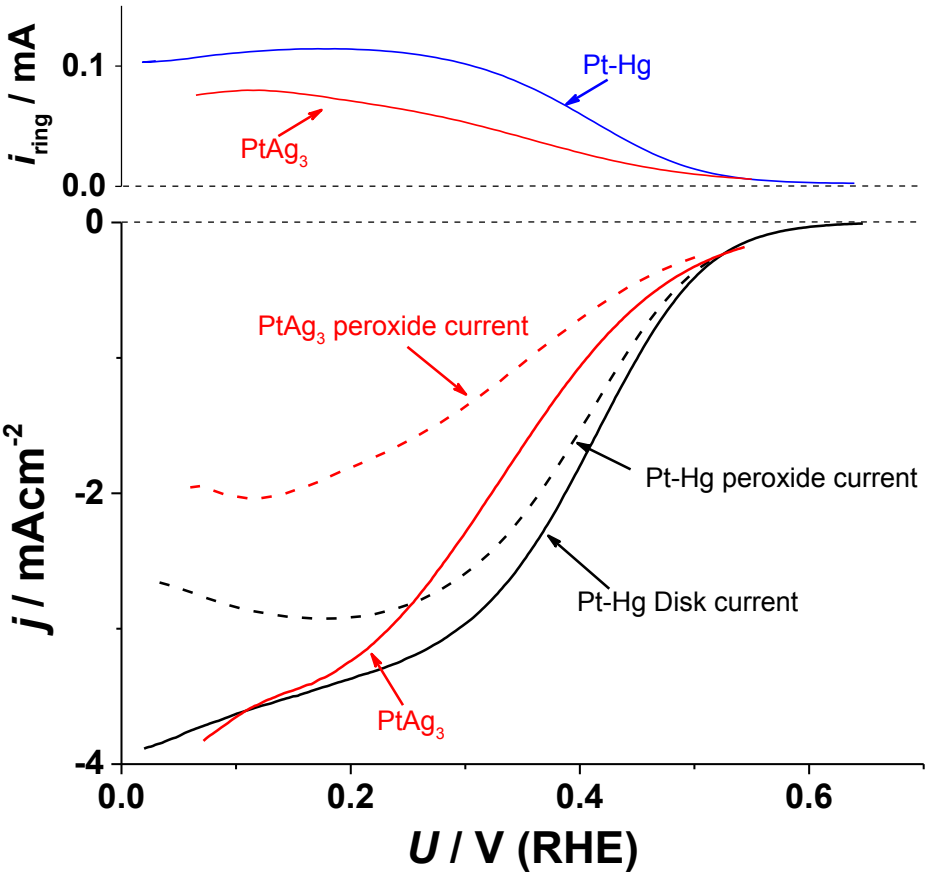

Figure S9. Oxygen reduction on Ag_3Pt (red) as compared to Pt-Hg (black). Measurements performed at 50 mVs^{-1} and 1600 rpm in O_2-saturated 0.1 M $HClO_4$. Importantly, the Ag_3Pt sample was inserted under potential control of ca 0.1 V into the electrolyte and the potential did not exceed 0.55 V during the experiment.

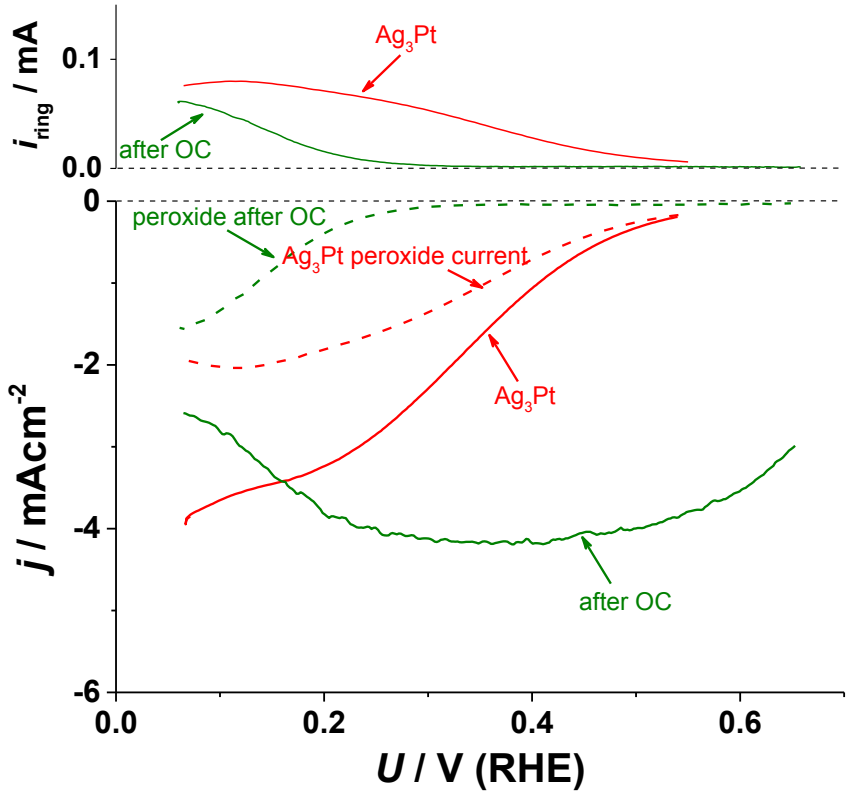

Figure S10. Comparison of oxygen reduction voltammograms for Ag_3Pt initially and after staying at open circuit potential (OC) for ten seconds. Measurements performed at 50 mVs^{-1} and 1600 rpm in O_2-saturated 0.1 M $HClO_4$.

Pt-Sn experimental characterization

In addition to Ag_3Pt, we tested Pt-Sn to evaluate its oxygen reduction activity. We synthetized this sample by electrodeposition of Sn from a Sn containing 0.2 mM $SnCl_2$ in 0.1M $HClO_4$ following the procedure by Kim et al. [12]. As described by Kim et al., this results in the formation of a bulk Pt-Sn alloy. The voltammograms in N_2 (Fig. S11) showed absence of the hydrogen adsorption/desorption peaks as for the other single-site catalysts. However, the sample was not stable under reaction conditions and had a behavior similar to Pt (Fig. S12). In fact, the voltammograms in N_2-saturated solution after oxygen reduction showed features characteristic of Pt (Fig. S11). This is consistent

DOI: 10.1038/NMAT3795

with Sn not being stable in the metallic form at high potentials, as explained in Figure 2 in the main text. It is also in agreement with experiments carried out by other groups [12, 13].

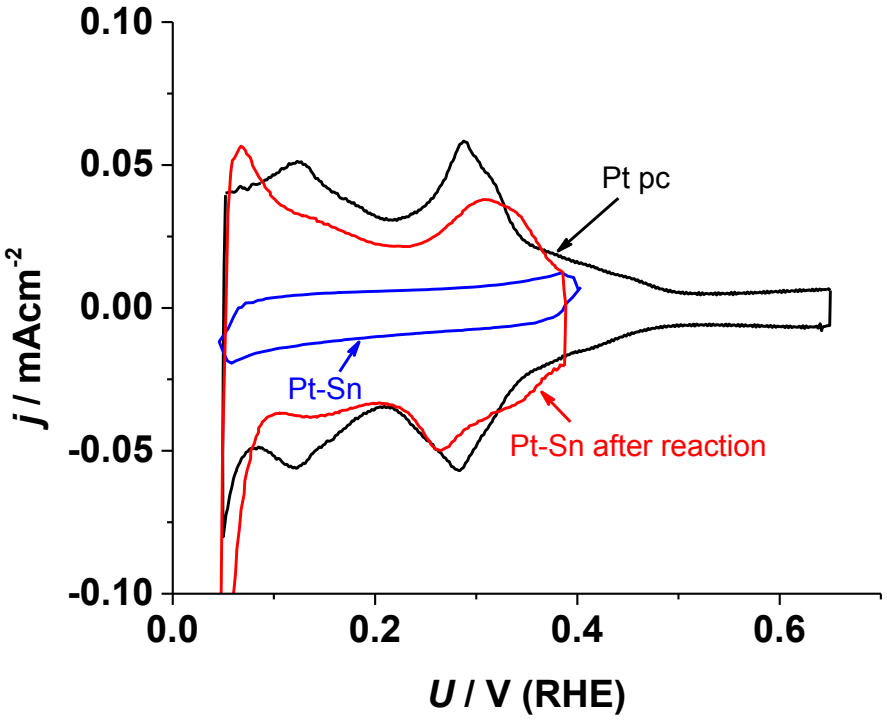

Figure S11. Cyclic voltammograms at 50 mVs^{-1} in N_2-saturated 0.1 M $HClO_4$ of Pt pc and Pt-Sn before and after oxygen reduction. Interestingly, Pt-Sn presents a flat profile before the reaction, while afterwards it becomes Pt-like. This is consistent with the notion that Sn is not stable under reaction conditions.

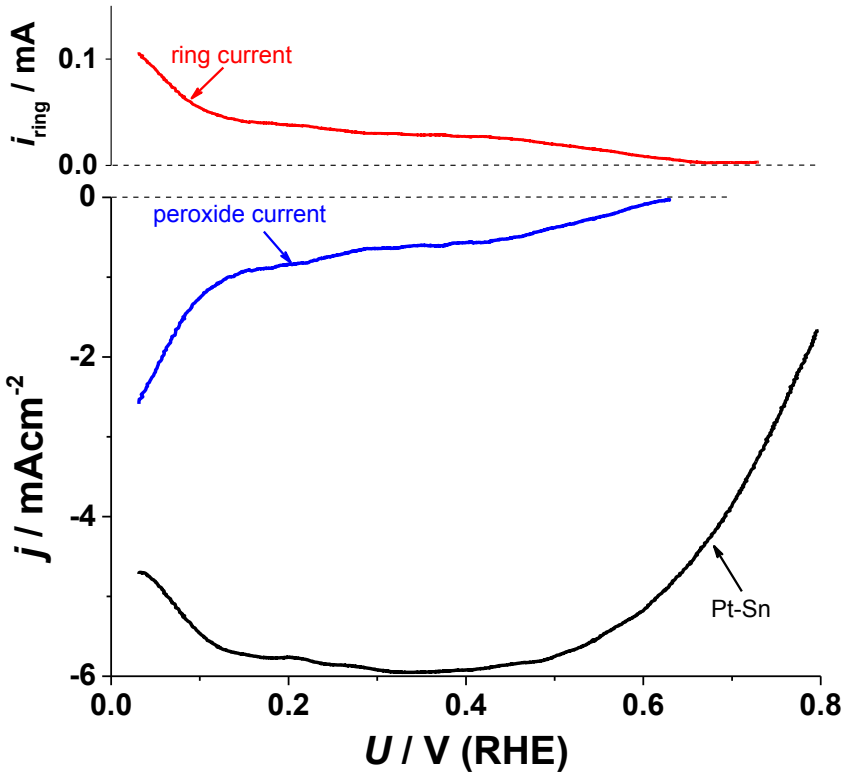

Figure S12. Oxygen reduction on Pt-Sn. The behavior is similar to pure Pt, consistent with the fact that Sn is unstable under reaction conditions. Measurements performed at 50 $mVs^{-1}$and 1600 rpm in O_2-saturated 0.1 M $HClO_4$.

Pt-Hg Extended surface characterization

We quantified the amount of Hg electrodeposited on polycrystalline Pt by electrochemical quartz crystal microbalance (EQCM) and integration of the Hg stripping peak. EQCM measurements were done with a QCM200 system (Stanford Research Systems) and a Pt covered 5 MHz quartz crystal. Mass change was obtained by transforming the shifts in resonance frequency using the Sauerbrey equation[14]. The analysis showed that there was no deposition of Hg (i.e a stable frequency) on Pt for potentials >0.8 V vs. RHE. When decreasing the potential to 0.2 V vs. RHE a constant mass increase caused by Hg deposition was observed and the rate corresponded to about 9.6 ng cm^{-2} s^{-1} (electrochemical Pt area). When the electrode was scanned up to 1.6 V vs. RHE, a stripping feature (see Fig. S13) corresponding to Hg stripping was observed. In

DOI: 10.1038/NMAT3795

the EQCM data, a large mass decrease took place simultaneously. The weight loss during the stripping (assuming it was only Hg leaving the electrode) and the stripping charge were in excellent agreement when assuming that mercury stripped as Hg^{2+}.

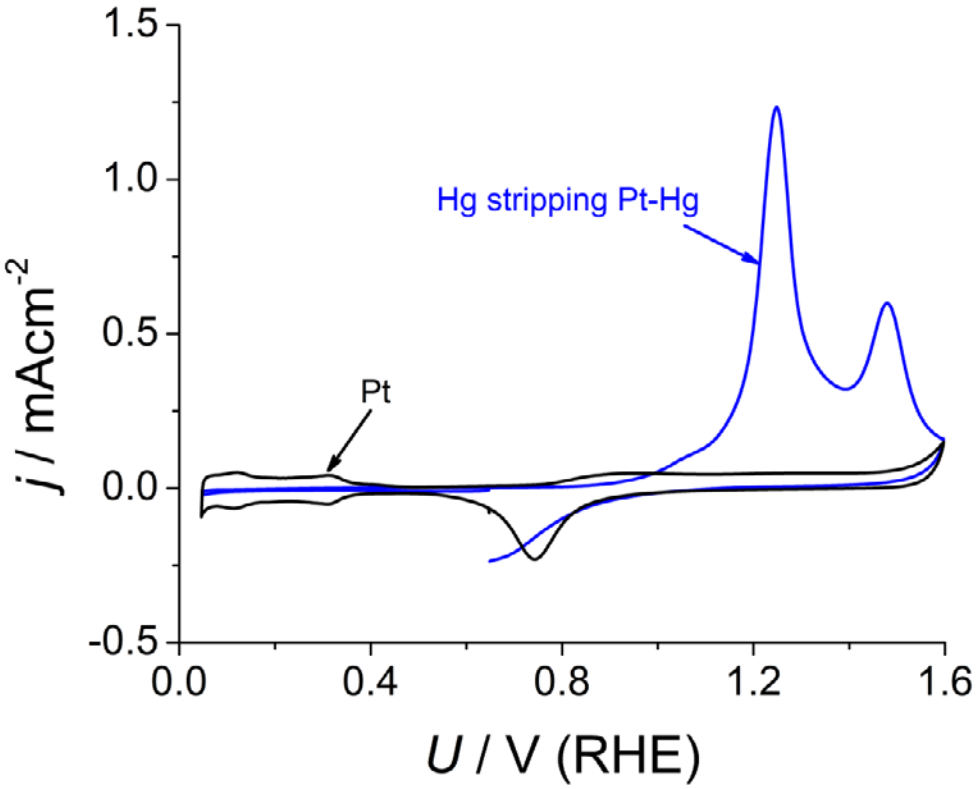

Figure S13. Hg stripping voltammetry on Pt-Hg (blue) and equivalent CV on Pt (black). The charge passed during Hg stripping is of 4.54 $mCcm^{-2}$, corresponding to 10.8 ML of Hg (1 ML gives 0.42 $mCcm^{-2}$). Measurement taken at 50 mVs^{-1} and 1600 rpm in 0.1 M $HClO_4$.

To ensure that Pt was present at the surface of the Pt-Hg polycrystalline electrode we carried out CO stripping measurements. The presence of a CO stripping charge on Pt-Hg shows that Pt is exposed at the surface.

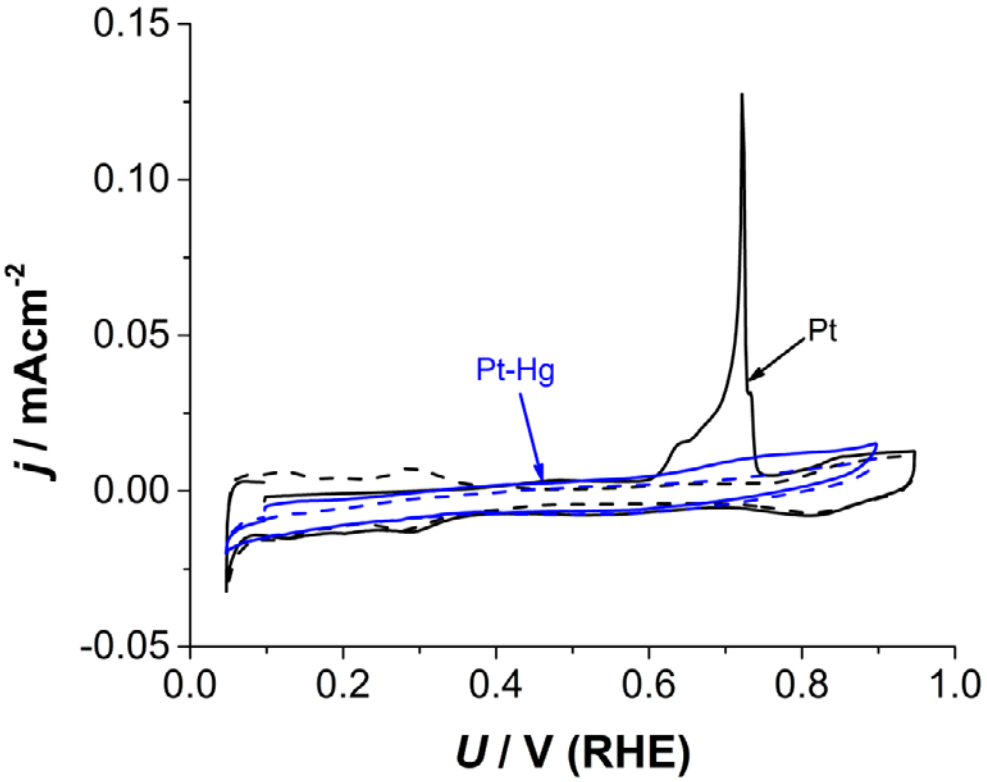

Figure S14. CO stripping for Pt (black, solid line) and Pt-Hg (blue, solid ine) and voltammetries in Ar-saturated solution (dashed lines). CO stripping charge is of 200 μCcm^{-2}, while for Pt is of 340 μCcm^{-2}. CO was adsorbed for 10 min at 0.05 V and the solution was saturated with Ar for 15 min before sweeping up the potential. Measurement taken at 50 mVs^{-1} in 0.1 M $HClO_4$.

DOI: 10.1038/NMAT3795

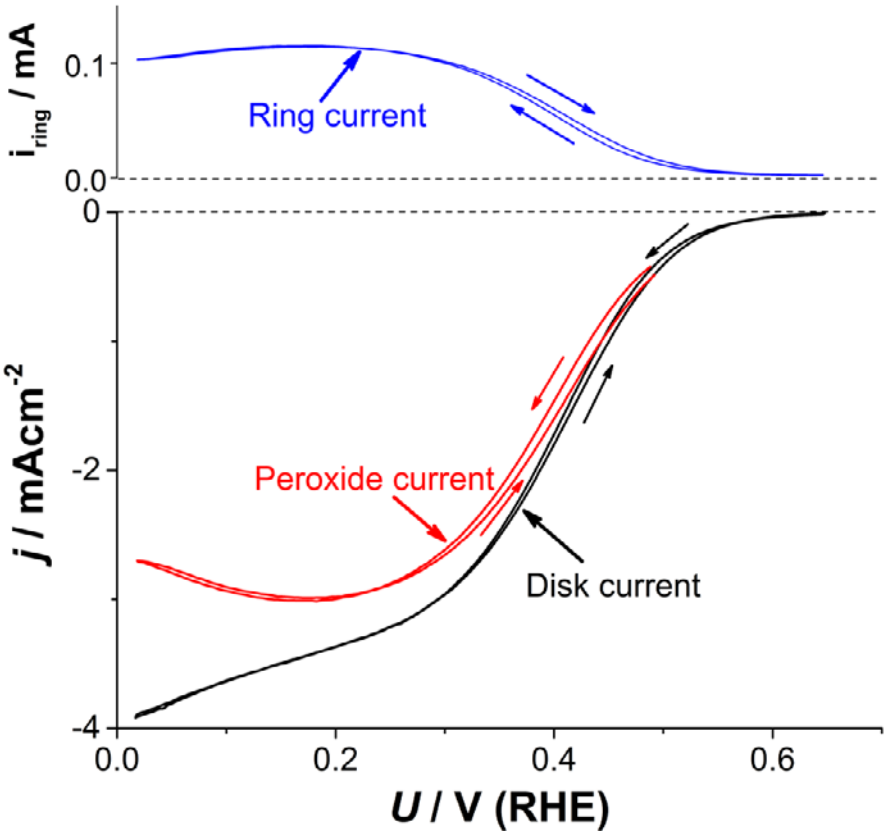

Figure S15. Cathodic and anodic RRDE voltammograms of Pt-Hg at 1600 rpm in O_2-saturated electrolyte with the disk current (black), ring current (blue) and corresponding current to hydrogen peroxide (red) obtained from the ring current. The arrows indicate the scan direction.

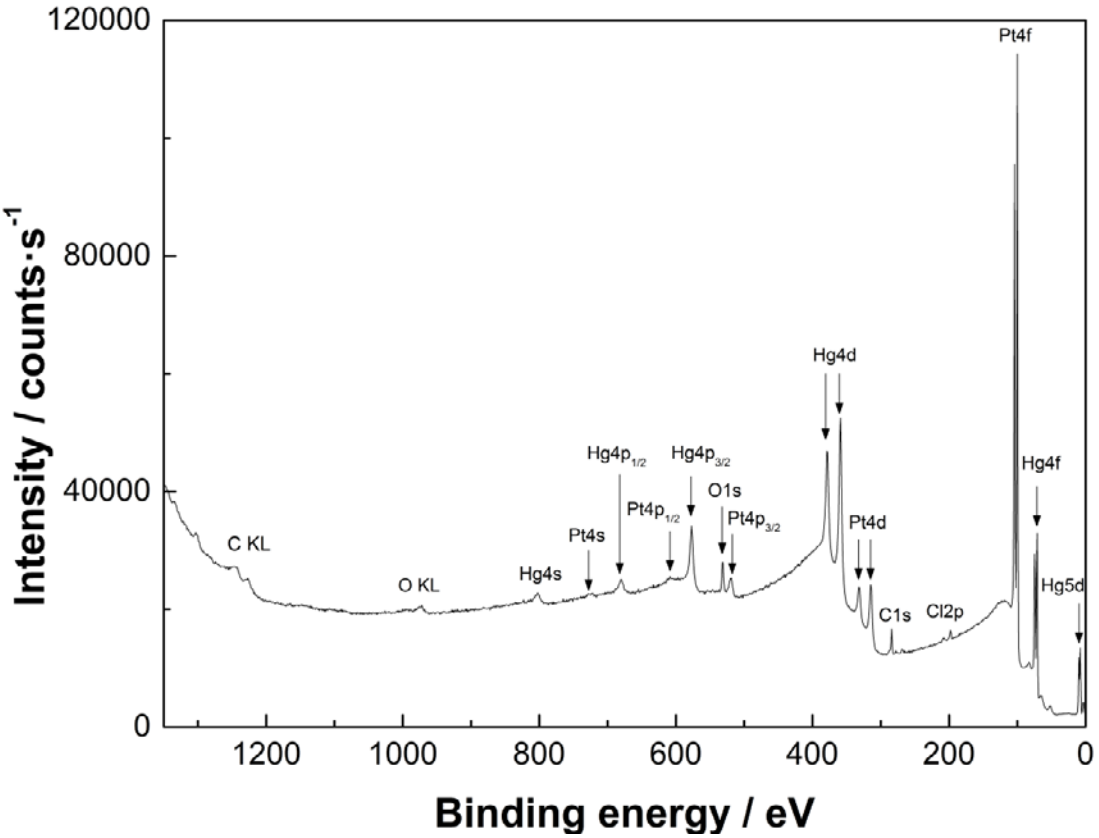

Figure S16. XPS survey of the Pt-Hg polycrystalline sample. The corresponding peaks have been signaled in the figure. C and O peaks arise from adventitious contamination in the transfer of the sample from electrolyte to the XPS system.

DOI: 10.1038/NMAT3795

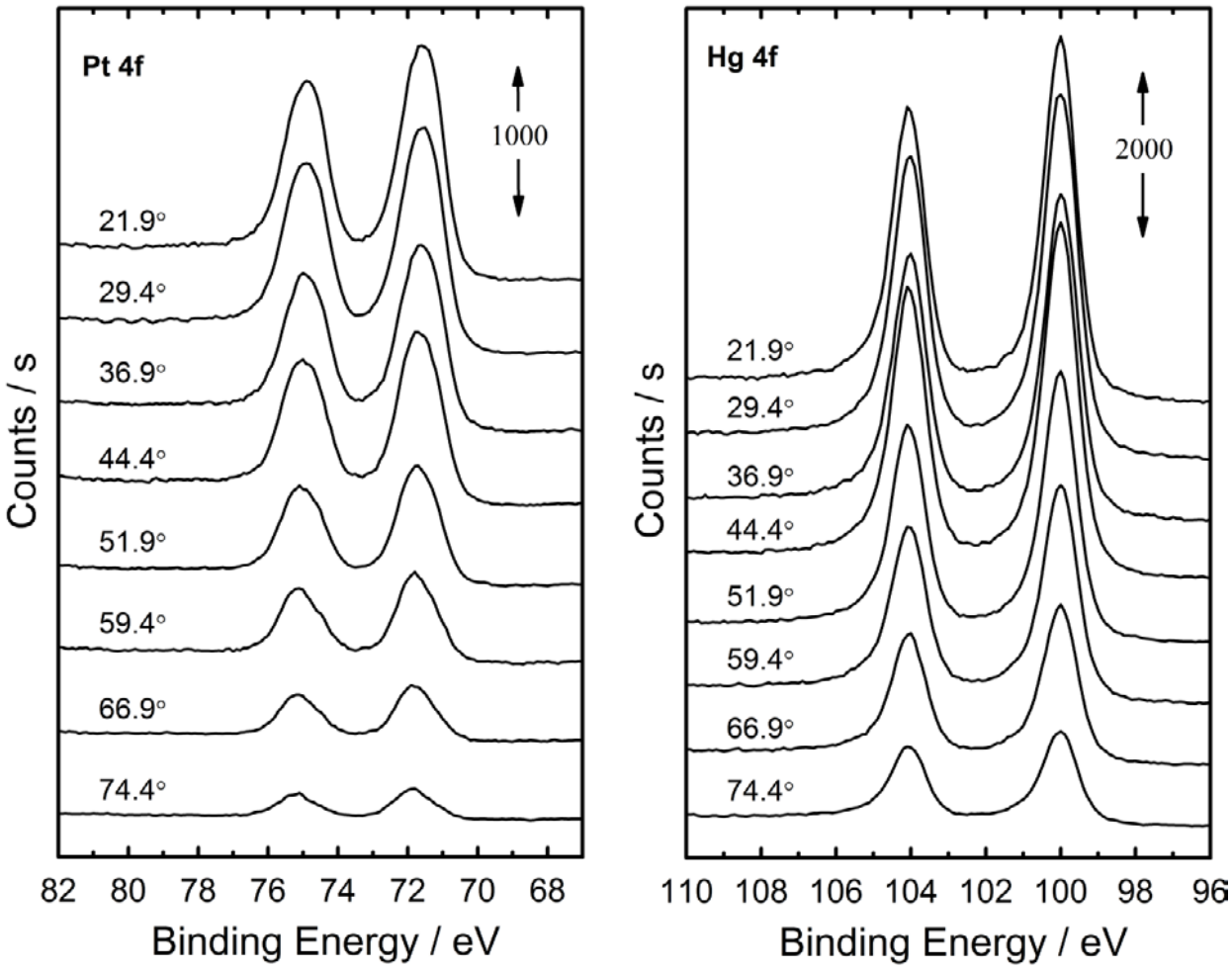

Figure S17. XPS for Pt (left) and Hg (right) peaks as a function of the angle.

Pt-Hg/C nanoparticles characterization

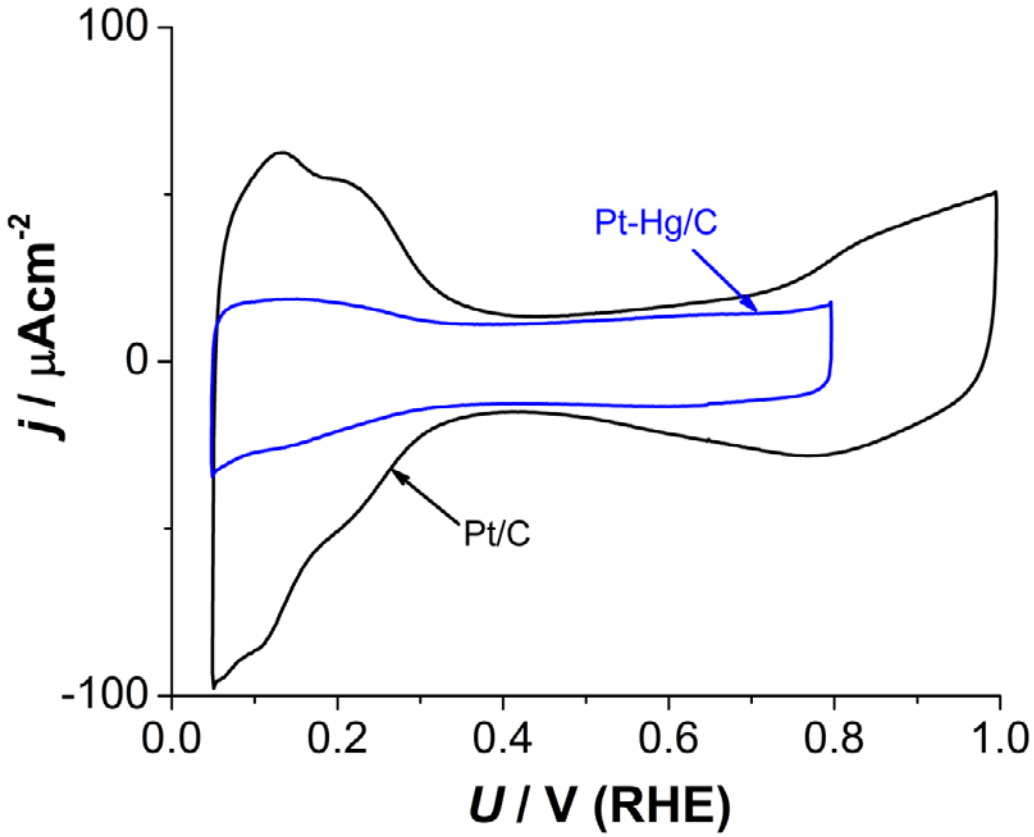

Figure S18. Voltammetries of Pt/C (black) and Pt-Hg/C (blue) in N_2 saturated solution. The flatter profile of Pt-Hg/C indicates that less contiguous Pt atoms exist. The charge in the H-upd region on Pt/C was used to calculate the surface area of both samples, corresponding to 1.07 ± 0.06 cm^2 (based on four independent measurements). Measurement taken at 50 mVs^{-1} in 0.1 M $HClO_4$ at room temperature.

DOI: 10.1038/NMAT3795

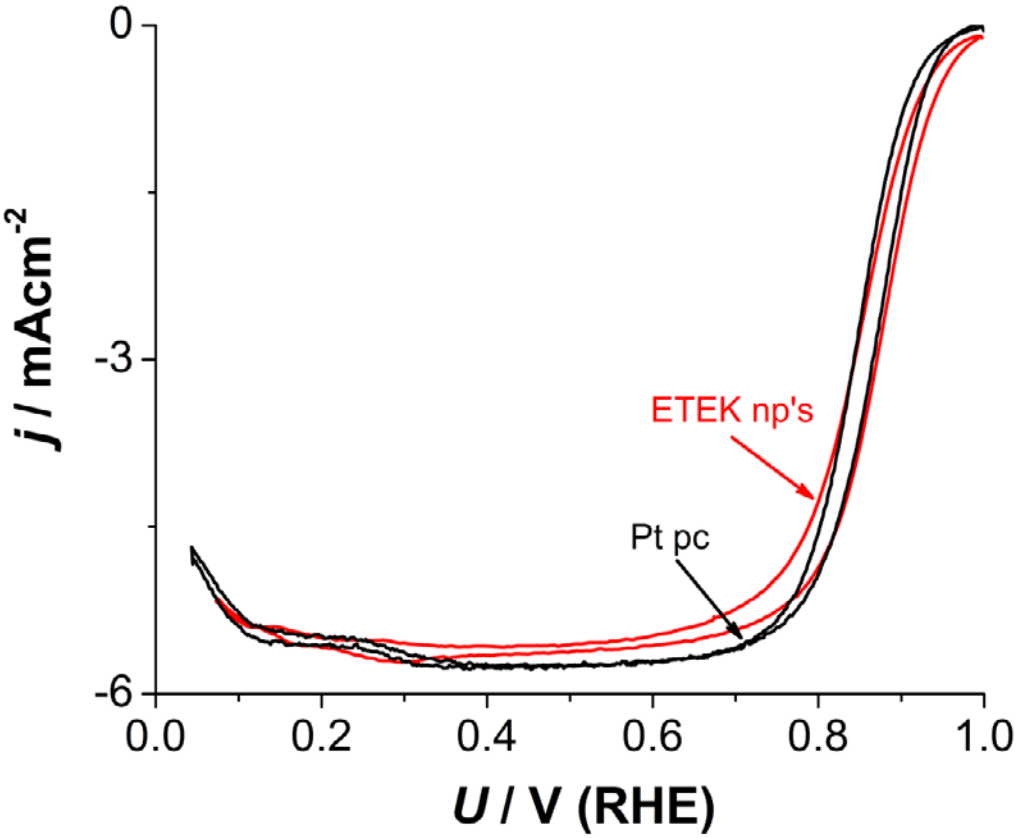

Figure S19. ORR on Pt ETEK nanoparticles (red) and Pt polycrystalline (black). The current has been normalized to geometrical surface area. Measurement taken at 50 mVs^{-1} and 1600 rpm in 0.1 M $HClO_4$ at room temperature.

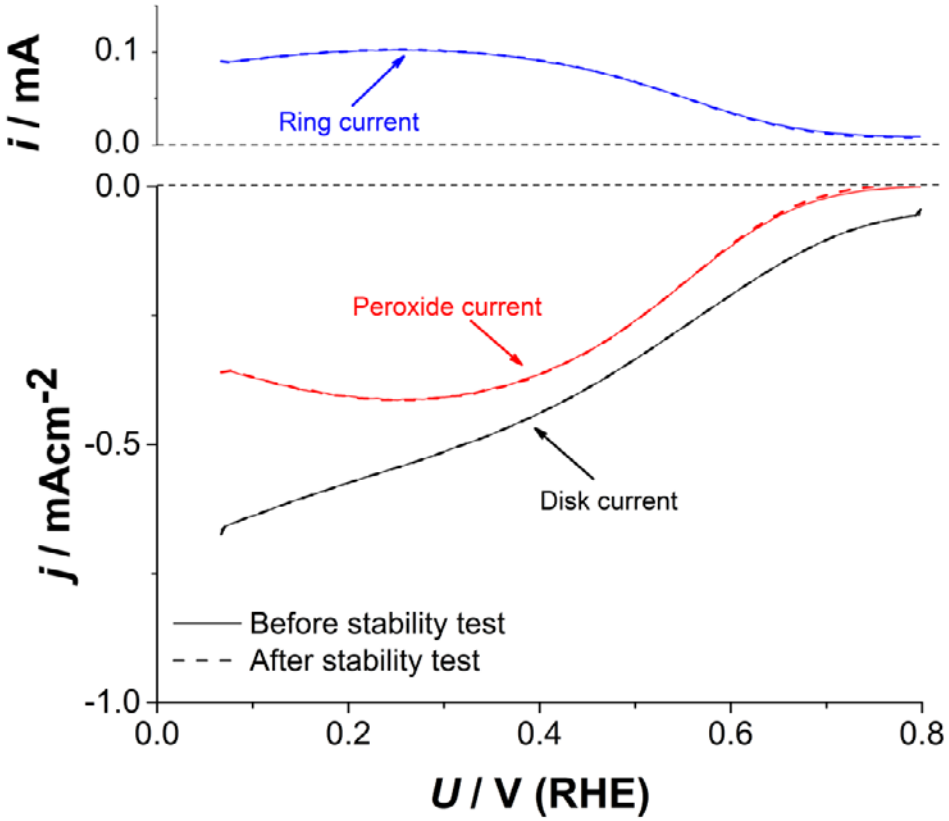

Figure S20. Stability test for Pt-Hg/C. Currents before stability test are shown in solid lines, while currents after the stability test are shown in dashed lines. Measurement taken at 50 mVs^{-1} and 1600 rpm in 0.1 M $HClO_4$ corresponding to the anodic cycle at room temperature. The stability test consisted of 8000 cycles at 200 mVs^{-1} between 0.05 and 0.8 V in oxygen saturated electrolyte. The electrolyte was replaced with a fresh one after the stability test.

To gain insight into the composition of the nanoparticles we used a combination of X-ray techniques: EDS and XPS. XPS is a surface sensitive technique, while EDS should represent the total atomic composition of the sample. From the measurements in figure S22 and S20, we obtained from XPS a 34 % Pt, 66 % Hg composition, while EDS showed a composition of 65 % Pt, 35 % Hg. Therefore, there is much more mercury on percentage near the surface than over the whole sample. This indicates that Hg is more abundant in the first layers of the nanoparticle after this type of deposition. These results are in agreement with the HRTEM images obtained showing a Pt core.

DOI: 10.1038/NMAT3795

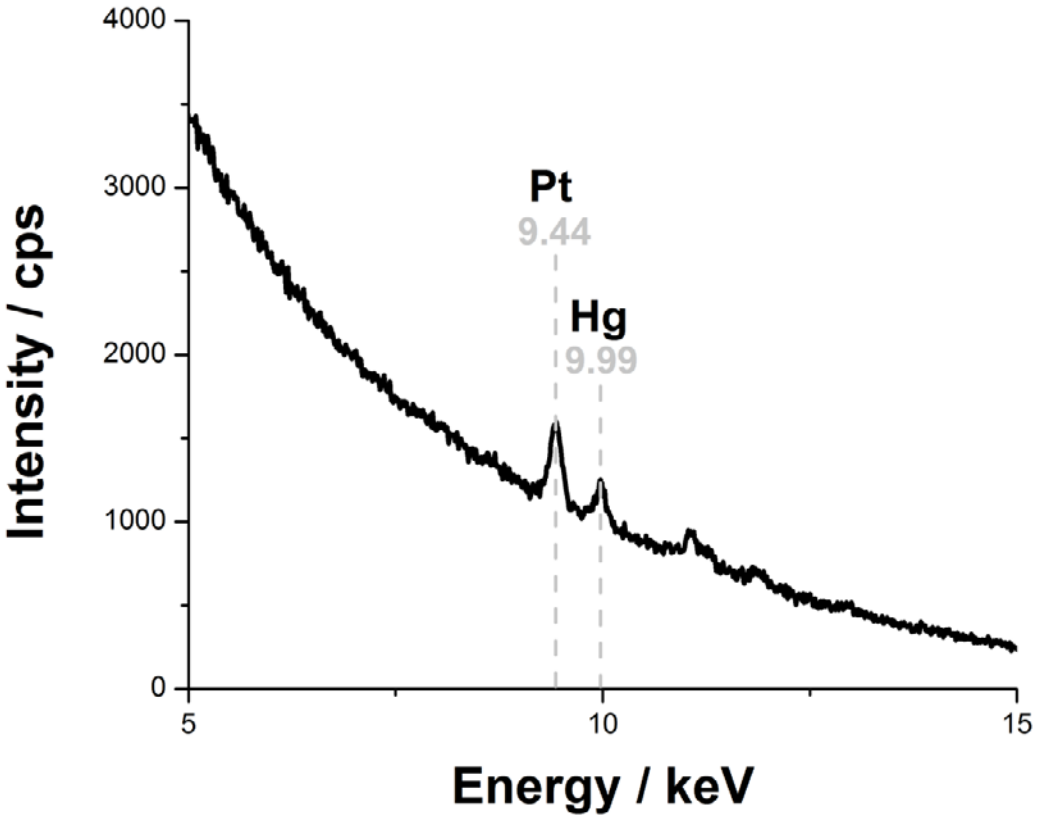

Figure S21. SEM X-Ray-EDS spectrum of Pt-Hg/C nanoparticles on a glassy carbon support. The corresponding Lα peaks of Pt and Hg used for quantitative analysis are signaled in the figure. The grey lines indicate the expected positions of such peaks. Quantification results in an atomic composition of 65 % Pt and 35 % Hg.

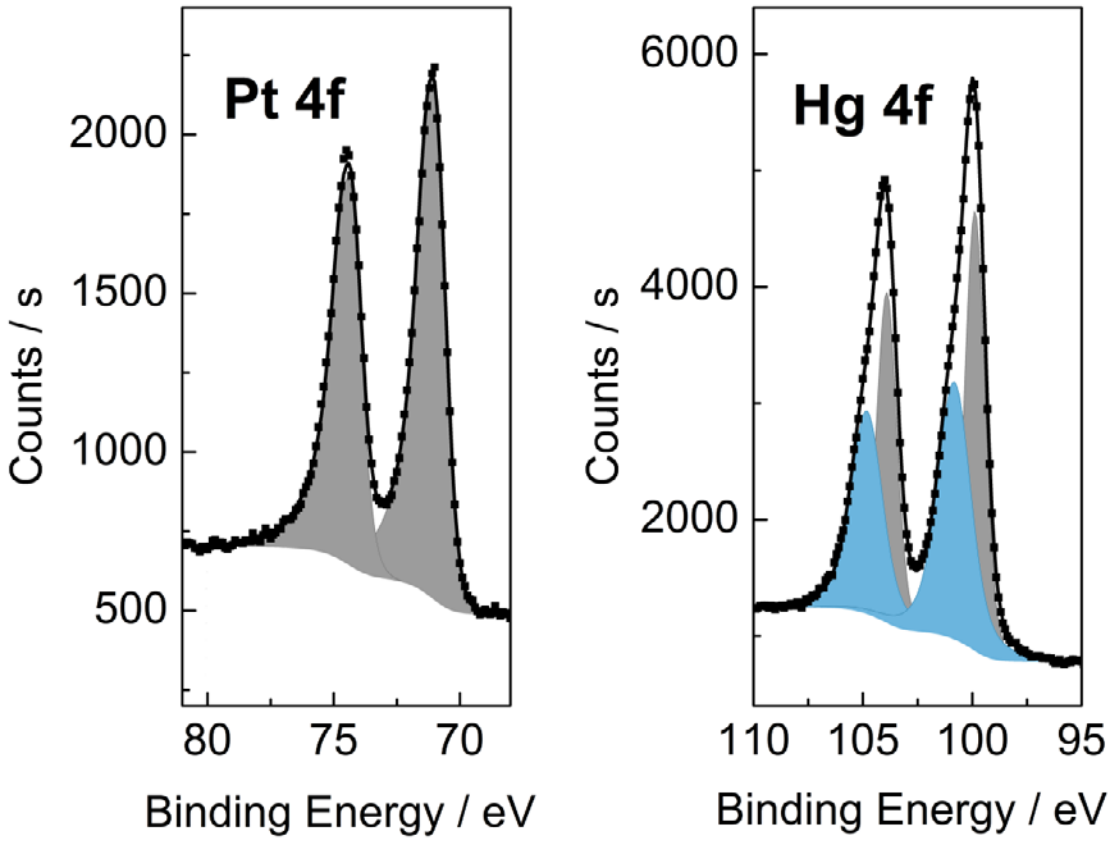

Figure S22. XPS for Pt (left) and Hg (right) in Pt-Hg/C nanoparticles. Grey areas correspond to metallic peaks, while blue ones correspond to oxidized ones (presumably due to exposure to air during the transfer of the sample). The sample atomic composition was 34 % Pt and 66 % Hg.

DOI: 10.1038/NMAT3795

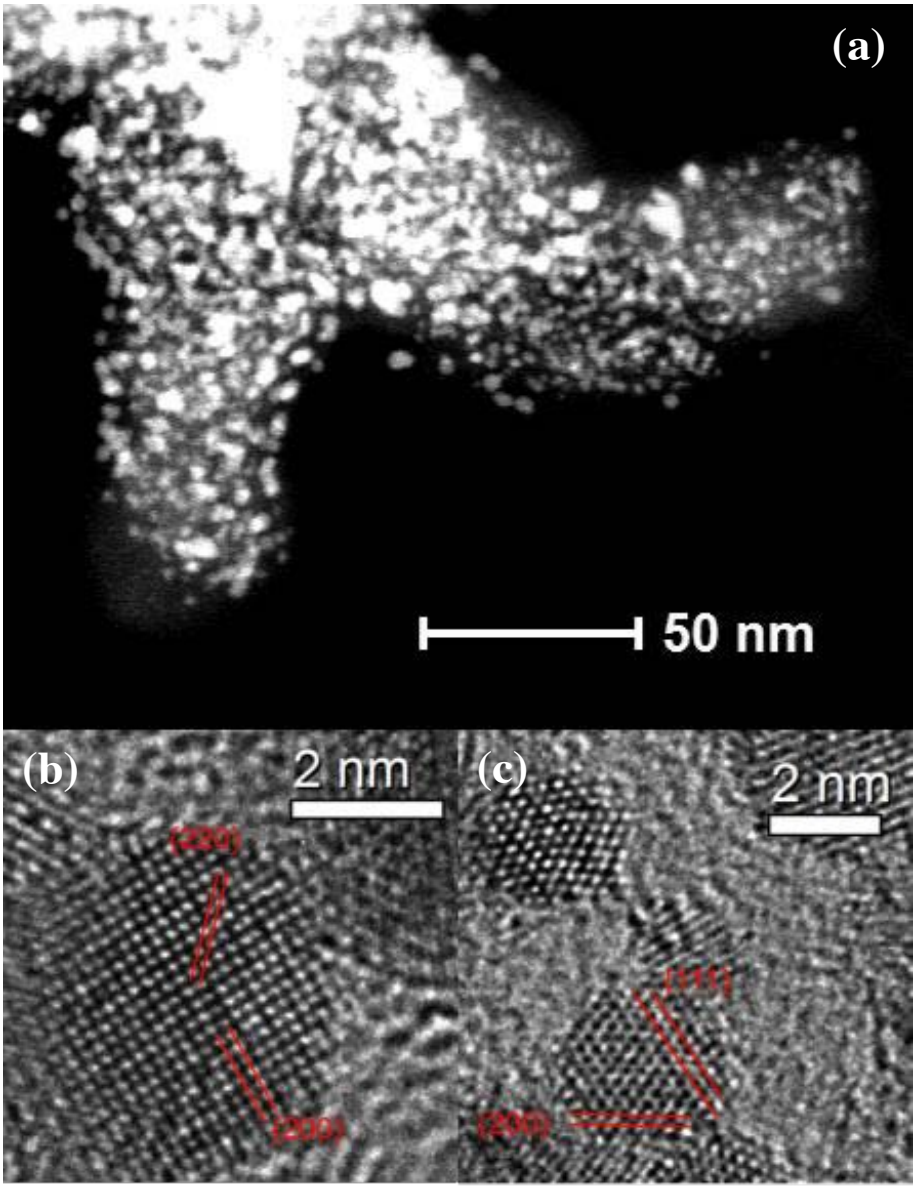

Figure S23. a) HAADF STEM image overview of the sample. b) and c) HRTEM images of different nanoparticles. Different families of planes are shown in the micrographs.

Permanganate titration

To ensure we were synthetising hydrogen peroxide we carried out an independent test not based on electrochemical methods: permanganate titration [15].

For this experiments, we used an H-cell with the counter electrode compartment separated from the working electrode by a Nafion membrane to avoid oxidation of hydrogen peroxide in the counter electrode. Additionally, in order to get higher concentrations of hydrogen peroxide the working electrode compartment had a volume of 15 mL. We then took a Pt foil (1.4 by 0.7 cm) and electrodeposited mercury in it. We transferred it to the H-cell and carried out oxygen reduction at 0.4 V for varying amounts of time, ranging from five minutes to one hour. Vigorous bubbling was used to stirr the solution and decrease mass transport limitations of oxygen to the electrode. After the selected time passed, we took a 10mL sample of the electrolyte and titrated it with 0.01 M potassium permanganate solution. We compared the values obtained from the titration to the charge passed to the experiment, as shown in Fig. S24. The good agreement between the results confirms the building up of hydrogen peroxide in the electrolyte.

DOI: 10.1038/NMAT3795

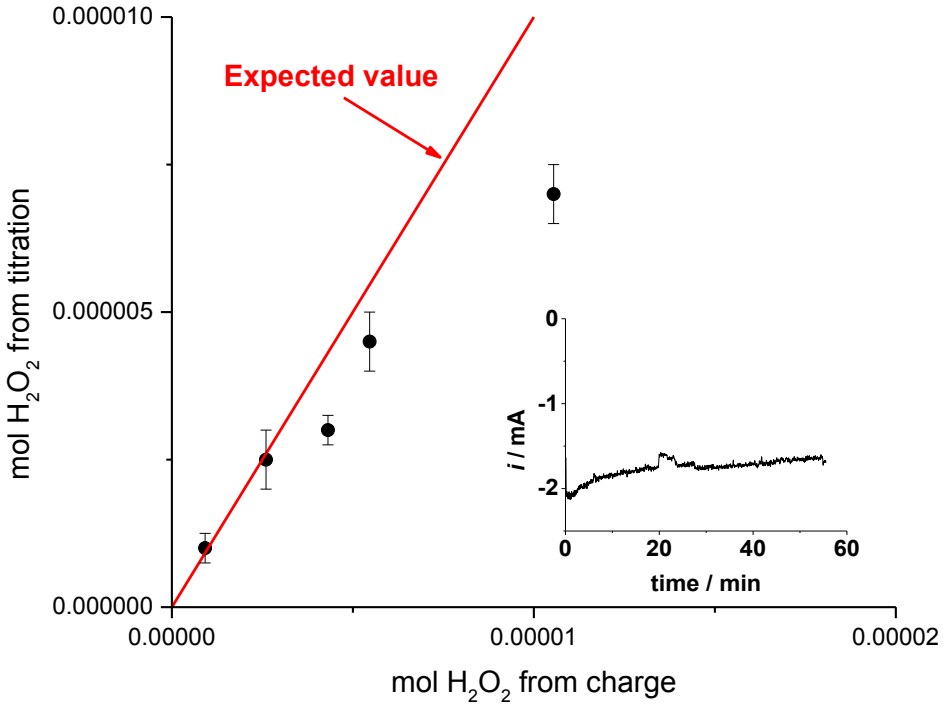

Figure S24. Comparison of two methods to measure hydrogen peroxide. On the X-axis, the mols of H_2O_2 expected from the charge (assuming a 96% selectivity to H_2O_2 as obtained in the RRDE experiments) are displayed. On the Y-axis, the mols of H_2O_2 obtained from potassium permanganate titration. The red line indicates the expected values of H_2O_2 from the charge. The experiments were performed for different amounts of time, ranging from five minutes to one hour, at a constant potential of 0.4 V in an H-cell. The titration was performed as described in the text. The error bars represent the uncertainty in the titration measurements. We note that for the longer experiments the results have a high inherent uncertainty due to evaporation of the electrolyte and possible hydrogen peroxide decomposition in contact with impurities or with the Nafion membrane.

Kinetic analysis and literature comparison

We performed various analysis to confirm that the equation $j_k = \frac{j \cdot j_d}{|j - j_d|}$ could be used. We first confirmed that the Koutecky-Levich equation was consistent with our measurements and then estimated the reaction order as one from measurements at different oxygen partial pressures.

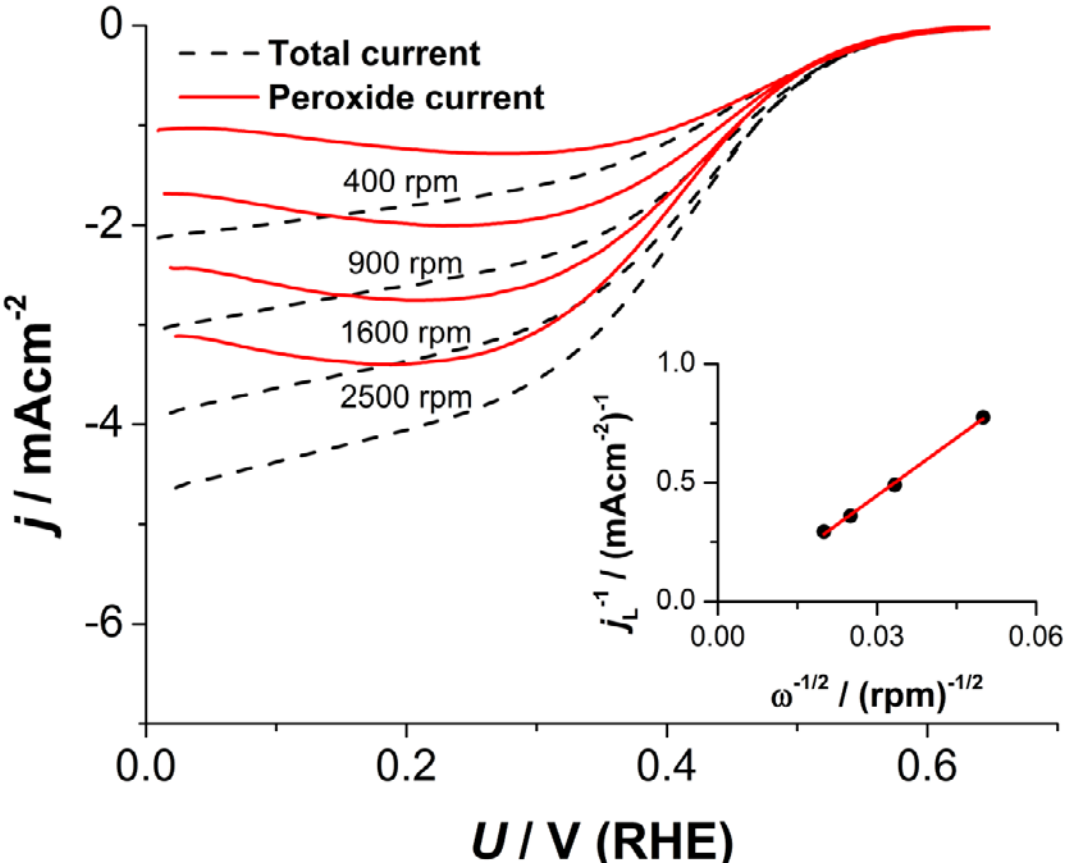

Figure S25. Oxygen reduction polarization curves at different rotation speeds (400, 900, 1600 and 2500 rpm). In the inset, Koutecky-Levich plot for the peroxide current (derived from the ring current). The total current is displayed in dashed black lines, while peroxide current is the red solid lines. The minimum of the peroxide current was taken as j_L for the Koutecky-Levich plot. Measurements on Pt-Hg polycrystalline sample at 50 mVs^{-1} in 0.1 M $HClO_4$ at room temperature.

DOI: 10.1038/NMAT3795

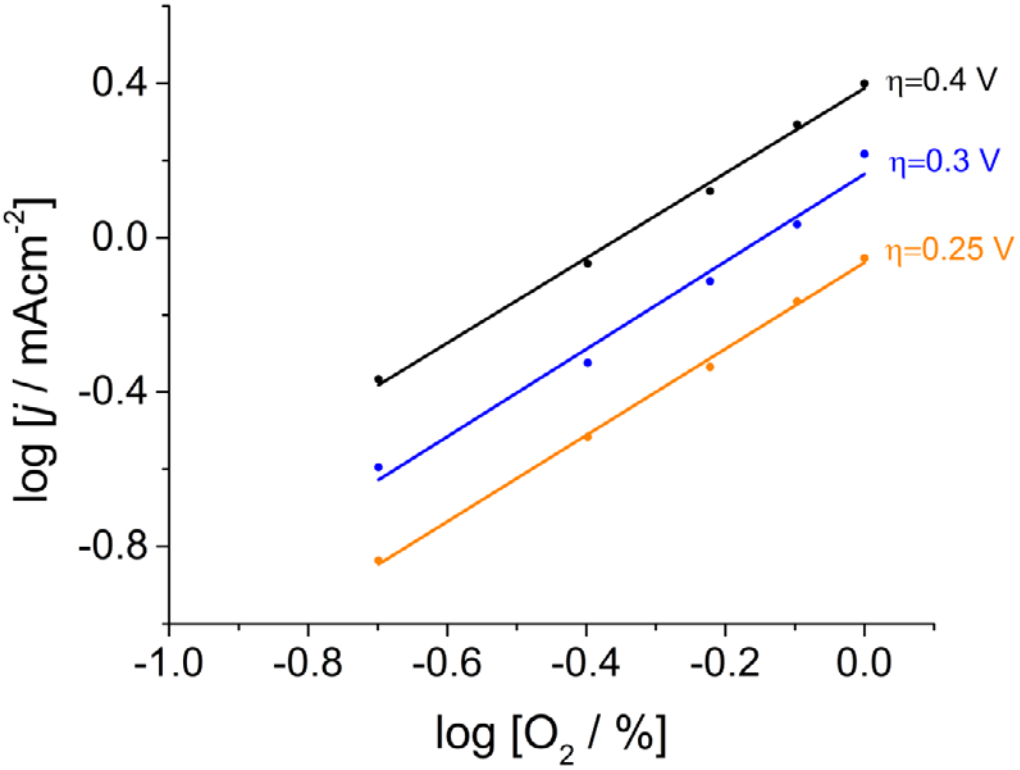

Figure S26. Double logarithmic plot of H_2O_2 current density (extracted from the ring current) at a fixed overpotential and partial pressure of O_2. Measurements for a Pt-Hg polycrystalline sample corresponding to the anodic cycle and taken at 50 mVs^{-1} and 1600 rpm. The overpotential is depending on the oxygen partial pressure and it was computed from the Nernst equation. The slope is of 1.1 for all potentials, but for simplicity we have assumed that the reaction order is one.

Electrode	Scan rate / mVs^{-1}	Reference	Comments
Pt pc	10	[16]	
Au 111	20	[17]	Assumed 100% of selectivity to H_2O_2
Au pc	10	[18]	
Ag 111	50	[10]	
Au/C	10	[19]	Surface area normalized according to Table 1in ref. [19]
Pd-Au/C	10	[19]	Surface area normalized according to Table 1 in ref. [19]
N doped C		[20]	Normalized to geometrical area; scan rate not specified
Pt-Hg	50	This work	
Pt-Hg/C	50	This work	

Table S2. Comparison of measurement conditions for different catalysts in the literature with activity for oxygen reduction to H_2O_2. All catalysts are measured at room temperature and in 0.1 M $HClO_4$ besides Au 111 where 0.5 M $HClO_4$ was used.

XPS measurements

Angle Resolved X-Ray Photoelectron Spectroscopy (AR-XPS) measurements were taken on a Theta Probe instrument (Thermo Scientific). The Ultra High Vacuum (UHV) chamber had a base pressure of 5 x 10^{-10} mbar. The X-ray source is monochromatized Al Kα (1486.7 eV), giving a resolution better than 1.0 eV at the employed pass energy of 100 eV. The analyser has an acceptance angle of 60°, between 20° and 80° to the surface normal. For the angle resolved profiles, 16 different channels were analyzed in parallel, without tilting the sample: this corresponds to 3.75° wide angle intervals. Angle resolved data were processed using the simulation tool, AR Process (Thermo Avantage software), which uses a maximum entropy method combined with a

DOI: 10.1038/NMAT3795

genetic algorithm to define the depth profiles: angles over 65° were omitted to minimize the effects of elastic scattering.

TEM analysis

To deposit the sample on the TEM grid, 10 μL of isopropanol were dropcasted on the glassycarbon electrode with freshly prepared Pt-Hg/C nanoparticles. After letting the isopropanol rest for a few seconds, it was pipetted back and deposited on a standard carbon-coated Cu TEM grid.

High resolution TEM measurements were performed in a FEI Titan 80-300 microscope at 300 kV accelerating voltage with a spherical aberration corrector on the objective lens. X-ray EDS analysis were carried out in High resolution STEM mode in a FEI Titan 80-300 microscope operated at 120 kV accelerating voltage equipped with a probe corrector on the condenser system and an EDS (Oxford Instruments) INCA x-sight detector. The spectra were acquired with the EDS detector set to 2000 channels, energy resolution set to 10 eV/channel and an integration time of 60 seconds.

Ag_3Pt deposition

Ag_3Pt thin films were deposited onto a Glassy Carbon disk, by a magnetron sputtering system (AJA International, Inc., A300), equipped with a confocal configuration. The sputtering targets were 2-inch disks of platinum and silver metal with purities of 99.95 % and 99.99 %, respectively (AJA International, Inc.). Platinum was deposited by RF sputtering and silver by DC magnetron sputtering. The vacuum chamber had a base pressure of 10^{-8} mTorr and the target-to-substrate distance was 15 cm. The deposition was carried out at 500 ºC and at a pressure of 3 mTorr in order to achieve the right phase [21]. The sputtering rates matched the 3:1 ratio at 40 W for platinum and 22 W for silver. The thickness of the film was 40 nm based on individual rates of the two metals measured with an *in situ* Quartz Crystal Microbalance.

Glancing angle XRD measurements

To identify the structure of the Ag_3Pt thin film, Glancing Angle XRD was performed with a Si wafer as substrate. The glancing angle XRD technique limits the signal from the substrate making it easier to single out information from the thin film. The measurements were conducted on PANalytical X'pert Pro XRD equipment with X-ray wavelength at 1.54 Å for the $Cu_{K\alpha}$ line. Alignment of the sample was performed with reflectometry and the incident angle set to $\omega = 0.5^o$. The scan range used was $2\theta = [35\ ;\ 85]$.

References

1. Eul, W., Moeller, A. & Steiner, N. in Kirk-Othmer Encyclopedia of Chemical Technology (John Wiley & Sons, Inc., 2000).
2. Hâncu, D., Green, J. & Beckman, E.J. H2O2 in CO2/H2O Biphasic Systems: Green Synthesis and Epoxidation Reactions. *Industrial & Engineering Chemistry Research* **41**, 4466-4474 (2002).
3. Mortensen, J.J., Hansen, L.B. & Jacobsen, K.W. Real-space grid implementation of the projector augmented wave method. *Physical Review B* **71**, 035109 (2005).
4. Lamy, C., Coutanceau, C. & Leger, J.-M. in Catalysis for Sustainable Energy Production 1-46 (Wiley-VCH Verlag GmbH & Co. KGaA, 2009).
5. Hammer, B., Hansen, L.B. & Nørskov, J.K. Improved adsorption energetics within density-functional theory using revised Perdew-Burke-Ernzerhof functionals. *Physical Review B* **59**, 7413-7421 (1999).
6. Nørskov, J.K. et al. Origin of the Overpotential for Oxygen Reduction at a Fuel-Cell Cathode. *The Journal of Physical Chemistry B* **108**, 17886-17892 (2004).
7. Jóhannesson, G.H. et al. Combined Electronic Structure and Evolutionary Search Approach to Materials Design. *Physical Review Letters* **88**, 255506 (2002).
8. Siahrostami, S., Bjorketun, M.E., Strasser, P., Greeley, J. & Rossmeisl, J. Tandem cathode for proton exchange membrane fuel cells. *Physical Chemistry Chemical Physics* **15**, 9326-9334 (2013).
9. Yan, X.S., Lin, P., Qi, X. & Yang, L. Finnis-Sinclair potentials for fcc Au-Pd and Ag-Pt alloys. *Int. J. Mater. Res.* **102**, 381-388 (2011).
10. Blizanac, B.B., Ross, P.N. & Markovic, N.M. Oxygen electroreduction on Ag(1 1 1): The pH effect. *Electrochim. Acta* **52**, 2264-2271 (2007).
11. Spreadborough, J. & Christian, J.W. HIGH-TEMPERATURE X-RAY DIFFRACTOMETER. *Journal of Scientific Instruments* **36**, 116-118 (1959).

DOI: 10.1038/NMAT3795

12. Kim, K.-W., Kim, S.-M., Kim, Y.-H., Lee, E.-H. & Jee, K.-Y. Sn Stability of Sn-Modified Pt Electrode for Reduction of Nitrate. *J. Electrochem. Soc.* **154**, E145-E152 (2007).
13. Hayden, B.E., Rendall, M.E. & South, O. Electro-oxidation of Carbon Monoxide on Well-Ordered Pt(111)/Sn Surface Alloys. *Journal of the American Chemical Society* **125**, 7738-7742 (2003).
14. Buttry, D.A. & Ward, M.D. Measurement of interfacial processes at electrode surfaces with the electrochemical quartz crystal microbalance. *Chemical Reviews* **92**, 1355-1379 (1992).
15. Huckaba, C.E. & Keyes, F.G. THE ACCURACY OF ESTIMATION OF HYDROGEN PEROXIDE BY POTASSIUM PERMANGANATE TITRATION. *Journal of the American Chemical Society* **70**, 1640-1644 (1948).
16. Verdaguer-Casadevall, A., Hernandez-Fernandez, P., Stephens, I.E.L., Chorkendorff, I. & Dahl, S. The effect of ammonia upon the electrocatalysis of hydrogen oxidation and oxygen reduction on polycrystalline platinum. *J. Power Sources* **220**, 205-210 (2012).
17. Alvarez-Rizatti, M. & Jüttner, K. Electrocatalysis of oxygen reduction by UPD of lead on gold single-crystal surfaces. *Journal of Electroanalytical Chemistry and Interfacial Electrochemistry* **144**, 351-363 (1983).
18. Jirkovsky, J.S., Halasa, M. & Schiffrin, D.J. Kinetics of electrocatalytic reduction of oxygen and hydrogen peroxide on dispersed gold nanoparticles. *Physical Chemistry Chemical Physics* **12**, 8042-8053 (2010).
19. Jirkovský, J.S. et al. Single Atom Hot-Spots at Au–Pd Nanoalloys for Electrocatalytic H2O2 Production. *Journal of the American Chemical Society* **133**, 19432-19441 (2011).
20. Fellinger, T.-P., Hasché, F., Strasser, P. & Antonietti, M. Mesoporous Nitrogen-Doped Carbon for the Electrocatalytic Synthesis of Hydrogen Peroxide. *Journal of the American Chemical Society* **134**, 4072-4075 (2012).
21. van der Vliet, D.F. et al. Mesostructured thin films as electrocatalysts with tunable composition and surface morphology. *Nat Mater* **11**, 1051-1058 (2012).

Paper IV

Intermetallic Alloys as CO_2/CO Reduction Electrocatalysts – the Role of Electronic and Geometric Effects

Mohammadreza Karamad, Vladimir Tripkovic and Jan Rossmeisl

Center for Atomic-scale Materials Design, Department of Physics, Technical University of Denmark, DK-2800 Kongens Lyngby, Denmark.

Abstract

Intermetallic alloys are investigated as CO_2/CO electroreduction (ER) catalysts. A novel strategy to direct the selectivity of these alloys to CO_2 reduction products is proposed. The strategy is based on suppressing the hydrogen evolution reaction (HER) by providing specific surface assemblies. These assemblies consist of transition metal (TM) elements that can reduce CO_2 (Ru, Co, Rh, Ir, Ni, Pd, Pt and Cu) separated by TM and post transition metal (PTM) elements (Ag, Au, Cd, Zn, Hg, In, Sn, Pb, Sb and Bi) that are very poor HER catalysts. Around 40 different stable binary bulk alloys forming from these elements are investigated. The electronic and geometric properties of the catalyst surface can be tuned by varying the size of the assemblies and the elements forming them. The strategy cannot prevent hydrogen poisoning of the metal assemblies when CO_2 is used as fuel. However, we have identified 5 different selective alloys on which CO can be reduced to methanol with overpotentials comparable to, or even lower than that on Cu. A common feature shared by these alloys is isolated single TM sites. The single TM sites play a key role in promoting the CO ER selectivity and blocking the HER.

Keywords: alloys, intermetallics, CO_2 reduction, CO reduction, standard hydrogen electrode, density functional theory.

Introduction

The electrochemical reduction (ER) of CO_2/CO to hydrocarbons and alcohols using intermittent renewable energy sources is a promising approach to store energy into chemical bonds for automotive and industrial applications [1]. The conversion of CO_2 to fuels would at the same time benefit environment by reducing the carbon footprint [2]. In the past, research efforts were concentrated on understanding the mechanism through which the CO_2 ER proceeds [3,4,5,6,7,8,9,10,11]. Hori was the first one to report CO_2 ER products categorized by the ability of

metals to bind CO and hydrogen [3,4]. According to his classification, formate is the primary product on metals with weak hydrogen and CO binding energies (Hg, Cd or Pb). On the other hand, metals with weak hydrogen and strong CO binding energies (Pt, Ni or Fe) reduce CO_2 to tightly adsorbed CO. As high overpotentials are required to further reduce CO, the primary reduction product for this group is hydrogen. The only metals that can catalyze carbon-oxygen bond breaking in CO_2, are those with moderate binding energies of CO and hydrogen (Cu, Au and Ag). However, Cu is the only metal on which CO can be uniquely reduced to hydrocarbons (methane and ethane), albeit accompanied with a very high overpotential [4].

There are three criteria that should be fulfilled in pursuit for new catalyst materials: 1) the stability criterion – the catalyst should be stable at potentials of interest so that the activity does not degrade over time. 2) the selectivity criterion - the catalyst should have a high selectivity towards desired products, 3) the activity criterion – the catalyst should have a high energy efficiency, i.e. a low reduction overpotential, [12]. Stability is not such a stringent requirement because negative potentials and neutral pHs make much milder environment compared to that in e.g. Proton Exchange Membrane Fuel Cells. [Gasteiger, Appl. Cat. B 2005]

The selectivity and activity towards the HER and CO_2 ER can be controlled via two effects: the *electronic effect* and the *geometric effect.* [13,14,15,16,17,18] The change in the electronic effect is accomplished by means of alloying, in which chemical properties of a host element are altered by the addition of a foreign element. This change can take place either through a ligand effect (vertical electronic effect) [] or stress (horizontal electronic effect) []. Changes in the electronic properties would reflect on the binding energies of H^* and different intermediates involved in the CO_2 ER. This could give rise to a catalytic activity and selectivity that is different from that of constituent elements [19]. The geometrical effect includes the changes in the surface geometry such as those when going from a terrace to a step surface. In addition, it also includes the changes brought by different number of atoms in small surface assemblies. The latter effect is usually called the ensemble effect. The ensemble effect can have profound influence on the activity. This has been well documented in the past. [1,2,3,4,5,6,7] For example, methanol and formic acid oxidation are very similar reaction in a sense that they both proceed through a same intermediate – CO; however, Pt_3Sn which is active for formic acid oxidation is at the same time very poor catalyst for methanol oxidation. [1, 4]

In the present study, we exploit the changes in the *electronic* and *geometric effects* with the aim to pinpoint new catalytic materials for the CO_2 ER. The strategy we propose is based on our current

theoretical understanding of catalytic activity of different metal elements towards the HER and CO_2 reduction [9,10,20,21,]. We set out to screen for new alloy catalysts of type A_xB_y, where element A is a metal capable of catalyzing the CO_2 ER and element B is a metal that has poor HER, as well as CO_2 ER activity. For element A we chose late TMs (Ru, Co, Rh, Ir, Ni, Pd, Pt and Cu) and for element B TMs (Ag, Au) and PTMs (Cd, Zn, Hg, In, Sn, Pb, Sb and Bi) [4,21]. The choice of the catalysts was guided by two rules. First, the alloys should be thermodynamically stable according to their phase diagrams (see Supporting Information) and second, they are not favored to form bulk oxides at potentials below 0 V vs. RHE [24]. The second rule practically eliminated early TMs and PTMs with lower principal quantum numbers (e.g. Al, Ga). To study ensemble effect the alloys were classified into two groups based on the distribution of TM atoms on the surface: 1) alloys with isolated TM sites, where single metal A is completely surrounded by atoms B and 2) metal A forms rows of atoms (every atom A has two nearest neighbors of the same type) embedded in the 'sea' of metal B. Fig. 1 shows the side and top view of two alloys, one with single active sites (Pt sites in $PtIn_2$) and the other with active rows of atoms (Cu rows in CuAu).

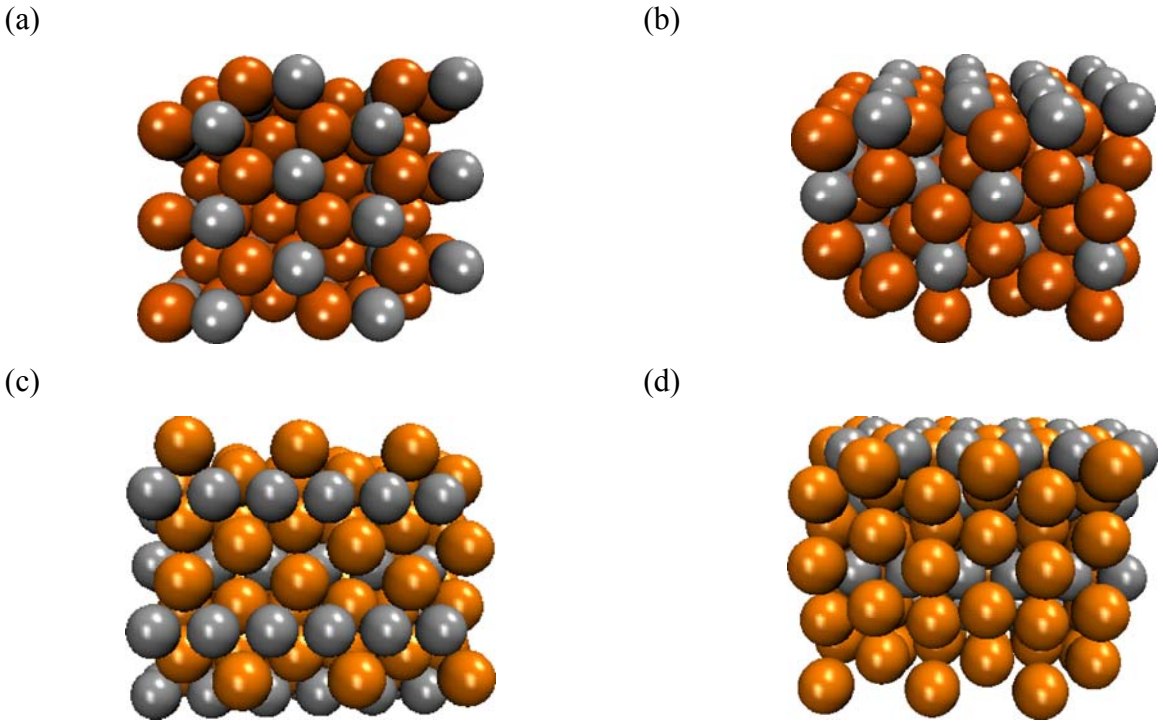

Figure 1: Top (a,c) and side (b,d) views of $PtIn_2$(111) and $PdPb_2$(100) alloys illustrating different arrangement of active sites. Gray (Pt and Pd) and orange (In and Pb) atoms stand for active and inert metals.

The alloys' surfaces with high A content were excluded because they resemble pure A solid

phases, which with exception of copper and nickel are not generally considered to be active for the CO_2 ER. The alloy selection principle is best illustrated on an example. According to the phase diagram Pt and Sn form five stable alloys PtSn, $PtSn_2$, $PtSn_4$, Pt_3Sn, and Pt_3Sn_2 depending on their mutual ratios. First three alloys are Sn rich phases and the last two are Pt rich phases. The Pt rich phases are excluded in the screening because the bare platinum surface produces only hydrogen. []

The concept of isolated reaction centers is not new. It has previously been applied for CO_2 ER on non-metallic catalysts and also for oxygen reduction reaction on metal catalysts [22,23]. Recently, we also examined various metal-functionalized porphyrin-like graphene for ER of CO_2 and CO [22]. This study has in fact prompted us to study metallic systems that share similar features with these graphene-porphyrin composites.

In this work, we set about to investigate the CO_2/CO ER selectivity by examining binary alloys forming from metals that are capable of catalyzing these reactions and metals that have poor HER activity. Establishing a selectivity criterion led us to the discovery of several alloys that are active for the CO ER.

Computational Details

The total energies of different surfaces with adsorbates were calculated with Density Functional Theory (DFT) calculations employing grid-based projector-augmented wave method (GPAW) [25] code integrated with Atomic Simulation Environment (ASE) [26]. The calculations were performed using the RPBE exchange-correlation functional [27]. The occupation of one-electron states was calculated at an electronic temperature of k_BT = 0.1 eV, and later on all the energies were extrapolated to T = 0 K.

Extended model slabs were constructed for all surfaces considered in this study. Successive slabs in the surface normal direction were separated by at least 16 Å of vacuum. In all the calculations, the adsorption was only allowed on one side of the slab. All adsorption sites were considered and only the most stable ones are reported here. Zero point energies and entropies were included in the free energy calculations [28]. For each bulk binary alloy, the lattice constants were optimized within its crystal system. The stable surface structure of each alloy is determined based on its crystal structure (see Supplementary Information).

The computational hydrogen electrode (CHE) method introduced in ref. [29] was used to calculate the free energy levels of all intermediate states. According to this model, the electrode potential, U is taken into account by shifting the electron energy by –eU when transferring an

electron. The potential at which reaction takes place is defined as the maximum positive free energy difference between any two successive electrochemical steps. The calculated potential is the theoretical counterpart to the half-way potential in standard electrochemical measurements. It is not to be confused with the onset potential for the reaction. The reaction onset potential depends on the reactions kinetics which is not included in the present work. It has been shown that the CO2/CO ER activity is qualitatively and quantitatively well described by the calculated binding energies of reaction intermediates. [Andy second paper] This fine agreement points to the fact that the charge transfer and other barriers are material and potential independent. The overpotential is obtained when the equilibrium potential for the reaction is subtracted from the theoretical potential where all the electrochemical steps become downhill in free energy.

A recent study has shown that the RPBE functional is poor in describing the reaction energy of gas-phase molecules containing the OCO backbone [9]. Very recently we have performed similar kind of analysis [22], and found out that the mean absolute error (MAE) for CO(g) and gas-phase molecules containing OCO backbone amounts to 0.04 and 0.43 eV, respectively. Therefore, the CO_2(g) energy is corrected by 0.43 eV, while the correction for CO(g) was neglected.

Results and Discussion

The CO_2 ER results in a range of different products. The product distribution strongly depends on the electrode material and the potential [2,4]. The main reactions are shown below along with their equilibrium potentials vs RHE [31].

$H^+ + e^- \rightarrow 1/2\ H_2$ (g)	U = 0.0 V	(1)
$CO_2 + 2(H^+ + e^-) \rightarrow HCOOH$(aq)	U = 0.20 V	(2)
$CO_2 + 2(H^+ + e^-) \rightarrow CO(g) + H_2O$	U = 0.12 V	(3)
$CO_2 + 4(H^+ + e^-) \rightarrow C + H_2O$(aq)	U = 0.07 V	(4)
$CO_2 + 6(H^+ + e^-) \rightarrow CH_3OH$(aq)	U = 0.03 V	(5)
$CO_2 + 8(H^+ + e^-) \rightarrow CH_4$ (aq)	U = 0.17 V	(6)

From the thermodynamic standpoint, the HER (reaction 1) occurs at U = 0 V vs. RHE. Although the equilibrium potentials for the CO_2 ERs are higher, at negative potentials the HER will most likely prevail due to a much lower reaction overpotential. [Egill and me 2010, Markovic 1997 HER].

Selectivity

Selectivity is the key challenge for making the CO_2 ER catalyst that can convert CO_2/CO to hydrocarbons/alcohols at high turnovers and low overpotentials. Selectivity is defined as the competition among different adsorbates for the same active sites. To promote the selectivity towards valuable CO_2 ER products, the unwanted side reactions should be suppressed. As already mentioned, the main side reaction that should be dodged is the HER. According to Hori's classification, [] the best CO_2 ER catalysts should bind CO and H* neither too strongly nor too weakly. Acoording to Sabatier's principle every catalyst good for the CO_2 ER will be also good for the HER. As the HER is very fast reaction that essentially features no overpotential, it is quite a challenging endeavor to find a catalyst that performs preferentially CO_2 reduction, and that at a reasonable overvoltage. From pure elements copper is the only metal that is able to produce hydrocarbons in significant amounts. Nonetheless, the reaction requires high overpotentials and it is followed by high hydrogen yields. A recent theoretical study revealed the reasons for poor activity and selectivity of Cu. In addition, there is a very small room for improvement in terms of reducing the reaction overpotentials. The hope in the present work is that different surface geometry of the investigated alloys can promote the selectivity and result in higher activities for the CO_2/CO ER.

All the TM assemblies in this work active for the CO_2 ER (Ru, Co, Rh, Ir, Ni, Pd, Pt and Cu) are also active for the HER. The competition between proton discharge reaction, $H^+ + e^- \rightarrow H^*$ and the first electrochemical step in the CO_2 reduction, $CO_2 + H^+ \rightarrow$ *COOH/*OCHO, will determine the outcome of the reaction. In other words, the issue is whether the proton wants to bind to the metal directly or to a CO_2 molecule. The first intermediate in the CO_2 reduction is either *COOH (carboxyl species) or *OCHO (formate species). To elucidate whether any of the catalysts is good for the CO_2 ER, the *COOH/*OCHO and H* binding energies were plotted against each other in Fig. 2a. The reaction energies for the proton discharge reaction to the active site or a CO_2 molecule are equal to the binding energies of H* and *COOH/*OCHO, respectively. The equality arises because CO_2 and H_2 in the gas phase are used as references for binding energies. The energy of a hydrogen molecule can be linked back to the energy of a proton and an electron according to the CHE method $H^+ + e^- = 1/2H_2(g)$. Actually, this is a very neat result because it allows electrochemical reactions to be treated as chemical. For simplicity reasons, the reaction energies will be henceforth denoted as $\Delta G(H^*)$ and $\Delta G(*COOH)/\Delta G(*OCHO)$.

To suppress the proton discharge reaction, the points should fall in the upper part of Fig. 2a, where *COOH/*OCHO binds stronger than H*, i.e. $\Delta G_{COOH*/OCHO*} < \Delta G_{H*}$. Apparently, the binding

of *COOH/*OCHO is so weak that regardless of the surface geometry and composition, the hydrogen poisoning always prevails. Furthermore, as both the H* and *COOH/*OCHO formation steps involve transfer of one electron-proton pair, the difference between their binding energies is not affected by the change in potential.

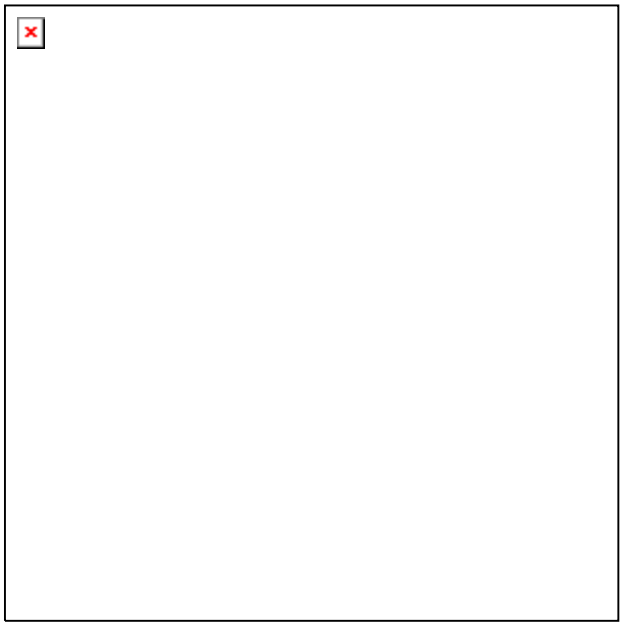

Figure 2. Correlation between the binding free energies of (a) *COOH/*OCHO and (b) *CHO versus H*. CO_2 (g) and H_2 (g) are used as references for *COOH and *OCHO, while CO(g) and H2(g) are used as references for *CHO.

In order to turn the reaction towards the CO_2 reduction products the *COOH/*OCHO binding energies have to be increased significantly. The only way to achieve this is to raise the CO_2 pressure by several orders of magnitude. This will add up huge energy costs to already high costs associated with the reaction at large overpotentials. The entire process will be therefore economically impractical. An alternative solution is to use CO(g) instead of CO_2(g). CO is the inevitable intermediate through which the CO_2 ER reaction must pass in order to produce hydrocarbons or alcohols. Besides, there are ways of getting CO from CO_2 both chemically and electrochemically. Hence, if the CO_2 reduction to CO is combined with the CO reduction to hydrocarbons/alcohols then the overall gain from a combined process might be as good as the direct CO_2 ER.

The first electrochemical step in the CO reduction is the formation of *COH or *CHO intermediate depending on whether hydrogen prefers to bind to the oxygen or the carbon atom. Again, the same approach is used to analyze whether the CO reduction precedes hydrogen

poisoning. As CO(g) and H_2(g) are now used as references, the reaction energy of the first electrochemical step equals the *CHO/*COH binding energy. Looking at Fig. 2b, there are several alloys ($PtIn_2$(111), $PtHg_2$(201), $PtPb_4$(001), $PdBi_2$(111) and $IrSn_2$(111)) above or close to the diagonal on which *CHO binds stronger than H^*, $\Delta G_{CHO*} < \Delta G_{H*}$. To account for the error bar in the DFT calculations we have also included those alloys that are just below the diagonal. For the alloys that are far below the diagonal, the hydrogen poisoning will surely set in before the CO_2 reduction.

The selectivity appears to be highly affected by the number of atoms in the active metal assemblies. Most of the selective alloys feature single active sites. To explain this point further we will compare the activities of $PtIn_2$ with single, isolated sites to that of extended Pt(111) surface. The co-adsorption of *CO and H* on single sites is excluded because only one adsorbate can bind to a metal atom at a time. On the Pt(111) surface the CO saturation coverage is 0.75 ML, while the rest of the surface is free for hydrogen to evolve. Furthermore, further reducing the potential will reduce the CO coverage below 0.75 ML because hydrogen from the proton discharge reaction will expel a more reactive and weakly bound CO state out of the surface. Consequently, this will even more increase the rates of the HER. This is why at very negative potentials on Pt(111) hydrogen is observed as the main reduction product [2,4].

In the introduction we named three conditions that a good catalyst should fulfill. Stability has been included by selecting only the stable binary alloy phases. Furthermore, we have shown there are around 10 alloys that might be selective enough for the CO_2 ER. Activity is the only condition that has not been considered so far. In order to establish at which potential the CO reduction takes place it is necessary to know the potential determining step (pds) for the reaction. The pds is commonly determined by calculating the free energies of all reaction intermediates involved in the reaction. This approach entails extensive use of computer resources and time. To avoid this, we will make an assumption about the reaction's pds. The first electrochemical step, i.e. the CO protonation to either *COH or *CHO is taken to be the pds. This assumption is reasonable given that on all calculated transition metal surfaces this step was always found to be the pds. [9,10] We have mapped out full reaction diagrams for the five selective alloys identified in this study (vide supra and SI). For all of them the assumption of the pds has proven valid. In Fig. 3, the binding free energies of *CHO/*COH are plotted against the corresponding energies for CO. The ideal catalyst with U_{OP} = 0 V by definition should lie right on the diagonal. However, Fig. 3 shows that all the alloys are located far from the diagonal indicating that high overpotentials are needed to reduce

CO*. The overpotential is given by the vertical distance of each alloy point from the diagonal. Noteworthy is also the existence of a nice linear trend between the *CHO/*COH and *CO binding energies. What this trend shows is that the *CHO binds in average 0.8 eV weaker than CO* on all the alloys.

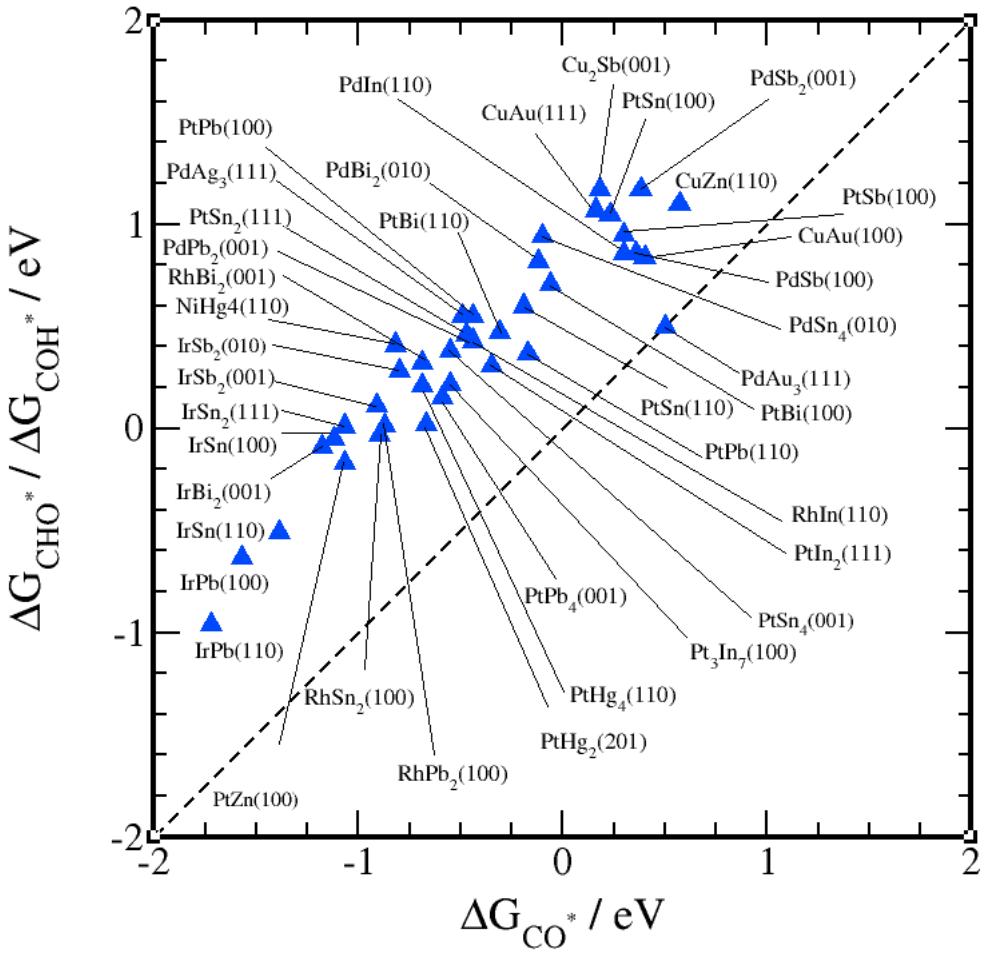

Figure 3. Binding free energies of *CHO/*COH and *CO. The reaction overpotential can be inferred from the plot by measuring the vertical distance from each point to the diagonal.

Activity and reaction product

Starting from an initial database of 40 alloys, applying the selectivity criterion reduced our pool to 5-10 alloys that might be selective enough for the CO reduction. To determine the overpotential for the reaction and the final reaction product, the free energy diagrams (FED) were constructed by calculating all possible reaction intermediates. The FED for $PtIn_2$ is shown in Fig. 4. For the other selective alloys the FEDs are provided in the Supporting Information (SI). As initially assumed, the pds on all the alloys is the reduction of *CO to *CHO. The final reaction product is always methanol. The most active catalyst is $PtIn_2$ followed by $PtHg_2(201)$, $PtPb_4(001)$, $PdBi_2(111)$ and $IrSn_2(111)$. The potentials at which CO is reduced to methanol are -0.67, -0.69, 0.75, 0.95 and 1.08

V, respectively. For comparison purposes, the onset potential for the CO ER on Cu was found to be -0.71 V using the same methodology as applied here. [Andy Peterson] It turns out that $PtIn_2$ and $PtHg_2$ are somewhat more active than Cu. Furthermore, these alloys are more selective in making methanol than copper is in making hydrocarbons. It is important to note that we have investigated just the most abundant crystal termination. Other reaction products cannot be a priori discarded because it is not excluded that other facets have different selectivities.

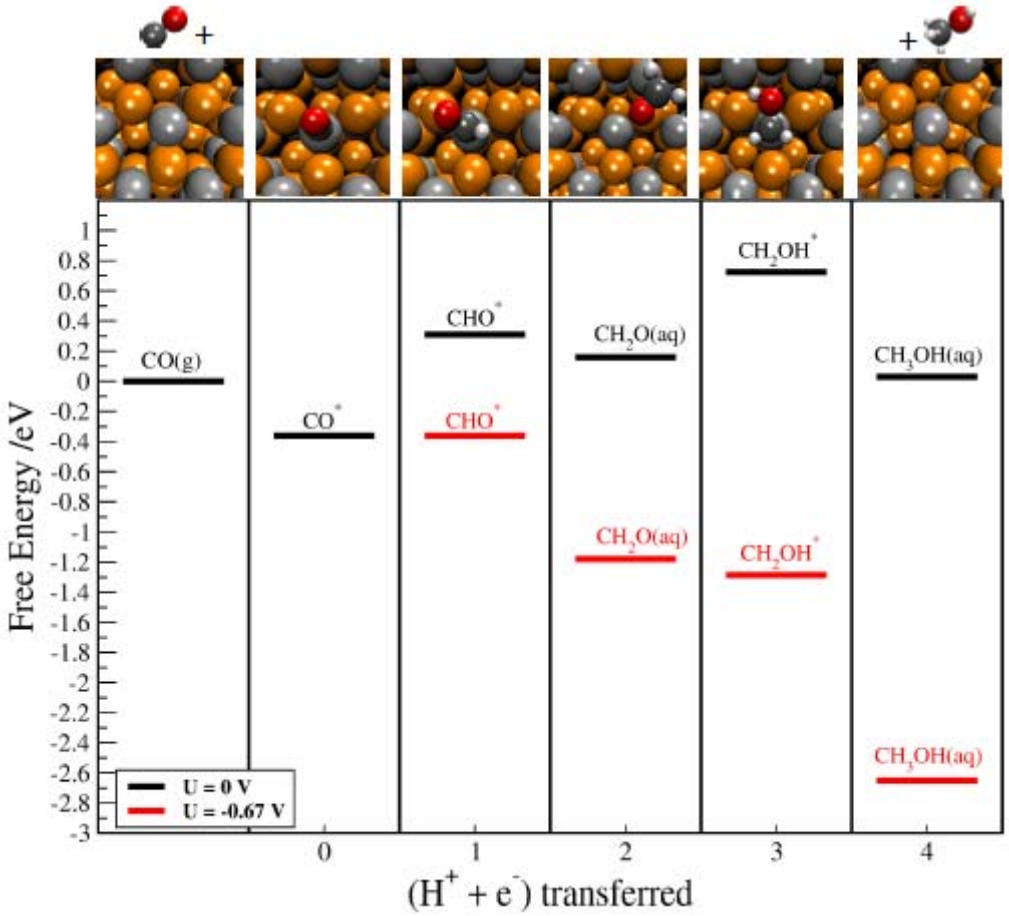

Figure 5. Free energy diagram for the CO reduction on $PtIn_2$. The black and red lines denote the free energy levels at 0 V and at the potential where all the reaction steps become downhill in free energy.

Conclusion

The main challenge for promoting the selectivity is to dodge the parasitic HER. In this work we have proposed a new strategy that exploits the changes in geometric and electronic effects to suppress the HER. The strategy is to provide single atom centers active for the CO_2 ER surrounded by inactive sites for the HER. Counter intuitively high faradaic efficiencies can be achieved by reducing the number of catalytically active sites. Following this strategy, we have examined stable binary bulk alloys forming from TMs that can catalyze the reduction of CO_2 and TM or PTMs that

are poor catalysts for the HER. None of the materials was however selective towards the CO_2 ER. As an alternative we proposed the CO reduction. Among the pool of binary alloys considered in this work (40 in total), only five alloys $PtIn_2$, $PtHg_2$, $PtPb_4$, $PdBi_2$ and $IrSn_2$ were found to be selective enough for the CO reduction. $PtIn_2$ and $PtHg_2$ have even lower reduction overpotentials than Cu, which is the best known metal catalyst for the reaction.

In this work we have not just identified good potential catalysts for the CO reduction but also revealed a class of materials that obeys different trends from those on pure metals. Intermetallic alloys can be used as electrocatalysts for all the reactions in non-oxidizing environments and at very low or negative potentials vs. RHE.

References

1. N. S. Lewis and D. G. Nocera, *Proceedings of the National Academy of Sciences*, 2006, **103**, 15729-15735.
2. M. Gattrell, N. Gupta and A. Co, *Journal of Electroanalytical Chemistry*, 2006, **594**, 1-19.
3. Y. Hori, K. Kikuchi and S. Suzuki, *Chemistry Letters*, 1985, **14**, 1695-1698.
4. Y. Hori, in *Modern Aspects of Electrochemistry*, eds. C. Vayenas, R. White and M. Gamboa-Aldeco, Springer New York, 2008, vol. 42, ch. 3, pp. 89-189.
5. Y. Hori, H. Wakebe, T. Tsukamoto and O. Koga, *Electrochimica Acta*, 1994, **39**, 1833-1839.
6. Y. Hori, K. Kikuchi, A. Murata and S. Suzuki, *Chemistry Letters*, 1986, **15**, 897-898.
7. Y. Hori, A. Murata, R. Takahashi and S. Suzuki, *Journal of the American Chemical Society*, 1987, **109**, 5022-5023.
8. K. J. P. Schouten, Y. Kwon, C. J. M. van der Ham, Z. Qin and M. T. M. Koper, *Chemical Science*, 2011, **2**, 1902-1909.
9. A. A. Peterson, F. Abild-Pedersen, F. Studt, J. Rossmeisl and J. K. Norskov, *Energy & Environmental Science*, 2010, **3**, 1311-1315.
10. A. A. Peterson and J. K. Nørskov, *The Journal of Physical Chemistry Letters*, 2012, **3**, 251-258.
11. C. W. Li and M. W. Kanan, *Journal of the American Chemical Society*, 2012, **134**, 7231-7234.
12. N. M. Marković and P. N. Ross Jr, *Surface Science Reports*, 2002, **45**, 117-229.
13. F. Maroun, F. Ozanam, O. M. Magnussen and R. J. Behm, *Science*, 2001, **293**, 1811-1814.
14. D. Strmcnik, M. Escudero-Escribano, K. Kodama, R. StamenkovicVojislav, A. Cuesta and N. M. Marković, *Nat Chem*, 2010, **2**, 880-885.
15. R. B. Rankin and J. Greeley, *ACS Catalysis*, 2012, **2**, 2664-2672.
16. A. Cuesta, *Journal of the American Chemical Society*, 2006, **128**, 13332-13333.
17. J. K. Norskov, T. Bligaard, J. Rossmeisl and C. H. Christensen, *Nat Chem*, 2009, **1**, 37-46.
18. GreeleyJ, I. E. L. Stephens, A. S. Bondarenko, T. P. Johansson, H. A. Hansen, T. F. Jaramillo, RossmeislJ, ChorkendorffI and J. K. Nørskov, *Nat Chem*, 2009, **1**, 552-556.
19. A. S. Bandarenka, A. S. Varela, M. Karamad, F. Calle-Vallejo, L. Bech, F. J. Perez-Alonso, J. Rossmeisl, I. E. L. Stephens and I. Chorkendorff, *Angewandte Chemie International Edition*, 2012, **51**, 11845-11848.

20. E. Skúlason, V. Tripkovic, M. E. Björketun, S. d. Gudmundsdóttir, G. Karlberg, J. Rossmeisl, T. Bligaard, H. Jónsson and J. K. Nørskov, *The Journal of Physical Chemistry C*, 2010, **114**, 18182-18197.
21. J. Greeley, T. F. Jaramillo, J. Bonde, I. Chorkendorff and J. K. Norskov, *Nat Mater*, 2006, **5**, 909-913.
22. V. Tripkovic, M. Vanin, M. Karamad, M. E. Björketun, K. W. Jacobsen, K. S. Thygesen and J. Rossmeisl, *The Journal of Physical Chemistry C*, 2013, **117**, 9187-9195.
23. F. Calle-Vallejo, J. I. Martínez, J. M. García-Lastra, E. Abad and M. T. M. Koper, *Surface Science*, 2013, **607**, 47-53.
24. M. Pourbaix, 1974, **Second ed.**
25. .
26. J. J. Mortensen, L. B. Hansen and K. W. Jacobsen, *Physical Review B*, 2005, **71**, 035109.
27. B. Hammer, L. B. Hansen and J. K. Nørskov, *Physical Review B*, 1999, **59**, 7413-7421.
28. P. Ferrin, A. U. Nilekar, J. Greeley, M. Mavrikakis and J. Rossmeisl, *Surface Science*, 2008, **602**, 3424-3431.
29. J. K. Nørskov, J. Rossmeisl, A. Logadottir, L. Lindqvist, J. R. Kitchin, T. Bligaard and H. Jónsson, *The Journal of Physical Chemistry B*, 2004, **108**, 17886-17892.
30. J. Rossmeisl, A. Logadottir and J. K. Nørskov, *Chemical Physics*, 2005, **319**, 178-184.
31. C. Oloman and H. Li, *ChemSusChem*, 2008, **1**, 385-391.
32. J. H. Montoya, A. A. Peterson and J. K. Nørskov, *ChemCatChem*, 2013, **5**, 737-742.

---

[1] K. Wang, A. Gasteiger, N.M. Markovic, P.N. Ross, Jr. On the Reaction Pathway for Methanol and Carbon Monoxide Electrooxidation on Pt-Sn Alloy versus Pt-Ru Alloy Surfaces. Electrochim. Acta **1996**, 41, 2587-2593

[2] M Escudero-Escribano, G. J. Soldano, P. Quaino, M. E. Z. Michoff, E. P. M. Leiva, W. Schmickler, A. Cuesta, Electrochim. Acta,

[3] D. Strmcnik, M. Escudero-Escribano, K. Kodama, V.R. Stamenkovic, A. Cuesta, N.M. Markovic, Nat. Chem. 2 (2010) 880.

[4] M. Neurock, M. Janik, A. Wieckowski Faraday Discussions 140 (2008) 363-378.

[5] Cuesta A. At least three contiguous atoms are necessary for CO formation during methanol electrooxidation on platinum. J. Am. Chem. Soc. 128, 13332–13333 (2006).

[6] F. Maroun, F. Ozanam, O. M. Magnussen, R. J. Behm, Science 293 (2001) 1811-1814

[7] M. Neurock, J. Catalysis, 216 (2003) 73-88.

Paper V

Mechanistic pathway in the electrochemical reduction of CO_2 to methanol on RuO_2

Mohammadreza Karamad[1,2], **Heine Anton Hansen**[1,2], **Jan Rossmeisl**[1] **and Jens Nørskov**[1,2,3]

[1]*Center for Atomic-scale Materials Design (CAMD), Department of Physics, Technical University of Denmark, DK-2800 Lyngby, Denmark*

[2]*Department of Chemical Engineering, Stanford University, Palo Alto, CA 94305, USA*

[3]*Center for Interface Science and Catalysis, SLAC National Accelerator Laboratory, 2575 Sand Hill Rd, Menlo Park, CA 94025, USA*

Abstract

RuO_2 have been reported to reduce CO_2 electrochemically to methanol at low overpotential. Herein, we use density functional theory (DFT) to gain insight into mechanism for CO_2 reduction on RuO_2(110). We investigate the thermodynamic stability of various surface terminations in the electrochemical environment and find CO covered surfaces to be particular stable, although their formation might be kinetically limited at mildly reducing conditions.

Next, we identify the lowest free energy pathways for CO_2 reduction on partially reduced RuO_2(110) covered with 0.25 and 0.5 ML CO and find CO_2 is reduced to formic acid which is further reduced to methanol at both CO coverages. The reduction of formic acid to H_2COOH is the thermodynamically most difficult step and becomes exergonic at potentials below -0.35 and -0.65 V vs the reversible hydrogen electrode at 0.25 and 0.5 ML CO* respectively. The mechanism for CO_2 reduction on RuO_2 is therefore different from Cu, where hydrocarbons are formed at high faradaic efficiency through reduction of CO, while formic acid is not reduced.

Our results suggest that by controlling CO* coverage on RuO_2, CO_2 can be reduced to methanol at low overpotentials that can open up an alternative path to reach for highly selective and active electrocatalysts for the reduction of CO_2.

Introduction

Electrochemical reduction of CO_2 has the potential to enable storage power from intermittent renewable energy sources as energy-dense chemical fuels[1]. Research over the past years have focused on the mechanism for CO2 reduction and development of improved catalysts [3–10].

Three criteria should ideally be met by an electro-catalyst: 1) high selectivity towards the desired products, 2) product formation at low reduction overpotential, and 3) the catalyst should be stable at and not degrade over time.

Diverse reaction products have been reported for the electrochemical reduction of CO_2 on pure metals that can be classified based on their binding energies of CO and hydrogen[2,6]. Formic acid (HCOOH) is the main reaction product on metals that bind CO and hydrogen weakly such as Cd and Hg. On the other hand, metals that bind CO and hydrogen strongly, such as Pt and Ni, are selective for evolution of hydrogen. Copper is the only metal with moderate binding energies of CO and hydrogen that can selectively catalyze the reduction of CO_2 to hydrocarbons, primarily CH_4 and C_2H_4, with significant quantities at high current densities. However, electrochemical reduction of CO_2 on Cu is accompanied with high overpotential that hinders this reaction to be energy efficient.Electrochemical reduction of CO_2 to methanol (CH_3OH) is very attractive because methanol as a liquid is conveniently used for

energy storage and automotive applications. applications[11], but unfortunately, methanol has not been observed as a major product in CO_2 reduction on pure metals[6].

By contrast, experiments on metal oxide catalysts, such as RuO_2 and CuO_2 have demonstrated selective reduction of CO_2 to methanol[12–17]. For example, Spataru and co-workers reported electrochemical reduction of CO_2 on boron-doped diamond supported RuO_2 at overpotentials less than 0.4 V and at current densities > 1 mA/Cm^2 [16]. Even though, RuO_2 has been studied extensively for oxygen evolution reaction (OER) both experimentally and theoretically, there are, to the best of our knowledge, no theoretical studies on the reduction of CO_2 on RuO_2 [18,19]. Density functional theory (DFT) calculations in conjunction with the computational hydrogen electrode (CHE) model have been used to elucidate reaction mechanism as well as intermediates that are involved in the reduction of CO_2 on Cu and late transition metals[8,9]. These insights have been used to search for catalysts with improved electrocatalytic activity and selectivity [20].

In the current study, we perform DFT calculations on RuO_2(110) to investigate the mechanism for CO_2 reduction and address why RuO_2 exhibits activity and selectivity different from Cu. To this end, we first identify the thermodynamically stable adsorbate phases of the surface as function of potential under reaction conditions[21,22]. We find that at reducing potentials the RuO_2 surface is partially reduced and structures covered with CO exhibit high thermodynamic stability, although the formation of CO at high coverage may be kinetically limited. Following this, we investigate the reaction mechanism for CO_2 reduction at two different CO coverages on RuO_2(110) and compare the activity and selectivity determining steps on RuO_2(110) to that on Cu(211).

Our results indicate that HCOOH and methanol are the main reaction products of CO_2 reduction on RuO_2(110) surface and that methanol is formed by reduction of HCOOH.

By contrast, hydrocarbons are formed on Cu(211) through the reduction of CO, while HCOOH is not reduced. Additionally, we find the catalytic activity depends on CO* coverage, which proposes a new strategy to tune the catalytic activity and selectivity for CO_2 reduction by controlling CO* coverage on the catalyst surface.

Methods

Computational Details

The total energies of adsorbates on RuO_2 are calculated with Density Functional Theory (DFT) using the grid-based projector-augmented wave method implemented in the GPAW code and integrated with the Atomic Simulation Environment (ASE) [23,24]. Calculations are performed using the RPBE exchange-correlation functional[25].

The calculated lattice constants for RuO_2 in the rutile crystal structure are a = 4.60 Å and c = 3.10 Å, in good agreement with previous reported DFT studies and experimental results [citations needed]. In all calculations, the RuO_2 (110) surface was modeled using a four-layer (2x1) slab. The successive slabs were separated by at least 16Å of vacuum.

For all calculations, adsorption was only allowed on one side of the slab. One-electron states in are populated at an electronic temperature of k_BT = 0.1 eV and energies extrapolated to T=0 K for the slab calculations. The first Brillouin zone was sampled using $4 \times 4 \times 1$ Monkhorst-Pack k-points and a grid spacing of 0.18 A°. In all calculations, the bottom two layers were fixed in their bulk structure while the upper layers and adsorbates were allowed to relax until residual forces in all directions were less than 0.05 eV/Å. Convergence of total energy with respect to grid spacing and the k-point set was considered. The computational hydrogen electrode (CHE) model introduced by Nørskov *et al.* is used to calculate the free energy of adsorbates and reaction intermediates[26]. In this model, the electrode potential, U vs. RHE is taken into

account by shifting the electron energy by –eU when an electron is transferred. According to CHE model, the limiting potential step is the last step that becomes downhill in free energy. Accordingly, the theoretical overpotential is defined as the maximum positive free energy difference between successive electrochemical steps. We note that this model is purely thermodynamic and assumes that kinetic barriers for electron-proton transfer are surmountable at room temperature[27].Zero point energies and entropies were included in the free energy calculations.

Previous studies have shown that the RPBE functional is poor in describing the reaction energy of gas-phase molecules containing the OCO backbone, whereas the PBE functional gives a poor description of the CO molecule[8,20]. It has been shown that the mean absolute error (MAE) for CO(g) and gas-phase molecules containing OCO backbone amounts to 0.04 and 0.45 eV, respectively. Therefore, the energy of CO_2(g) is corrected by 0.45 eV, while no correction is applied to CO(g).

Results and discussions

Surface structures under reaction conditions

The catalytic activity of the RuO_2 catalyst is expected to depend on the atomic structure of the catalyst, which may change as a function of reaction conditions. Experimental *in situ* and *ex situ* XPS studies after the hydrogen evolution on RuO_2 have shown that bulk reduction of RuO_2 to metallic Ru does not occur at potentials above -0.25 V (RHE) as evidenced by the unchanged Ru 3d level characteristic of the Ru(IV) oxidation state.[28,29] However, the same studies show the RuO_2 surface may be partially reduced[28].

To gain insight into which surface structures might be present on RuO_2(110) under reducing conditions, we first consider the thermodynamic stability of surface structures formed in an aqueous electrolyte in the absence of CO_2.

The RuO_2(110) surface may be reduced through exchange of water and protons with the electrolyte through either reduction of surface Oxygen

$$O^* + (H^+ + e^-) \rightarrow {}^*OH \qquad (1)$$

$$^*OH + (H^+ + e^-) \rightarrow H_2O + ^*, \qquad (2)$$

or adsorption of protons

$$^* + (H^+ + e^-) \rightarrow H^*, \qquad (3)$$

where * represents some surface site. The RuO_2(110) surface contains two different sites: the coordinatively unsaturated (cus) site atop the 5-fold coordinated Ru atom and a site bridging two Ru atoms [as shown in Fig. ??]. On the stoichiometric (110) surface, the bridging site is occupied by oxygen, while the cus site is vacant. It is generally found that bridge sites bind adsorbates stronger than cus sites [Rossmeisl].

The stability of RuO_2(110) surface terminations formed by the exchanges (1)-(3) are shown in Figure 1a relative to the surface where the bridging oxygen atoms have been reduced to H_2O. It is seen that below 0 V (RHE) it is favorable to reduce the bridging oxygen atoms present on the stoichiometric surface to H_2O and further cover half of the now empty bridge sites with hydrogen while the cus sites are vacant. The latter configuration therefore corresponds to 0.25-ML H*. At potentials below -0.14 V (RHE) it becomes favorable to cover the bridge sites completely with H*, while still leaving the cus sites vacant, corresponding to a total coverage of 0.5 ML H*. It should

be noted, however, that below 0 V (RHE), the production of H_2 by proton reduction becomes thermodynamically favorable, and below the onset potential for the HER, the hydrogen coverage will be determined by the steady state coverage under HER.

Our finding that the RuO2 surface is partially reduced at zero and negative potentials, is in agreement with XPS experiments[28]. Further reduction of RuO_2 takes place below ca. -0.43 V (RHE).

In the presence of CO_2, intermediates in the reduction of CO_2 may form on the bridge and cus sites. Initially, we focus on intermediates formed by 1 or 2 electron reduction of CO_2. Protonation of CO_2 may happen at an O atom leading to carboxyl

$$* + CO_2 + (H^+ + e^-) \rightarrow COOH*,$$

which may be further reduced to CO

$$COOH* + (H^+ + e^-) \rightarrow CO* + H_2O.$$

This mechanism for CO production has been suggested to take place on Au and Cu. Alternatively, CO_2 may be protonated at the C atom to produce formate:

$$* + CO_2 + (H^+ + e^-) \rightarrow OCHO*,$$

which may be further protonated to formic acid:

$$OCHO* + (H^+ + e^-) \rightarrow HCOOH*,$$

whereas protonation to OCH_2O* is thermodynamically difficult. Figure 1b shows the stability of the above intermediates at various coverages on the partially reduced RuO_2(110) surface. It is seen that CO* acts a thermodynamic sink, with ½ ML CO* becoming the most stable surface termination below 0.28 V (RHE) and the CO* coverage further increasing to ¾ ML CO* below -0.05(?) V (RHE). The reduction of CO* through formation either COH* and CHO* is difficult and requires potentials below -0.?? V (RHE) and -0.?? V(RHE) to become thermodynamically favorable on the surface with 0.75 ML CO. The removal of CO* through desorption will be slow due to the strong CO binding. The desorption energy is ** eV and 0.94 eV at 0.25 ML and 0.75 ML CO respectively. Slow CO desorption is consistent with the low faradaic efficiency observed for CO production on RuO_2(110) [16]. The high stability and the difficult removal of CO* suggests that CO* will build up on the electrode under CO_2 reduction. However, CO* is formed through the COOH* intermediate, which is rather unstable, so the formation of CO* may not always be kinetically accessible. Formation of 0.25 ML COOH* becomes thermodynamically favorable at potentials below -0.22 V (RHE) on the surface where the bridging oxygen atoms have been reduced to H_2O, while formation of 0.25 ML COOH* becomes thermodynamically favorable at potentials below -0.61 V (RHE) on the surface with 0.25 ML CO.

It is usually found that electrochemical reactions have onset close to the limiting potential where reactions steps become thermodynamically favorable [refs]. Consequently, we at least expect the formation of 0.25 ML CO* to be kinetically accessible below -0.22 V (RHE), while the formation of 0.5 ML CO* is kinetically accessible below -0.61 V (RHE). However, depending on the timescale of the electrolysis experiment, these CO* coverages likely become accessible at more positive potentials, because it is not necessary to sustain fast steady state CO* production in order to produce about 0.5 ML CO* to adsorb strongly on the catalyst surface without desorption.

Due to the uncertainties in the CO* coverage under reaction conditions, we investigate in the following the mechanism for CO_2 reduction on the surfaces with 0.25 ML and 0.5 ML CO, which we take as limits of low and high CO coverage respectively.

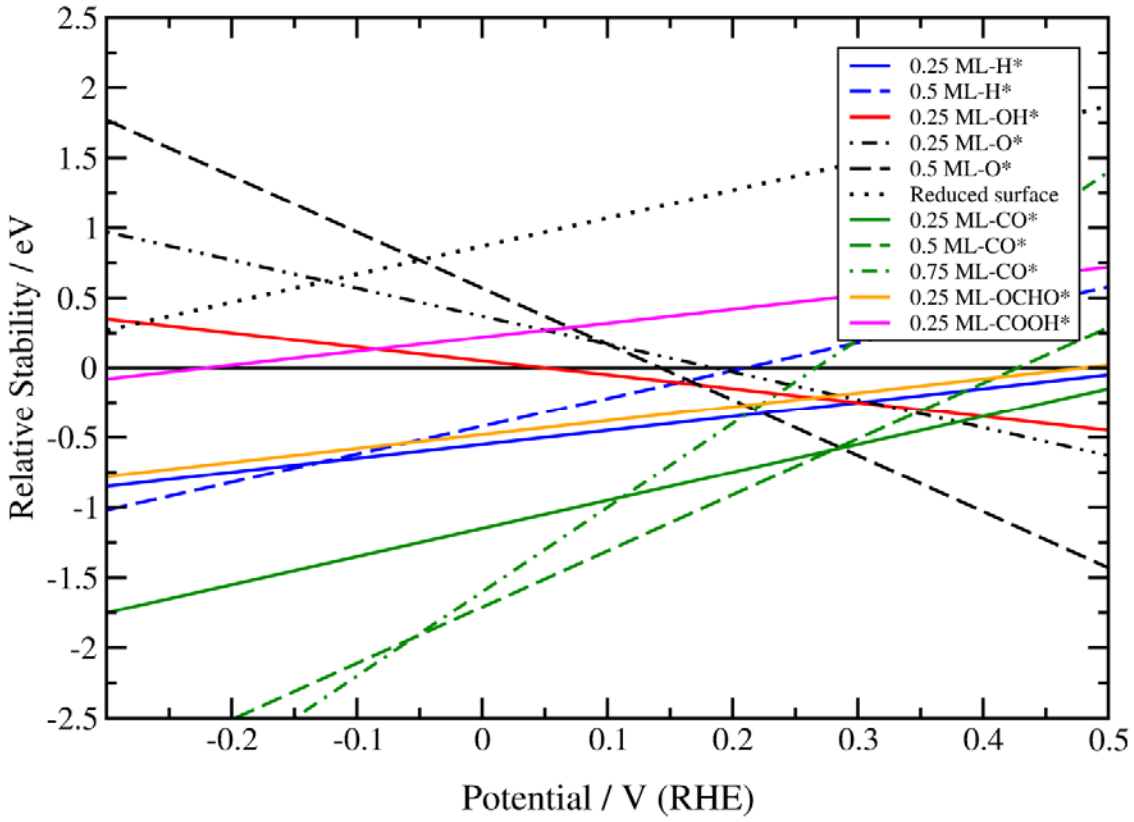

Figure 1. Relative stability of different adsorbates on RuO_2(110) present in the reduction of CO_2 as function of potential. The solid black line denotes partially reduced RuO_2(110) surface where all of the the bridge oxygen atoms are reduced, while the stoichiometric RuO_2 (110) surface is denoted as 0.5 ML-O*. The reduced surface denotes the surface where bulk oxygen atoms are reduced.

Mechanism for CO_2 reduction on $RuO_2(110)$

In this section, we examine the electrocatalytic activity of CO_2 reduction on the surface structures with 0.25 and 0.5 ML CO*. We inspect several possible reaction intermediates and construct free energy diagrams corresponding to different reaction pathways[8]. These free energy diagrams provide insight into the mechanism for CO_2 reduction on RuO_2 as well as activity and selectivity. Here we focus on the lowest-energy pathways for the formation of HCOOH and CH_3OH, at low and high CO* coverage. Full information about competing pathways is provided in the Supplementary Information (SI).

We note that the hydrogen evolution reaction (HER) competes with CO_2 reduction. However, since the focus of the present work is to gain insight into the mechanistic pathway of CO_2 reduction, HER is not considered the present study.

1) Low CO* coverage: Fig. 2 shows the lowest-energy pathways for the formation of HCOOH and CH_3OH at zero potential vs RHE.

   Fig.2a shows the reaction pathway to HCOOH on $RuO_2(110)$ at low CO* coverage . The protonation of CO_2 results in the formation of formate, OCHO, or carboxyl, COOH. While formation of COOH is endergonic by 0.61 eV, formation of OCHO is exergonic by 0.46 eV. The second electron-proton transfer results in the formation of formic acid, HCOOH*, on the bridge site.

   With a desorption energy of 0.9 eV, the desorption rate of HCOOH from the bridge sites will be kinetically slow. We suggest it is possible that HCOOH* will diffuse to the vacant cus sites, followed by reduction of another CO_2 to OCHO* on the now vacated bridge site. The formation of additional OCHO* on the bridge site provides a thermodynamic driving force for the spillover of HCOOH* to the cus sites.

   HCOOH* may desorb more easily from the cus site, where the desorption energy is 0.6 eV.

(a)

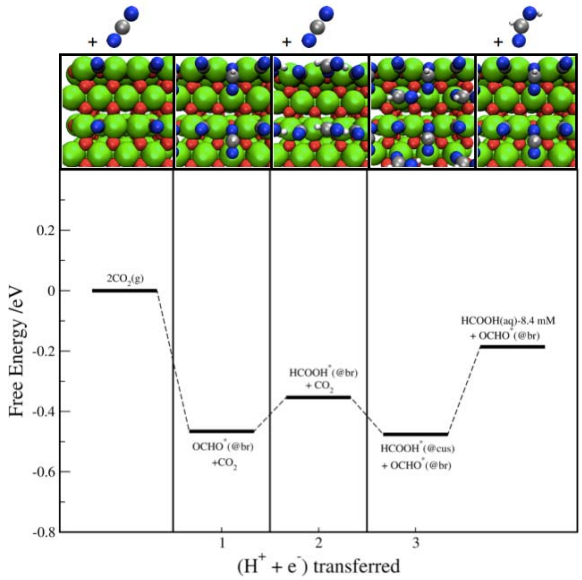

(b)

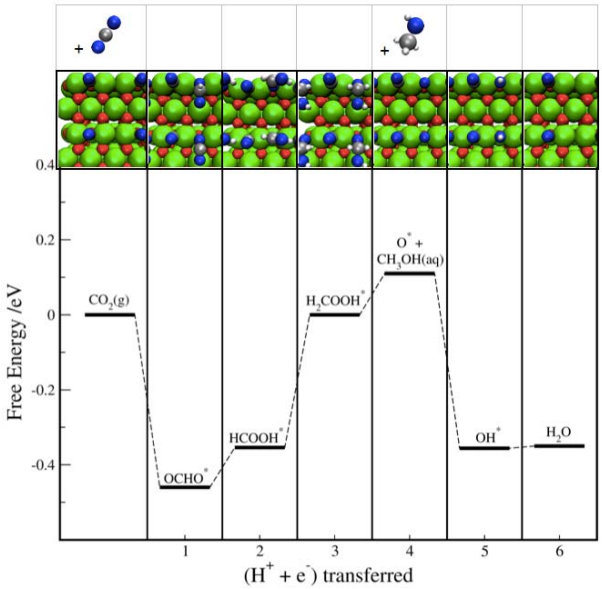

Figure 2. Free energy diagram for the lowest energy pathways to: (a) HCOOH(aq), (b) CH_3OH(aq) at 0 V (RHE) on RuO_2(110) at low CO* coverage. Concentrations of 8.4 and 1 mM were assumed for HCOOH(aq) and CH_3OH(aq) respectively following Ref.[16].

After formation of HCOOH*, further electron-proton transfer to HCOOH* might be possible before breaking an oxygen-carbon bond and producing hydrocarbons or

alcohols. The electron-proton transfer to HCOOH* could take place both before and after diffusion from the bridge to the cus site; however, as shown in the SI, the latter has lower energy pathway than the former. Fig.2b shows the lowest-energy pathway for the reduction of HCOOH*. The electron-proton transfer to HCOOH* results in the formation of H_2COOH*, which adsorbs with the oxygen and hydroxyl ends binding to the bridge and CUS sites respectively. In the next protonation step, methanol forms by protonation of the carbon atom, leaving adsorbed oxygen behind. This oxygen is reduced to water by two electron-proton transfer steps. The potential limiting step in methanol formation from CO_2 is the protonation of HCOOH* to form H_2COOH* and the change in free energy corresponding to this step is 0.35 eV at 0 V (RHE) resulting in a limiting potential of -0.35 V (RHE).

2) High CO* coverage: Fig.3a shows the lowest free-energy pathway to HCOOH on RuO_2(110) at high CO* coverage. Reduction of CO_2 to HCOOH at high CO* coverage regime follows the same reaction pathway as at low CO* coverage. The first electron-proton transfer to CO_2 results in the formation of formate, OCHO, that is thermoneutral. On the other hand, formation of COOH* is endergonic by 0.9 eV, hindering formation of CO* at significant rates and hence increase in the coverage of CO* at low overpotentials. The second electron-proton transfer results in the formation of formic acid, HCOOH*, adsorbed on the bridge. Diffusion of HCOOH* from bridge to neighboring CUS site, followed by the adsorption of OCHO on the bridge site is thermodynamically unfavorable and, HCOOH* may desorb directly from the bridge site.

(a)

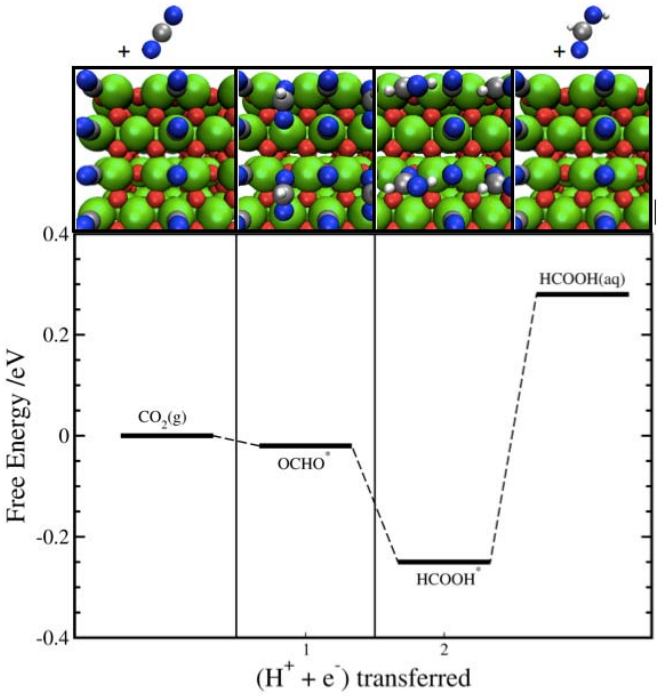

(b)

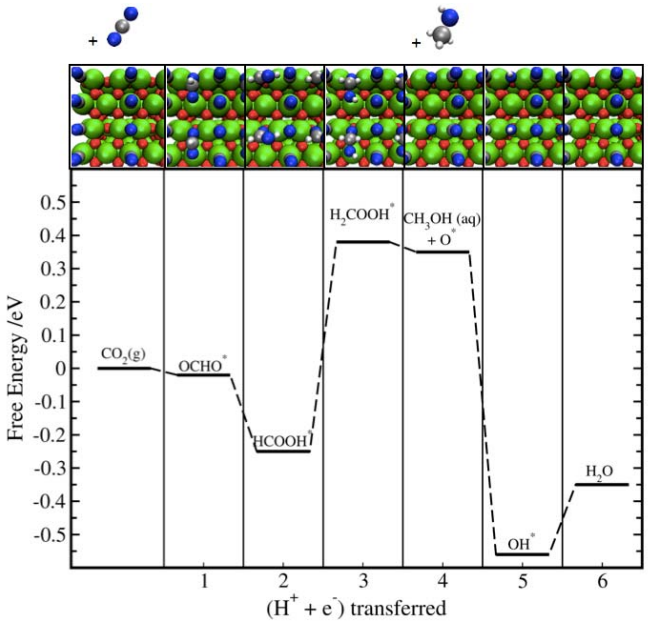

Figure 3. Calculated free energy diagram for the lowest energy pathways to: (a) HCOOH(aq), (b) CH_3OH(aq) at 0 V (RHE) on RuO_2(110) at high CO* coverage regime.

Further protonation of HCOOH* follows the same reaction pathway through H_2COOH* as for low CO* coverage and the final reaction product is methanol, as shown in Fig. 3b. Similar to low CO* coverage, the potential limiting step is the protonation of HCOOH* to H_2COOH*; however the change in free energy corresponding to this step is 0.65 eV at 0 V (RHE) resulting in a more negative limiting potential of -0.65 V (RHE) for methanol formation at high CO coverage.

3.3. CO_2 reduction: Cu(211) versus RuO_2(110)

In this section we compare the mechanism for CO_2 on RuO_2(110) to the mechanism on Cu(211). Fig. 4 shows the calculated lowest-energy pathways for CO_2 reduction on Cu(211) [30] and RuO_2(110) at low and high CO* coverage. The free energy diagrams corresponding to other possible reaction pathways for CO_2 reduction at low and high CO* coverage on RuO_2(110) are provided in the SI.

As can be seen from Fig.4, reduction of CO_2 on Cu and RuO_2 proceed through different pathways. On RuO_2, reduction of CO_2 proceeds through HCOOH; its subsequent protonation to H_2COOH* is the potential limiting step, and CO is not a reaction intermediate in the production of CH_3OH. On the other hand, in the reduction of CO_2 on Cu, HCOOH is not an intermediate in the production of CH_4, C_2H_4 and CH_3CH_2OH [Hori, Frese]. Instead, CO* is a key intermediate; it's protonation to CHO* is the potential limiting step for formation of CH_4, C_2H_4 and CH_3CH_2OH [Peterson2010, Montoya2013]. Most notably, different products are produced in the reduction of CO_2 on Cu and RuO_2: while methanol does not form in the reduction of CO_2 on Cu and methane and ethylene are the main reaction products, methanol is the only product in the reduction of CO_2 on RuO_2 apart from HCOOH.

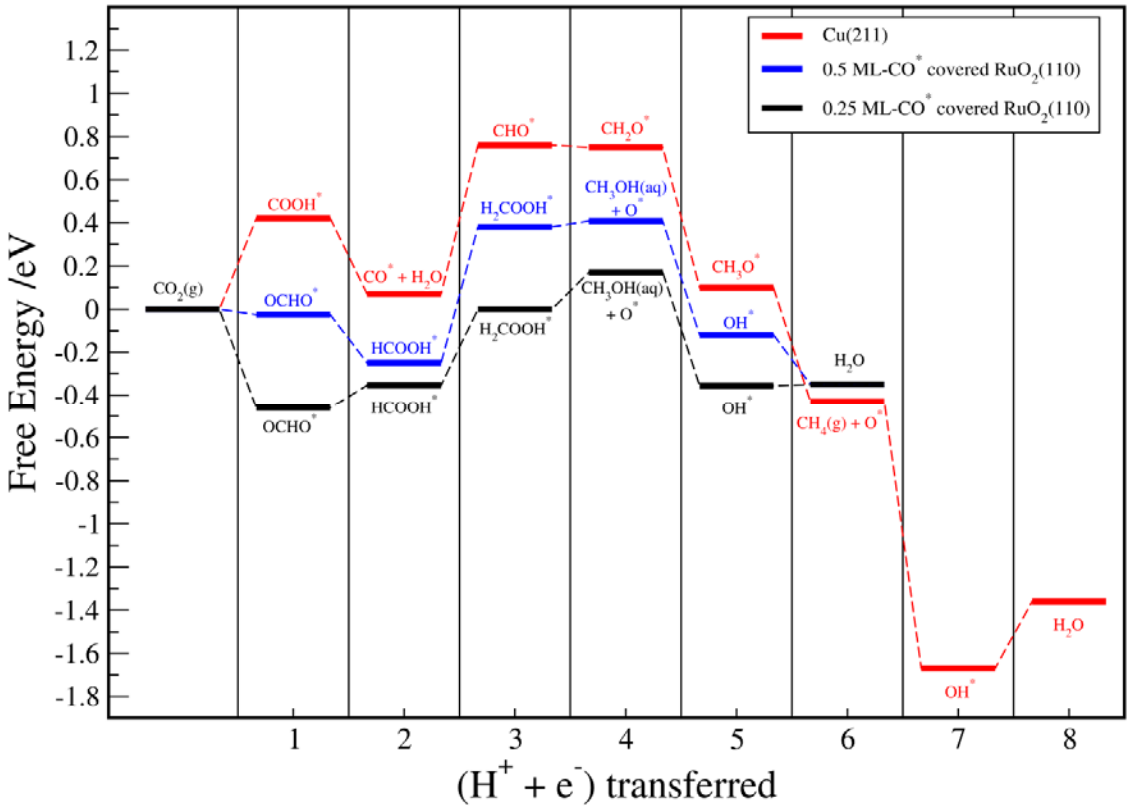

Figure 4. Calculated free energy diagram for the lowest energy pathways in the reduction of CO_2 on Cu(211) at low and high CO* coverage on RuO_2(110) at 0 V (RHE).

The calculations also predict higher catalytic activity for CO_2 reduction on RuO_2 than on Cu. The theoretical overpotentials for CO_2 reduction on RuO_2 are 0.35 and 0.61 V (RHE) for low and high CO* coverage regimes respectively.

Additionally, it is worth comparing reduction of CO_2 on low and high CO* covered regimes. Though the reduction of CO_2 on both low and high CO* covered regimes proceeds through the same reaction pathway with similar potential-limiting steps, the overpotential associated with low CO* coverage regime is lower than the one associated with high CO* coverage regime. We attribute the difference in overpotential to the lower repulsion from adsorbed CO on the neighboring sites.

Conclusion

Experimental studies have shown CO_2 is reduced to methanol on RuO_2. In the current theoretical study, we find that partial reduction of RuO_2 surface is thermodynamically favorable at negative potentials. Our calculations show that 0.25 ML CO* and 0.5 ML CO* covered RuO_2 surface structures, exhibit high thermodynamic stability during CO_2 reduction.

We find that the reduction of CO_2 at low and high CO* coverage follow identical reaction pathways and have identical potential-limiting steps. At both CO* coverages, CO* is a spectator and not as an intermediate, and methanol is the final product of CO_2 reduction. The reduction of CO_2 to methanol proceeds through reduction of formic acid, HCOOH*, whose protonation is the potential limiting step. The calculated theoretical overpotentials for reduction of CO_2 to methanol are 0.41 and 0.71 V at low and high CO* coverage respectively.

This pathway for CO_2 reduction on RuO_2 is in stark contrast with that of on Cu: 1) methane and ethylene is the main reduction product for the reduction of CO_2 on Cu, 2) HCOOH* is not an intermediate in the reduction of CO_2 to methane and ethane, 3) Formic acid is not reduced, 4) CO* is an inevitable intermediate whose protonation to CHO* is potential-limiting step.

Our results suggest that by controlling CO* coverage on RuO_2, CO_2 can be reduced to methanol at low overpotential. This proposes a new strategy to tune the catalytic activity and selectivity for CO_2 reduction by controlling CO* coverage on the catalyst surface. We believe that this can open up an alternative path to search for highly selective and active electrocatalyst for the reduction of CO_2 to methanol

References:

1. Lewis, N. S. & Nocera, D. G. Powering the planet: chemical challenges in solar energy utilization. *Proceedings of the National Academy of Sciences of the United States of America* **103,** 15729–35 (2006).

2. Gattrell, M., Gupta, N. & Co, A. A review of the aqueous electrochemical reduction of CO2 to hydrocarbons at copper. *Journal of Electroanalytical Chemistry* **594,** 1–19 (2006).

3. Hori, Y., Kikuchi, K., Murata, A. & Suzuki, S. PRODUCTION OF METHANE AND ETHYLENE IN ELECTROCHEMICAL REDUCTION OF CARBON DIOXIDE AT COPPER ELECTRODE IN AQUEOUS HYDROGENCARBONATE SOLUTION. *Chemistry Letters* **15,** 897–898 (1986).

4. Hori, Y., Murata, A., Takahashi, R. & Suzuki, S. Electroreduction of carbon monoxide to methane and ethylene at a copper electrode in aqueous solutions at ambient temperature and pressure. *Journal of the American Chemical Society* **109,** 5022–5023 (1987).

5. Hori, Y., Murata, A. & Takahashi, R. Formation of hydrocarbons in the electrochemical reduction of carbon dioxide at a copper electrode in aqueous solution. *Journal of the Chemical Society, Faraday Transactions 1* **85,** 2309 (1989).

6. Hori, Y. Electrochemical CO 2 Reduction on Metal Electrodes. 89–189

7. Schouten, K. J. P., Kwon, Y., van der Ham, C. J. M., Qin, Z. & Koper, M. T. M. A new mechanism for the selectivity to C1 and C2 species in the electrochemical reduction of carbon dioxide on copper electrodes. *Chemical Science* **2,** 1902 (2011).

8. Peterson, A. A., Abild-Pedersen, F., Studt, F., Rossmeisl, J. & Nørskov, J. K. How copper catalyzes the electroreduction of carbon dioxide into hydrocarbon fuels. *Energy & Environmental Science* **3,** 1311 (2010).

9. Peterson, A. A. & Nørskov, J. K. Activity Descriptors for CO 2 Electroreduction to Methane on Transition-Metal Catalysts. *The Journal of Physical Chemistry Letters* **3,** 251–258 (2012).

10. Durand, W. J., Peterson, A. a., Studt, F., Abild-Pedersen, F. & Nørskov, J. K. Structure effects on the energetics of the electrochemical reduction of CO2 by copper surfaces. *Surface Science* **605,** 1354–1359 (2011).

11. Olah, G. a. Beyond oil and gas: the methanol economy. *Angewandte Chemie (International ed. in English)* **44,** 2636–9 (2005).

12. Le, M. *et al.* Electrochemical Reduction of CO2 to CH3OH at Copper Oxide Surfaces. *Journal of The Electrochemical Society* **158,** E45 (2011).

13. Frese, K. W. Electrochemical Reduction of C02 at Intentionally Oxidized Copper Electrodes. **138,** 3338–3344 (1991).

14. Bandi, A. Electrochemical Reduction of Carbon Dioxide on Conductive Metallic Oxides. *Journal of The Electrochemical Society* **137,** 2157 (1990).

15. Popić, J. P., Avramov-Ivić, M. L. & Vuković, N. B. Reduction of carbon dioxide on ruthenium oxide and modified ruthenium oxide electrodes in 0.5 M NaHCO3. *Journal of Electroanalytical Chemistry* **421,** 105–110 (1997).

16. Spataru, N., Tokuhiro, K., Terashima, C., Rao, T. N. & Fujishima, A. Electrochemical reduction of carbon dioxide at ruthenium dioxide deposited on boron-doped diamond. *Journal of Applied Electrochemistry* **33,** 1205–1210 (2003).

17. Qu, J., Zhang, X., Wang, Y. & Xie, C. Electrochemical reduction of CO2 on RuO2/TiO2 nanotubes composite modified Pt electrode. *Electrochimica Acta* **50,** 3576–3580 (2005).

18. Rossmeisl, J., Qu, Z.-W., Zhu, H., Kroes, G.-J. & Nørskov, J. K. Electrolysis of water on oxide surfaces. *Journal of Electroanalytical Chemistry* **607,** 83–89 (2007).

19. Man, I. C. *et al.* Universality in Oxygen Evolution Electrocatalysis on Oxide Surfaces. *ChemCatChem* **3,** 1159–1165 (2011).

20. Tripkovic, V. *et al.* Electrochemical CO 2 and CO Reduction on Metal-Functionalized Porphyrin-like Graphene. *The Journal of Physical Chemistry C* **117,** 9187–9195 (2013).

21. Hansen, H. A., Rossmeisl, J. & Nørskov, J. K. Surface Pourbaix diagrams and oxygen reduction activity of Pt, Ag and Ni(111) surfaces studied by DFT. *Physical chemistry chemical physics : PCCP* **10,** 3722–30 (2008).

22. Su, H.-Y. *et al.* Identifying active surface phases for metal oxide electrocatalysts: a study of manganese oxide bi-functional catalysts for oxygen reduction and water oxidation catalysis. *Physical chemistry chemical physics : PCCP* **14,** 14010–22 (2012).

23. Mortensen, J., Hansen, L. & Jacobsen, K. Real-space grid implementation of the projector augmented wave method. *Physical Review B* **71,** 035109 (2005).

24. Atomic Simulation Environment (ASE); Center for Atomic-scale Materials Design (CAMD), Technical University of Denmark, Lyngby. https://wiki.fysik.dtu.dk/ase.

25. Hammer, B., Hansen, L. & Nørskov, J. Improved adsorption energetics within density-functional theory using revised Perdew-Burke-Ernzerhof functionals. *Physical Review B* **59,** 7413–7421 (1999).

26. Nørskov, J. K. *et al.* Origin of the Overpotential for Oxygen Reduction at a Fuel-Cell Cathode. *The Journal of Physical Chemistry B* **108,** 17886–17892 (2004).

27. Skúlason, E. *et al.* Modeling the Electrochemical Hydrogen Oxidation and Evolution Reactions on the Basis of Density Functional Theory Calculations. *The Journal of Physical Chemistry C* **114,** 18182–18197 (2010).

28. K□tz, E. R. & Stucki, S. Ruthenium dioxide as a hydrogen-evolving cathode. *Journal of Applied Electrochemistry* **17,** 1190–1197 (1987).

29. Rochefort, D., Dabo, P., Guay, D. & Sherwood, P. M. A. XPS investigations of thermally prepared RuO2 electrodes in reductive conditions. *Electrochimica Acta* **48,** 4245–4252 (2003).

30. Hansen, H. a. *et al.* Electroreduction of Methanediol on Copper. *Catalysis Letters* **143,** 631–635 (2013).